

# **Molecular Dynamics Simulations in Graphite and Carbon Materials**

Helen Jayne Christie

Materials and Physics Research Centre  
School of Computing, Science and Engineering  
University of Salford, Salford, UK

Submitted in partial fulfillment of the requirements of  
the degree of Doctor of Philosophy

2014

This thesis is dedicated to  
my Mum, Dad,  
Annette and Auntie Fiona

# Contents

List of Figures . . . . .	iii
List of Tables . . . . .	xi
Acknowledgments . . . . .	xii
<b>Abstract</b>	<b>xiii</b>
<b>1 Introduction</b>	<b>1</b>
1.1 Brief History of Nuclear Power . . . . .	3
1.2 Theory of Nuclear Power . . . . .	6
1.3 Reactors in the UK . . . . .	8
1.4 Graphite . . . . .	12
1.5 Thesis Plan . . . . .	14
<b>2 Theory</b>	<b>15</b>
2.1 Equations of Motion . . . . .	16
2.2 Molecular Dynamics Programs . . . . .	18
2.3 Integrating the Equations of Motion . . . . .	21
2.4 Potentials . . . . .	23
2.5 The Environment Dependent Interatomic Potential for Carbon (EDIP) . . . . .	27
2.6 The Ziegler-Biersack-Littmarck Potential (ZBL) . . . . .	32
2.7 Switching Function . . . . .	34
2.8 Kinchin and Pease Model . . . . .	36
2.9 Literature Review . . . . .	41
<b>3 Methodology</b>	<b>44</b>
3.1 Neutron Collisions . . . . .	45
3.2 The Simulation Cell . . . . .	47
3.2.1 Thermal Spike Regime . . . . .	47
3.2.2 Cascade Simulations . . . . .	50
3.2.3 Threshold Displacement Energy Simulations . . . . .	52
3.2.4 Carbon Materials Cascade Simulations . . . . .	53
3.3 The Thomson Problem . . . . .	54
3.4 Physical Properties of Graphite Cascades . . . . .	57
3.5 Thermal Spike and Cascade Simulations in Graphite . . . . .	59
<b>4 Cascades In Graphite</b>	<b>63</b>
4.1 Thermal Spike Results . . . . .	63

4.2	Preliminary Cascade Results . . . . .	66
4.3	Qualitative Cascade Data . . . . .	70
4.3.1	Individual Cascades . . . . .	70
4.3.2	Extreme Individual Cascades . . . . .	87
4.3.3	High Temperature Cascades . . . . .	97
4.4	Quantitative Cascade Data . . . . .	103
4.5	Threshold Energy Results . . . . .	115
<b>5</b>	<b>Cascades in Non-Graphitic Carbon Materials</b>	<b>121</b>
5.1	Diamond . . . . .	121
5.1.1	Diamond Cascade Simulations . . . . .	124
5.2	Amorphous Carbon Analysis . . . . .	141
5.2.1	High Density Amorphous Carbon . . . . .	141
5.2.2	Low Density Amorphous Carbon . . . . .	146
5.3	Glassy Carbon Analysis . . . . .	150
<b>6</b>	<b>Discussion</b>	<b>156</b>
6.1	Graphite and Diamond . . . . .	162
6.2	Carbon Materials . . . . .	168
6.2.1	High and Low Density Amorphous Carbons . . . . .	168
6.2.2	Glassy Carbon . . . . .	170
6.3	Future Work . . . . .	173
<b>7</b>	<b>Conclusion</b>	<b>174</b>
	<b>References</b>	<b>176</b>
	<b>Appendices</b>	<b>184</b>
<b>I</b>	<b>Cascades Through Graphite</b>	<b>184</b>
I	Low Energy Cascades Through Graphite . . . . .	187
II	Mid-Range Energy Cascades Through Graphite . . . . .	189
III	High Energy Cascades Through Graphite . . . . .	193
<b>II</b>	<b>Cascades Through Carbon Materials</b>	<b>198</b>
<b>III</b>	<b>Publications</b>	<b>206</b>

# List of Figures

1.1	Chicago pile . . . . .	4
1.2	Sellafield nuclear power station . . . . .	5
1.3	Fission of uranium . . . . .	7
1.4	Advanced-Gas Cooled reactor . . . . .	8
1.5	Very High Temperature reactor . . . . .	9
1.6	Nuclear reactors . . . . .	10
1.7	Stacking formation of graphite . . . . .	12
2.1	Molecular Dynamics Flow Chart . . . . .	18
2.2	Molecular Dynamics Time Scale . . . . .	22
2.3	Coulomb potential and Ziegler-Biersack-Littmarck potential . . . . .	33
2.4	Switching function between EDIP and ZBL . . . . .	34
2.5	Different values for EDIP and ZBL . . . . .	35
2.6	The Kinchin and Pease model for hard sphere collisions . . . . .	37
2.7	A branch of the Kinchin and Pease collision cascade . . . . .	37
2.8	Kinchin-Pease, Norgett-Robinson-Torrens models . . . . .	40
3.1	Graph showing the fraction of fission neutrons as a function of neutron energy . . . . .	46
3.2	Probability of fission in uranium-235 and uranium-238 . . . . .	46
3.3	The path of a primary knock-on atom through a cell . . . . .	47
3.4	The cell employed during thermal spike simulations . . . . .	49
3.5	The cell employed during cascade simulations . . . . .	51
3.6	Thomson problem points selected for cascade simulations . . . . .	55
3.7	A graph indicating the numerical values selected to simulate the thermal spike in graphite . . . . .	59
3.8	A graph showing the electronic stopping power of carbon in carbon . . . . .	60

4.1	Thermal spike simulation through graphite with initial energy $6 \times 10^3$ eV and initial cell temperature of $300^\circ\text{C}$ . . . . .	63
4.2	Thermal spike simulation through graphite with initial energy $2.5 \times 10^4$ eV and initial cell temperature of $300^\circ\text{C}$ . . . . .	64
4.3	Thermal spike simulation through graphite with initial energy $1.0 \times 10^5$ eV and initial cell temperature of $300^\circ\text{C}$ . . . . .	65
4.4	Preliminary collision cascade simulation through graphite with initial PKA energy of 500 eV, initial PKA temperature $300^\circ\text{C}$ and initial PKA direction $x = 1, y = 2$ and $z = 1$ . . . . .	66
4.5	Preliminary high energy collision cascade through graphite with initial PKA energy of 1000 eV, initial temperature $300^\circ\text{C}$ and initial PKA direction $x = 1, y = 2$ and $z = 1$ . . . . .	68
4.6	Graphite cascade with initial PKA energy 50 eV, initial temperature $300^\circ\text{C}$ and initial PKA direction 15 from table 3.1 . . . . .	70
4.7	Graph indicating the number of defects during a cascade with initial PKA energy 50 eV, initial temperature $300^\circ\text{C}$ and initial PKA direction 15 from table 3.1 . . . . .	71
4.8	Distance travelled by atoms during a graphite cascade with initial PKA energy 50 eV, initial temperature $300^\circ\text{C}$ and initial PKA direction 15 from table 3.1. . . . .	71
4.9	Graphite cascade with initial PKA energy 250 eV, initial temperature $300^\circ\text{C}$ and initial PKA direction 2 from table 3.1. . . . .	72
4.10	Graph indicating the number of defects during a cascade with initial PKA energy 250 eV, initial temperature $300^\circ\text{C}$ and initial PKA direction 2 from table 3.1. . . . .	73
4.11	Distance travelled by atoms during a graphite cascade with initial PKA energy 250 eV, initial temperature $300^\circ\text{C}$ and initial PKA direction 2 from table 3.1. . . . .	74
4.12	Graphite cascade with initial PKA energy 500 eV, initial temperature $300^\circ\text{C}$ and initial PKA direction 2 from table 3.1. . . . .	75
4.13	Graph indicating the number of defects during a cascade with initial PKA energy 500 eV, initial temperature $300^\circ\text{C}$ and initial PKA direction 2 from table 3.1. . . . .	76
4.14	Distance travelled by atoms during a graphite cascade with initial PKA energy 500 eV, initial temperature $300^\circ\text{C}$ and initial PKA direction 2 from table 3.1. . . . .	77
4.15	Graphite cascade with initial PKA energy 1000 eV, initial temperature $300^\circ\text{C}$ and initial PKA direction 15 from table 3.1. . . . .	78
4.16	Graph indicating the number of defects during a cascade with initial PKA energy 1000 eV, initial temperature $300^\circ\text{C}$ and initial PKA direction 15 from table 3.1. . . . .	79

4.17	Distance travelled by atoms during a graphite cascade with initial PKA energy 1000 eV, initial temperature 300°C and initial PKA direction 15 from table 3.1. . . . .	80
4.18	Graphite cascade with initial PKA energy 1500 eV, initial temperature 300°C and initial PKA direction 15 from table 3.1. . . . .	81
4.19	Graph indicating the number of defects during a cascade with initial PKA energy 1500 eV, initial temperature 300°C and initial PKA direction 15 from table 3.1. . . . .	82
4.20	Distance travelled by atoms during a graphite cascade with initial PKA energy 1500 eV, initial temperature 300°C and initial PKA direction 15 from table 3.1. . . . .	83
4.21	Graphite cascade with initial PKA energy 2000 eV, initial temperature 300°C and initial PKA direction 2 from table 3.1. . . . .	83
4.22	Graph indicating the number of defects during a cascade with initial PKA energy 2000 eV, initial temperature 300°C and initial PKA direction 15 from table 3.1. . . . .	84
4.23	Distance travelled by atoms during a graphite cascade with initial PKA energy 2000 eV, initial temperature 300°C and initial PKA direction 2 from table 3.1. . . . .	85
4.24	Graphite cascade with initial PKA energy 500 eV, initial temperature 300°C and initial PKA direction $x = 0.00$ , $y = 0.90$ and $z = 0.00$ . . . . .	87
4.25	Graph indicating the number of defects during a cascade with initial PKA energy 500 eV, initial temperature 300°C and initial PKA direction $x = 0.00$ , $y = 0.90$ and $z = 0.00$ . . . . .	88
4.26	Distance travelled by atoms during a graphite cascade with initial PKA energy 500 eV, initial temperature 300°C and initial PKA direction $x = 0.00$ , $y = 0.90$ and $z = 0.00$ . . . . .	89
4.27	Graphite cascade with initial PKA energy 500 eV, initial temperature 300°C and initial PKA direction $x = 0.00$ , $y = 0.00$ and $z = -1.00$ . . . . .	90
4.28	Distance travelled by atoms during a graphite cascade with initial PKA energy 500 eV, initial temperature 300°C and initial PKA direction $x = 0.00$ , $y = 0.00$ and $z = -1.00$ . . . . .	91
4.29	Distance travelled by atoms during a graphite cascade with initial PKA energy 500 eV, initial temperature 300°C and initial PKA direction $x = 0.00$ , $y = 0.00$ and $z = -1.00$ . . . . .	92
4.30	Graph indicating the number of defects during a cascade with initial PKA energy 500 eV, initial temperature 300°C and initial PKA direction $x = 0.00$ , $y = 0.00$ and $z = -1.00$ . . . . .	93

4.31	Graphite cascade with initial PKA energy 500 eV, initial temperature 300°C and initial PKA direction $x = 0.00$ , $y = 0.00$ and $z = 1.00$ . . . . .	94
4.32	Graph indicating the number of defects during a cascade with initial PKA energy 500 eV, initial temperature 300°C and initial PKA direction $x = 0.00$ , $y = 0.00$ and $z = 1.00$ . . . . .	95
4.33	Distance travelled by atoms during a graphite cascades with initial PKA energy 500 eV, initial temperature 300°C and initial PKA direction $x = 0.00$ , $y = 0.00$ and $z = 1.00$ . . . . .	95
4.34	Graphite cascades with initial PKA energy 1000 eV, initial temperatures 900°C and 300°C and initial PKA direction 1 from table 3.1. . . . .	97
4.35	Graph indicating the number of defects during cascades with initial PKA energy 1000 eV, initial temperatures 900°C and 300°C and initial PKA direction 1 from table 3.1. . . . .	98
4.36	Graphite cascades with initial PKA energy 1000 eV, initial temperatures 900°C and 300°C and and initial PKA direction 1 from table 3.1. . . . .	99
4.37	Graphite cascades with initial PKA energy 1000 eV, initial temperatures 900°C and 300°C and initial PKA direction 15 from table 3.1. . . . .	100
4.38	Graph indicating the number of defects during cascades with initial PKA energy 1000 eV, initial temperatures 900°C and 300°C and initial PKA direction 15 from table 3.1. . . . .	101
4.39	Graphite cascades with initial PKA energy 1000 eV, initial temperatures 900°C and 300°C and initial PKA direction 15 from table 3.1. . . . .	102
4.40	Kinetic energy of the energetic atoms as a function of time in a 1000 eV graphite cascade . . . . .	103
4.41	The number of atoms with kinetic energy greater than 10 eV and 1 eV . . . . .	104
4.42	Dependence of $t_{max}$ as a function of PKA energy. . . . .	105
4.43	A plot of the 20 simulated directions, initial PKA energy and final number of defects . . . . .	106
4.44	A plot of the 20 simulated directions, initial PKA energy and final number of defects . . . . .	107
4.45	Number of displaced atoms as a function of PKA energy (Nogrett-Robinson-Torrens) . . . . .	109
4.46	Number of displacements as a function of PKA energy based on simulation results . . . . .	110

4.47	Maximum number of displaced atoms (Kinchin and Pease) . . .	111
4.48	Cascade length and PKA range . . . . .	112
4.49	A plot of the 20 simulated directions, initial PKA energy and final number of defects . . . . .	114
4.50	The average final PKA displacement . . . . .	114
4.51	Grafted Interstitial . . . . .	115
4.52	Split Interstitial . . . . .	116
4.53	Bi-Pentagon I <sub>2</sub> Grafted Intralayer Bridge Interstitial . . . . .	116
4.54	Bi-Pentagon Interlayer Bridge Interstitial . . . . .	117
4.55	Bent Interlayer Bridge Interstitial . . . . .	117
4.56	Single Interlayer Interstitial . . . . .	118
4.57	Vacancy . . . . .	118
4.58	Stone-Wales Vacancy . . . . .	119
5.1	A thermal spike through diamond with initial energy of $6 \times 10^3$ eV and initial cell temperature 300°C . . . . .	122
5.2	A thermal spike through diamond with initial energy of $2.5 \times$ $10^4$ eV and initial cell temperature 300°C . . . . .	122
5.3	A thermal spike through diamond with initial energy of $1 \times 10^5$ eV and initial cell temperature 300°C . . . . .	123
5.4	Preliminary diamond collision cascade with initial PKA energy of 500 eV, initial cell temperature of 300°C and initial PKA direc- tion $x = 1$ , $y = 2$ and $z = 1$ . . . . .	124
5.5	Diamond cascade with initial PKA energy 50 eV, initial cell tem- perature of 300°C and initial PKA direction 1 from table 3.1 . . .	125
5.6	Graph indicating the number of defects during a cascade with initial PKA energy 50 eV, initial cell temperature of 300°C and initial PKA direction 1 from table 3.1 . . . . .	126
5.7	The distance travelled by atoms during a cascade through dia- mond with initial PKA energy 50 eV, initial cell temperature of 300°C and initial PKA direction 1 from table 3.1 . . . . .	126
5.8	Diamond cascade with initial PKA energy 1000 eV, initial cell temperature of 300°C and initial PKA direction 1 from table 3.1 .	128
5.9	Graph indicating the number of defects during a cascade with initial PKA energy 1000 eV, initial cell temperature of 300°C and initial PKA direction 1 from table 3.1 . . . . .	129
5.10	The distance travelled by atoms during a cascade through dia- mond with initial PKA energy 1000 eV, initial cell temperature of 300°C and initial PKA direction 1 from table 3.1 . . . . .	129

5.11	Diamond cascade with initial PKA energy 2000 eV, initial cell temperature of 300°C and initial PKA direction 1 from table 3.1 .	131
5.12	Graph indicating the number of defects during a cascade with initial PKA energy 2000 eV, initial cell temperature of 300°C and initial PKA direction 1 from table 3.1 . . . . .	132
5.13	The distance travelled by atoms during a cascade through diamond with initial PKA energy 2000 eV, initial cell temperature of 300°C and initial PKA direction 1 from table 3.1 . . . . .	133
5.14	Split Interstitial in diamond . . . . .	134
5.15	The average number of defects formed during cascades through diamond as a function of energy . . . . .	136
5.16	The maximum number of defects formed during cascades through diamond as a function of energy . . . . .	137
5.17	The final displacement of PKA after a cascade through diamond as a function of energy . . . . .	138
5.18	The maximum number of displaced atoms during cascades through diamond as a function of time . . . . .	139
5.19	Preliminary cascade through high density amorphous carbon with an initial PKA energy of 500 eV, initial cell temperature of 300°C and initial PKA direction $x = 1$ , $y = 2$ and $z = 1$ . . . . .	141
5.20	The distance travelled by atoms during a cascade in high density amorphous carbon cascades with initial PKA energy 50 eV, initial cell temperature 300°C and initial PKA direction 1 from table 3.1 . . . . .	142
5.21	The distance travelled by atoms during a cascade in high density amorphous carbon cascades with initial PKA energy 500 eV, initial cell temperature 300°C and initial PKA direction 1 from table 3.1 . . . . .	143
5.22	The distance travelled by atoms during a cascade in high density amorphous carbon cascades with initial PKA energy 2000 eV, initial cell temperature 300°C and initial PKA direction 1 from table 3.1 . . . . .	144
5.23	The maximum number of displaced atoms occurring during cascades through high density amorphous carbon as a function of energy . . . . .	145
5.24	Preliminary cascade simulations through low density amorphous carbon with an initial PKA energy of 500 eV, initial cell temperature of 300°C and initial PKA direction $x = 1$ , $y = 2$ and $z = 1$ . . . . .	146

5.25	Distance travelled by atoms during a low density amorphous carbon cascade with initial PKA energy 50 eV, initial cell temperature of 300°C and initial PKA direction 1 from table 3.1 . . .	147
5.26	Distance travelled by atoms during a low density amorphous carbon cascade with initial PKA energy 50 eV, initial cell temperature of 300°C and initial PKA direction x1 from table 3.1 . .	148
5.27	The maximum number of displaced atoms occurring during cascades through low density amorphous carbon as a function of energy . . . . .	149
5.28	Preliminary cascade through glassy carbon with initial PKA energy 250 eV, initial cell temperature 300°C and initial PKA direction $x = 1, y = 2$ and $z = 1$ . . . . .	150
5.29	Glassy carbon cascade with initial PKA energy 50 eV, initial cell temperature 300°C and initial PKA direction 1 from table 3.1 . .	151
5.30	The distance travelled by atoms during a cascade through glassy carbon with initial PKA energy 50 eV, initial cell temperature 300°C and initial PKA direction 1 from table 3.1 . . . . .	152
5.31	Glassy carbon cascade with initial PKA energy 250 eV, initial cell temperature 300°C and initial PKA direction 1 from table 3.1 . .	153
5.32	The distance travelled by atoms during a cascade through glassy carbon with initial PKA energy 250 eV, initial cell temperature 300°C and initial PKA direction 1 from table 3.1 . . . . .	154
5.33	The average number of defects present in the final cell after cascades through glassy carbon as a function of energy . . . . .	155
6.1	A comparison between graphite cascades simulated in this thesis and those taken from literature . . . . .	157
6.2	A comparison between graphite cascades with an initial PKA energy of 2000 eV . . . . .	158
6.3	Pseudo-channel as seen in graphite cascades simulated in the thesis . . . . .	159
6.4	A comparison between thermal spike simulations in graphite and diamond with an initial energy of $1 \times 10^5$ eV . . . . .	162
6.5	A comparison between cascade simulations in graphite and diamond with an initial PKA energy of 2000 eV . . . . .	163
6.6	A comparison between the number of displaced atoms in graphite and diamond cascades as a function of time . . . . .	164
6.7	A comparison between the average number of defects present in the final lattice cell of graphite and diamond as a function of energy . . . . .	165

6.8	A comparison between the average number of displaced atoms during cascades through graphite and diamond as a function of energy . . . . .	166
6.9	A comparison between the average final displacement of PKA in graphite and diamond . . . . .	167
6.10	A comparison between the final lattice cells from cascades in; graphite, high and low density amorphous carbon . . . . .	168
6.11	The average number of displaced atoms after cascades in; graphite, high and low density amorphous carbon as a function of energy	169
6.12	A comparison between cascades in graphite and glassy carbon .	170
6.13	The average number of defects and displaced atoms during cascades through graphite and glassy carbon as a function of energy	171

# List of Tables

1.1	Current operational nuclear reactors in the UK including: type, present capacity, first year of power and date of expected shutdown. . . . .	11
2.1	Parameters of EDIP as fitted to the <i>ab initio</i> data. . . . .	31
2.2	Elastic constants of diamond and a graphite sheet, in units of GPa. The computed graphite values presume a c-spacing of 3.35 Å. . . . .	31
2.3	Published values for the threshold displacement energy in irradiated graphite from experimental and theoretical simulations. . . . .	43
3.1	Initial PKA Positions (Solved with $N = 20$ ) . . . . .	56
4.1	The average number of defects formed at a given initial PKA energy. . . . .	108
4.2	The maximum number of displaced atoms at a given initial PKA energy. . . . .	111
4.3	The average displacement of the initial PKA at a given initial PKA energy. . . . .	113
4.4	The formation energy of defects and vacancy calculated in EDIP and DFT. . . . .	119
5.1	The average number of defects present in the final lattice after a cascades through diamond with initial PKA energies up to 1000 eV. The initial cell temperature was 300°C. . . . .	135
5.2	The average maximum number of displaced atoms during cascaded through diamond with initial PKA energies up to 1000 eV. The initial cell temperature was 300°C. . . . .	136
5.3	The final displacement of the PKA in diamond cascades with initial PKA energies up to 1000 eV. The initial cell temperature was 300°C. . . . .	138

## Acknowledgments

My most significant thanks goes to my supervisors Prof. D. Keith Ross and Dr. Daniel Roach for their continued support and advice throughout my PhD.

A most noticeable thanks to Prof. Nigel Marks and Dr. Marc Robinson without whom the ideas for this thesis would have remained just that.

Thank you also to Prof. Tony Sudbury for helping me take the first dive into academia and making sure I stayed afloat.

I would like to say a special thank you to my family for their continued confidence and support over the years. Most importantly to my Mum and Dad for always encouraging me to pursue my dreams and for never letting me give up on them. Thanks to my 'little sister' Annette, who secretly never gave up on me and for telling me so when I needed to hear it the most. Thanks to Auntie Fiona for showing me that with dedication and determination you can achieve the impossible. Thanks to James for the endless amounts of motivation and for always being able to make me smile.

I would like to thank fellow PhD students Emily and Chris, who when they said 'I understand' meant it. Thank you to the 'Yorkies' who were there from the beginning and I know always will be. Thanks also to Rachael, Kate, Lizzy and Nina for being the best friends I could ask for and for never being too busy for a cup of tea. Thanks to the 'FUN:GRAPH girls' for making meetings and conferences fun.

A final note of thanks to my grandparents, who sadly will never read this but I know would be proud.

# Abstract

Despite having significant applications in the nuclear industry, there have been virtually no molecular dynamics (MD) simulations of radiation damage in graphite. The difficulties in developing an accurate yet computationally inexpensive description of carbon have limited the number of detailed investigations. Although previous work has reported point defect energies and estimates of threshold displacement energies, very little is known about the cascade behaviour and the evolution of damage at the atomic level. Gaining an understanding of the processes caused by irradiation in graphite is central to extending the life span of the current advanced gas-cooled nuclear reactors in the UK. In addition, this will provide crucial information to aid next-generation nuclear technology such as the high-temperature graphite-moderated reactors, which were recently selected for development in the USA.

The Environment Dependent Interaction Potential (EDIP) has been employed along with the Zeigler-Biersack-Littmark potential to model radiation damage in graphite. Statistical sampling of 20 initial directions and over a range of energies has revealed that nuclear graphite behaves in a manner distinct from metals and oxides, with damage primarily in the form of isolated point defects as opposed to connected regions of transient damage. Simulations have given evidence of channelling occurring along the  $\langle 10\bar{1}2 \rangle$  channel which has previously not been observed in graphite simulations. Graphite cascades have exhibited a fractal-like branching structure and binary-collision-type behaviour. Results produced agree with historical defect prediction models. Important quantities such as the range of the primary knock-on atom and the average energy loss per collision have been calculated. Results indicate that graphite cascades are not dependent on the initial cell temperature.

EDIP has been further employed to simulate the effects of radiation damage in carbon allotropes. Results reveal how a material's structure affects the collision cascade and have highlighted the unique radiation response of graphite.



# Introduction

Remarkably, few molecular dynamics simulations have been performed to understand radiation response in graphite despite it being one of the original nuclear materials. A very extensive computational literature exists for radiation processes in metals and oxides [1] [2], whereas, only a handful of simulations exist for graphite due to historical difficulties associated with describing bonding in carbon [3]. Previous research has led to knowledge about point defects [4] [5] and threshold displacement energies [6] [7] in graphite. However, little is known atomistically about cascade behaviour and recovery following ballistic displacement of temperature-driven dynamical effects.

The understanding of radiation processes in graphite is motivated by lifetime extensions of existing graphite-moderated reactors in the UK [8] [9]. Further research into radiation damage in graphite is also key in the future development of Generation-IV technologies such as the high-temperature-graphite-moderated design [10].

The simulation of radiation damage using molecular dynamics (MD) has a long history which extends back to the first ever MD publication in 1960 on focused collision sequences in copper [11]. Over the following decades, numerous radiation simulations were performed in metals [12] [13], ionic solids and oxides [14] [15]. To the best of the author's knowledge, the first reported simulation of radiation cascade effects in graphite was performed by Smith [16] who used the Tersoff potential to study self-sputtering and related phenomena. Further work by Smith and Beardmore [6] led to the expansion of computational techniques to include potentials proposed by Brenner [17] and Heggie [18]. Work performed by Nordlund *et al.* [19] employed the Tersoff potential to quantify defect creation. Herh [7] employed a modified Brenner

potential to study the temperature dependence of the threshold displacement energy. This work was motivated by the next-generation reactor design. However, they did not report any calculations of radiation damage in cascades.

Radiation damage cascades in graphite presented in this thesis consider the effect the initial direction, energy and temperature have on the final lattice. Both qualitative and quantitative behaviour of cascades in graphite is described. A comparison is also presented between simulated data and previous literature.

Cascade simulations in graphite, diamond, glassy carbon and high and low density amorphous carbons simulated using the Environment Dependent Interaction Potential (EDIP) for carbon [20] [21] coupled with the standard Ziegler-Biersack-Littmack (ZBL) potential [22] to describe close-range pair interactions are presented in this thesis. Results highlight the unique behaviour of irradiated graphite.

## 1.1 Brief History of Nuclear Power

The human race has always utilised power. For centuries the main source of power has come from fossil fuels. Following the aftermath of the industrial revolution, this demand grew steeply leading to a heavy strain on natural resources such as oil, coal and gas [23]. As the industrial revolution drew to a close and the technological age began, the pressure to find a new sustainable energy source increased.

We live in the fossil fuel era, as evidenced by the fact that 80 percent of the energy used globally is derived from fossil fuels [24]. Over the past few decades, it has become clear that this heavy dependence on coal, oil and gas cannot continue indefinitely. The development and installation of nuclear power stations could help ease the strain faced by energy producers on a global scale.

Early chemists believed that the chemical elements could never be created or destroyed and that the atom could not be split [25]. However, in 1896, a French Physicist, Antoine Henri Becquerel, discovered that certain chemical elements undergo a spontaneous disintegration with the emission of energy in the form of particles; this process was called radioactivity [26]. It was noted that elements with an atomic number greater than 83 are radioactive. Most importantly, Becquerel discovered that uranium fell into the radioactive category [27].

The first major steps into developing the nuclear reactors in use today came as a direct result of World War II. During the War, the United States of America together with the support of the United Kingdom and Canada undertook a research and development project that produced the first atomic bombs. This project was named 'The Manhattan Project' and ran between 1942 and 1946 [28]. Whilst the research undertaken as part of the Manhattan Project was aimed at warfare, the data collected about the isotope uranium-235 would prove fundamental in the development of nuclear reactors.

The pioneering Italian physicist Enrico Fermi *et al.* constructed the first artificial nuclear reactor, Chicago Pile-1 (CP-1), at the University of Chicago [29]. CP-1 contained uranium pellets, which were separated from one another by graphite blocks. The graphite blocks acted as a moderator, they slowed the neutrons from fission in uranium down to increase the chance of nuclear fission occurring. On 2<sup>nd</sup> December 1942, CP-1 reached a self-sustaining reaction before being shut down 28 minutes later. CP-1 was de-commissioned in Jan-

uary 1943 and the nuclear project moved to Red Gate Woods, Illinois. However, the results produced from CP-1 opened the door to a new era of energy production.

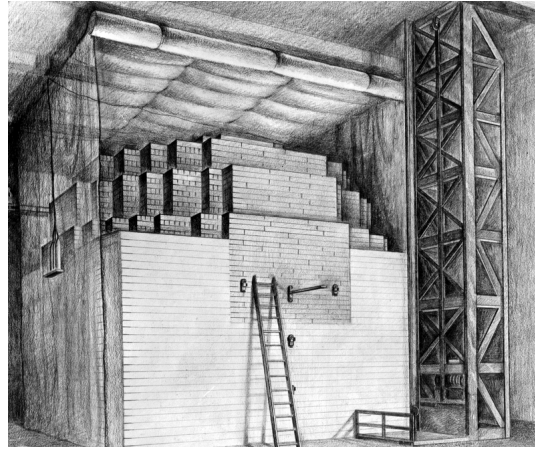


**Figure 1.1:** A sketch of the Chicago Pile. (*Photographic copy of drawing. Credit: Archival Photographic Files, apf2-00501, Special Collections Research Centre, University of Chicago Library.*)

The Manhattan Project [28], (1942-1946), was created as a direct response of the results obtained from CP-1. However, the main reactors primary purpose during this project was for the mass production of plutonium for nuclear warfare. The first nuclear power plant built for civilian use was Obninsk Nuclear Power Plant in the former Soviet Union [30]. Obninsk was a semi-experimental reactor which commenced operations on June 27<sup>th</sup> 1954, producing around 5MW of electrical energy [31]. It was another four years until a second nuclear power plant was commissioned and opened in the former Soviet Union. Obninsk was decommissioned and shut down on 29<sup>th</sup> April 2002 [32].

The world's first nuclear power station to deliver electricity on a commercial scale was Calder Hall in Sellafield, UK [30]. Calder Hall was connected to the National Grid on 27<sup>th</sup> August 1956 and remained active until 31<sup>st</sup> March 2003. Calder Hall was built for the military, with its main purpose to produce weapon-grade plutonium. Electricity production was secondary to weapon production until April 1995, when the UK government announced all production of plutonium for weapons purposes had ceased.



**Figure 1.2:** Sellafield Nuclear Power Station.

*(Image courtesy of <http://mosaic.cnfolio.com/B101CW2007A127>.)*

The evolution of nuclear reactors across the world has proceeded over the past few decades. Globally, there are over 400 civil nuclear reactors connected to the electrical grid with a further 71 nuclear reactors under construction [33]. Advances in scientific and engineering research over the last few decades have led to vast improvements in the reliability, safety and sustainability of nuclear power. Progress within the nuclear energy sector can be seen on a global scale and with further enhancements will hopefully be able to relieve some of the strain faced by energy suppliers.

## 1.2 Theory of Nuclear Power

Uranium was first discovered by German Chemist, Martin Klaproth in 1789 [34]. Uranium is a naturally occurring element in the Earth's crust and traces can be found almost everywhere. However, mining of uranium for nuclear use is limited to specific locations where a higher concentration can be found. Uranium is a heavy metal which can be used as an ample source of concentrated energy. It has three isotopes [35] [36]. These are: uranium-238 which has 146 neutrons, 92 protons and accounts for 99.275% of mined uranium, uranium-235 which has 143 neutrons and accounts for 0.720% of mined uranium and uranium-234 which accounts for 0.005% of mined uranium [30]. The most desirable isotope is uranium-235. This is because it undergoes thermal neutron induced fission. In order to employ uranium as a fuel source, the uranium must first be extracted from the rock in which it has been mined. Upon extraction from the rock, the uranium is enriched with uranium-235 before being shaped into pellets and loaded into a reactor. Uranium is employed as the fuel of choice in nuclear reactors. A single pellet of uranium fuel contains as much energy as 480 cubic metres of natural gas, 807 kilos of coal or 149 gallons of oil [10].

In a nuclear reactor, the uranium fuel is assembled in such a way that a controlled fission chain reaction can be achieved. Heat is produced from the fission chains which creates steam. The steam produced spins a turbine which in turn drives a generator producing electricity [30].

The breakdown of a large nucleus such as uranium into two smaller nuclei such as barium and krypton plus on average 2.5 fast neutrons is called nuclear fission [37]. Nuclear fission sees small amounts of matter converted directly into large amounts of energy. This happens because whenever a nucleus is formed, the mass of the nucleus is slightly less than the sum of the masses of the individual protons and neutrons the atom comprises of.

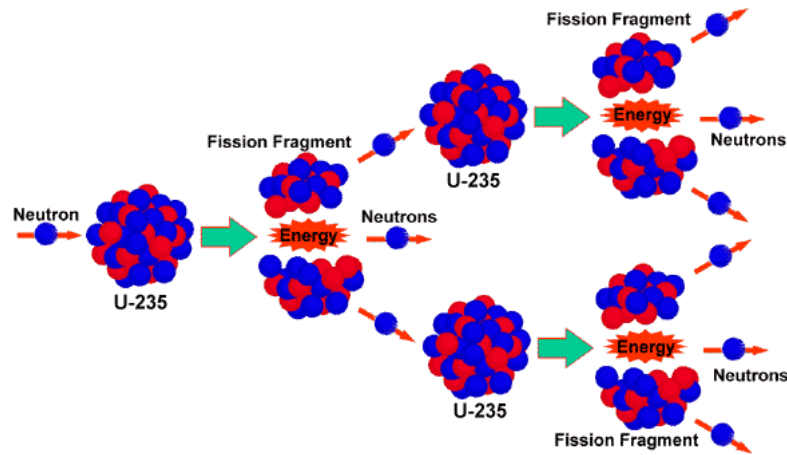


**Figure 1.3:** A schematic representation of the chain reaction in the fission of uranium. When a thermal neutron is absorbed by the nucleus of a uranium-235 atom, it results in spontaneous fission of the uranium nucleus. The fission produces more neutrons along with a large release of energy. The neutrons which are released can then go on to cause fission in other uranium nuclei thus creating a chain reaction. (image courtesy of <http://library.thinkquest.org/3471/abomb.html>.)

Radioactive materials decay naturally over time. However, this process is very slow and can span many millions of years [30]. Uranium-238 is considered not to be very radioactive because its half life is the same as the age of the earth. However, uranium-235 is fissile and can be split with a thermal neutron (figure 1.3). During fission, the nucleus of uranium-235 is split in two and an excess of three neutrons are emitted. The expelled neutrons can be collected by uranium-238 and this becomes plutonium-239, which is highly radioactive and the fission chain can then continue in both the plutonium and the uranium-235 [38].

Uranium is used in all but two or three fast nuclear reactors around the World [39]. The use of uranium in nuclear reactors has a variety of uses. It can generate electricity continuously for many months at a time unlike solar, wind or water power, which are reliant on the weather. Most importantly, nuclear energy has almost no greenhouse gas emissions.

### 1.3 Reactors in the UK

There are constant developments and improvements with nuclear reactors. Since the first civil nuclear reactors were connected to the National Grid in the 1950's, they have advanced in leaps and bounds. Enhancements made to reactors have seen improvements from economical, ethical and environmental points of view [40].

The first generation of nuclear reactors in the UK are the Magnox reactors [30]. These are Gas-Cooled reactors. Carbon dioxide is used to transfer the heat from the reactor core to a heat exchanger where electricity is generated. The fission reaction within a nuclear reactor can be controlled using graphite bricks as moderators. A moderator works by decreasing the speed neutrons are travelling at. Slowing the neutrons down by using the graphite bricks increases the probability of fission occurring. Power levels are controlled by rods containing reaction absorbers.

The Advanced Gas-Cooled reactor (AGR), is an advanced form of the Magnox reactor and is the second generation of nuclear power stations in use in the UK, figure 1.4. The AGR is of British design and the first was commissioned in 1964. AGR's make use of enriched fuel and can operate more efficiently and at much higher temperatures than the first generation of reactors [41].

As figure 1.4 shows, the AGR's still use graphite as a moderator, carbon dioxide as a coolant and a system of control rods. It is the enrichment of the fuel used and the operating temperature which makes the AGR's more efficient.

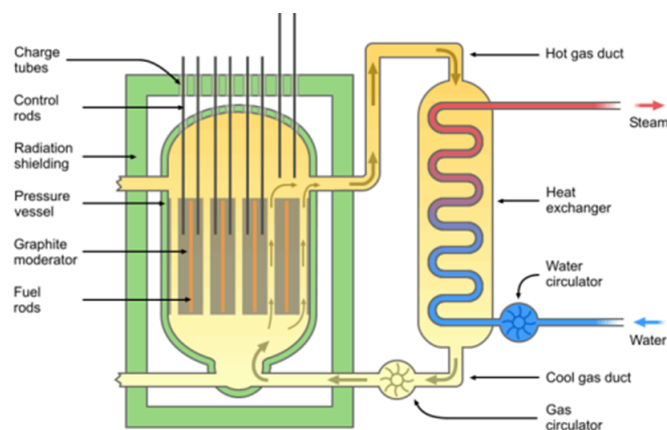


**Figure 1.4:** The Advanced-Gas Cooled reactor with graphite moderators and gas used as the cooling agent. (Image courtesy of <http://universe-review.ca/I14-03-reactorAGR.png>.)

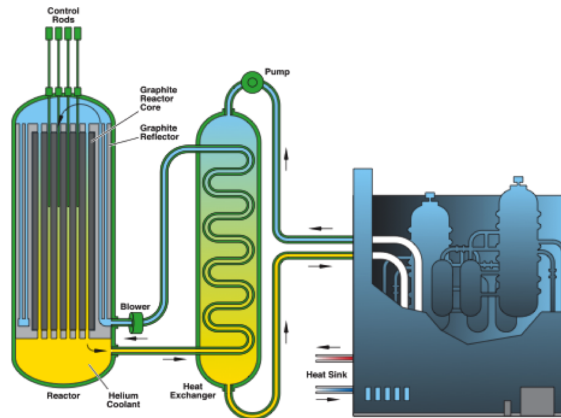


**Figure 1.5:** The Very High Temperature Reactor, (VHTR), is the next generation of reactors which has been commissioned for use in the USA. The VHTR uses graphite moderators. *(Image courtesy of Idaho National Laboratory.)*

The next generation of reactors will probably be the Very High Temperature Reactors (VHTR), figure 1.5. VHTR reactors will use graphite moderators and have been commissioned as the next wave of reactors to be used in the USA [42]. The VHTR is a generation IV reactor and uses a graphite moderated nuclear reactor with a uranium fuel cell. The VHTR reaches temperatures up to 1000°C. The gas used as the coolant in VHTR's is helium. Helium is an appropriate gas to chose because exposure to neutron radiation does not make it radioactive unlike most other possible coolants [43].

The UK is home to the first commercial nuclear reactor, Calder Hall, which was connected to the National Grid on 27<sup>th</sup> August 1956. After the success of Calder Hall, several sites around the UK were chosen to be the home of a nuclear power station. There are 16 nuclear reactors across the UK, figure 1.6 shows their location.



**Figure 1.6:** Nuclear reactor sites across the UK. (Image courtesy of The Department of Energy and Climate Change.)

Nuclear energy generates 18% of the electricity utilised in the UK. This figure has significantly decreased from 25% which was seen in the late 1990's. The decrease in the reliance of nuclear power is partially to do with the decommissioning of the nuclear reactors in the UK. By 2023, all but one of the current nuclear reactors will have been decommissioned. However, an extension of the operational life by energy companies could see the life span of some of the reactors extended for a further 10 years. The UK has also carried out a thorough assessment process for new reactor designs and locations [44]. It is hoped by 2023 that the new generation of nuclear reactors will be fully functioning and by 2030 will have an operating power of 16 GWe [45].

Table 1.1 gives details about the current operational nuclear reactors in the UK and their expected decommissioning dates [46].

Plant	Type	Present Capacity (MWe net)	First Power	Expected Shutdown
Wylfa 1	Magnox	490	1971	December 2015
Dungeness B 1 & 2	AGR	2 x 545	1989 & 1985	2018 or 2028
Hartlepool 1 & 2	AGR	2 x 595	1983 & 1984	2024
Heysham I-1 & I-2	AGR	2 x 580	1983 & 1984	2019
Heysham II-1 & II-2	AGR	2 x 615	1988	2023
Hinkley Point B 1 & 2	AGR	2 x 610 (operating at 70%)	1976	2023
Hunterston B 1 & 2	AGR	2 x 610 (operating at 70%)	1976 & 1977	2023
Torness 1 & 2	AGR	2 x 625	1988 & 1989	2023
Sizewell B	PWR	1188	1995	2035
<b>Total = 16 units</b>		<b>10, 038 MWe</b>		

**Table 1.1:** Current operational nuclear reactors in the UK including: type, present capacity, first year of power and date of expected shutdown.

## 1.4 Graphite

Carbon is the sixth element in the periodic table. It has an atomic weight of 12.011 on the chemical scale and consists of 98.9% of the isotope  $C^{12}$  with 1% of the isotope  $C^{13}$  [47]. Of the six electrons present in a neutral carbon atom, four in the outer shell are available to form chemical bonds. The isolated carbon atom contains the distribution of  $1s^2 2s^2 p^2$ , spectroscopically  $^3P$ . In diamond, the covalent bonds formed are of the type  $sp^3$ , they are distributed tetrahedrally and have a length of  $1.54\text{\AA}$ [48].

Graphite often occurs in close association with other forms of carbon. This can make it difficult to define its physical properties. When pure graphite is formed, carbon atoms are arranged in open hexagons which exist in layers. The layers of graphite form a stacking sequence ABAB with a spacing of  $3.3538\text{\AA}$ [48]. The interatomic distance in the hexagons is  $1.415\text{\AA}$ .

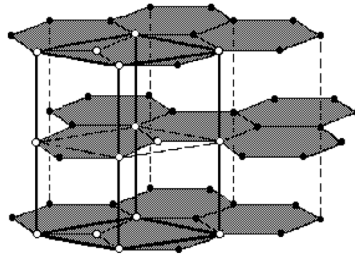


Figure 1.7: ABA stacking of a graphite lattice.

In a unit cell of graphite, there are four atoms (which are positioned  $(0,0,0)$ ;  $(0,0,\frac{1}{2})$ ;  $(\frac{2}{3},\frac{1}{3},0)$  and  $(\frac{1}{3},\frac{2}{3},\frac{1}{2})$ ), and two completely different atomic sites. The two types of atomic sites found in graphite can be categorised as those situated between immediate neighbours above and below and those with open hexagons immediately above and below.

Graphite in a highly perfect crystalline form, shows a planar morphology with a silvery surface. Graphite is extremely soft and can be deformed easily. When graphite is in polycrystalline form, it is dark grey, rather porous and soft. In polycrystalline form, graphite may be readily distinguished from ungraphitised carbons by the ability it shares with lead and molybdenite to mark paper.

Nuclear graphite is any grade of graphite that has been specifically manufactured for use as a moderator or reflector within a nuclear reactor [48]. The

nuclear graphite used in UK reactors is manufactured from petroleum coke mixed with a coal-based binder. This is then extruded into bricks and baked at 1,000°C for several days. The porosity of the graphite bricks is reduced and the density increased by adding coal tar to the bricks at a high temperature and a high pressure. The bricks are then baked again at 2,800°C before being cut into the desired shape [49].

The properties of nuclear graphite alter under irradiation [48]. There are changes to the dimensions, elastic modulus, coefficient of thermal expansion, thermal conductivity and electrical resistivity. The computational modelling produced in this thesis will demonstrate the effects irradiation has on graphite at the atomic level.

## 1.5 Thesis Plan

Chapter 2 explains the theory behind molecular dynamic simulations and clarifies the linking of the EDIP and ZBL potentials. The Kinchin and Pease model for hard sphere collisions is explained. A literature review into previous studies within this field is presented.

The methodology employed to simulate radiation damage cascades in graphite, diamond, glassy carbon, high and low density amorphous carbons is described in Chapter 3. A description of neutron collisions is also presented along side a discussion about the physical properties of cascades in graphite and carbon materials.

Chapter 4 considers the qualitative behaviour of cascades in graphite along with the presentation of quantitative results. Results are obtained from; thermal spike simulations, collision cascade and defects analysis. Collision cascades are simulated over 20 initial directions with initial energies between 25 and 2000 eV. Results obtained from cascades with a high initial temperature are also documented.

Cascade simulations in diamond, glassy carbon and high and low density amorphous carbons are presented in Chapter 5. Results include thermal spike simulations, collision cascades and defect analysis.

Chapter 6 links graphite cascades with historical models in the literature and discusses how fundamentally different radiation damage in graphite is compared to other carbon materials. Quantitative and qualitative data is presented to further highlight this. A plan for future work is also presented.

The thesis is concluded in Chapter 7 with a summary of key results.

## CHAPTER 2

# Theory

Molecular dynamics (MD) is a computational technique used for computing the equilibrium and transport properties of a classical many-body system [50]. Given the initial co-ordinates and velocities of an ensemble of particles that interact in an explicit manner, under certain conditions, this method integrates the equations of motion numerically, providing new sets of co-ordinates and velocities at each time step. The obtained particles trajectories allow one to calculate various system properties as statistical averages.

The simulation of radiation damage using MD has a long history, extending back to the first ever publication in 1960 of an MD simulation involving focused collision sequences in copper [51][52]. A great number of radiation cascade simulations were performed over the following decades facilitated by the development of the embedded atom method for metals and Buckingham-type potentials for ionic solids and oxides [1][2]. Whilst there have been vast MD simulations achieved within metals and oxides, there have been hardly any MD simulations in graphite. Further developments of MD potentials have been found to be essential to accurately simulate radiation damage in graphite.

MD simulations are in many respects very similar to real experiments. It is for this reason that it is useful to employ MD simulations before conducting experimental research in order to gain a greater understanding of the effects to be expected in experiments. Simulations can be used to explain experiments, to reveal processes, develop intuition and suggest directions of research.

The MD simulations described in Chapters 4 and 5 have been used to simulate the effect that neutron irradiation has on graphite and carbon allotropes. The results have been used to pinpoint areas of damage, analyse defects and to demonstrate the effect the irradiation has on the rest of a cell.

## 2.1 Equations of Motion

The MD simulation method is based on Newton's Second Law, equation 2.1. The knowledge of the force acting on atoms allows the acceleration of each atom in the system to be calculated. Integration of the equations of motion then yields a trajectory that describes the positions, velocities and acceleration of the particles as they vary with time. The trajectory obtained as a direct result of integration allows average values of a systems properties to be determined [53].

$$\mathbf{F}_i = m_i \mathbf{a}_i \quad (2.1)$$

where  $F_i$  is the total force exerted on particle  $i$  ( $i = 1, 2, 3 \dots n$ ) and  $m_i$  is the mass of particle  $i$  and  $\mathbf{a}_i$  is the acceleration of particle  $i$ .

The force can also be expressed as the gradient of the potential energy, equation 2.2.

$$\mathbf{F}_i = -\nabla_i V \quad (2.2)$$

where  $V$  is the potential energy of the system and is assumed to depend only on the particle positions.

Combining equations 2.1 and 2.2 produces:

$$-\frac{dV}{dr_i} = m_i \frac{d^2 \mathbf{r}_i}{dt^2} \quad (2.3)$$

To calculate the trajectory of an atom, one only needs the initial positions of the atoms, an initial distribution of velocities and the acceleration, which is determined by the gradient of the potential energy function. The Verlet algorithm is employed to integrate equation 2.3 and is described in section 2.3.

To measure an observable quantity in an MD simulation, the observable function must be able to be expressed as a function of the positions and momenta of all the particles in a system. A prime example of an observable quantity in MD simulations is temperature. In a classical, many-body system, a reliable definition of the temperatures makes use of the equipartition of energy over all degrees of freedom that enter quadratically in the Hamiltonian of the system. The theorem of equipartition of energy states that molecules in thermal

equilibrium have the same average energy associated with each independent degree of freedom of their motion and the average kinetic energy is given in equation 2.4 [50]. This alters depending on the degrees of freedom, for example, in polyatomic molecules where there are  $3N$  degrees of freedom and in diatomic molecules where there are  $2N$  degrees of freedom, the thermal energy will be distributed between rotations and vibrations of the molecule. The equipartition theorem begins to break down if the system is not in thermal equilibrium. This is because when a system reached thermal equilibrium, each sub-system is guaranteed to have the energy which is attributed to it by the equipartition theorem.

$$\left\langle \frac{1}{2} m v_{\alpha}^2 \right\rangle = \frac{1}{2} k_B T \quad (2.4)$$

Where  $m$  is the mass,  $v_{\alpha}$  is the velocity of the particle where  $\alpha$  labels the translational degree of freedom,  $k_B$  is the Boltzmann constant and  $T$  is the temperature.

Equation 2.4 can be employed as an operational definition of the temperature. However, in practice, the total kinetic energy of the system would be measured and divided by the number of degrees of freedom. During an MD simulation, the total energy of a system fluctuates as does the instantaneous temperature (equation 2.5). These fluctuations occur as a direct result of the finite size of the cell. The relative fluctuations in the temperature will be of the order  $1/\sqrt{N_f}$  and as  $N_f$  is typically of the order of  $10^2 - 10^3$ , the statistical fluctuations in the temperature are of the order of 5-10% (where  $N_f$  is the number of fluctuations). To get an accurate estimate of the temperature, one should average over many fluctuations [50].

$$T(t) = \sum_{i=1}^N \frac{m_i v_i^2(t)}{k_B N_f} \quad (2.5)$$

## 2.2 Molecular Dynamics Programs

A successful MD simulation has the same initial foundations as a practical experiment. A sample must first be prepared. Both the sample and the sample's environment must be equilibrated to a predetermined temperature. Following equilibration, the experiment can then be conducted. The results yielded from the experiment can then be used for further analysis. Figure 2.6 highlights the main stages during an MD simulation.

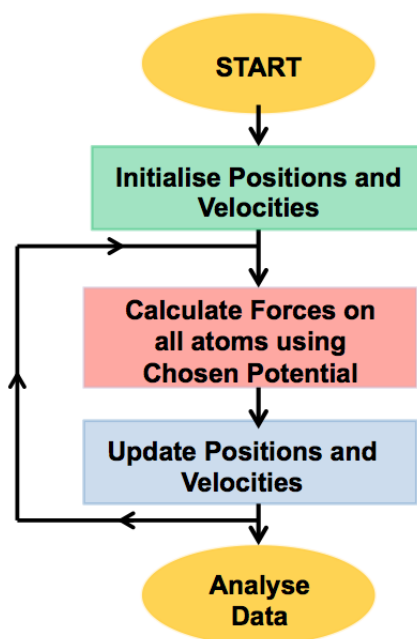


**Figure 2.1:** A flow chart symbolising the different stages in a molecular dynamics simulation.

MD simulations follow a set of rules as explained below [50].

1. Parameters which specify the conditions of the simulation are defined by the chosen potential (e.g.; initial temperature, number of particles, density and time step).
2. The system is initialised (i.e., the initial positions and velocities of the atoms are selected). The particles' positions should be chosen compatible with the desired crystallographic structure. There should be no overlapping at the atomic or molecular cores because of the repulsive Pauli exclusion principle. Once each particle has been placed on its lattice site, a velocity component is assigned to each particle drawn from a uniform

distribution in the interval  $[-0.5, 0.5]$ . The velocities are multiplied by a constant to ensure the total momentum in the system is zero. In thermal equilibrium, equation 2.6 i.e., a Maxwell-Boltzmann distribution, should hold ( $v_\alpha$  is the  $\alpha$  component of the velocity of a given particle).

$$\langle v_\alpha^2 \rangle = k_B \frac{T}{m} \quad (2.6)$$

Equation 2.5 defined the instantaneous temperature. This can be altered slightly by employing equation 2.6 to define an instantaneous temperature at time  $T(t)$  (equation 2.7).

$$k_B T(t) \equiv \sum_{i=1}^N \frac{mv_{\alpha,i}^2(t)}{N_f} \quad (2.7)$$

The instantaneous temperature can be adjusted to match a prescribed desired temperature,  $T$ , by scaling all velocities with a factor  $(T/T(t))^{\frac{1}{2}}$ .

3. Computation of the forces on all particles. This is the most time-consuming part of an MD simulation. To calculate the force on a single atom,  $i$ , the contributions of all the atom's neighbours must be taken into account. If the contribution to atom  $i$ 's force was from its nearest neighbour, for a system of  $N$  particles,  $N(N-1)/2$  pair distances must be evaluated. Therefore, the time needed for the evaluation of the forces scales as  $N^2$ .

To accurately calculate the force, the current distance in the  $x$ ,  $y$ , and  $z$  directions between each pair of particles  $i$  and  $j$  must be computed. If simple cubic periodic boundary conditions are employed, the distance between  $i$  and the nearest image of  $j$  should always be less than the diameter of the periodic box/2. A cut-off distance,  $r_c$ , is chosen, this is always less than half the diameter of the periodic box [50]. To calculate the  $x$ -distance between  $i$  and  $j$ , equation 2.8 is used.

$$xd = xd - box * nint(xd/box) \quad (2.8)$$

where  $xd$  is the  $x$ -distance between  $i$  and  $j$ ,  $nint$  is the nearest integer function and  $box$  is the diameter of the periodic box.

Equation 2.8 is repeated until all the Cartesian components of  $r_{ij}$  have been calculated, the equation only applies when boundary conditions are taken into consideration. The vector distance between  $i$  and  $j$  can now be

computed,  $r_{ij}^2$  and tested against the square of the cut-off radius,  $r_c^2$ . The vector distance should be less than the square of the cut-off radius.

If particles  $i$  and  $j$  are close enough to interact (i.e., their vector distance squared is less than the square of the cut-off radius), the force between the two particles must be computed. Equation 2.9 is an example of how the  $x$ -component of the force can be calculated.

$$\begin{aligned} \mathbf{f}_x(r) &= -\frac{\partial V(r)}{\partial x} \\ &= -\left(\frac{x}{r}\right) \left(\frac{\partial V(r)}{\partial(r)}\right) \end{aligned} \tag{2.9}$$

4. Integrate Newton's Equations of Motion. (Steps 3 and 4 are the core parts of an MD simulation, they are repeated until the system has computed the time evolution of the system for the desired length of time. Stage 4 is discussed in further detail in the next section).
5. After the simulation has been computed for the desired time, the averages of measured quantities are printed and the simulation is stopped.

## 2.3 Integrating the Equations of Motion

There are a variety of methods of integrating the equations of motion during an MD simulation. Algorithms have been designed to aid with the integration process, in particular the Verlet algorithm can be employed [50].

The starting point to successfully derive the equations of motion using the Verlet method begins with a Taylor expansion of the co-ordinate of a particle, around time  $t$  (equation 2.10) [50].

$$\mathbf{r}(t + \Delta t) = \mathbf{r}(t) + v(t)\Delta t + \frac{\mathbf{F}(t)}{2m}\Delta t^2 + \frac{\Delta t^3}{3!}\ddot{\mathbf{r}} + \mathcal{O}(\Delta t^4) \quad (2.10)$$

similarly,

$$\mathbf{r}(t - \Delta t) = \mathbf{r}(t) - v(t)\Delta t + \frac{\mathbf{F}(t)}{2m}\Delta t^2 - \frac{\Delta t^3}{3!}\ddot{\mathbf{r}} + \mathcal{O}(\Delta t^4) \quad (2.11)$$

where  $\mathbf{F}(t)$  refers to the force and  $\mathbf{r}$  is the cartesian coordinate.

The sum of equations 2.10 and 2.11 gives equation 2.12.

$$\mathbf{r}(t + \Delta t) + \mathbf{r}(t - \Delta t) = 2\mathbf{r}(t) + \frac{\mathbf{F}(t)}{m}\Delta t^2 + \mathcal{O}(\Delta t^4) \quad (2.12)$$

$$\mathbf{r}(t + \Delta t) \approx 2\mathbf{r}(t) - \mathbf{r}(t - \Delta t) + \frac{\mathbf{F}(t)}{m}\Delta t^2$$

The estimate of the new position contains an error that is of order  $\Delta t^4$ , where  $\Delta t$  is the time step in our MD scheme. The Verlet algorithm does not use the velocity to compute the new position, however, the velocity can be derived by utilising knowledge of the trajectory (equation 2.13).

$$\mathbf{r}(t + \Delta t) - \mathbf{r}(t - \Delta t) = 2v(t)\Delta t + \mathcal{O}(\Delta t^3) \quad (2.13)$$

$$v(t) = \frac{\mathbf{r}(t + \Delta t) - \mathbf{r}(t - \Delta t)}{2\Delta t} + \mathcal{O}(\Delta t^2)$$

The expression for the velocity, equation 2.13, is only accurate to order  $\Delta t^2$ . The velocities can be used to compute the kinetic energy and instantaneous temperature of the system. At the end of each time step, the current temperature, current potential energy and the total energy should be calculated. The

total energy should be conserved throughout the MD simulation [50] [53].

Once all calculations are complete, the old positions and velocities at time  $t - \Delta t$  can be discarded. The new positions and velocities become the next starting point and thus the process can be repeated a given number of times until the desired time frame has been reached.

Time in molecular dynamics simulations works quite differently to time in 'real life' experiments. On average, molecular dynamics simulations are run for a few pico-seconds or nano-seconds whereas in a laboratory, the same experiment could take seconds, minutes or hours. However, this does not necessarily mean that a simulation is not a true representation of an experiment. Figure 2.2 gives an example of the time step in a molecular dynamics simulation.

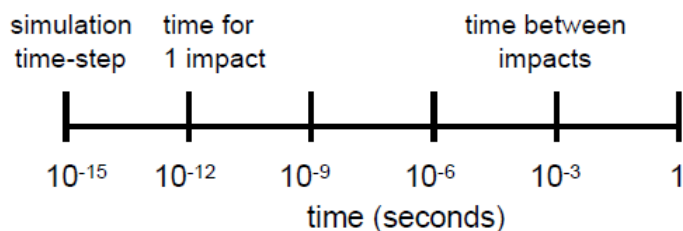


**Figure 2.2:** Time line showing important values in a molecular dynamics simulation.

A useful way of effectively running MD simulations is to employ a multiple time step. Multiple time steps are ideal when simulating short- and long-range interactions. A variable time step is employed in simulations from Chapters 4 5 as the simulations give rise to short-lived but highly energetic events.

## 2.4 Potentials

Empirical interatomic potentials are frequently employed in MD simulations because they provide interactions in a conveniently extractable form. There are a variety of empirical interatomic potentials for carbon, the most commonly used are those developed by Tersoff and Brenner [54][17].

The Tersoff and Brenner empirical interatomic potentials are convenient, short-ranged and bond-ordered. In molecular orbital theory, bond order is defined as the number of chemical bonds between a pair of atoms. The analytical form for the Tersoff pair-potential, can be seen in equations 2.14 - 2.15.

$$E = \sum_i = \frac{1}{2} \sum_{i \neq j} V_{ij} \quad (2.14)$$

$$V_{ij} = f_c(r_{ij}) (a_{ij}f_R(r_{ij}) - b_{ij}f_A(r_{ij})) \quad (2.15)$$

Where  $E$  is the total energy of the system, which is decomposed for convenience into site energy  $E_i$  and bond energy  $V_{ij}$  [55],  $r_{ij}$  is the distance between atoms  $i$  and  $j$ . The function  $f_R$  represents a repulsive pair potential and  $f_A$  represents an attractive pair potential associated with bonding. The function  $f_c$  is a smooth cut-off function which limits the range of the potential [55]. The terms  $b_{ij}$  measures the bond order and  $a_{ij}$  consists solely of range-limiting terms [55] [56] [57].

Following Tersoff's advance, Brenner released the Reactive Bond Order (REBO) potential [17]. The Brenner potential for solid-state carbon structures is given using equation 2.16.

$$E_b = \sum_i \sum_{j(>i)} [V_R(r_{ij}) - \bar{B}_{ij}V_A(r_{ij})] \quad (2.16)$$

Where  $E_b$  is the binding energy,  $B_{ij}$  represents a many-body coupling between the bond from atom  $i$  to atom  $j$ ,  $V_R$  and  $V_A$  are the pair-additive repulsive and attractive interactions respectively [17] [58] [59].

The Tersoff and Brenner potentials are short-ranged potentials which employ switching functions to identify nearest neighbour atoms. This process inverts the density relationship between graphite and diamond. The Tersoff and Brenner potentials did not significantly advance fundamental understanding of

amorphous carbons. This is because, the potentials do not successfully predict high  $sp^3$  fractions or densities. Both potentials produced poor results when compared to experimental data. Liquid-quench simulations show that both potentials underestimate the proportion of four-fold co-ordination by at least a factor of two. As a consequence, much more computationally intensive techniques such as density-functional theory have been used to investigate the properties of amorphous carbons [60].

Density Functional Theory, (DFT), is considered to be one of the highest level theory for which MD is practical. Central to density functional theory is the Hohenberg-Kohn theorems.

1. If two systems of electrons, one trapped in a potential  $v_1(\vec{r})$  and the other in  $v_2(\vec{r})$ , have the same ground-state density  $n(\vec{r})$  then necessarily  $v_1(\vec{r}) - v_2(\vec{r}) = \text{const.}$
2. For any positive integer  $N$  and potential  $v(\vec{r})$  there exists a density function  $F[n]$  such that  $E_{v,N}[n] = F[n] + \int v(\vec{r})n(\vec{r})d^3r.$

The Hohenberg-Kohn theorems allow the  $3N$  co-ordinates needed to describe  $N$  electrons with the Schrödinger equation to the three spatial dimensions required to describe the charge-density distribution with the Kohn-Sham equation. The Kohn-Sham equation is the Schrödinger equation of a fictitious system of non-interacting particles that generate the same density as any given system of interacting particles.

Whilst DFT yields high quality results, it is computationally expensive to run MD simulations using DFT. For simulations where full DFT is not required, approximate treatments of electronic structures are extremely useful, the Local Bias Density Functional Approach, (LBDF), can be used in these instances [60]. LBDF enables calculations which are comparable to full DFT at a reduced cost. However, they are not appropriate for in-depth studies.

The Long-Range Carbon Bond Order potential, (LCBOP I and II), is perhaps one of best potentials for pure carbon systems [61] [62]. LCBOP uses a Brenner-type bond-order-based description along with a Morse-like potential to describe long-range effects. The long-range of the potential ensures that inter-layer graphitic attraction is well-described. Related properties such as elastic constants compare well to experimental data. The main draw back of LCBOP is the computational resources required to run simulations.

One of the most commonly used long-range potentials for carbon is the Adaptive Interaction Reactive Bond Order, (AIREBO), potential [63]. AIREBO is an extension of Brenner's potential. Long-ranged interactions between  $sp^2$  sheets are described through a Lennard-Jones interaction. AIREBO is time consuming and computationally expensive to run. Intermolecular interactions are modelled through a Lennard-Jones potential, equation 2.17.

$$V_{LJ} = 4\epsilon \left[ \left( \frac{\sigma}{r} \right)^{12} - \left( \frac{\sigma}{r} \right)^6 \right] \quad (2.17)$$

Where  $\epsilon$  is the depth of the potential well (the region surrounding a local minimum of potential energy),  $\sigma$  is the finite distance at which the inter-particle potential is zero and  $r$  is the distance between the particles.

The AIREBO potential only takes four parameters as independent:  $\sigma_{CC}$ ,  $\sigma_{HH}$ ,  $\epsilon_{CC}$  and  $\epsilon_{HH}$ . The parameters are fixed by Lorentz-Berthelot combining rules, equations 2.18 and 2.19.

$$\sigma_{CH} = \frac{1}{2} (\sigma_{CC} + \sigma_{HH}) \quad (2.18)$$

$$\epsilon_{CH} = \sqrt{\epsilon_{CC}\epsilon_{HH}} \quad (2.19)$$

To merge equations 2.18 and 2.19 with a reactive potential, the Lennard-Jones potential may be either completely or partially turned off in response to the chemical environment of the interacting pair. The key feature of the AIREBO potential is that it provides a means of smoothly interpolating between pure bonded and pure non-bonded interactions. To accomplish the smooth transition, AIREBO makes use of three switching functions:  $S_{distance}$ ,  $S_{bond}$  and  $S_{connectivity}$ . Each one of these switching functions may turn off the Lennard-Jones interaction partially or entirely, (equation 2.20).

$$E_{LJ} = (1 - S_{distance}S_{bond}) (1 - S_{connectivity}) V_{LJ} \quad (2.20)$$

The Stillinger-Weber (SW) potential has been employed in the modelling of graphite and diamond [64]. The value of the SW potential for any atomic configuration,  $V$ , is a sum of interactions among pairs and triplets of atoms (it is based on a two-body term and a three-body term), equation 2.21.

$$V = \frac{1}{2} \sum_{ijk} \phi(\mathbf{r}_{ijk}) + \sum_{ijk} g(\mathbf{r}_{ij}) g(\mathbf{r}_{ik}) \left( \cos\theta_{jik} + \frac{1}{3} \right)^2 \quad (2.21)$$

Where  $\theta_{jik}$  is the angle formed by the  $ij$  bond and the  $ik$  bond and  $g(r)$  is a decaying function with a cut-off between the first and second neighbour shell.

The SW potential gives a fairly realistic description of graphite and diamond. However, it uses fixed co-ordination and so has found only niche applications.

The potential selected to model the carbon structures described in chapters 4 and 5 is the Environment Dependent Interatomic Potential (EDIP). The EDIP potential was first developed for silicon systems by Justo *et al.* [65] and was adapted for use in carbon systems by Marks [65] [66]. An atom-centred bond order is employed on the earlier silicon EDIP method. Generalisation of the silicon EDIP to carbon involved three main steps [60].

1. The non-bonded terms were used to increase the graphite c-spacing
2. Dihedral rotation penalties for  $\pi$ -bonded atoms were added
3. Variable range pair interactions

The alteration to the silicon EDIP changes the hybridisation from  $sp^2$  to  $sp^3$  by tailoring the cut-off functions to density-functional theory data. This process leads to an accurate description of liquid and amorphous carbons being obtained (further detail is provided in section 2.5).

EDIP has been chosen as the potential for simulations carried out in this report. The EDIP potential allows the interactions to vary according to the environment (i.e., the number of neighbours), it provides an accurate description of bond-making and breaking processes, it gives good elastic properties of the crystalline state and can also describe liquids well [60]. Originally developed to study thin film deposition of amorphous carbon, EDIP has since been applied to study numerous other carbon forms including carbon onions [67] [68], glassy carbon [68] [69], peapods [70], nanotubes [68] [71] and nano-diamond [72].

## 2.5 The Environment Dependent Interatomic Potential for Carbon (EDIP)

The Environment-Dependent Interaction Potential (EDIP) is a transferable empirical potential for carbon which is well suited for studying disordered systems [20] [21]. The functional form of EDIP consists of three components; a two-body pair energy, a three-body angular penalty and a generalised coordination. The two-body and three-body terms have environment dependence controlled by the atomic co-ordination  $Z$ . Within this framework, the total energy is written as a sum of on-site energies, equation 2.22.

$$U_i = \sum_j U_2(r_{ij}, Z_i) + \sum_{j < k} U_3(r_{ij}, r_{ik}, \theta_{jik}, Z_i) \quad (2.22)$$

Where  $U_2(r_{ij}, Z_i)$  is an interaction between atoms  $i$  and  $j$  ( $i$  is the on-site species and  $j$  and  $k$  are neighbours).  $U_3(r_{ij}, r_{ik}, \theta_{jik}, Z_i)$  is the interaction between atoms  $i$ ,  $j$ , and  $k$  centred at atom  $i$  representing angular forces [66]. The two types of interactions depend on the local environment of atom  $i$ . This depends on its local environment and is defined by its effective co-ordination number, equation 2.23 [65].

$$Z_i = \sum_{m \neq i} f_c \quad (2.23)$$

where  $f_c$  is the cut-off function defined further in equation 2.24 [66].

$$f(r) = \begin{cases} 1, & \text{if } r < c \\ \exp\left(\frac{\alpha}{1-x^3}\right), & \text{if } c < r < a \\ 0, & \text{if } r > a \end{cases} \quad (2.24)$$

where  $x = (r - c)/(a - c)$ .

The cut-offs are constrained to reproduce the co-ordinations of important crystal structures, e.g.,  $Z_i = 4$  for the diamond lattice [66].

The co-ordination  $Z_i$ , equation 2.22, has a fractional value and consists of two components, a spherical contribution  $z_i$  and an aspherical term which is vital for describing distorted configurations involving  $\pi$ -electrons. In graphite and diamond, the aspherical term vanishes due to the highly symmetric con-

figurations of the structures. The spherical term counts precisely the number of nearest neighbours and the co-ordination then assumes its intuitive integer value.

The pair potential,  $U_2$  resembles the SW potential (equation 2.21). The pair potential is short ranged and decays to zero at a distance set by the denominator in the exponential term. Equation 2.25 gives the functional form for distances smaller than the cut-off [73].

$$U_2(r, Z) = \epsilon \left[ \left( \frac{B}{r} \right)^4 - e^{-\beta Z^2} \right] \exp \left( \frac{\sigma}{r - a - a'Z} \right) \quad (2.25)$$

The bond-order is described by the exponential  $-\beta Z^2$  term. This term moderates the balance between attraction and repulsion. The parameter  $a'$  controls the variable cut-off, which was absent from the earlier silicon model.

The three-body term in EDIP uses a SW-like radial and angular terms, these terms have environmental dependence. Equation 2.26 describes the three-body term for distances  $r_{ij}$  and  $r_{ik}$  less than the cut-off.

$$U_3(r_{ij}, r_{ik}, \theta, Z) = \lambda(Z) g(r_{ij}, Z) g(r_{ik}, Z) h(\theta, Z) \quad (2.26)$$

The three components of  $U_3$  can be defined as equations 2.27 to 2.29.

$$\lambda(Z) = \lambda_0 \exp \left[ -\lambda' (Z - Z_0)^2 \right] \quad (2.27)$$

and

$$g(r, Z) = \exp \left[ \frac{\gamma}{r - a - a'Z} \right] \quad (2.28)$$

and

$$h(\theta, Z) = 1 - \exp \left\{ -q [\cos\theta + \tau(Z)]^2 \right\} \quad (2.29)$$

where  $\tau(Z) \equiv -\cos(\theta_0)$  describes the variation in ideal bonding angle which follows the SW philosophy of an ideal angle  $\theta_0$  for which there is no angular penalty [73].

The strength of the three-body interactions is controlled by the magnitude

function  $\lambda(Z)$ . The middle terms of equation 2.26 ( $g(r_{ij}, Z), g(r_{ik}, Z)$ ) are the radial functions (equation 2.28). These equations are generalised to include a variable range for the pair potential and the cut-off in the exponential denominator. The final term in equation 2.26 is the angular term,  $h(\theta, Z)$ , this term captures the energy cost of distortions away from the ideal angle  $\theta_0$ .

The spherical co-ordination contribution  $z_i$  is a function of distance and is determined by the sum  $z_i = \sum f(r_{ij})$ , where  $f(r)$  is a three-parameter function which is unity for  $r < f_{low}$ , zero for  $r > f_{high}$  and between these limits varies continuously according to the expression in equation 2.30.

$$f(r) = \exp\left(\frac{\alpha}{1 - x^{-3}}\right) \quad (2.30)$$

Where  $x = (r - f_{low}) / (f_{high} - f_{low})$ .

There is a second important factor in the co-ordination term of carbon EDIP, the aspherical term applying for sites with  $Z < 4$  which exhibit  $\pi$ -like bonding [73]. There are two mechanisms within the aspherical term which must be considered, the dihedral rotation term and the non-bonded  $\pi$ -repulsion term. The dihedral rotation term promotes a locally planar structure and the non-bonded  $\pi$ -repulsion term fixes the equilibrium spacing of graphite and thus prevents the collapse of planar  $sp^2$  units. The two mechanisms are included in the generalised co-ordination  $Z_i$  which can be seen in equation 2.31.

$$Z_i = z_i + \pi_3(z_i)X_i^{dih} + \pi_3(z_i)X_i^{rep3} + \pi_2(z_i)X_i^{rep2} \quad (2.31)$$

Where  $\pi_2$  and  $\pi_3$  are switching functions identifying two and three-co-ordinated atoms, and the  $X_i$  described dihedral rotation,  $\pi$ -repulsion at a threefold site and  $\pi$ -repulsion at a twofold site.

Vector products describe the co-ordination increment. These capture the appropriate symmetries via the functions in equations 2.32 to 2.34.

$$X_i^{dih} = Z_{dih} \sum \pi_3(z_j) (\hat{R}_{jm} \cdot \hat{R}_{ik} \times \hat{R}_{il})^2 C_{ijklm}^{dih} \quad (2.32)$$

and

$$X_i^{rep3} = Z_{rep} \sum \pi(z_j) (\hat{R}_{ij} \cdot \hat{R}_{ik} \times \hat{R}_{il})^2 C_{ijkl}^{rep3} \quad (2.33)$$

and

$$X_i^{rep2} = Z_{rep} \sum \pi(z_j) \left[ 1 - (\hat{R}_{ij} \cdot \hat{R}_{ik})^2 \right] C_{ijk}^{rep2} \quad (2.34)$$

Where  $jkl$  are neighbours of  $i$ ,  $m$  is a neighbour of  $j$  and  $\pi(z)$  selects for two- or threefold sites [73].

The distance-based cut-off function  $C$  can be seen in equations 2.35 to 2.37. These equations help avoid various unwanted first- and second-neighbour interactions.

$$C_{ijklm}^{dih} = p(R_{ij}) p(R_{il}) p(R_{jm}) \quad (2.35)$$

and

$$C_{ijkl}^{rep3} = (R_{ij} - c_0)^2 [1 - p(R_{ij})] p(R_{ik}) p(R_{il}) \quad (2.36)$$

and

$$C_{ijk}^{rep2} = (R_{ij} - c_0)^2 [1 - p(R_{ij})] p(R_{ik}) \quad (2.37)$$

With the function  $p(r)$  equivalent to  $f(r)$  except for different end-points  $p_{low}$  and  $p_{high}$  [73]. Both repulsive cut-offs are identically zero for  $R_{ij} > c_0$ , while the two switching functions  $\pi(z)$  are polynomials of the form  $[(z - x)^2 - 1]^2$  for  $|z - x| < 1$  and zero otherwise. The third switching function  $\pi(z)$  is equal to  $\pi_3(z)$  for  $z > 3$  and unity elsewhere.

The six pair potential parameters are effectively fitted to scaled Hartree-Fock cluster calculations, using data extracted from the SW pair potentials for graphite and diamond. Table 2.1 gives the parameters of EDIP as fitted to *ab initio* data [73].

Two-Body	$\epsilon = 20.09 \text{ eV}$ $\sigma = 1.257$	$B = 0.9538$ $\alpha = 1.892$	$\beta = 0.0490$ $\alpha' = 0.170$
Three-Body	$Z_0 = 3.615$ $\gamma = 1.354$	$\lambda_0 = 19.86 \text{ eV}$ $q = 3.5$	$\lambda' = 0.30$
Co-ordination	$f_{low} = 1.547$ $p_{low} = 1.481$ $Z_{dih} = 0.30 \text{ eV}$	$f_{high} = 2.27$ $p_{high} = 2.0$ $Z_{rep} = 0.06 \text{ eV}$	$\alpha = 1.544$ $c_0 = 3.2$

**Table 2.1:** Parameters of EDIP as fitted to the *ab initio* data.

Where  $B$  and  $\beta$  help to describe the bond order,  $\lambda$ ,  $\gamma$  and  $q$  define the cut-off for the three-body term;  $Z$  is the atomic co-ordination (*dih* is the dihedral rotation and *rep* is the  $\pi$  repulsion);  $\alpha$  is the spherical co-ordination;  $f_{low}$  and  $f_{high}$  are the co-ordination functions and are equal to  $p(r)$  except at  $p_{low}$  and  $p_{high}$ ,  $c$  determines the repulsive cut-off;  $\epsilon$  is the depth of the potential well and  $\sigma$  is the finite distance at which the inter-particle potential is zero [73].

Table 2.2 compares the elastic constants of the EDIP potential along experimental data for graphite and diamond. One can deduce from table 2.1 that carbon EDIP produces pleasing results when compared to experimental data. This is partially due to its resemblance to the SW potential which for theoretical reasons describes well the elastic properties of tetrahedral materials. It is for this reason that the carbon EDIP potential has been selected for undertaking the simulations in Chapters 4 and 5 [73].

		Expt.	EDIP
<b>Diamond</b>	B	442	418
	$c_{11} - c_{12}$	951	958
	$c_{44}$	576	472
<b>Graphite</b>	$c_{11} + c_{12}$	1232	1233
	$c_{11} - c_{12}$	880	849

**Table 2.2:** Elastic constants of diamond and a graphite sheet, in units of GPa. The computed graphite values presume a c-spacing of 3.35 Å.

## 2.6 The Ziegler-Biersack-Littmarck Potential (ZBL)

The Ziegler-Biersack-Littmarck potential (ZBL), is now universally employed in ion implantation simulations [22]. The ZBL potential is a screening electrostatic potential of nucleon-nucleon interaction. Equation 2.38 shows how the ZBL potential is calculated.

$$V_{zbl} = \frac{Z_1 Z_2 e^2}{r} \phi(r/a) \quad (2.38)$$

where:

$e$  = electronic charge

$r$  = the interatomic distance between the two atoms

$\phi(\frac{r}{a})$  = the screening function

$Z_1$  and  $Z_2$  are the charge on each atom

The screening length  $a$ , is defined by equation 2.39 [22].

$$a = \frac{0.8853a_0}{(\sqrt{Z_1} + \sqrt{Z_2})^2} \quad (2.39)$$

where  $a_0 = 0.529 \text{ \AA}$ .

The Ziegler-Biersack-Littmarck potential is a Coulomb potential with a screening function,  $\phi(\frac{r}{a})$  [74]. A Coulomb potential results from the configuration of a particular set of point charges within a system. Figure 2.3 shows a graph with the Coulomb potential (green) and the ZBL potential (red). The screening function,  $\phi(\frac{r}{a})$ , allows ZBL to work with a higher accuracy at smaller bond lengths. This is clear from figure 2.3 [75].

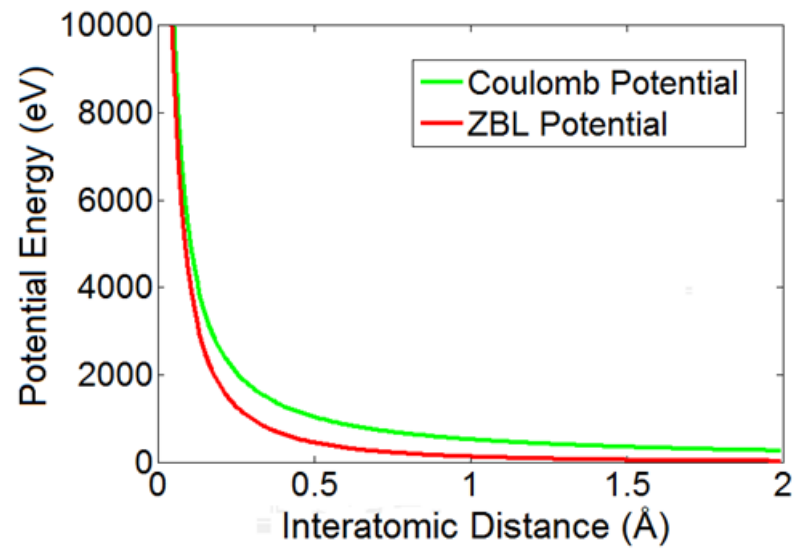


**Figure 2.3:** Graph showing the Coulomb potential plotted alongside the Ziegler-Biersack-Littmarck potential for Carbon.

## 2.7 Switching Function

The simulations undertaken in this report employ the use of EDIP alongside the ZBL potential. The energy of a system depends strongly on the interatomic separation. In this system, there are two different regimes. The chemical bonding regime, which is appropriate for distances greater or equivalent to  $1\text{\AA}$ . These are normally valence electrons. It is in the chemical bonding regime where EDIP will be deployed. The second is the nuclei-nuclei regime, which is appropriate for distances less than or equivalent to  $0.5\text{\AA}$ . The nuclei-nuclei regime will make use of the ZBL potential.

To switch from one potential to another you cannot simply change instantaneously from one to the other, there must be a 'change-over window' to allow the simulation to run smoothly. Figure 2.4 shows the 'change-over window' from EDIP to ZBL.

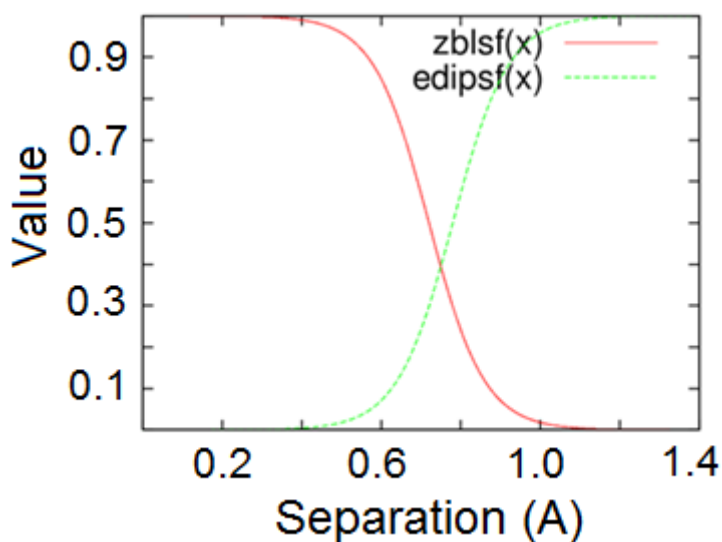


**Figure 2.4:** Graph showing the change-over window between EDIP and ZBL.

In order to successfully move between the two potentials, an interpolation function is required. An interpolation function is the transition of many systems by using a switching function. Figure 2.5 shows the graph of the transition between EDIP and the ZBL potential.

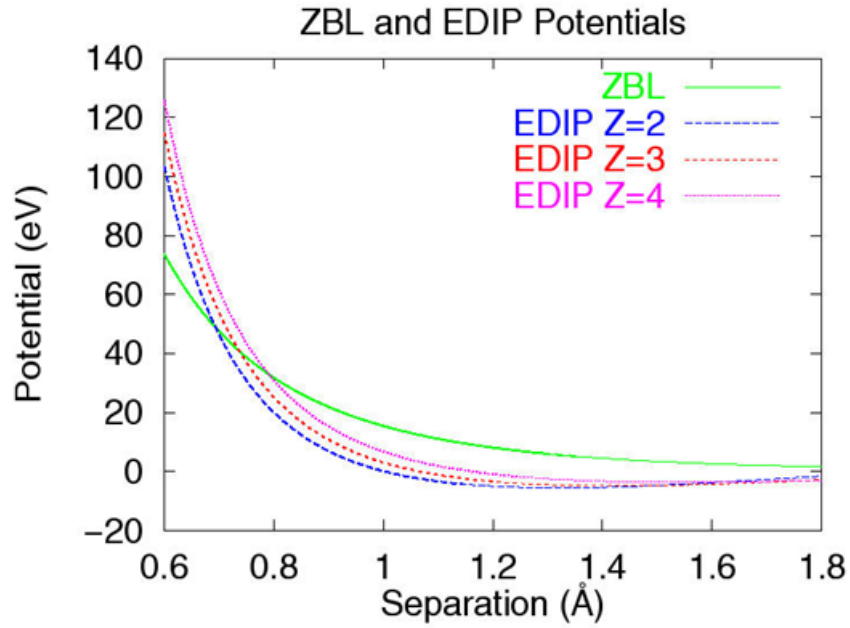


**Figure 2.5:** Graph showing three different configurations for EDIP and the ZBL potential. EDIP is shown for the atomic co-ordination ( $Z_i$ ) of: graphite ( $Z = 3$ ), diamond ( $Z = 4$ ) and low density amorphous carbon  $Z = 2$ ).

The approach to switch between the EDIP and ZBL potentials in simulations undertaken in Chapters 4 and 5 employed two Fermi-type scaling functions ( $SF_{EDIP}$ ,  $SF_{ZBL}$ ). The two functions are defined using three parameters of the positions of the mid-point of each function ( $r_{EDIP}$  and  $r_{ZBL}$ ) and the width  $w$  of the switching region. For simulations in Chapters 4 and 5 the values selected for the parameters were;  $r_{EDIP} = 1.05\text{\AA}$ ,  $r_{ZBL} = 0.45\text{\AA}$  and  $w = 0.07\text{\AA}$ . These values were selected to ensure a smooth transition between the two regimes. This is the same approach employed in previous EDIP simulations of ion impact [76] [77].

## 2.8 Kinchin and Pease Model

Kinchin and Pease first presented their model for the calculation of the damage function  $N(E_2)$  in 1954 [78]. The damage function  $N(E_2)$  gives the average number of displaced atoms due to a recoil at  $E_2$  and it also allows an estimate of the spatial distribution of the defects produced to be calculated. The collision cascade as described by Kinchin and Pease can be represented diagrammatically (figures 2.6 and 2.7). To fully understand figures 2.6 and 2.7, the following assumptions must be made [79]:

1. Atoms in collision behave like hard spheres.
2. All collisions are elastic and no energy is dissipated in electron excitation.
3. The cascade proceeds as a series of two-body collisions.
4. These collisions are independent of each other and any spatial correlations implied by the periodicity of the crystal structure will be ignored.
5. In a collision such as that illustrated in figure 2.7, when an atom with  $E$  emerges with  $E'$  and generates a new recoil with  $E''$  it is assumed that no energy passes to the lattice and
$$E = E' + E''$$
6. A stationary atom which receives less than a critical energy  $E_d$  is not displaced, similarly if an incident atom emerges from collision with  $E' < E_d$ , it does not contribute further to the cascade.

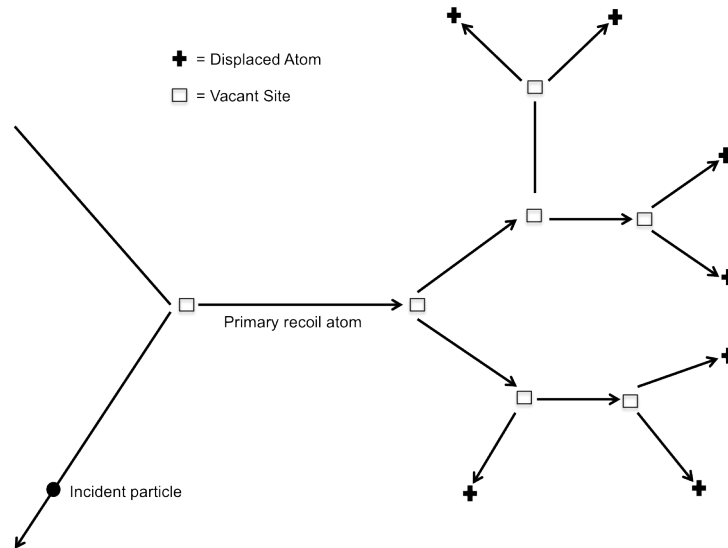


**Figure 2.6:** The Kinchin and Pease model collision cascade.

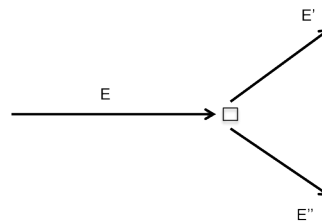


**Figure 2.7:** A single branch of the Kinchin and Pease collision cascade model.

The incident particle in figure 2.6 collides with an atom resulting in the formation of a cascade. Energy is transferred from the incident particle to the primary recoil atom during the collision. The primary recoil atom is displaced from its original starting position resulting in a vacancy being left in the lattice. As the primary recoil atom continues its journey through the lattice, further collisions occur; the result of these collisions is the formation of a cascade. Once the kinetic energy of the displaced atoms has fallen below the threshold energy, the atoms come to rest either in vacancies or as interstitials.

Figure 2.7 demonstrates the conservation of energy during a collision cascade. A collision cascade is a sequence of collisions between atoms induced by an energetic particle. The energy of the incident particle,  $E$ , is equal to the sum of the energy of the two recoil atoms,  $E'$  and  $E''$ , equation 2.40 [79].

$$E = E' + E'' \quad (2.40)$$

The above statements along with figures 2.6 and 2.7, form the basis of the Kinchin and Pease definition of the mean displacement energy,  $E_d$ . Employing this theory, the probability of displacing an atom is zero below the energy  $E_d$  and one at  $E = E_d$ . It follows that an atom with  $E_d < E < 2E_d$  cannot produce any increase in the number of displaced atoms and  $N(E)$  is a step function, defined in equation 2.41 [79].

$$\left. \begin{aligned} N(E) &= 0, \text{ if } E \leq E_d \\ N(E) &= 1, \text{ if } E_d < E < 2E_d \end{aligned} \right\} \quad (2.41)$$

The probability of finding a scattered atom with energy  $dE'$  at  $E'$  and a recoil atom with energy in  $dE''$  at  $E''$  in a collision with  $E > E_d$  is  $d\sigma/\sigma$ , where  $\sigma$  and  $d\sigma$  are the total and differential cross-sections for the atomic collision [79]. Equation 2.42 gives the probability.

$$\frac{d\sigma}{\sigma} = \frac{dE''}{E} \text{ or } = \frac{dE'}{E} \quad (2.42)$$

The integral of the product of  $N(E')$  and the probability (equation 2.42) over the energy range,  $E_d$  to  $E$ , will give the average number of displaced atoms produced by the scattered atom, statement 2.43.

$$\int_{E_d}^E N(E') \frac{dE'}{E} \quad (2.43)$$

Statement 2.43 is also equivalent to the average number of displaced atoms produced by the recoil atom. This implies the average number of displaced atoms produced by an atom with  $E$ :  $N(E)$  is equal to equation 2.44.

$$N(E) = \frac{2}{E} \int_{E_d}^E N(x) dx \quad (2.44)$$

when  $E > E_d$ ,  $N(E) = kE$ ,  $k$  is a constant whose value may be found by putting  $N(2E_d) = 1$ . Hence,  $k = 1/2E_d$ . Therefore,  $N(E)$  can be defined as in equation 2.45.

$$N(E) = \frac{E}{2E_d} \quad (2.45)$$

for  $E > E_d$ .

Equation 2.45 states an atom would continue to produce cascades until its kinetic energy falls below  $2E_d$ . The number of atoms with  $2E_d$  should be  $E_2/2E_d$  [79].

High energy cascades can be employed to calculate the threshold displacement energy using the modified Kinchin and Pease (KP) model and the Norgett-Robinson-Torrens (NRT) model [80]. Both models employ the threshold displacement energy,  $E_d$  as a single parameter. The number of displacements in the KP model is computed utilising equation 2.45.

The NRT model is a modified Kinchin and Pease model used to calculate the number of defects generated by a PKA [80] [81]. Equation 2.46 is used to generate the model.

$$N_d = \frac{kE}{2E_d} \quad (2.46)$$

where  $N_d$  is the number of defects,  $E$  is the initial PKA energy,  $E_d$  is the threshold displacement energy and  $k$  is the displacement efficiency.

The displacement efficiency  $k$  is given the value 0.8 [80]. This value is independent of the PKA energy, the target material and the temperature. This model was originally fit to MD simulations in copper [11] and iron [82] [83].

Consistent with the experimental and computation literature, table 2.3, a value of  $E_d = 25$  eV was assumed for the two models. Graph 2.8 show plots of the two models.

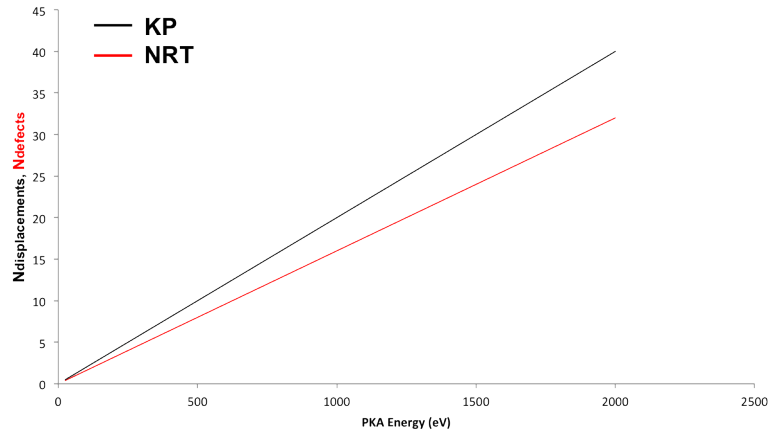


**Figure 2.8:** The solid black line shows the number of displaced atoms as a function of PKA energy (Kinchin-Pease model). The solid red line shows the number of stable defects as a function of PKA energy (Norgett-Robinson-Torrens model). Both models assume a threshold displacement energy of 25 eV.

## 2.9 Literature Review

Despite the ample use of graphite within the nuclear industry, there is very little published data using molecular dynamics for carbon based materials. Papers involving closely related work have been used to set initial parameters for cascade simulations. The literature below describes past work studied, explains ideas which can be developed and gives an explanation as to why further research needs to be conducted into each area.

Nordlund *et al.* published a paper in 1996 [19] using an improved Tersoff potential in very small cells involving only a few tens of atoms. Nordlund used these simulations to investigate the defects created by a collision cascade. These simulations were computed on a very small scale and therefore cannot give a general overview of the effects a cascade produces. Nordlund's simulations could be reproduced using larger cells and a different range of energies. This would give a better insight into the effects cascades have on cells.

Smith *et al.* published work in 1990 and 1996 [16] [6] using the Brenner hydrocarbon potential to look at displacement energies. The paper explains clearly how to set up a cascade. Simulations produced are in a two-layer cell and have provided a starting point for simulations computed in Chapter 4. With the major advances in computer technology, cascades on a much larger scale with 100s of 1000s of atoms can be produced. The larger cell sizes allow cascades with higher initial PKA energies to be analysed.

Yazyev *et al.* published a paper in 2007 [84] employing ab initio quantum mechanical molecular dynamics. They calculated defects, estimated threshold displacements and published movies including the formation of a Frenkel pair which have been re-created in the present work using EDIP and the ZBL potential. The defects produced in Yazyev's calculations were in very small cells. Therefore, the overall effect of the defects cannot be seen. The simulations could be repeated in larger cells and the whole structure analysed.

Zinkle and Kinoshita's work in 1997 studied defect production in ceramics [85]. Whilst this work does not involve graphite, the content was useful in understanding radiation effects, defect production and migration and how threshold displacement energies can be calculated. The paper also gives references to results found using diamond which can be compared to results obtained for diamond using the EDIP potential.

Heggie and Latham in 2011 studied the atomic-, nano-. and mesoscale origins

of graphite's response to energetic particles - see [86]. Simulations were produced using density functional theory. Results from this work include: values for the bonding and elastic parameters of graphite, defects, interstitials and vacancies produced also, observed dislocations. The main idea taken from this work is the different types of defects which may be seen in irradiated graphite. The theoretical results explained in reference [86] make a good comparison to experimental data. In the Chapter 4, defects found using molecular dynamics are compared to the results obtain by Heggie and Latham.

Table 2.3 reports the difference values for the threshold displacement energy published from experimental results and simulations on irradiated graphite. The value for the threshold displacement energy has varied from 12 eV to 60 eV depending on the method employed.

Author	Methodology	$E_d$ (eV)
Eggen (1950)	Electron Bombardment (Experimental)	$24.7 \pm 0.9$
Lucas (1963)	Electron Irradiation (Experimental)	$60 \pm 10$
Montet (1967)	Electron Irradiation (Experimental)	$33 \pm 1$
Nakai (1991)	He <sup>+</sup> , Ar <sup>-</sup> , Xe <sup>+</sup> Irradiation (Experimental)	12
Marton (1993)	Noble-Gas Ions Irradiation (Experimental)	$34.5 \pm 1$
Smith (1996)	Tersoff & Brenner MD Simulation	34.5
Zaiser (1997)	Electron Irradiation (Experimental)	10 - 20
Hehr (2007)	Carbon Cascade Collisions (REBO MD Simulation) at 300 K	44.5
Yazyev (2007)	Carbon Cascade Collisions <i>ab initio</i> MD Simulation	20
Christie <i>et al.</i> (2014)	Carbon Cascade Collisions (EDIP) MD Simulation	25

**Table 2.3:** Published values for the threshold displacement energy in irradiated graphite from experimental and theoretical simulations.

## Methodology

The radiation damage cascades produced in graphite, diamond, glassy carbon and high and low density amorphous carbon are simulated using molecular dynamics (MD). The MD simulations are employed with equilibrium interactions governed by the Environment Dependent Interatomic Potential (EDIP) for carbon.

To accurately model the close-range interactions between atoms, the pair potential within the EDIP formalism  $\phi_{EDIP}(rij, zi)$  [73] [21], is smoothly switched to the Ziegler-Biersack-Littmark (ZBL) potential  $\phi_{ZBL}(rij)$  [22].

MD simulations were carried out at 300°C with lattices equilibrated for 5 ps. Periodic boundary conditions were employed in each of the Cartesian directions along with a 3.5Å thermal layer to remove excess kinetic energy during the cascade simulations. In addition, a layer of atoms perpendicular to the basal plane were held fixed to prevent any net transverse motion of the planes.

Cascades were initiated with PKA energies of: 25, 50, 75, 100, 250, 500, 750, 1000, 1500 and 2000 eV. The cascades were contained within orthorhombic supercells as large as 157.7 x 152.6 x 153.6 Å and containing up to 440,448 atoms (figure 3.5).

The initial directions of the PKA were determined by uniformly distributing points on a unit sphere (the so called Thomson Problem [87]) to select the direction of the initial velocity in a similar vein to the work done in reference [88]. The initial motion of the PKA is towards the centre of the cell. This makes it more likely that the cascade remains within the cell.

After successful completion of the MD cascades, AVAS (a visualisation software package) was used to analyse results both statistically and analytically.

### 3.1 Neutron Collisions

In order for fission to occur, the neutrons have to collide with the small number of uranium-235 nuclei present in the reactor. As the neutrons are initially travelling with extremely high velocities, this lowers the chance of a collision taking place [89]. In order to improve the efficiency of a reactor, the number of collisions occurring needs to be increased. This can be achieved by slowing the neutrons down and allowing them to collide with the atoms of lighter elements also known as moderators. The collisions allow a transfer of energy to occur and continue in the same way a moving billiard ball does when it strikes a stationary ball. The nuclear reactors running in the UK use graphite moderators [42].

In graphite nuclear reactors, there is a broad range of neutron energies present [90]. The neutrons of interest in a nuclear reactor are fast neutrons and thermal neutrons. Fast neutrons have a velocity of several MeV and are produced in fission. Thermal neutrons have an energy of around 0.025 eV. To create a self-sustaining nuclear reactor, the fast neutrons need to be thermalised (slowed down). The moderator inside a nuclear reactor thermalises the fast neutrons until they become thermal neutrons. Thermal neutrons have an energy of around 0.025 eV and have a higher probability of initialising fission in uranium than fast neutrons [89]. This process is called fission and results in the production of fast neutrons. The fast neutrons are then free to continue on in further fission reactions. In reactions using thermal neutrons, there is an increase in fission probability of approximately 500 times that of fission with fast neutrons.

The neutrons produced by fission are at high energy. The majority of all fission neutrons have energies between 0.1 MeV and 10 MeV [91]. The neutron energy distribution or spectrum is shown in figure 3.1. The graph from figure 3.1 can be used to show the most probable energy for a neutron which is about 0.7 MeV. The average energy of fission neutrons is about 2 MeV. Figure 3.1 refers only to uranium-235, values vary for other nuclides.

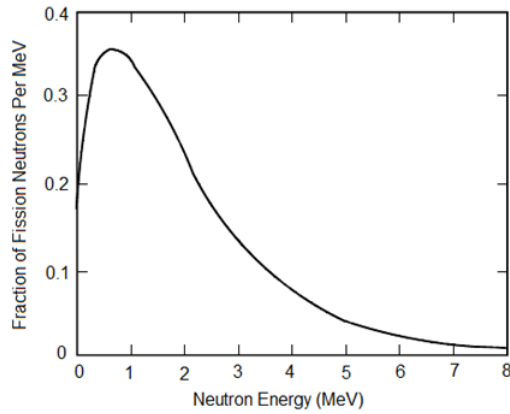


**Figure 3.1:** Graph showing the fraction of fission neutrons per MeV as a function of neutron energy. (Image courtesy of DOE Fundamentals Handbook, Nuclear Physics and Reactor Theory.)

Figure 3.2 shows the graph of the probability of a neutron causing a fission for uranium-235 and uranium-238 as a function of neutron energy [92]. The higher the cross-section the greater the probability that fission will occur.

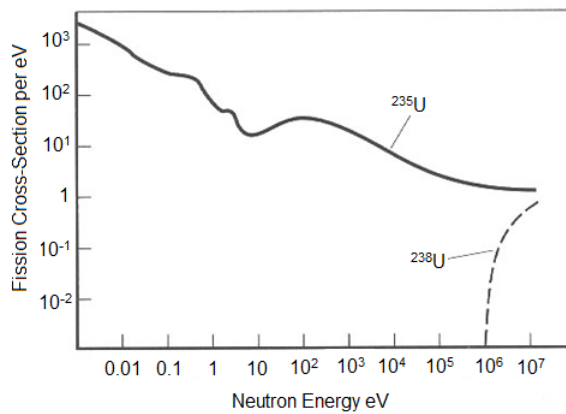


**Figure 3.2:** Graph showing the probability of fission occurring in uranium-235 and uranium-238. Uranium-238 fission is a threshold reaction. (Image courtesy of DOE Fundamentals Handbook, Nuclear Physics and Reactor Theory.)

## 3.2 The Simulation Cell

There are three different areas of interest within this work, shown in figure 3.3 [93];

1. The thermal spike
2. Collision cascades
3. Threshold displacement energy simulations

In order to simulate each area effectively, the structure of the graphite cell used in the simulation must be modified appropriately.

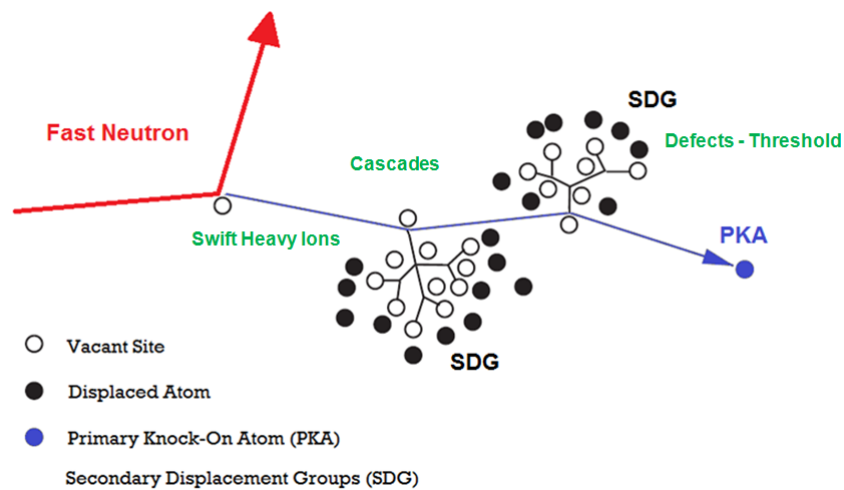


**Figure 3.3:** The path a primary knock-on atom (PKA) takes through a cell and the resultant interstitials and vacancies which are formed.

### 3.2.1 Thermal Spike Regime

The first regime of interest occurs with the swift heavy ions. Swift heavy ions are a special form of particle radiation for which the electronic stopping dominates over nuclear stopping [94] [95]. Electronic stopping refers to the slowing down of a projectile ion due to the inelastic collisions between bound electrons in the lattice and the ion moving through it. Nuclear stopping refers to the elastic collisions between the projectile ion and atoms in the lattice. A carbon atom also known as the primary knock-on atom (PKA), passes through the cell without colliding with any atoms. However, the PKA transfers electron energy

to the surrounding atoms which causes them to vibrate; these vibrations in the cell can result in displacements of carbon atoms along with the formation of interstitials and vacancies in the cell. A thermal spike in a graphite cell can be used to simulate this effect. The thermal spike model transfers kinetic energy to atoms in the graphite cell over a set radius. The radius can be altered as can the initial energy. This is equivalent to the PKA going straight past the atoms but transferring energy to them.

Figure 3.4 represents the cell used to simulate a thermal spike. As the PKA atom passes through the cell, kinetic energy can be transferred between atoms in the layers in a 'wave-like' manner. The wave of kinetic energy can have drastic effects if the wave hits the side of the graphite structure and reflects back. As a direct response of the reflection wave, atoms could be displaced. This effect would not be seen in an actual graphite moderator because the overall structure is so large compared to the collision site. In a graphite moderator, a wave of kinetic energy created as a direct response to a thermal spike, would continue to travel down the layers of graphite constantly losing energy. Once the kinetic energy remaining in the wave is less than the threshold displacement energy of carbon, the wave has no further effect on the cell.

A second issue occurring as a direct result of the wave of kinetic energy is movement of the graphite layers. To ensure this is not going to be a problem in the computational simulation two options are considered. An extremely large cell which can contain the wave until it has less kinetic energy than the threshold displacement energy of carbon could be constructed. This idea would also show any point defects such as interstitials and vacancies created by the resulting wave of kinetic energy. However, this method is computationally expensive and would take a very long time to compute. The larger the cell used in a simulation the more difficult it becomes to analyse defects which implies gathering data from the simulations would prove difficult. The thermal spike and resulting kinetic energy wave leave nominal damage in the final lattice cell when simulated under the energies and temperatures presented in this thesis. Outside the initial thermal spike region, there is minimal, if any, damage created. The second option is to insert a layer of fixed atoms into the cell to stop the layers of graphite from moving. In a real life graphite structure, the effect of the spike would be so small compared to the block of graphite, the individual layers would not move so the fixed atoms force the wave to end and hold the graphite layers in place. The main advantage of the present method is speed, the simulations can be computed much quicker using a smaller cell,

the analysis will be easier and the structure is still a very realistic model of a radiation damage point in a graphite moderator.

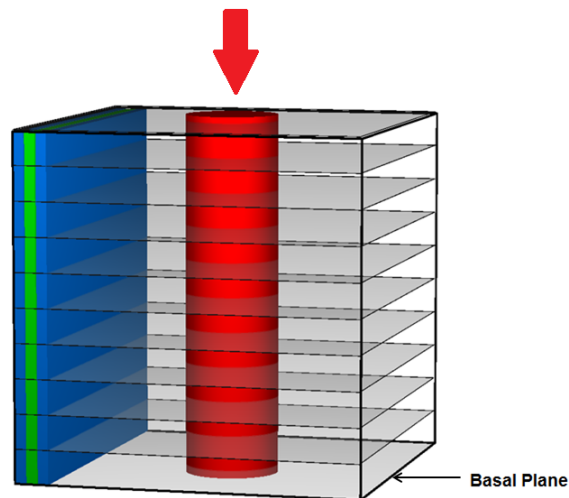


**Figure 3.4:** Diagram of the thermal spike cell cylinder used in simulations presented in this thesis. The axis of the thermal spike is indicated by the red arrow. The graphite planes are denoted in grey, thermostats are indicated in blue, the fixed atoms in green and the red cylinder denotes the thermal spike region.

During fission heat is produced. In a graphite moderator, the heat produced by one collision would not stimulate a vast change in temperature within the structure. In a cell consisting of a few thousand atoms, a change in temperature can alter the effect of collisions and thus the amount of damage created within the cell could be increased. The AGR reactors are kept at a regulated temperature of around  $300^{\circ}\text{C}$ , this is achieved by the gas cooling system. It is important that the core temperature of the cell is kept as consistent as possible to replicate the conditions of an AGR. In order to achieve this, a thermostat is employed. The thermostat removes any excess energy as this extra energy would affect the temperature of the structure. There are two thermostats required in the thermal spike cell on either side of the fixed atoms. The thermostat on the inside of the fixed atoms draws any excess energy created during the simulation. The fixed atoms stop the excess atoms from re-bounding back into the cell. If this happens, the temperature could be altered along with the number of defects produced. The second layer of thermostated atoms is placed outside the fixed atoms at the edge of the structure to ensure atoms cannot 'wrap' around and re-enter the cell (wrap implies an atom has left the cell from one side and re-enters the cell from the opposing side).

To ensure wrapping of cells is not an issue during simulations, a sufficiently large structure should be chosen. If the PKA atom hits the cell wall of the structure and passes through during a simulation, the simulation will automatically stop.

The red cylinder in figure 3.4 represents the thermal spike. The radius of the spike can be altered. The size of the radius required for a simulation depends on the size of the cell and the amount of initial energy given to the system. If a high value for the initial energy is chosen then a larger cell radius would be required to contain the simulation. As already discussed, there are three relevant values for the thermal spike, the most probable energy of a neutron during fission, the average energy of a neutron in fission and the maximum energy of a neutron during fission that can safely be contained. Each will require a different sized radius and cell. The most probable energy of a neutron during fission is much less than the maximum energy of a neutron during fission, the result of this is a larger radius is required for the maximum energy compared to a smaller radius which would be sufficient for the probable energy.

### **3.2.2 Cascade Simulations**

The second area of interest, figure 3.3, the cascade region, requires a slightly modified cell. Unlike the thermal spike cell where the main movement in the cell occurs in a specific region, the cascades produced as a direct result of the PKA can cause damage in the whole cell and not just in a concentrated region. The sporadic movement of atoms in the cell and the considerable distances they can travel mean that it is crucial that an appropriate size cell is selected. If the cell is too small, the PKA will pass outside the cell wall and the simulation will be void. However, if the cell is too large, the simulation will be unnecessarily time consuming and computationally expensive. The size of the cell will also depend on the direction of the initial PKA. If the initial PKA direction is such that the PKA travels between two layers, the cell will need to be larger as the PKA will tend to travel further through the cell before colliding with another atom. However, if the initial direction of the PKA is such that collisions with neighbouring atoms will be instantaneous then it would be expected the cascade would remain close to the initial PKA site therefore a smaller cell would be appropriate. Every time a collision takes place, there is a transfer of energy between the atoms, therefore, the damage would remain

closer to the initial starting position. In general, a smaller cell could be used for this type of simulation.

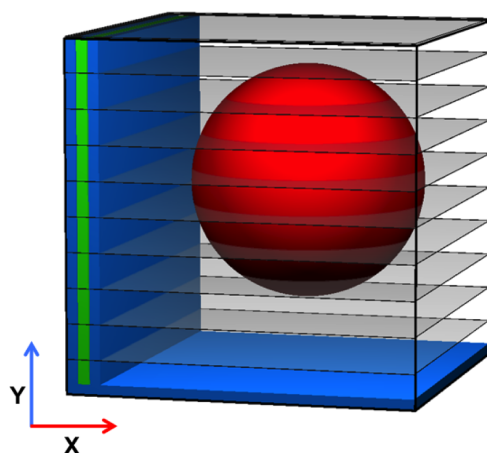


**Figure 3.5:** Diagram of the cascade cell used in simulations presented in this thesis. The graphite planes are denoted in grey, thermostats are indicated in blue, the fixed atoms in green and the surface of the red sphere denotes the PKA region.

Figure 3.5 is a diagram of the cell used for cascade simulations in Chapters 4 and 5. The cascade cell has a layer of fixed atoms in the same place as seen in the thermal spike cell. These fixed atoms stop the graphite layers from sliding and ensure that if an atom hits the fixed atoms, it cannot re-bounce into the cell and cause further damage. The thermostat atoms employed within the thermal spike cell are also used within a cascade cell. The thermostat atoms on the inside of the cell remove any excess energy which helps to moderate the temperature during a cascade simulation. The thermostat atoms halt any atoms attempting to escape from the cell. This is a main priority during cascade simulations as wrapped atoms could enter from the opposite side of the cell resulting in cascades being formed in a new part of the cell. There is a third thermostat in a cascade simulation which is not present in the thermal spike cell. The third thermostat, figure 3.5, can be seen at the bottom of the cell. The third thermostat works in partnership with the other thermostats to regulate the temperature and remove any excess energy from the system. The third thermostat cannot be used in the thermal spike cell. This is because the energy from the thermal spike runs from the bottom to the top of the cell. The introduction of this thermostat would not allow the spike to run as it would remove the energy from the spike at the edges of the cell.

The red sphere in the cell represents the region in which the PKA is selected.

The PKA is selected from a point on the circumference of the sphere using the centre point of the sphere as a reference. The initial direction of the PKA alters the atom's starting position. Cascade simulations are directionally dependent. Therefore, it is crucial that the starting position of the PKA can be altered. To assist in retaining the cascade within the simulation cell, the location of initial motion was selected towards the centre of the supercell.

### 3.2.3 Threshold Displacement Energy Simulations

The final region of interest, figure 3.3, are the threshold displacement energies. The same cell structure as the cascade regime is used for threshold displacement energy simulations. At the threshold energy, atoms have very little kinetic energy compared to the initial kinetic energy of the PKA. This is because of the transfer of energy which occur during collisions in cascades. There are two ways of observing the threshold displacements. One method would be to follow the final stages of a cascade simulation or alternatively, run an independent threshold simulation using a smaller value for the initial kinetic energy. To observe defects produced at the end of a cascade simulation, the same size cell should be used as the cell in the cascade simulations. However, to run an independent threshold displacement simulation, a small cell can be used. The advantage of using a small cell is that it is quick and computationally efficient. The threshold displacement energies are concentrated on one small volume within the cell thus using a small cell that does not affect results on a large scale.

The size of the cell used in simulations depends entirely on the initial direction and energy of the PKA, as has been explained above. The cell sizes used for simulations in this report range from a few tens of atoms for threshold displacement calculations up to 440, 448 atoms for high energy cascade simulations.

As with experimental equipment, the simulation cell must be equilibrated before use. The cell is first equilibrated for 5 ps. The equilibration of the system ensures the temperature is stable. As the simulations are being tested across a range of different temperatures, a stable temperature is crucial.

Once the structure has been equilibrated, the environment inside the structure is stable. The final position, temperature and energy of the atoms in the structure can now be used as the initial positions for a cascade or thermal spike

simulation.

### 3.2.4 Carbon Materials Cascade Simulations

Cascades in diamond are simulated using the same method described in sections 3.2.1, 3.2.2 and 3.2.3.

The process for simulating high and low density amorphous carbons and glassy carbon differs from methods used in graphite and diamond cascades.

To simulate high and low density amorphous carbons, a cubic liquid at fixed density is quenched to form the amorphous solid. To achieve this, a simple cubic lattice containing 4096 atoms with slightly randomised co-ordinates and spanning densities between 1.5 and 3.0 g/cc is generated [68]. The densities are as follows; 1.5 g/cc for glassy carbon, 2.0 g/cc for low density amorphous carbon and 3.0 g/cc for high density amorphous carbon. Calculations are performed employing the micro-canonical ensemble (NVE) which enables spontaneous melting to occur [21]. Once the lattice has melted, the velocity of atoms is rescaled to the desired temperature, typically 5000 K. The liquid is equilibrated for 0.5 ps before being allowed to cool to form an amorphous solid over a period of 0.5 ps [68].

To form glassy carbon, the quenching was followed by a long annealing cycle. The annealing process consists of heating the amorphous solid to the desired temperature and maintaining it for a period of 200 ps before cooling the sample to 300°C. These are the required conditions for simulations presented in Chapter 5.

The initial positions and energies of atoms for high and low density amorphous carbon and glassy carbon were obtained from reference [68].

### 3.3 The Thomson Problem

To accurately determine the defect formation as a function of PKA energy, a robust sampling method of PKA energy and direction must be taken. The most intuitive way of accomplishing this is to uniformly sample across the surface of a sphere. However, uniformly distributing a large number of points on the surface of sphere is a non-trivial task with no analytical solution. This problem was first outlined by Thomson in 1904 [87] whilst attempting to determine the arrangement of point charges in the atom.

The Thomson problem has been generalised to finding the minimum energy for  $N$  point charges on a sphere and has formed a significant area of research applicable to a multitude of real-world problems. The values of the minimum energy for  $N < 100$  are well documented. However, for large  $N$ , the number of local minima increases exponentially and finding the global minimum using simple numerical algorithms becomes a time-consuming task.

The primary knock-on trajectories for the simulations undertaken in cascades in graphite were generated by sampling from a unit sphere obtained by solving the Thomson problem with the number of points  $N = 20$ . An MD minimisation technique incorporating the velocity Verlet algorithm (a numerical method to integrate Newton's equations of motion) [50] has been adapted with each point given a unit mass and with the time step set to a nominal small value. The temperature can be controlled through velocity scaling. This can help the system escape out of the local minima. The effective force,  $F_{eff}$ , used during the minimisation process is given by the Coulomb force,  $F_i^{True}$  with the radial component removed, equations 3.1 to 3.4 [88].

$$F_i^{Eff} = F_i^{True} - \left( F_i^{True} \cdot \hat{r}_i \right) \quad (3.1)$$

where

$$F_i^{True} = -\nabla \phi_i (r_1, r_2, \dots, r_n) \quad (3.2)$$

where

$$\phi_i (r_1, r_2, \dots, r_n) = \sum_{i \neq j} \frac{1}{r_{ij}} \quad (3.3)$$

and

$$r_{ij} = |r_i - r_j| \quad (3.4)$$

The radial component,  $\mathbf{F}_i^{True}$ , can be removed. This results in  $\mathbf{F}_i^{Eff}$  being tangential to the surface of the sphere. The positions of the points are re-normalised to ensure each point remains on the surface by using equation 3.5.

$$\hat{r}_i = \frac{r_i}{|r_i|} \quad (3.5)$$

The initial random configuration of 20 points on the unit sphere is shown in figure 3.6. The initial directions are listed in table 3.1.

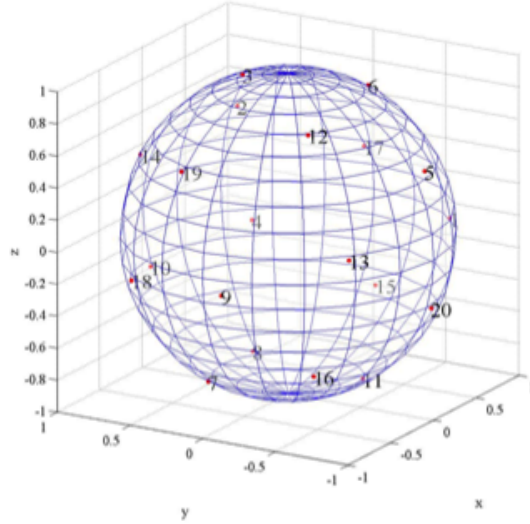


**Figure 3.6:** Diagram of the initial 20 random configuration of 20 points on the unit sphere as solved using the Thomson problem with  $N = 20$ .

Point Number	<i>x</i> -component	<i>y</i> -component	<i>z</i> -component
1	0.737604927	-0.675232531	0
2	0.522585211	0.658223546	0.541891559
3	-0.05135572	0.283547788	0.957581977
4	0.709991918	0.667304275	-0.22498107
5	0.133015703	-0.859841041	0.492930225
6	0.501642205	-0.255035814	0.826626779
7	-0.501642199	0.255035813	-0.826626783
8	0.266221815	0.399429572	-0.877258207
9	-0.988188563	-0.121277127	-0.093676158
10	-0.021417929	0.934795772	-0.354539329
11	0.193601742	-0.398660276	-0.896430895
12	-0.44418536	-0.397849345	0.802754797
13	-0.613562575	-0.778509191	0.132152962
14	-0.22134945	0.885903477	0.407651137
15	0.834911985	-0.10739429	-0.539804079
16	-0.562747905	-0.506113571	-0.65357773
17	0.961985389	0.045702006	0.269249768
18	-0.747119269	0.637275258	-0.188926026
19	-0.783014609	0.272356297	0.559204945
20	0.073022689	-0.939660623	-0.334223877

**Table 3.1:** Initial PKA Positions (Solved with  $N = 20$ )

### 3.4 Physical Properties of Graphite Cascades

Advanced Gas Cooled Reactors employ graphite moderators to slow neutrons following fission (see Section 3.2). Figure 3.3 shows the path of neutrons through graphite [93]. The red arrow indicates the path of a fast neutron. The fast neutron collides with the nucleus of the PKA which causes the PKA to be displaced from its initial starting position. The PKA passes through the initial part of the cell without colliding with any atoms. Energy is transferred from the PKA to neighbouring atom's electrons. This effect can be created by using a thermal spike in the cell. When the fast neutron collides with a carbon atom (indicated in figure 3.3), the neutron transfers, on average, 15% of its kinetic energy to the carbon atom. It takes approximately 100 collisions for the fast neutron to thermalise. This is because the mass of the carbon is 12 times greater than the mass of the neutron.

The first part of the diagram refers to swift heavy ions (indicated in figure 3.3). The primary knock-on atom (PKA), passes through this region without colliding with any atoms. However, the PKA transfers kinetic energy to the surrounding atoms. This causes them to vibrate which can result in the formation of interstitials and vacancies. The electron energy transfer has been simulated using a thermal spike.

The second part of the diagram represents cascades produced as a direct result of a collision between the PKA and atoms in the cell, (indicated in Figure 3.3). Cascades are produced when the PKA hits one or several atoms resulting in the displacement and collision of other atoms in the cell. Simulations computed using a PKA with a high initial energy results in carbon nuclei with a small cross section and the production of a larger number of cascades. Thompson states the structure of a material can exert some influence on the spreading of the collision cascade [79]. Moving atoms can move in open channels that exist between the atomic rows of the lattice and find an easy route through the lattice, a phenomena known as channelling. Kinetic energy can also be passed from one atom to another atom in a sequence of collisions along the rows. This is known as focusing. Both types of phenomena have been observed in cascades presented in Chapters 4 and 5.

Channelling can influence the collision cascade by reducing the number of displaced atoms,  $N(E_2)$ . It could also result in the spread of damage being over a larger volume [79]. Statement 2.43 gives the average number of displacements

in a hard sphere collision. There is a probability  $c$  of the atom with energy  $E$  becoming channelled and lost to the cascade. If this occurs, the channelled atom would be the only displaced atom which would result in  $N(E) = 1$ . There is also the probability  $(1 - c)$  which results in statement 3.6.

$$2 \int_{E_d}^E N(x) \frac{dx}{E} \quad (3.6)$$

This would result in the average number of displacements being equal to equation 3.7.

$$N(E) = c + 2(1 - c) \int_{E_d}^E N(x) \frac{dx}{E} \quad (3.7)$$

If  $c$  is taken to be independent of energy then equation 3.8 holds.

$$N(E) = (E/2E_d)^{(1-2c)} \quad (3.8)$$

where  $E > E_d$  and  $c < 1$ .

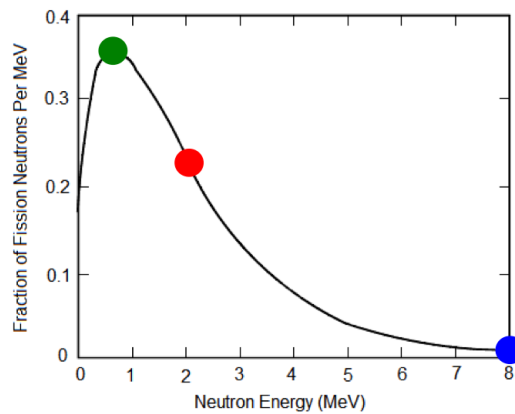
Although expression 3.8 may be a rather poor approximation for the average number of displacements, it shows that the larger  $E$  is, the more recoils are involved and the greater the overall chance of channelling [79].

The final part of the diagram represents any defects formed (indicated in figure 3.3). Atoms displaced from their initial position leave behind vacancies. Vacancies can be filled by another displaced atom or the bonds from surrounding atoms may close. Displaced atoms can also form interstitials both within a layer and between layers.

### 3.5 Thermal Spike and Cascade Simulations in Graphite

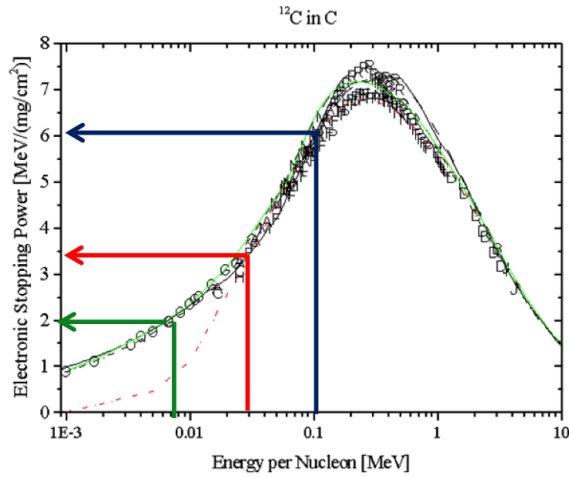
Figure 3.3 shows the path a primary knock-on atom (PKA) takes through the graphite structure. The first regime of interest occurs for the swift heavy ions. In this region, the PKA passes straight through without colliding with any atoms. However, the PKA transfers kinetic energy to the surrounding atoms. This process has been simulated using a thermal spike, figure 3.4.

Figure 3.7 shows the fraction of fission neutrons per MeV against the neutron energy. There are three points of interest on the graph; the most probable, the average and the maximum energy for fission to take place. Figure 3.7 shows these three energies [92].



**Figure 3.7:** Graph showing the three main regions of interest during a thermal spike simulation. The most probable (green), The average (red) and the maximum (blue), energy to cause fission.

To simulate the three cases, the electronic stopping power of a carbon atom is required. As a fast particle passes through a material it gradually loses energy. The stopping power of a particle is defined as the conservative force acting on the particle due to interaction with matter. Figure 3.8 shows the energy per nucleon and the electronic stopping power of the atoms in a thermal spike [96]. The three main regions of interest during a thermal spike simulation are marked on the graph. The most probable (green), The average (red) and the maximum (blue), energy to cause fission.



**Figure 3.8:** Graph showing the energy per nucleon vs. the electronic stopping power of carbon in carbon. The three main regions of interest during a thermal spike simulation are marked on the graph. The most probable (green), the average (red) and the maximum (blue), energy to cause fission.

During a thermal spike simulation, a large amount of kinetic energy is transferred to atoms within a given radius. Around one quarter of this energy is transferred back into the nuclei creating a transient, liquid-like state. The energy change has to be accounted for when choosing the initial energy value for the thermal spike.

The most probable value for fission occurs when the energy per carbon nucleon is  $6.0 \times 10^3$  eV (figure 3.8). Values for the average value of fission occurs when the energy per nucleon is  $2.5 \times 10^4$  eV, figure 3.8. The maximum value of fission that can occur before the cell cannot contain the simulation has an energy per nucleon of  $1 \times 10^5$  eV, figure 3.8. These values are obtained by calculating the differential at the three points on the graph in figure 3.8, converting the result into eV and then quartering the value. The value is quartered because on average only 25% of the energy in electronic stopping is transferred back into the nuclei.

The recoil energy of a carbon atom after a neutron has collided with its nucleus can be calculated using equation 3.9 [79].

$$E_2 = \Lambda E_1 \sin^2(\phi/2) \quad (3.9)$$

where

$$\Lambda = 4M_1M_2/(M_1 + M_2)^2 \quad (3.10)$$

$M_1$  and  $M_2$  are the masses of a carbon atom and a neutron,  $E_1$  is the average kinetic energy,  $E_2$  is the recoil energy and  $\phi$  is the recoil angle. Figure 3.8 and equations 3.9 and 3.10 allows the recoil energy of a carbon atom to be calculated during a head-on collision, equation 3.11.

$$E_2 = \frac{2.5 \times 10^3 \times 4 \times 12}{13^2} = 710 \text{ keV} \quad (3.11)$$

where:  $\phi = \pi$  which implies  $\sin^2(\phi/2) = 1$ .

The maximum recoil energy of a carbon atom is 710 keV hence the average recoil energy is 355 keV [79].

Figure 3.3 shows the path a primary knock-on atom (PKA) takes through the graphite structure. The second region of interest is the cascade regime. In this region, the PKA collides with an atom in the cell. This atom is then displaced and travels through the cell before colliding with a different atom. The collisions create a cascade effect throughout the cell. During a collision, energy transfer occurs between the atoms. As more cascades occur there is less energy transferred in each collision. Collisions will continue until the kinetic energy of an atom is less than the threshold displacement energy (the minimum amount of energy required to displace an atom). At the threshold displacement energy, interstitials and vacancies can be seen. This process has been simulated using a cascade cell, figure 3.5.

The final part of figure 3.3 refers to the threshold displacement energies. The threshold displacement energy is the minimum amount of energy required to displace an atom. The effects of the threshold displacement energy can be seen at the end of thermal spike simulations or cascade simulations. They can also be created by computing simulations with a very small initial energy.

Threshold displacement simulations allow the formation energy of defects to be calculated. The formation energy represents the least amount of energy required to break the bonds between the carbon atoms and to cause vacancies and interstitials. The formation energy of defects calculated using the EDIP potential are pleasingly similar to those calculated from DFT in the literature [86] (see table 4.4). The comparison of EDIP results to DFT justifies the use of the EDIP potential [73]. DFT performs very accurate simulations in carbon

based materials as discussed in Chapter 2. However, it is computationally expensive to run. EDIP can produce results of comparable accuracy but requires much less computational resources.

A variable time step has been employed to simulate graphite cascades. For example, during a simulation with initial PKA energy of 1000 eV, the following time steps are employed; when the PKA is initiated, the equations of motion are integrated using an average time step of 0.018 fs. During the first collision this falls to just 0.0022 fs before increasing to a maximum of 0.025 fs midway between the first and second collisions. With each collision the time step is temporarily reduced and the cycle repeats. The time step gradually trends upwards towards a constant value of 0.23 fs by the end of the simulation. Due to the efficiency of the variable time step, the total simulation of 5 ps completes on average in fewer than 30,000 time steps with around 10,000 steps required to cover the first pico-second.

## Cascades In Graphite

There are three regimes of interest which occur in a graphite cascade; the thermal spike, the cascade and the threshold energy regimes. Examples of each regime are presented in this chapter. Further explanation and discussion of results is given in Chapter 6.

### 4.1 Thermal Spike Results

The thermal spike is the first regime of interest within graphite cascades. A set amount of energy is given to a graphite lattice to simulate a PKA passing through the cell, transferring electronic energy without causing any collisions.

Figure 4.1, shows a snap-shot of the final image after a thermal spike cascade with initial energy  $6 \times 10^3$  eV. The radius of the spike was set to  $2.7\text{\AA}$ .

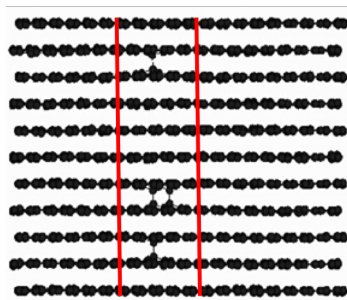


**Figure 4.1:** A thermal spike cascade representing the most probable energy for fission,  $6 \times 10^3$  eV, Radius  $2.7\text{\AA}$ . The cell temperature is  $300^\circ\text{C}$ . The thermal spike region is denoted by the red lines.

Figure 4.1 simulates the most probable energy for fission to occur in an advanced gas-cooled reactor (AGR). The radius of the thermal spike was  $2.7\text{\AA}$ .

This value was selected because generally at this energy, the atoms do not travel far from their initial position. The initial cell temperature was 300°C to simulate the conditions seen in AGRs.

The total ‘real time’ value from when the initial energy was given to the system until the cell stabilised, (depicted in figure 4.1) is 0.14 ps. The initial energy sees the atoms within the thermal spike radius vibrate. This results in the displacement of  $\sim 20$  atoms. The excited kinetic energy of the carbon atoms in the graphite lattice is dispersed through the in-plane layers via standard phonon processes. At small energies, the vibrations are contained within each layer and cause no lasting damage to the overall cell structure. After the lattice has stabilised, there are four interstitials present in the original thermal spike region. Analysis of the final cell shows the presence of a grafted interstitial, spiro interstitials and vacancies. This was a significant amount of energy to give a small cell and, remarkably, there is very little damage to the final structure.

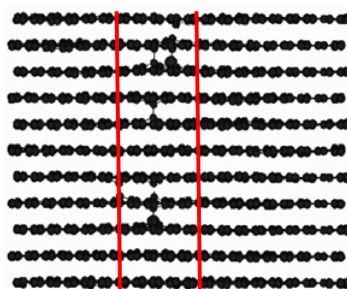


**Figure 4.2:** A thermal spike cascade representing the average energy for fission,  $2.5 \times 10^4$  eV, Radius  $3.7\text{\AA}$ . The cell temperature is 300°C. The thermal spike is denoted by the red lines.

Figure 4.2, is a snap-shot of the final image produced after a thermal spike simulation with an initial energy of  $2.5 \times 10^4$  eV. The radius of the thermal spike was  $3.7\text{\AA}$  and the initial cell temperature was set to 300°C. Due to the higher initial energy given to the system, a larger radius is required than that employed in figure 4.1. The simulation ran for 0.21 ps in ‘real time’ before stabilising. Initial interstitials and vacancies were created within the thermal spike region. As the simulation continued and the energy of displaced atoms fell below their threshold energy, displaced atoms came to rest in vacancies within the lattice or formed interstitials between the planes. No defects were formed outside of the thermal spike region despite vibrations through the planes (the vibrations were created as a direct result of the thermal spike). Figure 4.2 shows the final lattice after the simulation has stabilised. There are

10 defects present. The cascade at  $2.5 \times 10^4$  eV left no significant damage to the overall structure of the cell.

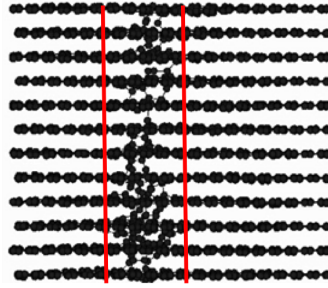


**Figure 4.3:** A thermal spike cascade representing the maximum energy for fission,  $1.0 \times 10^5$  eV, Radius  $5.0\text{\AA}$ . The cell temperature is  $300^\circ\text{C}$ . The thermal spike is denoted by the red lines.

Figure, 4.3, shows a thermal spike radius of  $5.0\text{\AA}$ , initial energy of  $1.0 \times 10^5$  eV and the initial cell temperature was set to  $300^\circ\text{C}$ . The initial energy  $1.0 \times 10^5$  eV was selected to represent the maximum energy the structure can contain. Unlike previous thermal spike simulations, there was significant movement from atoms in the entire cell during the simulation. The simulation took 0.33 ps in 'real time' to stabilise. Figure 4.3 shows the final graphite cell. Analysis of the cell showed no significant damage caused outside the thermal spike region. Within the thermal spike region, there is a considerable amount of damage i.e., interstitials and vacancies are created. Analysis has shown that at these high energies, Frenkel pairs are created and also Stone-Wales defects can be seen (these are discussed in section 4.5).

The structure of graphite allows large values of energy to pass through the lattice, without causing major damage to the overall cell. Despite the large initial energy given to the cell, the overall structure has remained intact and layers within the graphite can clearly be seen. The lack of structural damage at high energies is unlike thermal spikes seen within other materials [97]. Graphite behaves differently from other materials because of its strongly bonded layered structure.

Simulations using the thermal spike, up to an energy of  $1.0 \times 10^5$  eV, have produced a remarkable result. It was not expected that such a large amount of kinetic energy given to the system would produce so little damage. The examples in figures 4.1, 4.2 and 4.3, have been selected as examples to demonstrate the three main energy values occurring during nuclear fission.

## 4.2 Preliminary Cascade Results

The second regime of interest, the cascade region, has been the primary area of focus for this thesis. To simulate a cascade through graphite, the cell must first be prepared (as described in Chapter 3) and a primary knock-on atom (PKA) must be selected with a given direction and energy.

Cascade simulations are directionally dependent. The direction of the PKA has to be chosen carefully. Initially, over 100 different directions were selected and simulated in a graphite cell using a variety of different initial temperatures and energies. Each simulation gives a unique result and the results produced, do not show any resemblance to results previously obtained in other carbon materials.

Figure 4.4 shows two snap-shots of graphite cascades. Each cascade had an initial energy of 500 eV applied in two different initial directions.

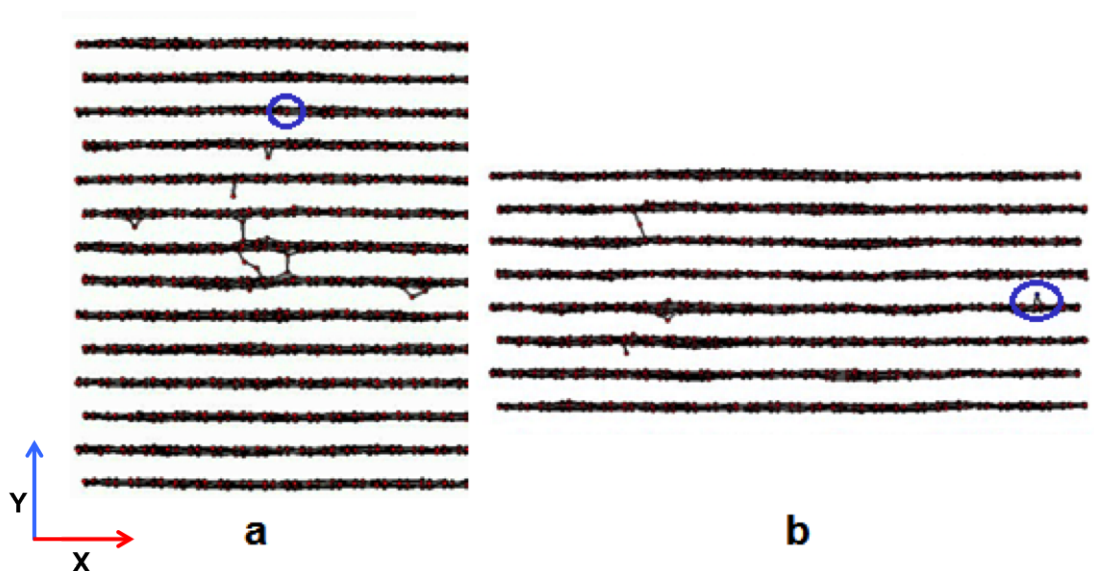


**Figure 4.4:** (a) The displacements produced by a graphite cascade with initial PKA direction  $x = 1$ ,  $y = 2$  and  $z = 1$ , initial PKA energy 500 eV and an initial cell temperature 300°C. (b) The displacements produced by a graphite cascade with initial PKA direction  $x = 2$ ,  $y = 1$  and  $z = 0.1$ , initial PKA energy 500 eV and an initial cell temperature 300°C. The final position of the PKA is denoted by a blue ring. There are around 30,000 atoms in this structure.

These examples of cascades (figure 4.4) have been picked at random to show extreme movement both normal and through the plane. Figure 4.4 (a) is taken from the end of the cascade. This cascade ran for 0.16 ps ('real time') before

the structure stabilised. A cascade simulation is stable when the energy of the atoms in the cell is less than the formation energy of interstitials.

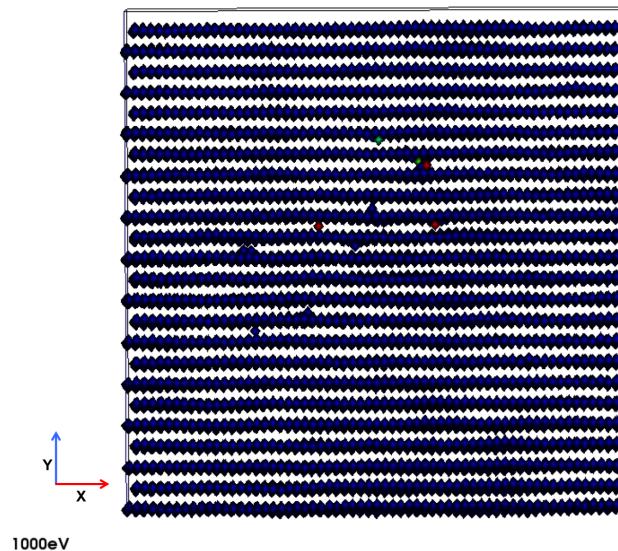
The initial energy and direction shown in figure 4.4 (a) was 500 eV and  $x = 1$ ,  $y = 2$  and  $z = 1$  respectively. The initial cell temperature was 300°C. The direction was chosen to simulate a cascade with an initial direction normal to the graphite plane. This direction was selected so the PKA would be able to pass through the hexagonal lattice above with the aim of finding evidence of channelling. The PKA travelled through the first three layers within the structure before colliding with an atom. This is an example of channelling. The PKA continued to travel normal to the plane after the initial collision. Further collisions occurred as the cascade proceeded until the energy of atoms in the lattice falls below the threshold energy (25 eV). The PKA came to rest in a vacancy created as a result of the cascade (denoted by the blue ring figure 4.4 (a)). Upon completion of the simulation, the final structure remained intact and there was very little structural damage. There are clearly defined layers of graphene visible within the final cell. The displaced atoms created by the cascade have filled vacancies left by displaced atoms or formed interstitials between the planes. Figure 4.4 (a) is the final structure after the cascade. Analysis of the final image shows the presence of: a grafted interstitial, a bent interlayer bridge and a spiro interstitial. There are also vacancies present in the structure. The presence of these interstitials and vacancies agree with those found in the literature (section 4.5) [86].

Figure 4.4 (b) is taken from a cascade with an initial direction close to the plane. The initial energy and direction of the PKA is 500 eV and  $x = 2$ ,  $y = 1$  and  $z = 0.1$ , respectively. The initial cell temperature is 300°C. During the simulation, the PKA appeared to ‘bounce’ between two layers in the cell, a phenomena known as assisted channelling [87]. The second collision caused the PKA to change direction and this resulted in a collision with an atom in the layer below. This process continued through the simulation until the PKA reached its threshold displacement energy. Displacements of atoms occurred each time the PKA collided with an atom, these displacements caused secondary cascades throughout the cell. Energy is transferred between atoms during a collision which results in secondary cascades being produced. The energy transferred between the PKA and atoms in the cell decreases with each collision. This results in a greater number of secondary cascades being produced around sites of the PKA’s initial collisions. Figure 4.4 (b) shows the initial resting point of the PKA. It came to rest between two layers and formed

a grafted interstitial. Analysis of the final cell gave evidence of the presence of a spiro interstitial, grafted interstitials and vacancies.

Cascades at high energies produce a higher number of interstitials and vacancies. This is because the initial PKA has more energy which in turn results in an increase in the energy transferred between atoms in a collision. Figure 4.5 is an example of a high energy cascade simulation.

Cascade simulations at these higher energies require a larger structure to ensure atoms do not leave the cell throughout the duration of the simulation. Figure 4.5 demonstrates how the addition of further atoms makes analysis by human eye difficult. AVAS (visualisation and analysis software) has been employed at high energies to calculate the number of interstitials and vacancies present after a cascade has stabilised.



**Figure 4.5:** A high energy graphite cascade with initial PKA direction  $x = 1$ ,  $y = 2$  and  $z = 1$ , initial PKA energy 1000 eV and initial cell temperature 300°C. There are approximately a quarter of a million atoms in this structure.

Figure 4.5 has the same initial direction but a different initial energy as compared to figure 4.4 (a). The path taken by the PKA in figure 4.5 is similar to figure 4.4 (a) the main difference here being at the higher energy, there is greater movement from atoms in the cell. The path of the PKA stays normal to the plane. Damage to the structure can be seen throughout the whole cell. This is a result of higher kinetic energies being transferred through initial collisions. High energy cascades lead to a rise in the number of interstitials and vacan-

cies being produced. Figure 4.5 shows evidence of split interstitials, grafted interstitials, bent interlayer bridges, spiro interstitials and vacancies.

To conclude the comments on the preliminary simulations, cascades in graphite are directionally dependent and even cascades with the same initial direction but a different initial energy can produce different results.

## 4.3 Qualitative Cascade Data

The preliminary results led to the conclusion that a systematic and uniform sample of PKA directions is required to accurately analyse the effect of cascades. As a direct result of preliminary results, it was decided to employ the Thomson problem [87] to uniformly distribute points around a sphere. Twenty directions were selected and analysed over energies: 25, 50, 75, 100, 250, 500, 750, 1000, 1500 and 2000 eV.

### 4.3.1 Individual Cascades

To highlight the directional dependence of graphite cascades, a selection of the initial 20 directions is presented below. The number of defects were computed using a vacancy radius of  $0.9\text{\AA}$ .

#### Low Energy (25 - 250 eV) Cascades in Graphite

Low energy cascades have been simulated with initial PKA energies of 25, 50, 75, 100 and 250 eV. Figure 4.6 represents an example of a low energy cascade in graphite with an initial PKA energy of 50 eV.

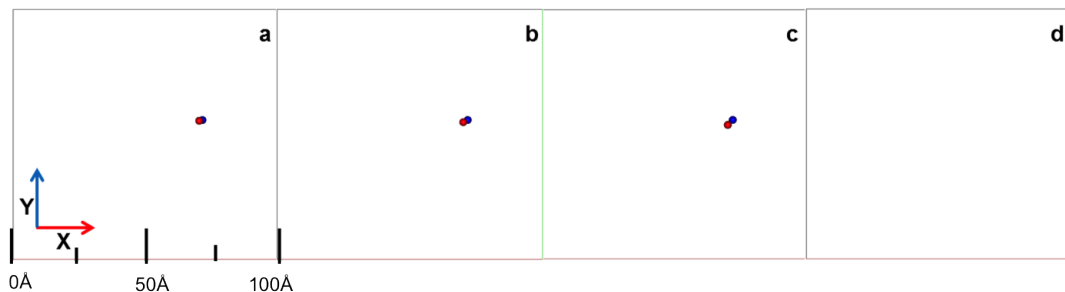
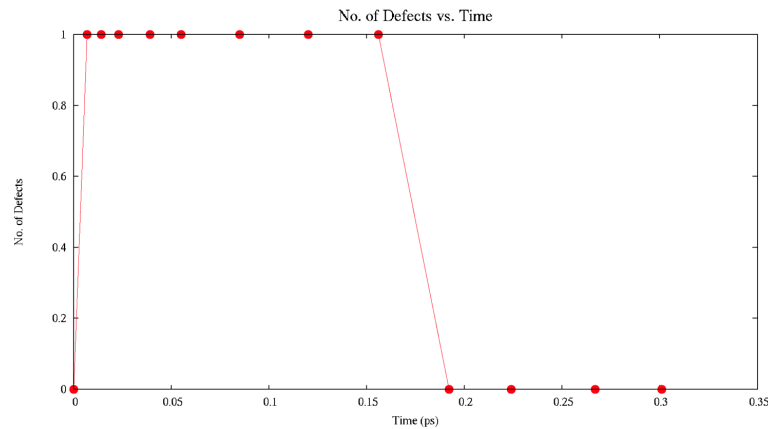


**Figure 4.6:** Graphite cascade with initial PKA energy 50eV after: (a) 0.007 ps, (b) 0.014 ps, (c) 0.023 ps and (d) 0.192 ps. Initial PKA direction 15 from table 3.1. The cell temperature is  $300^{\circ}\text{C}$ . The red circles denote interstitials and the blue squares denote vacancies.

Figure 4.6 had an initial PKA direction of  $x = 0.834911985$ ,  $y = -0.010739429$  and  $z = -0.539804079$ . The image in figure 4.6 (a) shows the cascade after 0.007 ps, the PKA (red circle) has been removed from its initial position leaving a vacancy (blue square) behind. Image 4.6 (b) shows the cascades after 0.014 ps. Here the PKA has travelled slightly further from its initial position. However,

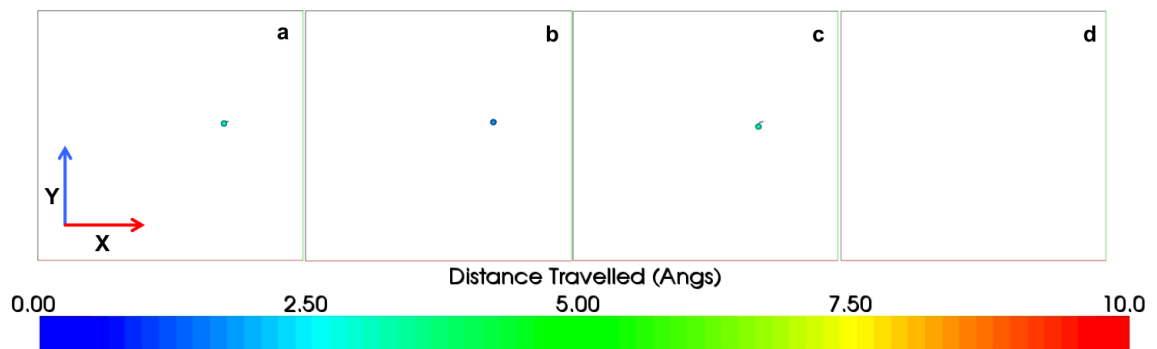
it has not travelled far enough to collide with surrounding atoms. The PKA has travelled slightly further after 0.023 ps, figure 4.6 (c). However, here the distance travelled is still less than the interatomic separation of the carbon atoms within the graphite lattice and, therefore, no defects are formed. The final image, figure 4.6 (d), shows no defects or interstitials. This is because the PKA has come to rest in its initial starting position.

Figure 4.7 shows the number of defects created during the cascade as a function of time. The total number of defects throughout the whole cascade was one and the PKA settled into its initial position after 0.16 ps.



**Figure 4.7:** Graph indicating the number of defects present during a graphite cascade at 50 eV. Initial PKA direction 15 from table 3.1. The cell temperature is 300°C.

The distance the PKA travelled from the initial starting point can be seen in figure 4.8.



**Figure 4.8:** Graphite cascade with initial PKA energy 50 eV after: (a) 0.007 ps, (b) 0.014 ps, (c) 0.023 ps and (d) 0.192 ps. The colour on the scalar bar indicates the distance moved by atoms during the cascade (Angs). Initial PKA direction 15 from table 3.1. The cell temperature is 300°C.

The images in figure 4.8 are taken from the same time periods as in figure 4.6. The PKA moves further away from the initial starting position as the time increases. However, the PKA does not have sufficient energy to continue to travel through the cell and comes to rest in the initial starting position therefore the PKA has a displacement of  $0\text{\AA}$ .

At 50 eV there is no damage to the final graphite cell with a PKA with initial direction 15 from table 3.1.

Figure 4.9 represents a cascade through graphite with an initial PKA energy of 250 eV.

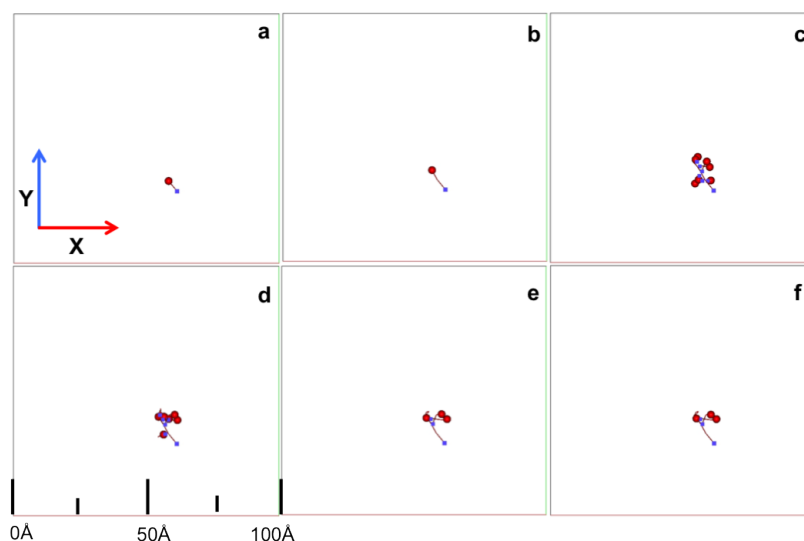


**Figure 4.9:** Graphite cascade with initial PKA energy 250 eV after: (a) 0.00 ps, (b) 0.01 ps, (c) 0.04 ps, (d) 0.17 ps, (e) 0.35 ps and (f) 3.21 ps. Initial PKA direction 2 from table 3.1. The cell temperature is  $300^{\circ}\text{C}$ . The red circles denote interstitials and the blue squares denote vacancies. The path of each displaced atom is traced.

Figures 4.9 (a) and (b) demonstrate the initial direction of the PKA. At 0.04 ps, collisions have started to occur and a cluster of defects can be seen, figure 4.9 (c). The energy transferred between collisions is relatively small resulting in many atoms having an energy only slightly greater than the threshold energy resulting in the cascade staying in a cluster formation. As the cascade reaches 0.17 ps, shown in figure 4.9, the atoms have started to fill vacancies and by 0.35 ps the displaced atoms do not have sufficient energy to cause further cascades (figures 4.9 (e) and (f)). The final number of interstitials and vacancies present is three.

Figure 4.10 shows the number of defects present at any given point during

the cascade. The graph shows an initial increase at 0.028 ps to seven defects, the maximum obtained during this cascade. Figure 4.10 decreases from seven defects present to six but jumps back to seven after 0.01 ps. The change in the number of defects present is due to an atom briefly leaving the lattice site without breaking any bonds before re-combining with the lattice.

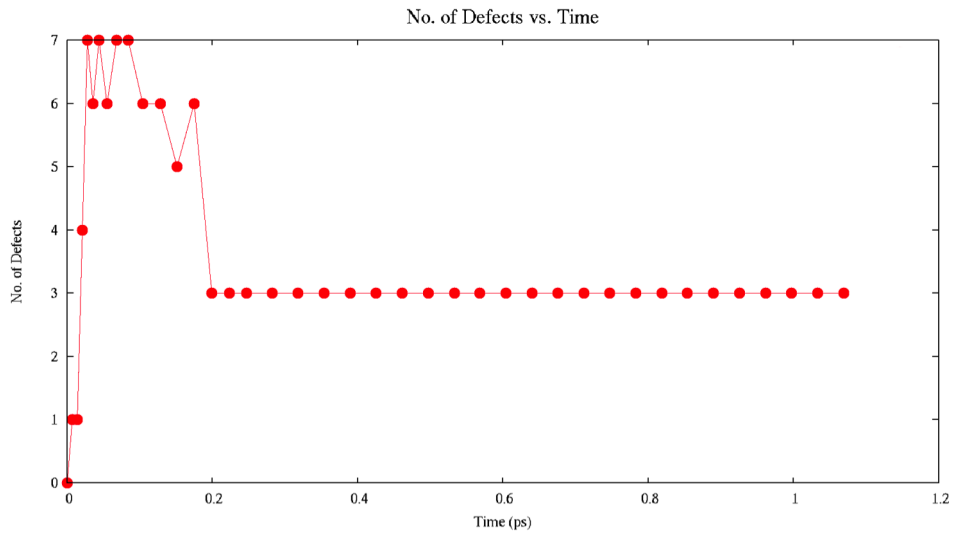


**Figure 4.10:** Graph indicating the number of defects present during a graphite cascade at 250 eV. Initial PKA direction 2 from table 3.1. The cell temperature is 300°C.

Figure 4.11 shows the distances travelled by displaced atoms through the lattice.

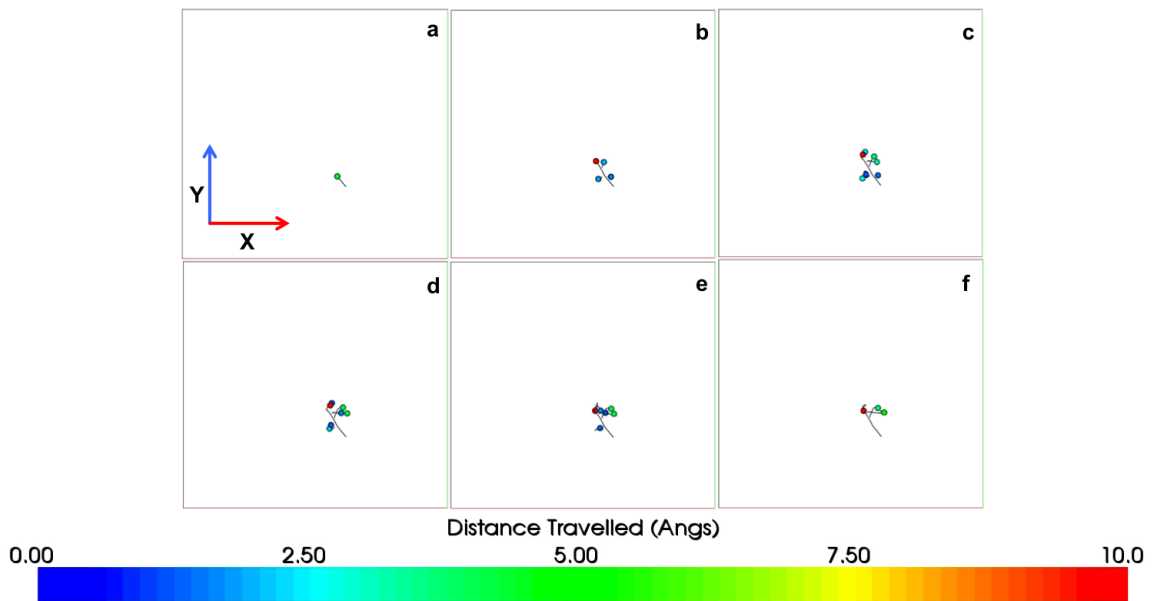


**Figure 4.11:** Graphite cascade with initial PKA energy 250 eV after: (a) 0.007 ps, (b) 0.021 ps, (c) 0.044 ps, (d) 0.068 ps, (e) 0.175 and (f) 2.498 ps. The colour on the scalar bar indicates the distance moved by atoms during the cascade. Initial PKA direction 2 from table 3.1. The cell temperature is 300°C.

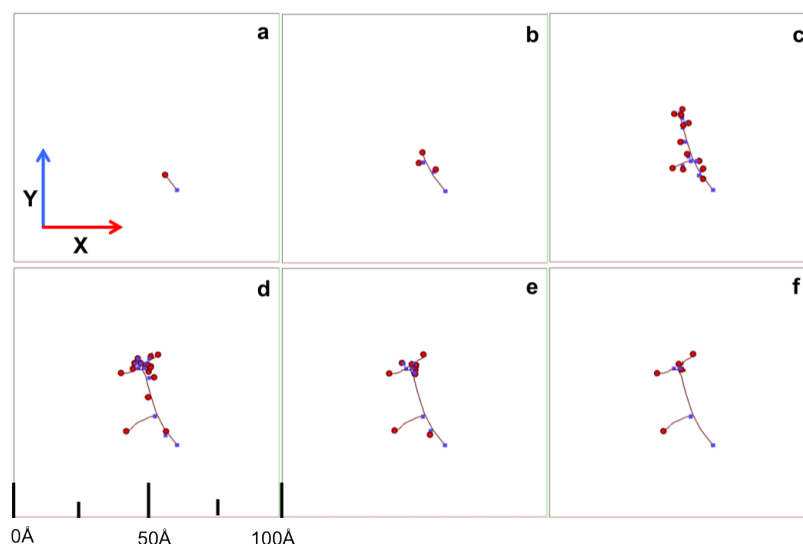
The PKA reaches its final position after 0.021 ps, figure 4.11 (b), and travels a total displacement of 7.44Å. Atoms displaced as a direct result of secondary collisions move no further than 3.5Å from their initial starting position. Secondary displacement atoms moving less than 2Å from their initial starting position re-combine with the graphite lattice. This is supported by the diagrams in figures 4.11 (e) and (f).

Low energy cascades cause very little final damage to the lattice. The maximum number of defects formed as a result of a low energy cascade was six and the average is two. The average number of displaced atoms during a cascade with an initial PKA energy of 50 eV is one. The top end of the low energy cascades produced an average of four displaced atoms which is 11% greater than the average number of final defects present. The average final displacement of the PKA with initial energy 1500 and 2000 eV is 4.823 and 14.519Å respectively.

Further examples of low energy cascades are presented in Appendix I.

## Mid-Range Energy (500 - 1000 eV) Cascades in Graphite

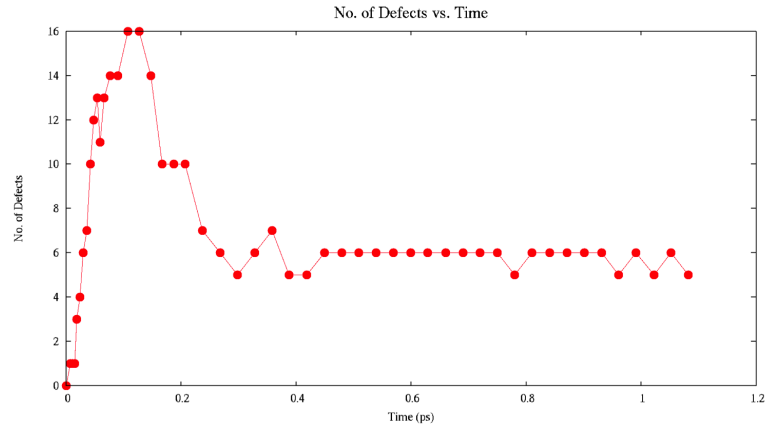
Mid-range energy cascades have been simulated with initial PKA energies of 500, 750 and 1000 eV. Figure 4.12 represents an example of a mid-range energy cascade in graphite with an initial PKA energy of 500 eV.



**Figure 4.12:** Graphite cascade with initial PKA energy 500 eV after: (a) 0.00 ps, (b) 0.02 ps, (c) 0.05 ps, (d) 0.10 ps, (e) 0.16 ps and (f) 3.16 ps. The cell temperature is 300°C. Initial PKA direction 2 from table 3.1. The red circles denote interstitials and the blue squares denote vacancies. The path of each displaced atom is traced.

Figure 4.12 (a) denotes the initial path of the PKA, after 0.02 ps there is evidence of secondary cascades (figure 4.12 (b)). At 0.10 ps, figure 4.12 (d) there is a cluster of interstitials and vacancies forming. The interstitials (red circles) and vacancies (blue squares) are closely packed together. As the displaced atoms continue to collide and transfer energy, the displaced atoms come to rest in a vacancy site. The re-combining of the interstitials formed is supported by figures 4.12 (d) and (e). The final number of interstitials and vacancies present in the cell is six.

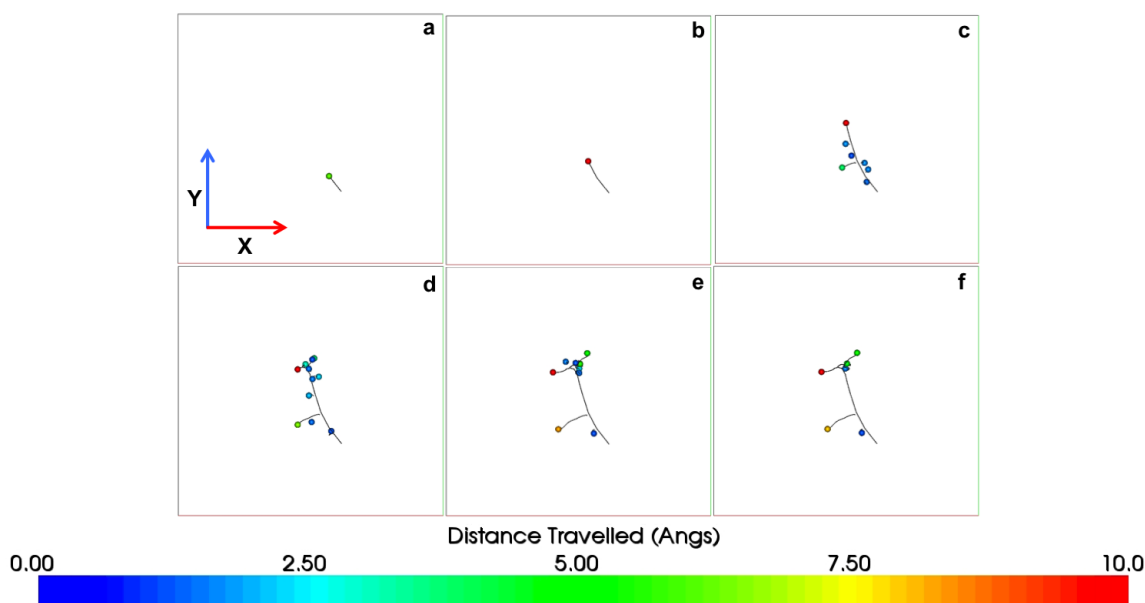
Figure 4.13 shows the total number of defects present at any given point in time during this cascade.



**Figure 4.13:** Graph indicating the number of defects present during a graphite cascade at 500 eV. Initial PKA direction 2 from table 3.1. The cell temperature is 300°C.

The initial steps of this cascade are subject to channelling. This can be seen between 0.007 and 0.015 ps. The maximum number of defects formed during the cascade at 500 eV was 16 after a time period of 0.107 ps. After the initial peak of 16 defects, (figure 4.13) the number of defects decreases to 10 where the cell remains stable for 0.04 ps before displaced atoms re-combine within the lattice. The number of defects present within the cell alternates between seven and five. This is because atoms have enough kinetic energy to escape the lattice and form an interstitial between planes but do not have enough kinetic energy to break further bonds and cause secondary cascades.

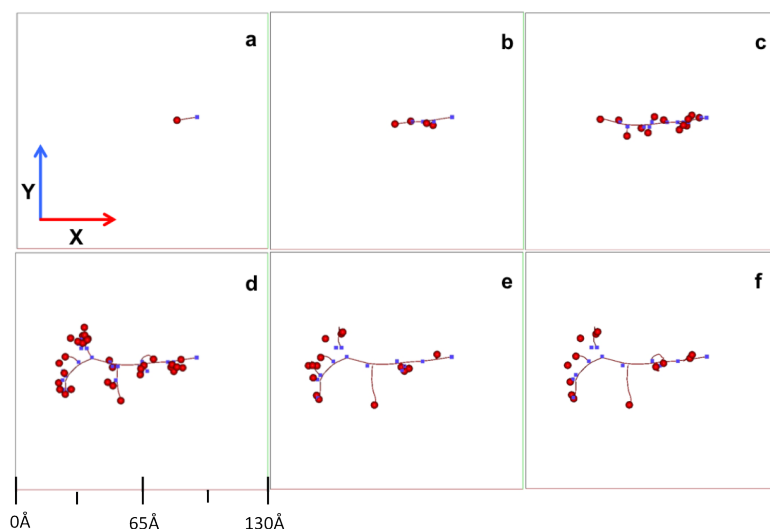
Figure 4.14 represents the distance travelled by each displaced atom.



**Figure 4.14:** Graphite cascade with initial PKA energy 500 eV after: (a) 0.007 ps, (b) 0.015 ps, (c) 0.036 ps, (d) 0.059 ps, (e) 0.167 and (f) 2.590 ps. The colour on the scalar bar indicates the distance moved by atoms during the cascade. Initial PKA direction 2 from table 3.1. The cell temperature is 300°C.

The PKA in figure 4.14 (a) and (b) show evidence of channelling between 0.007 and 0.015 ps. At 0.036 ps, shown as figure 4.14 (c), the PKA has collided with atoms in the cell, as a direct result of the collisions, cascades have been produced. With the exception of one atom, the displaced atoms from the secondary cascades have travelled on average  $1.25\text{\AA}$  from their initial position by 0.059 ps (figure 4.14 (d)). The atom omitted from the calculation collided with the PKA at an angle of  $43^\circ$ . As a consequence, a large amount of energy was transferred giving the second carbon atom energy to penetrate further through the cell. The final image, figure 4.14 (f), shows the majority of defects have travelled over  $5\text{\AA}$  from their initial lattice position. The final displacement of the PKA was  $8.88\text{\AA}$ .

Figure 4.15 shows a graphite cascade with initial PKA energy of 1000 eV. This is the top end of the mid-range energies. The increase in the initial PKA energy allows the PKA to penetrate further through the cell. The cluster like cascades witnessed at lower energies have now been replaced and the number of secondary cascades produced has increased dramatically.



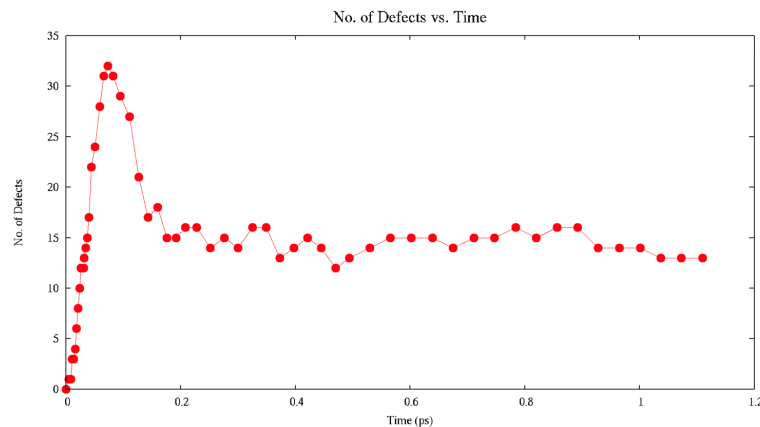
**Figure 4.15:** Graphite cascade with initial PKA energy 1000 eV after: (a) 0.00 ps, (b) 0.01 ps, (c) 0.03 ps, (d) 0.08 ps, (e) 0.63 ps and (f) 4.87 ps. Initial PKA direction 15 from table 3.1. The cell temperature is 300°C. The red circles denote interstitials and the blue squares denote vacancies. The path of each displaced atom is traced

Figure 4.15 (a) shows the initial direction the PKA took. After 0.01 ps (figure 4.15 (b)) a number of secondary collisions can be seen. Initially, the secondary collisions remain in close proximity to the path of the PKA as witnessed in figure 4.15 (c). Figure 4.15 (d) shows the PKA has collided with another carbon atom. The result of this collision is that the PKA's path is altered but, most importantly, the second carbon atom is displaced from its original lattice position. With each collision the PKA transfers energy, due to the angle at which the collision between the PKA and second carbon atom occurred, the energy transferred to the second carbon atom is high. This results in the second carbon atom forming a series of secondary cascades. The kinetic energy of the carbon atoms gradually becomes less than the threshold energy. As a result, the atoms form defects or come to rest in a vacancy (figures 4.15 (e) and (f)). The final number of interstitials and vacancies present after the cell has stabilised is 14.

Every graphite cascade is unique. It is for this reason channelling can be present during one cascade at a given energy and not during a second cascade at a different energy, even when both cascades have the same initial PKA direction. The cascades described at 500 and 1000 eV are prime examples of this.

Figure 4.16 shows all the defects present during a graphite cascade at 1000 eV.

The maximum peak of 32 defects occurs at 0.073 ps. The graph shows that no channelling occurs. The slight variation in the number of defects present after 0.2 ps is a direct result of the carbon atoms at the edge of the secondary cascades reaching their threshold energies. Once the atoms have reached their threshold energies they no longer have enough kinetic energy to break away from the lattice sites. However, the carbon atoms may have enough kinetic energy to move slightly out of their position in the lattice resulting in the formation of a defect between the planes. The atoms may stay in their defect position or may re-combine with a vacancy, removing the defect.



**Figure 4.16:** Graph indicating the number of defects present during a graphite cascade at 1000 eV. Initial PKA direction 15 from table 3.1. The cell temperature is 300°C.

Figure 4.17 shows the distance travelled by displaced atoms during the graphite cascade. As the initial PKA energy given to the system is at the top end of the mid-range cascades, the distances moved by atoms in the cell is expected to be higher. It is clear from figures 4.17 (b), (c), (d), (e) and (f) that the PKA has travelled over 10Å throughout the cascade. Unlike the lower energy cascades, other carbon atoms in the cell have travelled distances greater than 10Å. An example of this situation can be seen in the final image (figure 4.17 (f)). The atoms surrounding the secondary cascades have not travelled over 3Å from their initial lattice position. This is to be expected as the energy transferred to atoms during a cascade is proportional to the number of collisions (i.e., the energy transfer decreases as the number of collisions increases). The individual energies of the atoms on the edge of the secondary collisions are approximately equal to the threshold displacement energy. This allows an atom to vacate its initial site, form an interstitial between planes but it does not have the kinetic energy to travel further through the cell and cause further secondary cascades.

The final displacement of the initial PKA is 55.21Å.

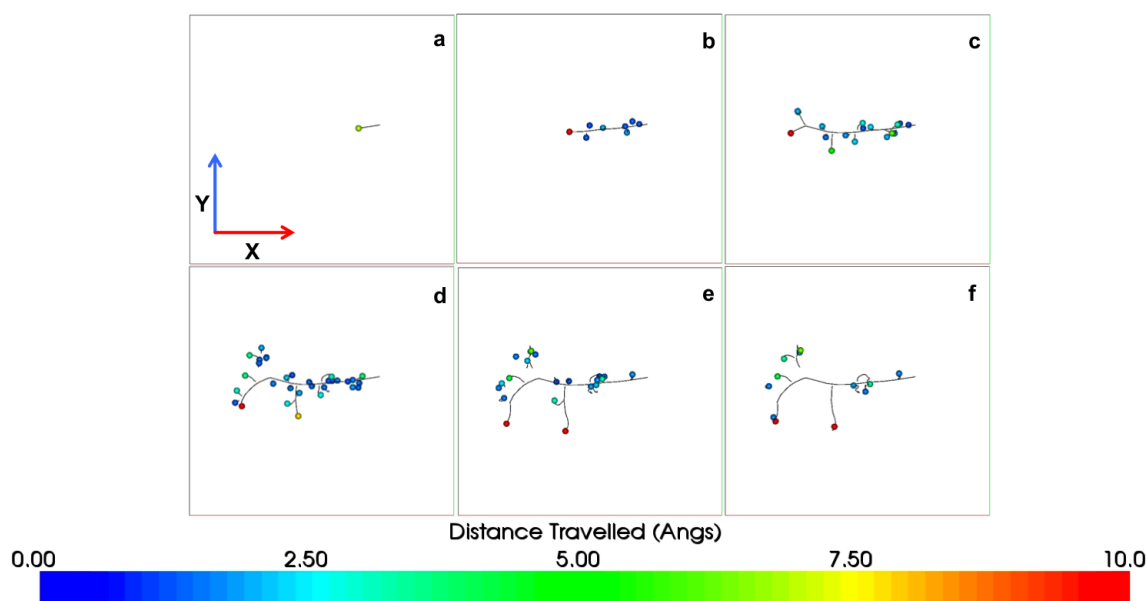


**Figure 4.17:** Graphite cascade with initial PKA energy 1000 eV after: (a) 0.005 ps, (b) 0.022 ps, (c) 0.040 ps, (d) 0.066 ps, (e) 0.127 ps and (f) 3.320 ps. The colour of the scalar bar indicates the distance moved by atoms during the cascade. Initial PKA direction 15 from table 3.1. The cell temperature is 300°C.

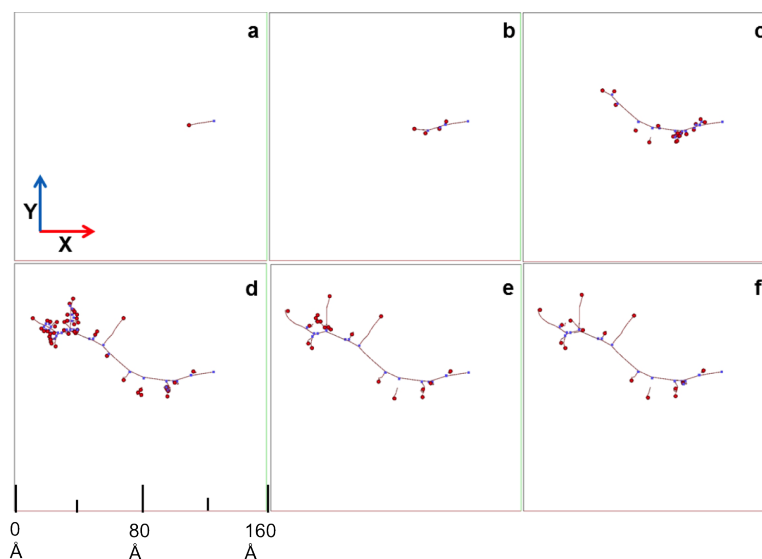
Mid-range energy cascades produce noticeable damage to the final cell. A maximum of 22 defects was observed during a cascade with initial PKA energy of 1000 eV. The average number of defects in the final lattice cell during mid-range energy cascade was 12. Cascades with an initial PKA energy of 500 eV had an average of 10 atoms displaced during a cascade. This is on average 21% greater than the final number of defects present in the lattice. The average number of displaced atoms during a 1000 eV cascade was 21. There is a difference of 24% between the number of displaced atoms and the final number of defects present in the lattice. The average displacement of the PKA was 19.155Å and 28.431Å respectively.

Further examples of mid-range energy cascades are presented in Appendix I.

### High Energy (1500 - 2000 eV) Cascades in Graphite

High energy cascades have been simulated with initial PKA energies of 1500 and 2000 eV. Cascades simulated at high energies see dynamic atom movement, produce a greater number of defects and alter significantly depending

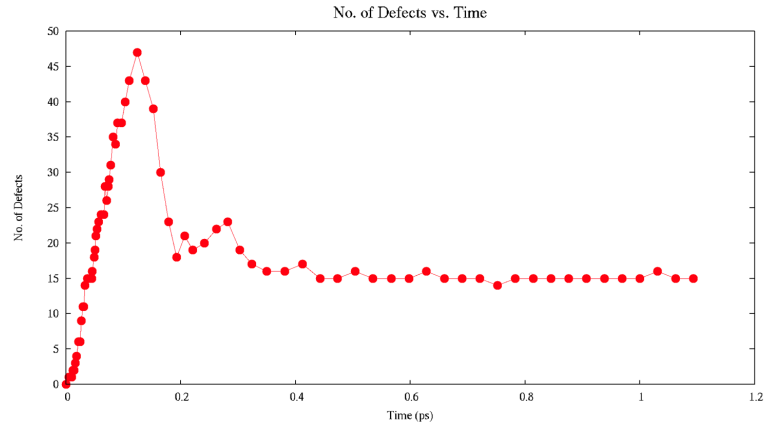
on their initial PKA direction. Figure 4.18 represents an example of a high energy cascade in graphite with an initial PKA energy of 1500 eV.



**Figure 4.18:** Graphite cascade with initial PKA energy 1500 eV after: (a) 0.00 ps, (b) 0.01 ps, (c) 0.04 ps, (d) 0.12 ps, (e) 0.26 ps and (f) 4.28 ps. Initial PKA direction 15 from table 3.1. The cell temperature is 300°C. The red circles denote interstitials and the blue squares denote vacancies. The path of each displaced atom is traced.

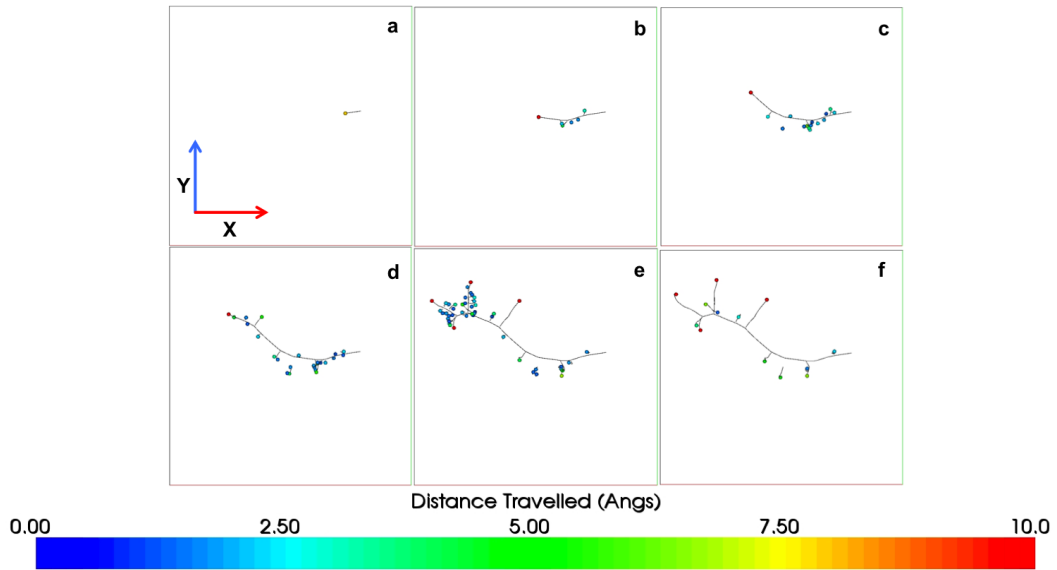
Figure 4.18 (a) shows the initial path of the PKA. By 0.01 ps (figure 4.18 (b)) there are already six displaced atoms. A collision with a carbon atom at 0.0225 ps results in the PKA's initial direction altering. The new path of the PKA begins with channelling between 0.0225 and 0.03 ps. The PKA continues to collide with carbon atoms (figure 4.18 (c)) and results in a large cluster of secondary collisions occurring at 0.12 ps (figure 4.18 (d)). When the carbon atom's kinetic energy begins to fall below the threshold energy, no further collisions occur and atoms either re-combine within the lattice or form defects (figures 4.18 (e) and (f)). The final number of interstitials and vacancies present after the cell has stabilised is 16.

Figure 4.19 shows the number of defects present through a cascade at 1500 eV. The channelling can just be seen by the small plateau in the initial peak at 15 defects. The time period when the channelling occurred is too small to be seen clearly from the graph. The maximum number of defects, 47 occurred at 0.124 ps. The small peak seen in figure 4.19 is a result of secondary cascades forming and re-combining back into the lattice simultaneously.



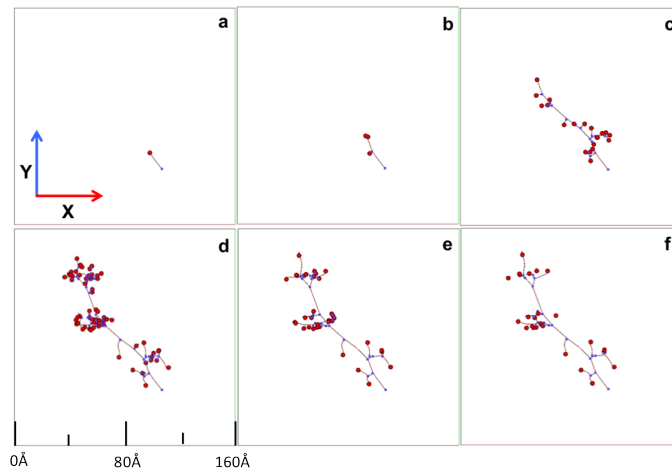
**Figure 4.19:** Graph indicating the number of defects present during a graphite cascade at 1500 eV. Initial PKA direction 15 from table 3.1. The cell temperature is 300°C.

Figure 4.20 represents the distance travelled by atoms during the cascade. Due to the large amount of initial energy given to the PKA, secondary atoms have travelled distances greater than 10Å through the cell (figures 4.20 (e) and (f)). The majority of defects caused as a direct result of a secondary cascade have moved less than 2.5Å from their original lattice position. During the energy transfer in a collision, eight atoms received enough kinetic energy to travel over 5.0Å from their original lattice position (figures 4.20 (e) and (f)). The PKA has a final displacement of 79.8Å.



**Figure 4.20:** Graphite cascade with initial PKA energy 1500 eV after: (a) 0.005 ps, (b) 0.024 ps, (c) 0.041 ps, (d) 0.061 ps, (e) 0.124 ps and (f) 3.045 ps. The colour of the scalar bar indicates the distance moved by atoms during the cascade. Initial PKA direction 15 from table 3.1. The cell temperature is 300°C.

The final cascade we considered is 2000 eV. Figure 4.21 is an example of a 2000 eV cascade.



**Figure 4.21:** Graphite cascade with initial PKA energy 2000 eV after: (a) 0.00 ps, (b) 0.01 ps, (c) 0.04 ps, (d) 0.10 ps, (e) 0.30 ps and (f) 3.80 ps. Initial PKA direction 2 from table 3.1. The cell temperature is 300°C. The red circles denote interstitials and the blue squares denote vacancies. The path of each displaced atom is traced.

The initial phase of the cascade shows the initial direction of the PKA along with the start of a cascade, figures 4.21 (a) and (b). As the cascade progresses to

0.04 ps, secondary collision cascades can be identified (figure 4.21 (c)). Figure 4.21 (d) shows evidence of three main areas of defect formation. The cascade has followed a primary path through the lattice leaving a wake of secondary cascades. The kinetic energy of the atoms in the lattice begins to fall below the threshold energy and defects begin to re-combine within the lattice, as seen in figures 4.21 (e) and (f). The final number of interstitials and vacancies present in the cell is 27.

Figure 4.22 shows the total number of defects present as a function of time during a 2000 eV cascade.

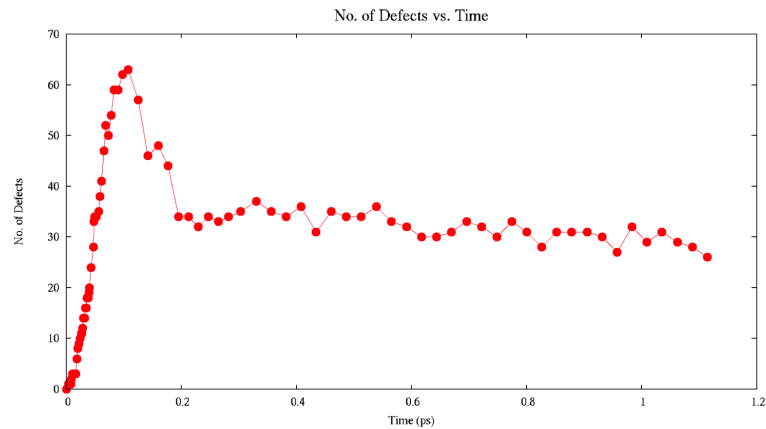


**Figure 4.22:** Graph indicating the number of defects present during a graphite cascade at 2000 eV. Initial PKA direction 2 from table 3.1. The cell temperature is 300°C.

Figure 4.22 has an initial peak of defects at 0.107 ps where the maximum number of defects formed was 63. A collision between the PKA and a neighbouring atom caused the formation of two cascade regions. The angle at which the PKA hits the neighbouring carbon atom results in the majority of the PKA's kinetic energy being transferred into the neighbouring carbon atom. As a result, the PKA has less kinetic energy to create further secondary cascades. It is because of this that there is a plateau in figure 4.22 at 0.2 ps.

The distance travelled by displaced atoms is represented in figure 4.23.

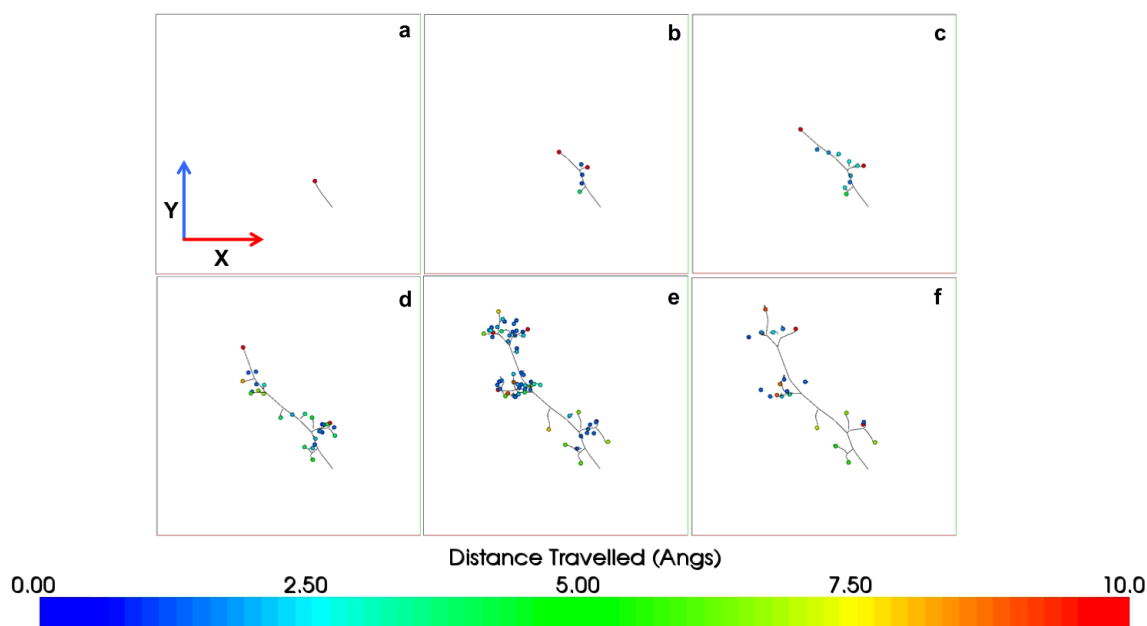


**Figure 4.23:** Graphite cascade with initial PKA energy 2000 eV after: (a) 0.008 ps, (b) 0.018 ps, (c) 0.027 ps, (d) 0.047 ps, (e) 0.107 and (f) 4.199 ps. The colour of the scalar bar indicates the distance moved by atoms during the cascade. Initial PKA direction 2 from table 3.1. The cell temperature is 300°C.

Figure 4.23 (a) represents this original direction of the PKA. The collision which alters the path of the PKA occurs at 0.11 ps, the effect of the collision can be seen in figure 4.23 (b). The PKA is the red atom to the right of the cell, the carbon atom involved in the collision is the red atom to the left of the cell. The PKA comes to rest and re-combines back into the lattice (figure 4.23 (e)). The cascade continues displacing atoms from their original site, figures 4.23 (c) and (d). Figure 4.23 (e) highlights the distances travelled by atoms displaced as a direct result of secondary cascades. The final image, figure 4.23 (f), shows the atoms which have travelled the greatest distance through the cell does not include the PKA. This is significant as it gives rise to evidence of a large energy transfer occurring during initial collisions between the PKA and neighbouring carbon atoms. The final displacement of the PKA is 7.52Å. This is significantly lower than previous cascades at 2000 eV because of the high energy transfer which occurred during the PKA's initial collisions.

High energy cascades through graphite saw on average 27 defects formed in the final lattice cell with a maximum of 42 observed during a 2000 eV cascade. The maximum final number of defects present in cascades with an initial PKA energy of 1500 and 2000 eV was 29 and 42 respectively. On average 21% of

atoms displaced during the cascade re-combined with the lattice during cascades at 1500 eV. The remaining 79% formed interstitials between planes. During cascades with an initial PKA energy of 2000 eV, the maximum number of atoms displaced during a single cascade was 53 and the average was 40. There is a difference of on average 23.6% between the maximum number of displaced atoms and the final number of defects. The average final displacement of the PKA during high energy cascades was 49Å.

Further examples of high energy cascades are presented in Appendix I.

### 4.3.2 Extreme Individual Cascades

The initial 20 directions for cascades selected using the Thomson problem have been employed to accurately represent the possible directions a PKA could travel. To give a full picture of cascade results, there are other extreme directions which are to be examined. The extreme directions are: directly along the plane and normal to the plane. The cascades have been simulated at 500 eV and the results are presented below.

#### Initial PKA Direction Through the Plane

In order to simulate a cascade through the plane, the initial PKA direction was selected to be  $x = 0.00$ ,  $y = 0.90$  and  $z = 0.00$ . Figure 4.24 follows the interstitials and vacancies which are formed throughout the cascade.

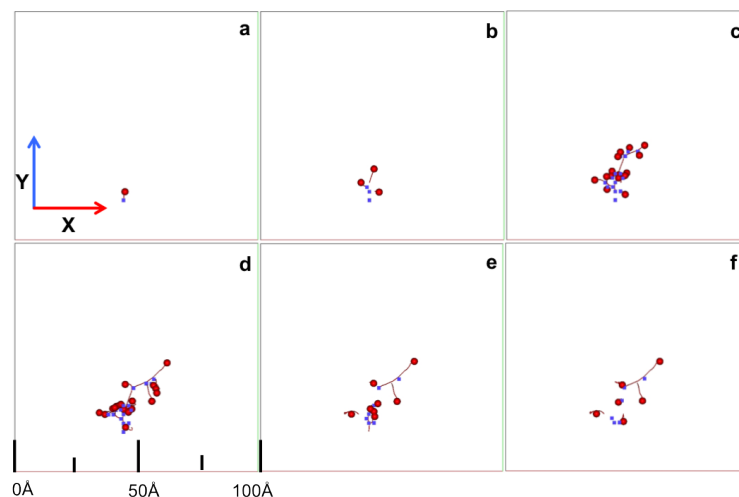


**Figure 4.24:** Graphite cascade with initial PKA energy 500 eV after: (a) 0.00 ps, (b) 0.01 ps, (c) 0.04 ps, (d) 0.11 ps, (e) 0.27 ps and (f) 2.97 ps. Initial PKA direction  $x = 0.00$ ,  $y = 0.90$  and  $z = 0.00$ . The cell temperature is 300°C. The red circles denote interstitials and the blue squares denote vacancies. The path of each displaced atom is traced.

Figure 4.24 (a) shows the initial direction of the PKA. After 0.01 ps there are three clearly defined interstitials and vacancies (figure 4.24 (b)). As the cascade continues, a cluster of defects begins to form and displaced atoms continue to travel through the cell creating secondary cascades (figures 4.24 (c) and (d)). After 0.27 ps (figure 4.24 (e)) the cell begins to stabilise and by 2.97 ps the lattice is stable (figure 4.24 (f)). The total number of interstitials and vacancies

present in the final lattice is six.

Figure 4.25 shows the number of defects created during this simulation as a function of time.

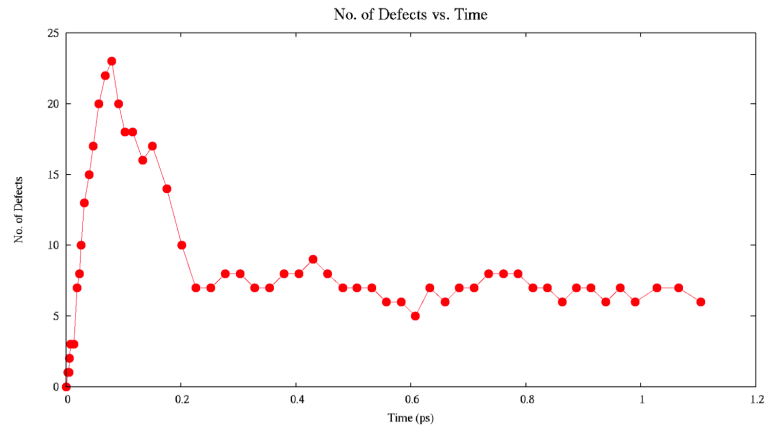


**Figure 4.25:** Graph indicating the number of defects present during a graphite cascade at 500 eV. Initial PKA direction  $x = 0.00$ ,  $y = 0.90$  and  $z = 0.00$ . The cell temperature is  $300^{\circ}\text{C}$ .

Figure 4.25 has an initial peak of defects, the maximum number of defects formed is 23 and occurs at 0.079 ps into the cascade. The number of defects begins to decrease until the system begins to stabilise at 0.2 ps.

Figure 4.26 tracks the distance travelled by displaced atoms. The PKA travels along its initial path for 0.32 ps before colliding with a carbon atom in the cell. The collision forces the PKA to alter its direction before re-combining in a lattice plane, figure 4.26 (f). The final displacement of the PKA is  $4.40\text{\AA}$ .

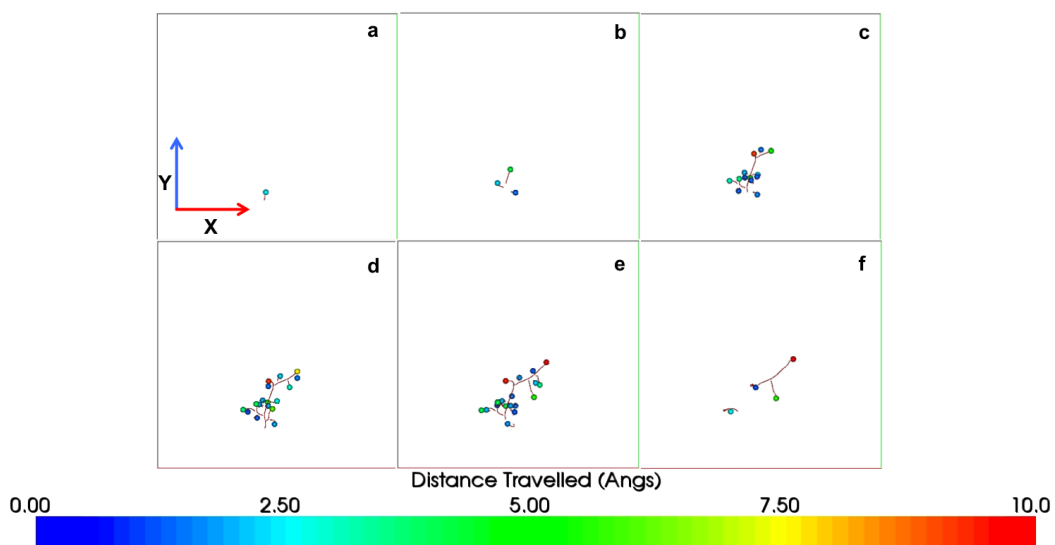
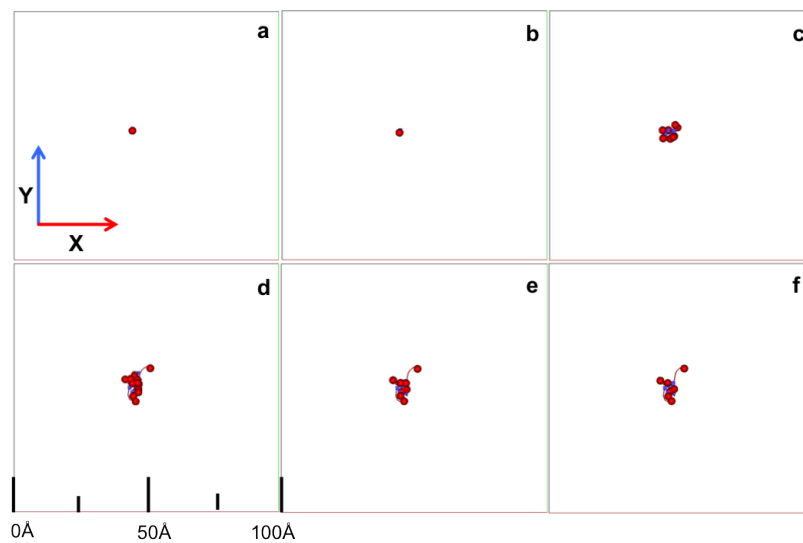


**Figure 4.26:** Graphite cascade with initial PKA energy 500 eV after: (a) 0.00 ps, (b) 0.01 ps, (c) 0.04 ps, (d) 0.11 ps, (e) 0.27 ps and (f) 2.97 ps. Initial PKA direction  $x = 0.00$ ,  $y = 0.90$  and  $z = 0.00$ . The colour of the scalar bar indicates the distance moved by atoms during the cascade. The cell temperature is  $300^{\circ}\text{C}$ .

## Initial PKA Direction Normal to the Plane

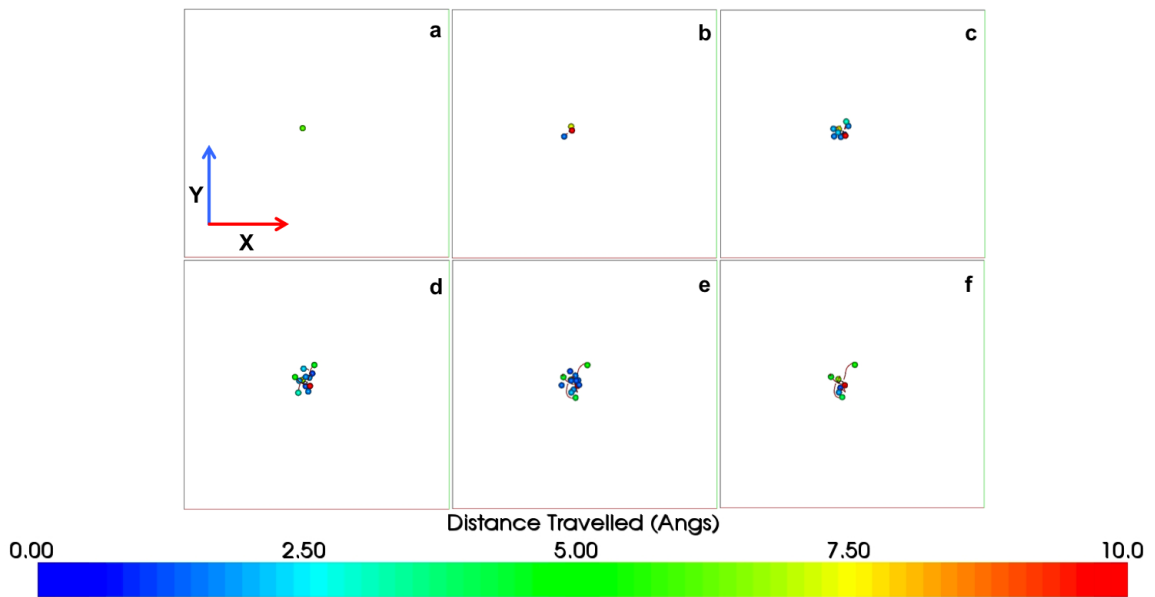
Examples of two simulations with an initial PKA direction normal to the plane are presented to highlight the directional dependence of cascades through graphite.

Figure 4.27 follows the interstitials and vacancies formed during a cascade with an initial PKA direction normal to the plane. The initial PKA direction was set to  $x = 0.00$ ,  $y = 0.00$  and  $z = -1.00$ .



**Figure 4.27:** Graphite cascade with initial PKA energy 500 eV after: (a) 0.00 ps, (b) 0.01 ps, (c) 0.04 ps, (d) 0.12 ps, (e) 0.25 ps and (f) 2.99 ps. Initial PKA direction  $x = 0.00$ ,  $y = 0.00$  and  $z = -1.00$ . The cell temperature is  $300^{\circ}\text{C}$ . The red circles denote interstitials and the blue squares denote vacancies. The path of each displaced atom is traced.

Figures 4.27 (a) and (b) show the initial position of the PKA. There is little movement from displaced atoms in the  $x$  and  $y$  planes (figures 4.27 (c), (d), (e) and (f)). Figure 4.28 highlights the distance travelled by displaced atoms.



**Figure 4.28:** Graphite cascade with initial PKA energy 500 eV after: (a) 0.007 ps, (b) 0.025 ps, (c) 0.048 ps, (d) 0.070 ps, (e) 0.148 ps and (f) 2.991 ps. The colour of the scalar bar indicates the distance moved by atoms during the cascade. Initial PKA direction  $x = 0.00$ ,  $y = 0.00$  and  $z = -1.00$ . The cell temperature is  $300^{\circ}\text{C}$ .

Figures 4.27 and 4.28 (from the perspective of the  $x$  and  $y$  directions) suggests the cascade formed a cluster of defects. However, this proposition is contradicted when studying the images in figure 4.28 (from the perspective of the  $y$  and  $z$  directions). The distance travelled by the PKA can be seen to be greater than  $10\text{\AA}$  after 0.025 ps (figure 4.28 (b)). If the cascade remained as a cluster of interstitials and vacancies a displacement of over  $10\text{\AA}$  of the PKA would be unlikely. Figure 4.29 shows the same cascade from the view point of the  $y$  and  $z$  directions.

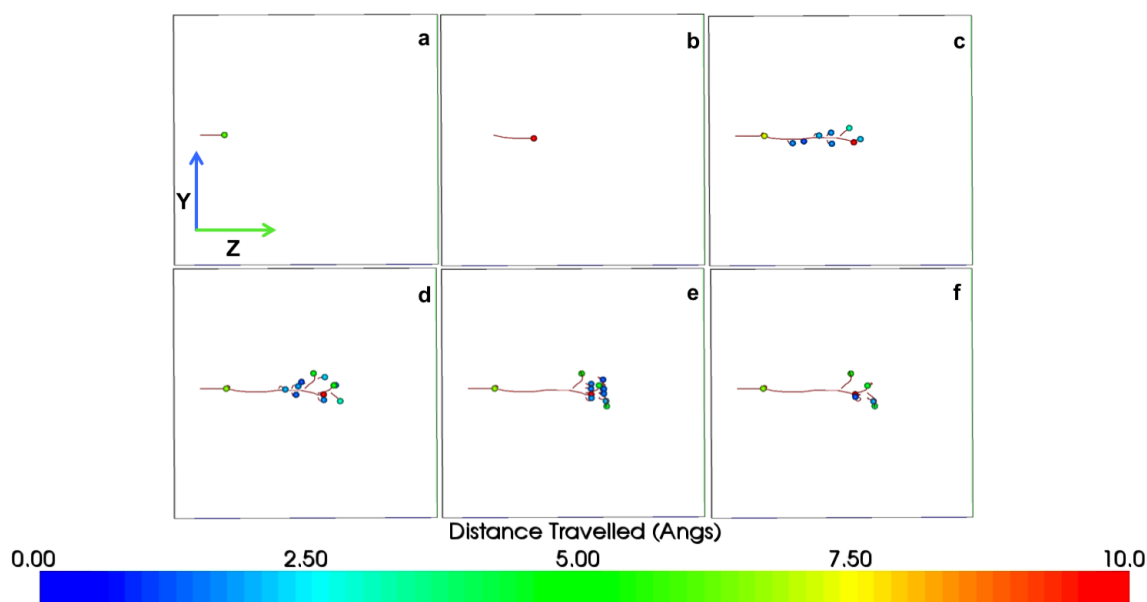


**Figure 4.29:** Graphite cascade with initial PKA energy 500 eV after: (a) 0.007 ps, (b) 0.020 ps, (c) 0.048 ps, (d) 0.070 ps, (e) 0.148 ps and (f) 2.991 ps. The colour of the scalar bar indicates the distance moved by atoms during the cascade. Initial PKA direction  $x = 0.00$ ,  $y = 0.00$  and  $z = -1.00$ . The cell temperature is  $300^{\circ}\text{C}$ .

The images in figure 4.29 demonstrate that the PKA travels through the cell. Figures 4.29 (a) and (b) show the initial path of the PKA. It is involved in a head-on collision with a carbon atom at 0.022 ps which causes it to retrace the original path for 0.026 ps before forming an interstitial between the graphite layers as seen in figure 4.29 (d). The second carbon atom continues to travel through the cell causing secondary cascades (figure 4.29 (e)) until the cell stabilises (figure 4.29 (f)). The final cell has eight interstitials and eight vacancies present and the PKA has a final displacement of  $5.94\text{\AA}$ .

Figure 4.30 denotes displaced atoms as a function of time during this cascade.

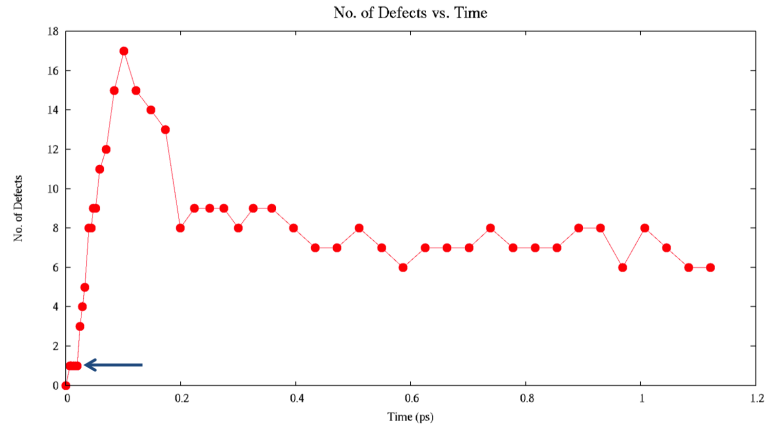


**Figure 4.30:** Graph indicating the number of defects present during a graphite cascade at 500 eV. Initial PKA direction  $x = 0.00$ ,  $y = 0.00$  and  $z = -1.00$ . The cell temperature is  $300^{\circ}\text{C}$ . The blue arrow indicates a head-on collision between the PKA and a neighbouring atom.

The head-on collision between the PKA and the second carbon atom is highlighted by the blue arrow in figure 4.30. The second carbon atom proceeds through the cell creating a cascade of defects to be formed. The maximum number of defects formed is 17 at 0.101 ps. After the initial spike of defects, displaced atoms come to rest in vacant sites or collide with neighbouring atoms until the cell stabilises.

Figure 4.31 follows the interstitials and vacancies formed during a cascade with an initial PKA direction normal to the plane. The initial PKA direction was set to  $x = 0.00$ ,  $y = 0.00$  and  $z = 1.00$ .

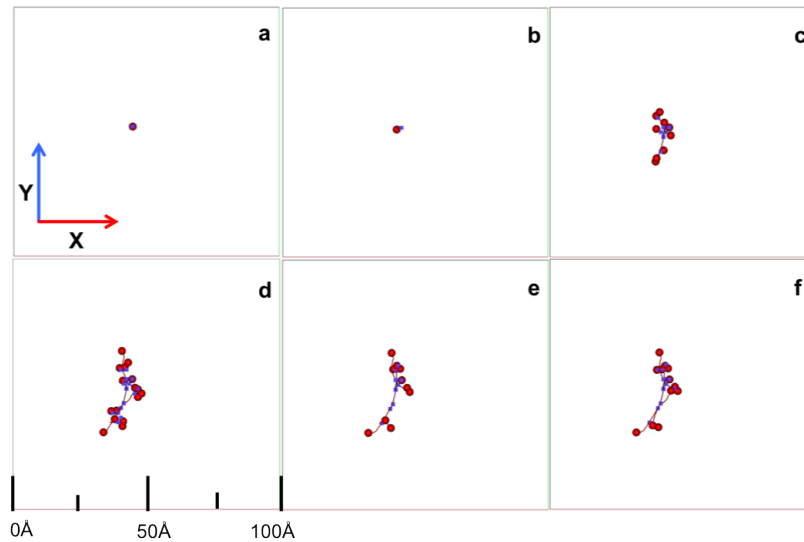


**Figure 4.31:** Graphite cascade with initial PKA energy 500 eV after: (a) 0.00 ps, (b) 0.01 ps, (c) 0.04 ps, (d) 0.11 ps, (e) 0.26 ps and (f) 2.91 ps. Initial PKA direction  $x = 0.00$ ,  $y = 0.00$  and  $z = 1.00$ . The cell temperature is  $300^{\circ}\text{C}$ . The red circles denote interstitials and the blue squares denote vacancies. The path of each displaced atom is traced.

Figures 4.31 (a) and (b) highlight the initial direction of the PKA. It collides with two carbon atoms and comes to rest forming an interstitial 0.04 ps into the cascades (figure 4.31 (c)). Figure 4.31 (c) shows that the displaced carbon atoms produce two individual secondary cascades in opposing directions. The secondary cascades continue to form interstitials and vacancies until 0.26 ps (figure 4.31 (e)) where channelling occurs resulting in the increased presence of interstitials and vacancies before the cell stabilises (figure 4.31 (f)). The number of interstitials and vacancies present in the final cell is 10.

Figure 4.32 highlights the channelling occurring during the cascade.

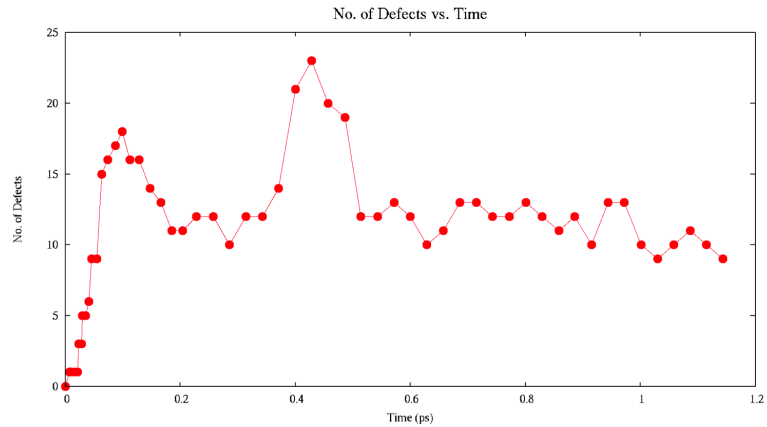


**Figure 4.32:** Graph indicating the number of defects present during a graphite cascade at 500 eV. Initial PKA direction  $x = 0.00$ ,  $y = 0.00$  and  $z = 1.00$ . The cell temperature is  $300^{\circ}\text{C}$ .

Figure 4.32 has an initial peak of 18 defects at 0.099 ps. The number of defects present in the cell gradually decreases as interstitials re-combine in the lattice. A second peak can be seen in figure 4.32. This is evidence of channelling and can clearly be seen between 0.2 and 0.4 ps. The second peak gradually decreases leaving the cell to stabilise. The maximum number of defects 23 occurs at 0.428 ps.

Figure 4.33 follows the distance travelled by displaced atoms.

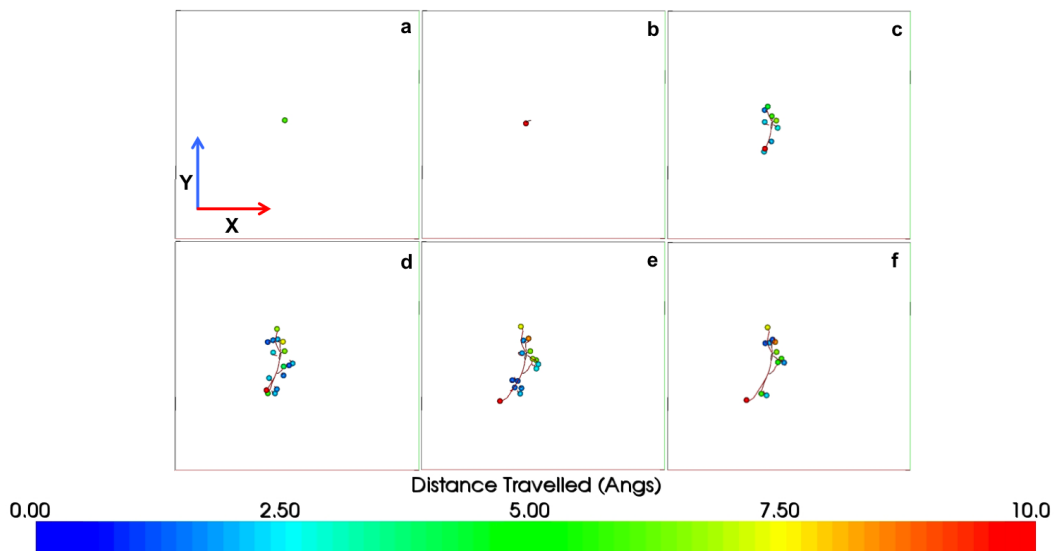


**Figure 4.33:** Graphite cascade with initial PKA energy 500 eV after: (a) 0.007 ps, (b) 0.021 ps, (c) 0.046 ps, (d) 0.074 ps, (e) 0.128 ps and (f) 2.919 ps. The colour of the scalar bar indicates the distance moved by atoms during the cascade. Initial PKA direction  $x = 0.00$ ,  $y = 0.00$  and  $z = 1.00$ . The cell temperature is  $300^{\circ}\text{C}$ .

Figures 4.33 (a) and (b) indicate the initial path of the PKA. As the cascade continues, the PKA collides with two carbon atoms. This alters the path of the PKA forcing it back along its initial path before the PKA comes to rest. In figure 4.33 (c) the red atom is not the PKA but rather it is a second carbon atom which was displaced as a direct result of a collision with the PKA. Figures 4.33 (d), (e) and (f) continue to track displaced atoms from secondary cascades. The final displaced atoms (figure 4.33 (f)) have travelled an average of  $5.17\text{\AA}$ . The final displacement of the PKA is  $5.86\text{\AA}$ .

### 4.3.3 High Temperature Cascades

The next generation of nuclear reactors employing a graphite core will operate at 900°C. To demonstrate the effect of the increased temperature cascades, the initial 20 directions have been simulated using an initial temperature of 900°C and initial PKA energy 1000 eV. The results of two cascades simulations are presented below.

Figure 4.34 represents a cascade through graphite with the initial temperature set to 900°C, initial PKA energy set to 1000 eV and the initial PKA direction 1 from table 3.1.

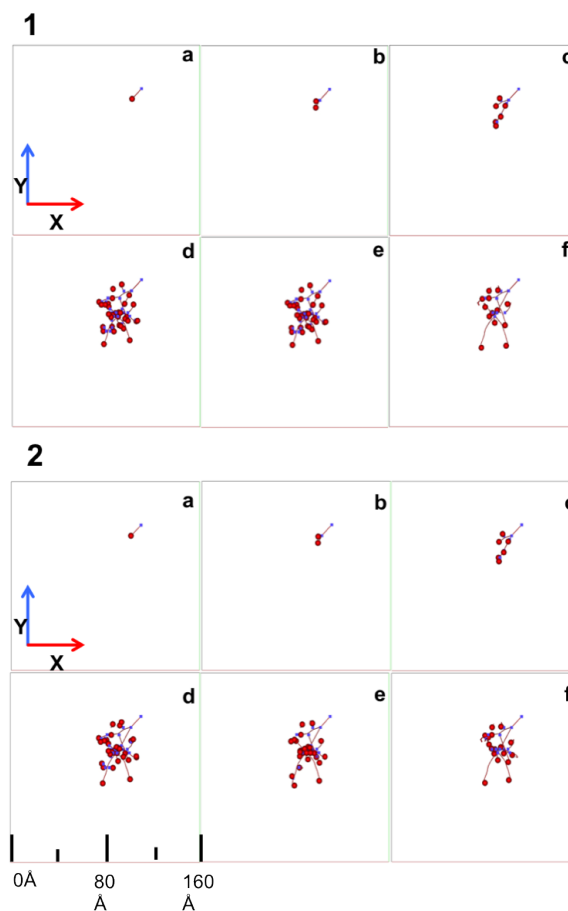


**Figure 4.34:** Graphite cascades with initial PKA energy 1000 eV after: (a) 0.04 ps, (b) 0.08 ps, (c) 0.18 ps, (d) 0.37 ps, (e) 0.71 ps and (f) 2.365 ps. Initial PKA direction 1 from table 3.1. Initial Temperatures **(1)** 900°C and **(2)** 300°C. The red circles denote interstitials and the blue squares denote vacancies. The path of each displaced atom is traced.

Figures 4.34 (1a) and (1b) show the initial path of the PKA. As the cascade

proceeds, secondary cascades begin to form, these can be observed in figures 4.34 (1c), (1d) and (1e). The cascade begins to stabilise, after 2.365 ps, figure 4.34 (1f). After the cascade has stabilised there are 15 interstitials and vacancies present in the cell. Figure 4.34 (2), shows the same cascade simulated at 300°C. Figures 4.34 (1) and 4.34 (2) on the surface look close to being identical. Further analysis of the data produced highlights slight differences. The final number of interstitials and vacancies present in the cell in the 300°C is 18, three more than seen in the 900°C.

Figure 4.35 highlight the differences found within the simulations.

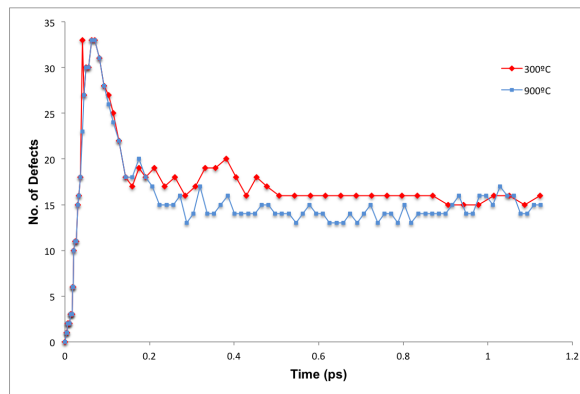


**Figure 4.35:** Graph indicating the number of defects present during a graphite cascade at 1000 eV. Initial PKA direction 1 from table 3.1. Initial Temperatures 900°C (blue) and 300°C (red).

The cascades both have an initial peak followed by a decrease in the number of defects present in the cell. At 300°C, figure 4.35 there is evidence of channelling between 0.041 and 0.050 ps, a phenomenon which is not seen at 900°C. The maximum number of defects present during both cascades is 33 and occurs at 0.041 ps during the 300°C cascade and 0.063 ps during the 900°C. Both graphs continue to see small changes in the number of defects present until they stabilise.

Figure 4.36 tracks the path of the PKA through the cell.

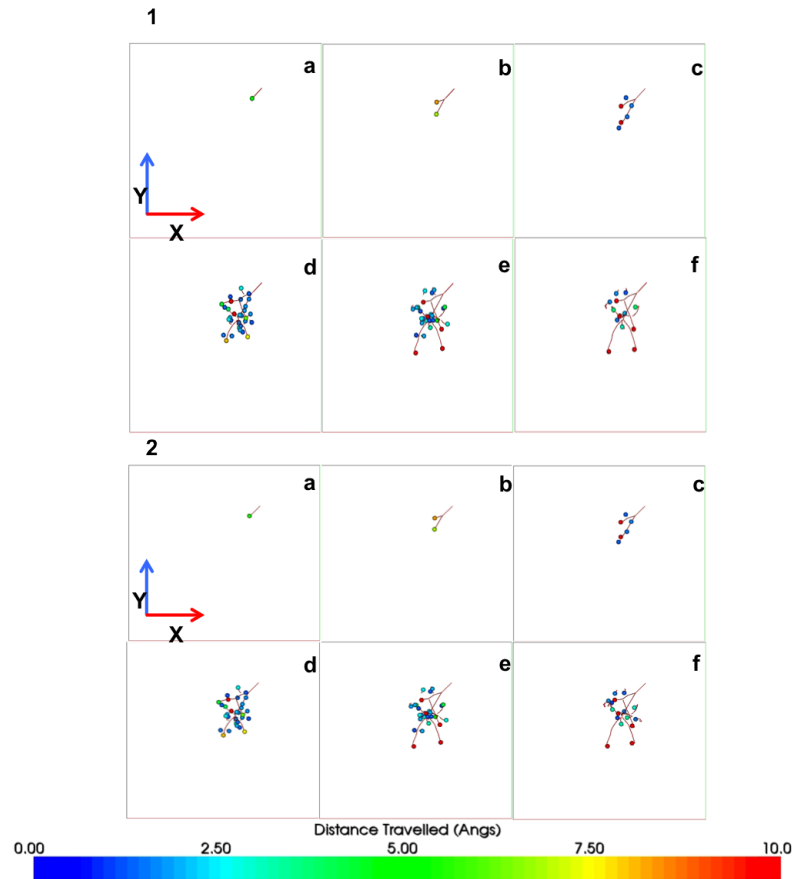


**Figure 4.36:** Graphite cascade with initial PKA energy 1000 eV after: (a) 0.04 ps, (b) 0.11 ps, (c) 0.021 ps, (d) 0.50 ps, (e) 0.92 ps and (f) 2.397 ps. Initial PKA direction 1 from table 3.1. The colour of the scalar bar indicates the distance moved by atoms during the cascade. Initial Temperatures **(1)** 900°C and **(2)** 300°C.

Figure 4.36 (1) and 4.36 (2) form very similar cascade patterns. The defect discrepancy can be seen by comparing Figures 4.36 (1f) and 4.36 (2f). Figure 4.36 (1f) has three more defects present in final cell than in figure 4.36 (2f). The final displacement of the PKA at 300°C is 15.52Å and the final displacement of the PKA at 900°C is 15.41Å.

Figure 4.37 shows a cascade in graphite simulated with an initial PKA energy of 1000 eV, initial PKA direction 15 from table 3.1 and initial temperatures set to 900°C and 300°C.

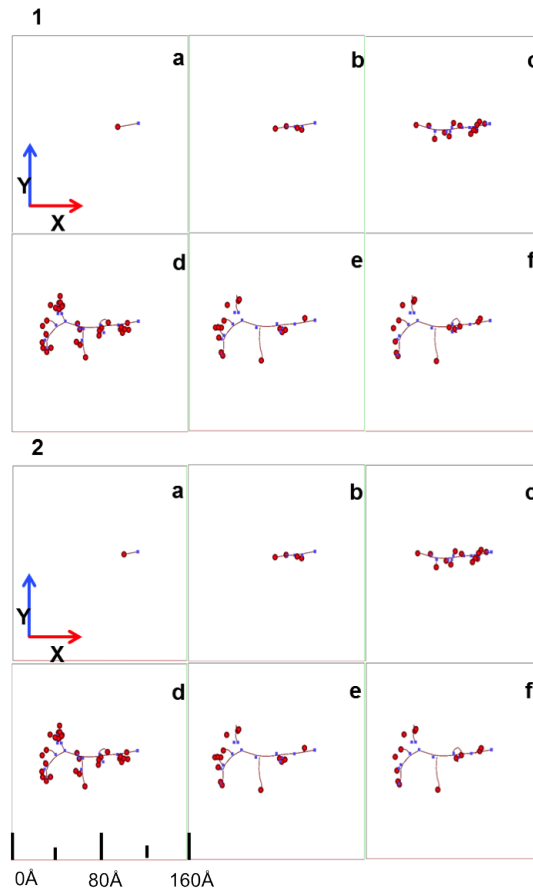


**Figure 4.37:** Graphite cascade with initial PKA energy 1000 eV after: (a) 0.00 ps, (b) 0.01 ps, (c) 0.03 ps, (d) 0.08 ps, (e) 0.63 ps and (f) 4.87 ps. Initial PKA direction 15 from table 3.1. Initial Temperature **(1)** 900°C and **(2)** 300°C. The red circles denote interstitials and the blue squares denote vacancies. The path of each displaced atom is traced.

Image (a) in figures 4.37 (1) and (2) shows the initial direction of the PKA. The two cascades follow the same path throughout the simulation. After 0.01 ps, secondary cascade collisions can be seen forming alongside the path of the initial PKA direction, (images (b), (c), (d), (e) and (f)). The cell stabilises after 0.70 ps leaving 14 interstitials and vacancies present in the 300°C cell and 15 in the 900°C.

Figure 4.38 denotes each displaced atom at any given point in time during the 900°C and 300°C cascades.

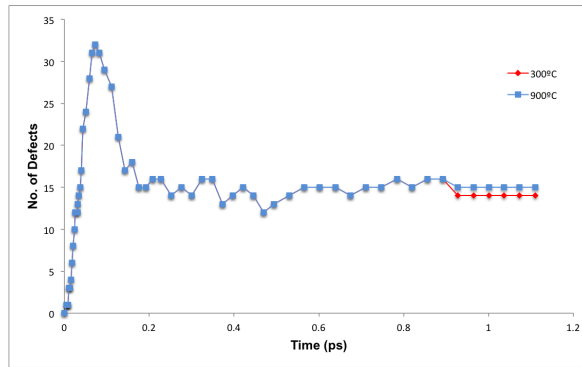


**Figure 4.38:** Graph indicating the number of defects present during a graphite cascade at 1000 eV. Initial Temperatures 900°C (blue) and 300°C (red). Initial PKA direction 15 from table 3.1.

The cascades are identical until the final stage of the simulation where there is one more interstitial formed in the 900°C cascade than there is in the 300°C cascade. The maximum peak of 32 defects occurs at 0.073 ps in figure 4.38. There is no channelling observed in either of these cascades. The slight variation in the number of defects present after 0.2 ps is a direct result of the carbon atoms at the edge of the secondary cascades reaching their threshold energies. Once the atoms have reached their threshold energies they no longer have enough kinetic energy to break away from the lattice sites. However, the carbon atoms may have enough kinetic energy to move slightly out of their position in the lattice, without breaking any bonds and form an interstitial between planes. The atoms may stay in their defect position or they may re-combine with the lattice in which case there will no longer be a defect present. In the case of these two cascades, this phenomena affects the number of interstitials and vacancies present in the final lattice.

Figure 4.39 shows the distance travelled by displaced atoms during the graphite cascade. To begin with, the PKA follows the same initial path in both cascades. It is only in the final stages that the displacements of the PKA and surrounding atoms alter. The PKA's kinetic energy falls below its threshold energy at 0.56 ps in figure 4.39 (1d) compared to 0.66 ps in figure 4.39 (2d). The difference in time for the PKA's kinetic energy to fall less than the threshold energy contributes to the displacement of the PKA being greater in the 300°C cascade. Images (1f) and (2f) from figure 4.39 highlight the difference in the number of interstitials and vacancies in the final lattice cell. The extra atom which appears in the 900°C cascade has a displacement less than 1Å. As the displacement of the atom is so small, this supports the postulation that the

atom has just enough kinetic energy to leave the lattice site and form a defect within the plane but not enough kinetic energy to break the bonds and create further secondary cascades. The final displacement of the initial PKA is 48.6Å in the 900°C cascade and 55.21Å in the 300°C cascade.

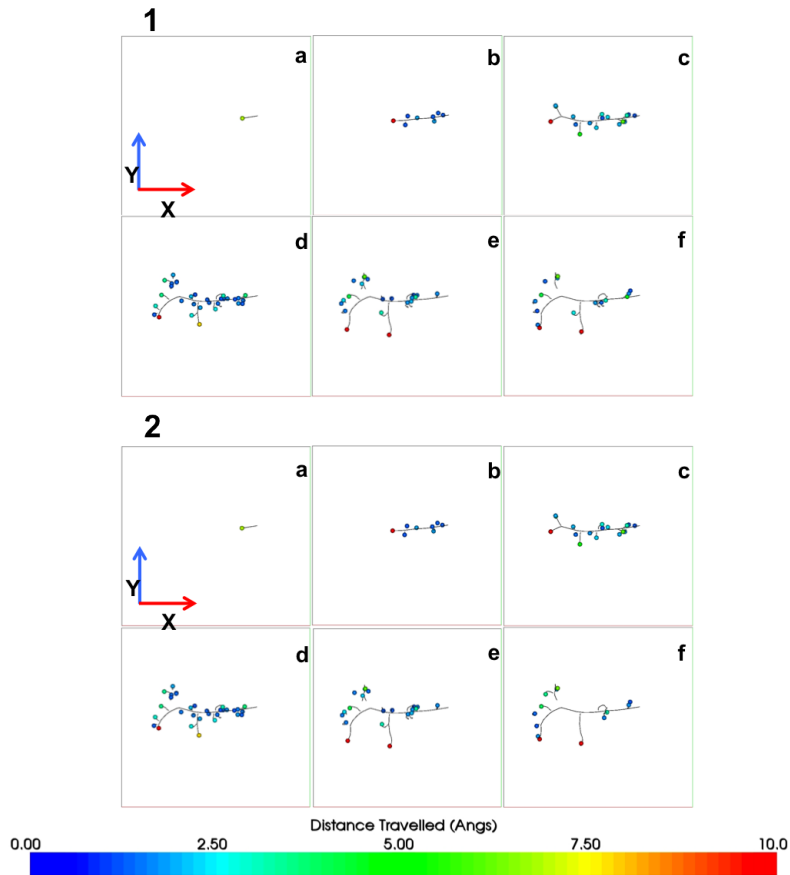


**Figure 4.39:** Graphite cascade with initial PKA energy 1000 eV after: (a) 0.005 ps, (b) 0.022 ps, (c) 0.040 ps, (d) 0.066 ps, (e) 0.127 ps and (f) 3.320 ps. Initial PKA direction 15 from table 3.1. The colour of the scalar bar indicates the distance moved by atoms during the cascade. Initial Temperatures **(1)** 900°C and **(2)** 300°C.

High temperature graphite cascades, 900°C, have produced results similar to those found during cascades at 300°C. Whilst there are slight differences between the final number of defects present in the final lattice, the collisions occurring at both temperature mirror each other. Further discussion of high temperature cascades can be found in Chapter 6.

## 4.4 Quantitative Cascade Data

Statistical sampling is a crucial element of any cascade simulation analysis. It is particularly so for graphite because the low packing fraction and anisotropic crystalline structure facilitates strong variations in radiation response as a function of energy and direction [48]. Twenty directions have been sampled for each PKA energy, providing a high degree of precision which enables extraction of clear trends in the data.

One of the striking features observed during cascades is the fractal-like branching structure of the defect trajectories. These trajectories occur as a result of highly energetic collisions involving the PKA and subsequent displaced atoms. Figure 4.40 shows the maximum kinetic energy of atoms during a cascade with an initial PKA energy of 1000 eV.

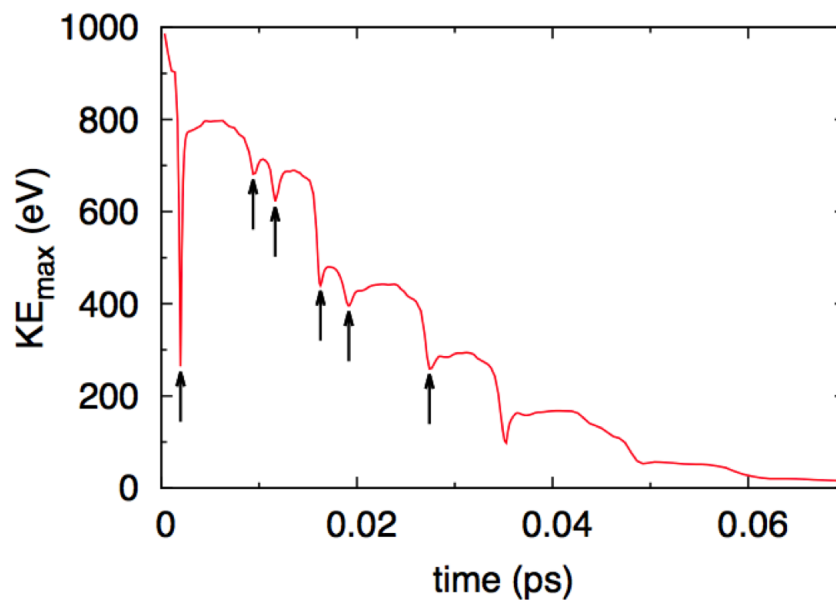


**Figure 4.40:** The kinetic energy of the most energetic atom as a function of time in a graphite cascade with initial PKA energy of 1000 eV. The vertical arrows indicate collisions with small impact parameters that transfer large amounts of kinetic energy to a lattice atom.

The arrows in figure 4.40 highlight the moments of close approach in which the PKA (or another energetic atom) interacts strongly with an atom on a lattice site. Atoms have very small velocities and experience great forces at the instant of close approach. The repulsion between the two atoms results in the cascade being split. Potential energy is converted into kinetic energy which is

spread between the two atoms resulting in the fractal-like branching observed. Figure 4.40 reveals it is only for an extremely short time period that atoms have substantial kinetic energy. This is in stark contrast to metal and oxides cascades which typically evolve on the timescale of a picosecond [1] [98] [97] [2]. Whereas in graphite, the maximum kinetic energy has fallen below 10 eV after just 90 fs. To quantify this behaviour, the number of atoms with a kinetic energy exceeding thresholds of 1 (warm atoms) and 10 (fast atoms) eV were counted. Figure 4.41 shows the time-dependence of both quantities as a function of time.

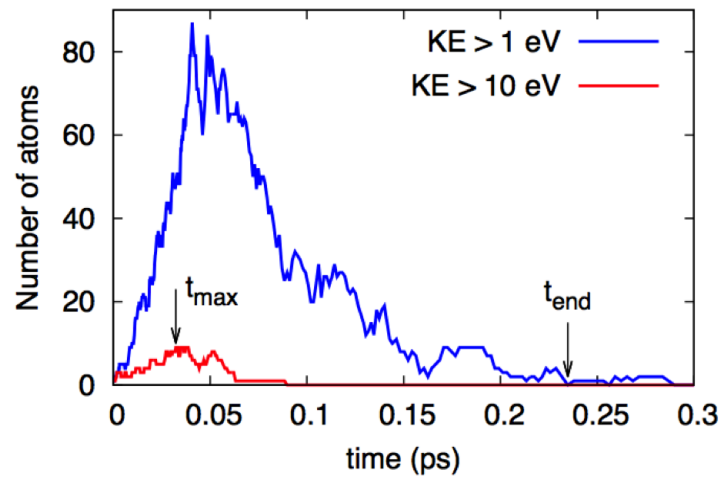


**Figure 4.41:** The number of atoms with kinetic energy greater than 10 eV (red) and 1 eV (blue). Where  $t_{max}$  is the maximum number of fast atoms and  $t_{end}$  is the time taken for warm atoms to reduce to zero.

Figure 4.41 shows that the maximum number of fast atoms is achieved after just 32 fs ( $t_{max}$ ). The number of warm atoms takes 235 fs to reach zero ( $t_{end}$ ). This rapid time evolution is common to all cascades considered in this study. Figure 4.42 shows the average energy dependence of the quantities  $t_{max}$  and  $t_{end}$  across the 20 simulated directions.

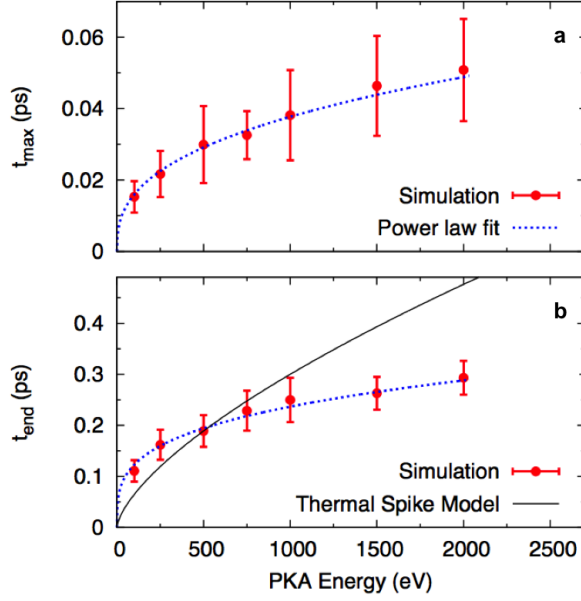


**Figure 4.42:** (a) The dependence of  $t_{max}$  as a function of PKA energy (i.e.  $KE > 10$  eV). (b) The dependence of  $t_{end}$  as a function of PKA energy (i.e.  $KE > 1$  eV).

The magnitude of the error bars in figure 4.42 indicate the high degree of variability between individual graphite cascades. Figure 4.42 shows there is a weak energy dependence of the time of peak defects (figure 4.42 (a)) and the spike cooling time (figure 4.42 (b)). An increase in the initial PKA energy by a factor of four from 500 eV to 2000 eV changes  $t_{max}$  by only 70% and  $t_{end}$  by 55%. This provides further evidence that cascade behaviour through graphite is almost entirely ballistic.

To further highlight the uniqueness of graphite, the energy dependence for a thermal spike produced when the energy of the PKA is delivered into a relatively compact region and induces local melting is plotted in figure 4.42 (b) (black line) [99]. The heat diffusion equation shows the cooling times varies as  $E^{2/3}$ , where  $E$  is the PKA energy. Figure 4.42 shows clearly the graphite cascades have an energy dependence entirely unlike the thermal spike model. Figure 4.42 reveals that both data sets can be described by a power-law expression, equations 4.1 and 4.2.

$$t_{max} = aE^x \quad (4.1)$$

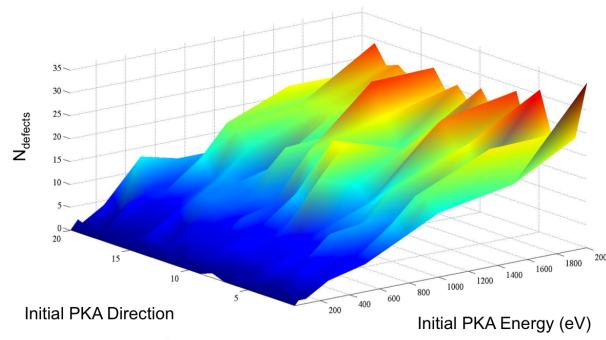
where  $x = 0.37$ .

$$t_{end} = aE^x \quad (4.2)$$

where  $x = 0.28$ .

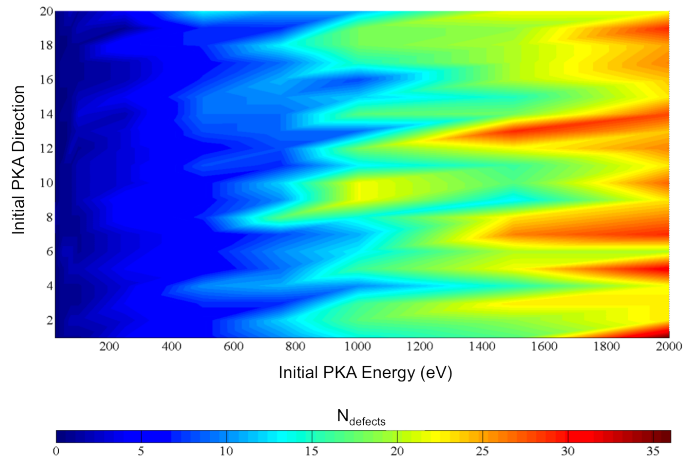
The exponents in equations 4.1 and 4.2 allow the lifetime of a spikes with a much larger initial PKA energy to be calculated. For example, a 20 keV spike would only see a 80% increase in lifetime compared to a 2.5 keV spike.

Figure 4.43 shows a plot of the 20 simulated directions (where the Initial PKA Direction point refers to the initial PKA directions given in table 3.1), as a function of the initial PKA energy (eV) and the final number of defects present in the lattice in the vertical direction.



**Figure 4.43:** A plot of the 20 simulated directions, initial PKA energy (eV) and the final number of defects ( $N_{defect}$ ) present in the lattice. (Numbers 1-20 refer to the 20 coordinates in table 3.1)

Figure 4.43 as expected shows a clear trend; the greater the initial PKA energy, the greater number of defects produced. Figure 4.44, shows the data from a 2D perspective.



**Figure 4.44:** A plot of the 20 simulated direction, initial PKA energy (eV) and the final number of defects ( $N_{defect}$ ) present in the lattice. The colour of the scalar bar indicates the number of defects present in the final lattice cell. (Numbers 1-20 refer to the 20 co-ordinates in table 3.1)

Figure 4.44 highlights the three energy regions within the cascade simulations. Low energy cascades below 500 eV, produced a minimum and maximum of zero and seven defects respectively in the final cell. There was very little damage seen to the overall graphite structure during these energies. Mid-range energies between 500 and 1000 eV, produced a minimum and maximum of 5 and 19 defects respectively in the final cell. During this region minor structural damage was witnessed in the final cell. The third region is high energy cascades with energies greater than 1000 eV. During these simulations a minimum and maximum of 16 and 42 defects respectively were produced in the final cell. Even at high energies, there was little damage to the overall structure despite the increase in the number of final defects present in the cell.

Two of the most crucial quantities in radiation cascade simulations are the number of atoms displaced and the number of defects created. Table 4.1 states the average, standard deviation, mode, median and range of the number of defects produced at a given initial PKA energy.

Initial PKA Energy (eV)	Average Number of Defects	Standard Deviation	Mode	Median	Range
25	0.10	0.489	0	0	1
50	0.85	0.641	1	1	2
75	1.25	0.681	1	1	1
100	1.50	0.681	1	1	2
250	3.35	1.334	5	3	5
500	7.20	2.012	7	7	8
750	10.00	2.434	10	10	10
1000	14.70	2.434	15	15	14
1500	19.80	4.082	24	20	16
2000	25.00	4.891	27	29	17

**Table 4.1:** The average number of defects formed at a given initial PKA energy.

The values of final defects from table 4.1 can be compared to the displacement predictions from the Norgett-Robinson-Torrens (NRT) model (figures 4.45).

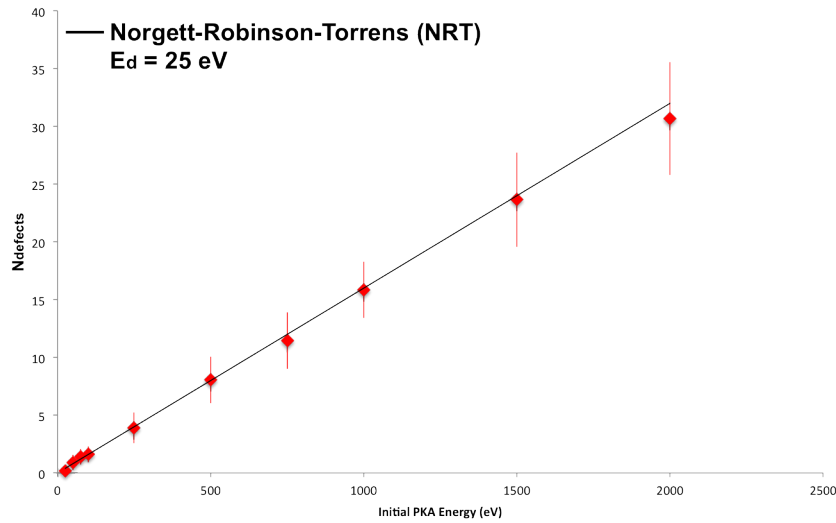


**Figure 4.45:** Number of displacements as a function of PKA energy. Error bars denote one standard deviation. The solid line shows the Norgett-Robinson-Torrens model for defect prediction, assuming a threshold displacement energy of 25 eV.

The NRT model, which is a modified KP model, is computed assuming a threshold displacement energy of 25 eV. This value was chosen to be consistent with experimental and computational literature [78] [80] [84]. The simulated data in figure 4.45 fits to linear equation 4.3.

$$N_{defects} = 0.0155E \quad (4.3)$$

where  $E$  is the initial PKA energy.

The  $c$  intercept is set to zero because there were no defects formed with an initial PKA energy of 0 eV.

The NRT model is a modified Kinchin and Pease model used to calculate the number of defects generated by a PKA [80] [81]. Equation 4.4 is used to generate the model.

$$N_d = \frac{kE}{2E_d} \quad (4.4)$$

where  $N_d$  is the number of defects,  $E$  is the initial PKA energy,  $E_d$  is the threshold displacement energy and  $k$  is the displacement efficiency.

The displacement efficiency  $k$  is given the value 0.8 [80]. This value is independent of the PKA energy, the target material and the temperature. This model was originally fitted to MD simulations in copper [11] and iron [82] [83]. However, due to computational limitations, the initial PKA energy given to a system could not exceed 1000 eV [80]. Evidence of this can be seen in figure 4.45. The NRT model fits to data simulated in this thesis below initial PKA energies of 1000 eV. There is a discrepancy between simulated data and the NRT model at high energies. To account for these discrepancies, a displacement efficiency,  $k$ , of 0.77 yields results with a higher degree of accuracy for initial PKA energies greater than 1000 eV.

Equation 4.5 is a modified version of the NRT [80] model based on the simulated results (assuming a threshold displacement energy of 25 eV).

$$\frac{0.77E}{2E_d} = N_{defects} \quad (4.5)$$

Figure 4.46 shows the average number of defects calculating using the NRT model and equation 4.5 compared to simulated data presented in this chapter.

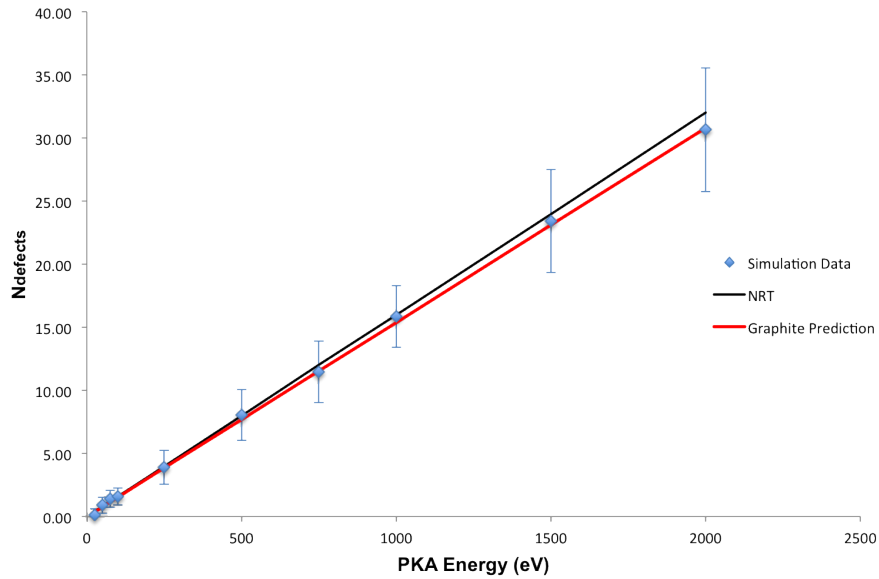


**Figure 4.46:** Number of displacements as a function of energy. The solid line shows the equation  $\frac{0.77E}{E_d}$  for defect prediction, assuming a threshold displacement energy of 25 eV.

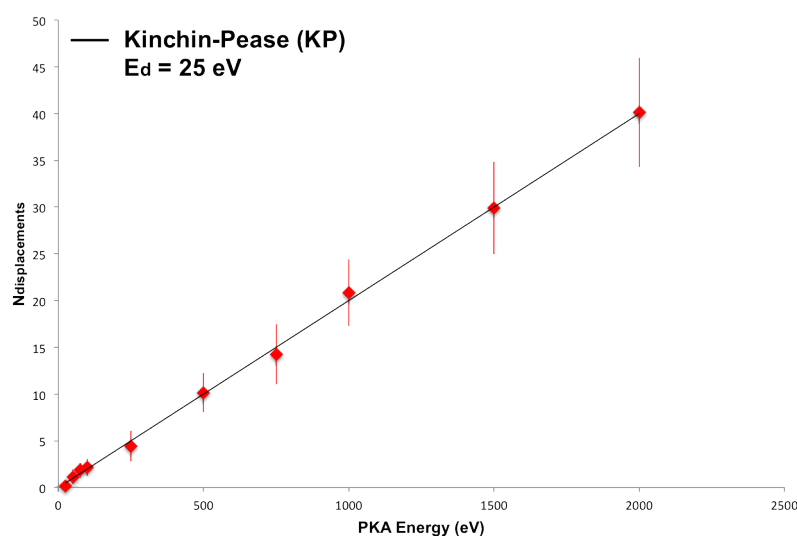
Figure 4.46 highlights that at high energies, equation 4.5 yields results of greater accuracy than the NRT model (i.e., it has a lower value for graphite).

Table 4.2 shows the average maximum number of displaced atoms at a given initial PKA energy.

Initial PKA Energy (eV)	Average Maximum No. of Displacements of PKA (Å)
25	0.15
50	1.15
75	1.85
100	2.15
250	4.4
500	10.15
750	14.25
1000	20.85
1500	29.9
2000	40.1

**Table 4.2:** The maximum number of displaced atoms at a given initial PKA energy.

The values from table 4.2 can be compared to the predicted displacements from the Kinchin and Pease Model (KP) model (figures 4.47).



**Figure 4.47:** The maximum number of displaced atoms. Error bars denote one standard deviation. The solid line shows the Kinchin and Pease model for defect prediction, assuming a threshold displacement energy of 25 eV.

The simulations show pleasing correlation with the Kinchin and Pease model. The graph in figure 4.47 has a linear trend. The number of displaced atoms increases as the initial PKA energy increases. Equation 4.6 is the linear equation of the simulation points. The intercept is zero as there will never be any

displaced atoms as a result of a cascade with no initial PKA energy given to the cell.

$$N_{displacements} = 0.02E \quad (4.6)$$

where  $E$  is the initial PKA energy.

Figure 4.48 show the size of cascades and the range of the PKA as a function of energy. The size of the cascade is calculated using the greatest distance between any two defects present in the cascade. The PKA range is the difference between the PKA's initial and final position. For the purpose of this analysis, a defect was defined as any atom with a local potential energy greater than -7 eV/atom.

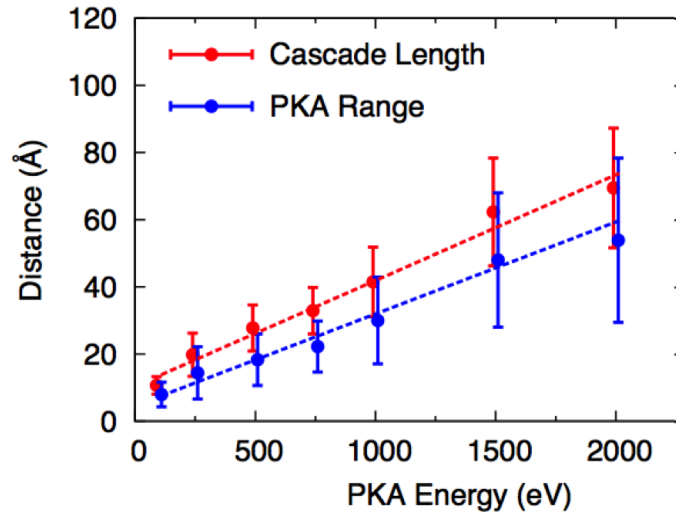


**Figure 4.48:** The cascade length (red) and the PKA range (blue) as a function of PKA energy. Error bars denote one standard deviation. (The data sets are slightly offset to the left and right of relevant energies for clarity)

Figure 4.48 shows there is a linear trend between the size of the cascade and the PKA range. Equations 4.7 and 4.8 give the linear line equations fitted to the data in figure 4.48.

$$D_{range} = 0.27E \quad (4.7)$$

For the PKA range, where  $D_{range}$  is the PKA's range and  $E$  is the initial PKA

energy.

$$D_{length} = 0.31E \quad (4.8)$$

For the size of the cascade, where  $D_{length}$  is the cascade's length and  $E$  is the initial PKA energy.

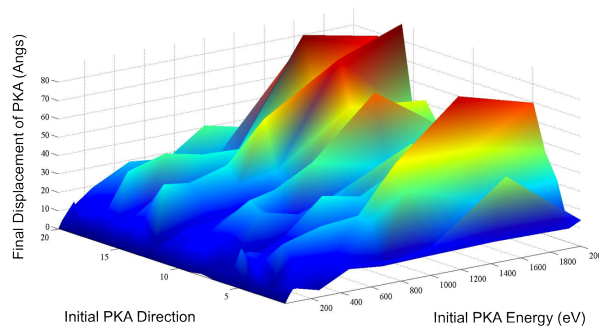
The intercept is zero as no atoms were displaced in a graphite cascade with an initial PKA energy of zero.

Table 4.3 shows the average displacement of the initial PKA at a given initial PKA energy.

Initial PKA Energy (eV)	Average Displacement of PKA (Å)
25	0.054
50	4.823
75	6.832
100	8.962
250	14.519
500	19.155
750	21.868
1000	28.431
1500	49.535
2000	44.949

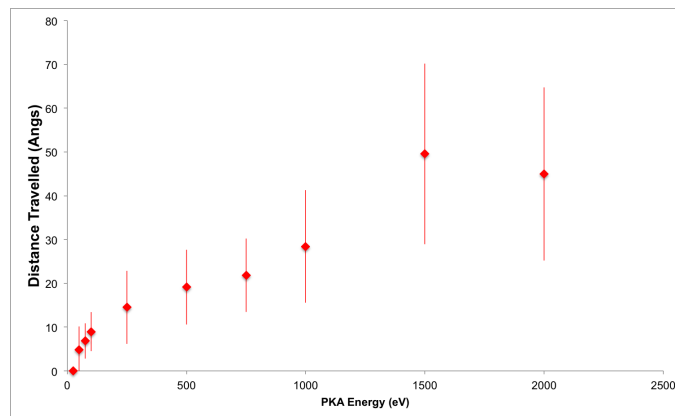
**Table 4.3:** The average displacement of the initial PKA at a given initial PKA energy.

Figure 4.49 shows a plot of the 20 simulated directions, initial PKA energy (eV) and the final displaced of the PKA.



**Figure 4.49:** A plot of the 20 simulated directions, initial PKA energy (eV) and the final number of defects ( $N_{defect}$ ) present in the lattice. (Numbers 1-20 refer to the 20 Thomson point co-ordinates)

The simulations with a large final PKA displacement witnessed evidence of channelling. The PKA penetrated through the cell for significant periods of time without colliding with surrounding atoms resulting in the PKA having a large final displacement. Graph 4.50 shows the average final displacement of the PKA at a given energy.



**Figure 4.50:** The average final PKA displacement ( $\text{\AA}$ ). Error bars denote one standard deviation.

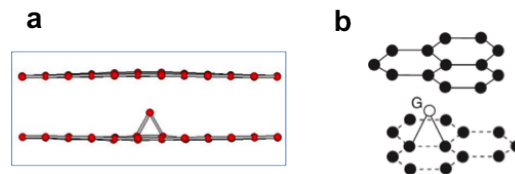
Figure 4.50 shows an increase in the PKA's final displacement as a function of PKA energy in energies up to 1500 eV. At 2000 eV the average final PKA displacement has decreased. The most probable reason for this is channelling as a direct result of the large initial PKA energy given to the system. The individual cascade results gave evidence channelling can occur in one simulation but not in another, even if both simulations have the same initial PKA direction just different initial PKA energies.

Further discussion of statistical results can be seen in Chapter 6.

## 4.5 Threshold Energy Results

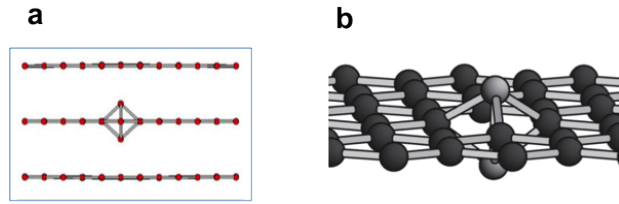
The third regime of interest refers to the threshold displacement energy range. The threshold displacement energy is the minimum amount of energy required to displace an atom. Effects of the threshold displacement energy can be seen at the end of thermal spike simulations or cascade simulations. Threshold displacement energies can be observed by computing MD cascades with an initial energy of  $\approx 30$  eV.

Final threshold displacement energy calculations have produced results which have been seen in previous published literature and experimental work [5] [100] [101]. The comparison between defects observed in cascades produced in this thesis and previous literature emphasises the quality of the statistical data produced in this chapter. Figure 4.51 (a) shows a grafted interstitial produced in a low energy cascade. The carbon atom resting between the two graphite layers has been displaced from its original position, bonds have been formed with two atoms in the layer directly below. Figure 4.51 (b) is an example of a grafted interstitial seen in literature. The binding energy for a grafted interstitial is 2.78 eV [5].



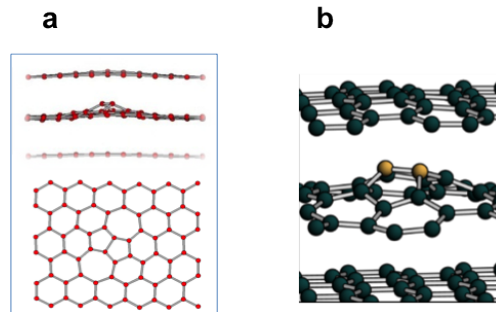
**Figure 4.51:** (a) Grafted interstitial as seen in EDIP cascades presented in this thesis. (b) Grafted interstitial as seen in the literature (*Telling & Heggie, Phil Mag.* **87**, 4797 (2007)) [5].

A second example of interstitials formed as a direct result of cascades through graphite is the split interstitial. In a split interstitial, two atoms share the same lattice site. An example of split interstitials seen in EDIP cascades presented in this thesis and previous literature can be seen in figure 4.52. The binding energy for a split interstitial is 1.34 eV [100].



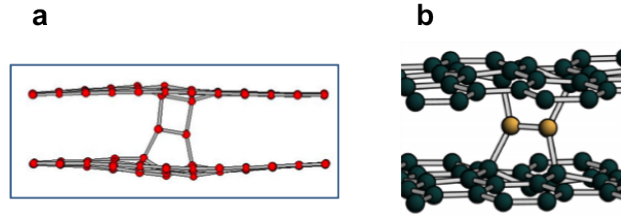
**Figure 4.52:** (a) Split interstitial as seen in EDIP cascades presented in this thesis. (b) Split interstitial as seen in the literature (*Latham et al., Journal of Physics: Condensed Matter* **20**, 39 (2008))[100].

Figure 4.53 shows a bi-pentagon  $I_2$  grafted intralayer bridge interstitial. This defect is the lowest energy structure for a pair of self-interstitial atoms in graphite. The binding energy for a bi-pentagon grafted intralayer bridge interstitial is  $\approx 3$  eV [100].



**Figure 4.53:** (a) Bi-pentagon  $I_2$  grafted intralayer bridge interstitial as seen in EDIP cascades presented in this thesis. (b) Bi-pentagon  $I_2$  grafted intralayer bridge interstitial as seen in the literature (*Latham et al., Journal of Physics: Condensed Matter* **20**, 39 (2008))[100].

Figures 4.54 (a) and (b) are examples of a bi-pentagon interlayer bridge interstitial in EDIP cascades presented in this thesis and in previous published literature. The binding energy of the bi-pentagon interlayer bridge interstitial is 1.5 eV [100].



**Figure 4.54:** (a) Bi-pentagon interlayer bridge interstitial as seen in EDIP cascades presented in this thesis. (b) Bi-pentagon interlayer bridge interstitial as seen in the literature (*Latham et al., Journal of Physics: Condensed Matter* **20**, 39 (2008))[100].

A bent interlayer bridge interstitial formed in EDIP cascades presented in this thesis can be seen in figure 4.55 (a). Figure 4.55 (b) is a bent interlayer bridge interstitial as seen in previous literature. The binding energy is 2.4 eV [100].

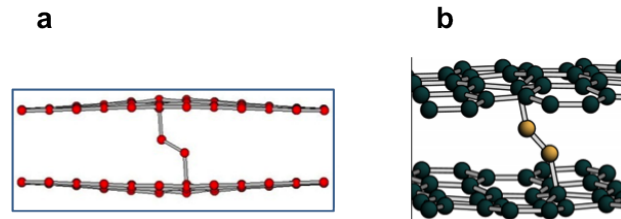


**Figure 4.55:** (a) Bent interlayer bridge interstitial as seen in EDIP cascades presented in this thesis. (b) Bent interlayer bridge interstitial as seen in the literature (*Latham et al., Journal of Physics: Condensed Matter* **20**, 39 (2008))[100].

The final example of defects formed in graphite cascades is the single interlayer interstitial. Figures 4.56 (a) and (b) show the single interlayer interstitial as formed in EDIP cascades presented in this thesis and from previous literature respectively. The binding energy is 1.8 eV [100].

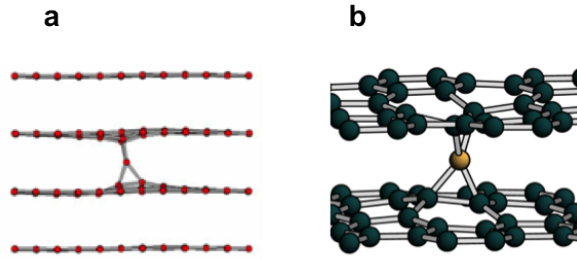


**Figure 4.56:** (a) Single interlayer interstitial as seen in EDIP cascades presented in this thesis. (b) Single interlayer interstitial as seen in the literature (*Latham et al., Journal of Physics: Condensed Matter* **20**, 39 (2008))[100].

A further defect referred to as the spiro interstitial has been identified in density function theory calculations [102]. Some of the structural details of the spiro interstitial (specifically, the two sets of triangular C-C bonds) differ from the MD simulation. However, the origin of this discrepancy is well-known. The spiro interstitial form in MD arises from the neglect of three-centre terms, a common approximation in pair potentials and tight-binding methodologies [103]. The key observation is that the interlayer defect is indeed prevalent in the simulations and is strongly correlated with over-coordinated atoms created by interstitials.

Vacancies produced after cascade simulations are a result of atoms being displaced. Vacancies observed in EDIP cascades presented in this thesis have agreed with previous experimental and theoretical research. Figure 4.57 (a) is an example of a vacancy found upon completion of a collision cascade using the EDIP potential presented in this thesis. The structure of the vacancy agrees with previous literature, figure 4.57 (b) [101].

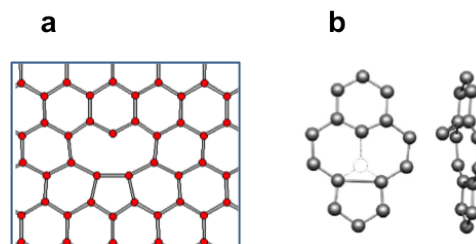


**Figure 4.57:** (a) Vacancy as seen in EDIP cascades presented in this thesis. (b) Vacancy as seen in the literature (*El-Barbary, et al, Physical Review B* **68**, 144107 (2003)) [101].

There are several types of vacancy which can be observed in graphite cas-

cases. The Stone-Wales defect has been identified in the final stable lattice of a graphite collision cascade simulation. Figure 4.58 (a) shows the Stone-Wales defect as seen in EDIP cascades presented in this thesis, the structure of which matches to the Stone-Wales defect found in previous literature, figure 4.58 (b) [100].

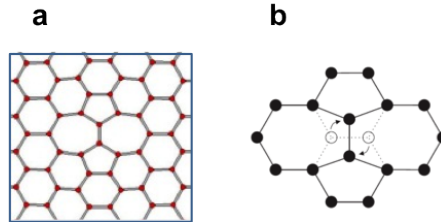


**Figure 4.58:** (a) Stone-Wales Vacancy as seen in EDIP cascades presented in this thesis. (b) Stone-Wales Vacancy as seen in the literature (*Latham et al., Journal of Physics: Condensed Matter* **20**, 39 (2008))[100].

Analysis of defects, interstitials and vacancies after a simulation shows the statistical structural damage of a cascade through graphite. Defects analysed after cascade simulations have agreed with those found in previous literature.

Table 4.4 compares the formation energies of interstitials in EDIP compared to DFT calculations.

Defects	Formation Energy (eV)	
	EDIP	DFT
Grafted Interstitial	7.84	7.55
Single Interlayer Interstitial	5.85	5.86
Split Interstitial	9.61	7.16
Bi-Pentagon Grafted Intralayer Bridge	10.97	8.63
Stone-Wales Defect	4.81	3.5
Vacancy	5.87	3.5

**Table 4.4:** The formation energy of defects and vacancy calculated in EDIP and DFT.

Table 4.4 shows the formation energies calculated using EDIP are similar to those calculated using DFT [100]. This comparison justifies the choice of EDIP as a potential for modelling graphite.

In summary, cascades through graphite have produced minimal damage to

the final lattice cell. Thermal spike simulations with initial energies up to  $1 \times 10^5$  eV resulted in very little structural damage to the cell. Results generated in this chapter are in agreement with previous literature and fit to historical predictive models [78] [80]. As expected, the average final displacement of the PKA increases as a function of the initial PKA energy. Evidence of channelling has been observed. It predominately occurs during high energy cascades. Cascades in graphite are directionally dependent but are independent of the initial temperature. Threshold displacement energy cascades produced interstitial and vacancies which are consistent with previous literature [100] [101].

# Cascades in Non-Graphitic Carbon Materials

Graphite is a unique material. The hexagonal arrangement of atoms and the layers of graphene within a graphite structure result in cascade simulations being directionally dependent and damage caused to the cell tends to be localised. Diamond, high and low density amorphous carbons and glassy carbon have been simulated to highlight how unique the behaviour of graphite is.

## 5.1 Diamond

Diamond is a very strong and robust material [35]. Unlike graphite, diamond is not formed in layers, it is isotropic and is tetrahedrally bonded ( $sp^3$ ).

Figure 5.1 shows a thermal spike simulation through diamond with initial energy  $6 \times 10^3$  eV.

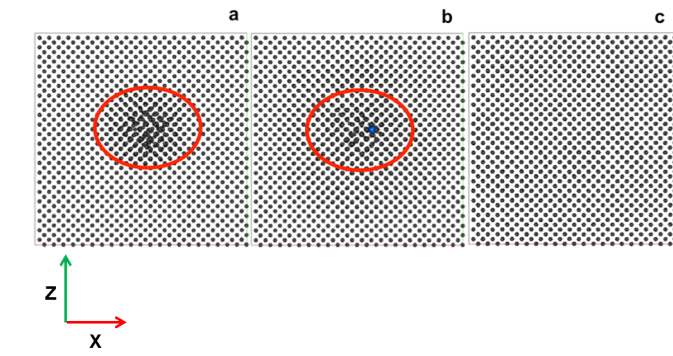


**Figure 5.1:** A thermal spike simulation through a diamond lattice with an initial energy of  $6 \times 10^3$  eV after (a) 0.021 ps, (b) 0.088 ps and (c) 0.120 ps. The initial cell temperature was  $300^\circ\text{C}$ . Displaced atoms are coloured blue and the red ring indicates the thermal spike region.

Figure 5.1 (a) shows the thermal spike after 0.021 ps. The thermal spike creates a shock wave through the cell which results in the vibration of atoms increasing. Despite the increase in vibrations, only one atom is displaced, as seen in figure 5.1 (b) at 0.088 ps. The displaced atom does not possess enough energy to travel further through the cell and cause collisions. The atom then re-combines with the lattice in its initial position. Figure 5.1 (c) shows the cell after it has stabilised. The thermal spike left no damage to the lattice.

Figure 5.2 shows a thermal spike simulation through diamond with initial energy  $2.5 \times 10^4$  eV.

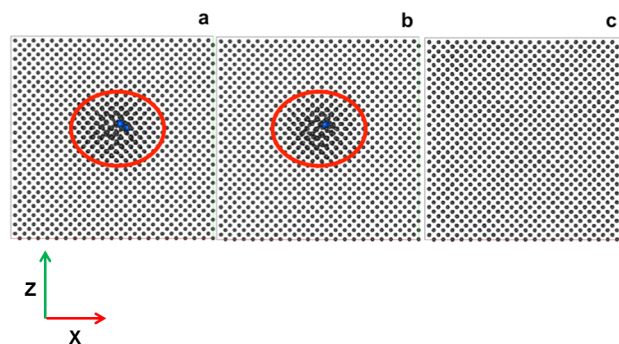


**Figure 5.2:** A thermal spike simulation through a diamond lattice with an initial energy of  $2.5 \times 10^4$  eV after (a) 0.026 ps, (b) 0.079 ps and (c) 0.122 ps. The initial cell temperature was  $300^\circ\text{C}$ . Displaced atoms are coloured blue and the red ring indicates the thermal spike region.

A shock wave is created through the diamond lattice as a direct result of the

thermal spike. Figure 5.2 (a) shows the simulation after 0.026 ps, vibrations have led to the displacement of three atoms. As the simulation continues, the kinetic energy of the displaced atoms falls below their threshold energy causing the atoms to re-combine in their original lattice positions. Figure 5.2 (b) highlights the re-combining process, 0.079 ps into the simulation where there is only one displaced atom remaining. The thermal spike simulation stabilises leaving no damage to the the final cell (figure 5.2 (c)).

Figure 5.3 shows a thermal spike simulation through diamond with initial energy  $1 \times 10^5$  eV.

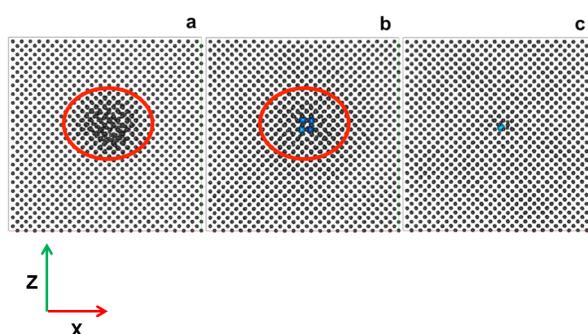


**Figure 5.3:** A thermal spike simulation through a diamond lattice with an initial energy of  $1 \times 10^5$  eV after (a) 0.021 ps, (b) 0.136 ps and (c) 0.213 ps. The initial cell temperature was 300°C. Displaced atoms are coloured blue and the red ring indicates the thermal spike region.

A shock wave passes through the cell and displaces atoms, the effect if this can be seen in figure 5.3 (a). The shock wave results in four displaced atoms, figure 5.3 (b). Atoms continue to vibrate 0.136 ps into the cascade. This is due to the large initial kinetic energy given to the system. After the cell has stabilised, one defect has been formed (figure 5.3 (c)).

Low energy thermal spike simulations through diamond thus have very little effect on the final lattice. This is due to diamond's structure and the  $sp^3$  nature of bonding that keeps the atoms tightly bound. It is only at high energies that defects are seen in the final lattice. This is in stark contrast to thermal spike cascades through graphite.

### 5.1.1 Diamond Cascade Simulations

Diamond cascades are simulated using the same method as was used for graphite cascades (described in chapter 3). Results from preliminary simulations showed that diamond cascades are very different from graphite cascades.

Figure 5.4 shows a diamond cascade with an initial PKA energy of 500 eV, initial PKA direction  $x = 1$ ,  $y = 2$  and  $z = 1$  and cell temperature 300°C.

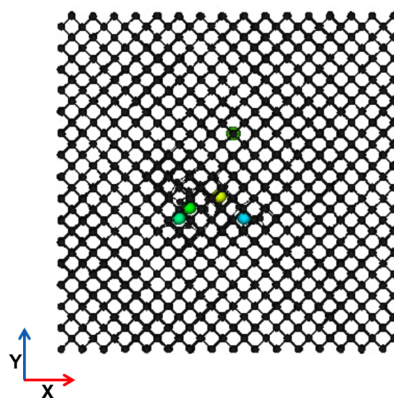


**Figure 5.4:** A diamond cascade with initial PKA energy of 500 eV after 2.316 ps, initial PKA direction  $x = 1$ ,  $y = 2$  and  $z = 1$ . The initial cell temperature was 300°C.

Figure 5.4 is a snap-shot of the final image in a diamond cascade. Due to the robustness of diamond, there are only a few defects present in the final cell. These are mainly localised around the original lattice position of the PKA. A shock wave can occur during diamond cascades resulting in atoms being displaced throughout the cell. The final cell took 0.21 ps to stabilise and contained five interstitials and vacancies.

#### Qualitative Results

Preliminary diamond cascade results did not behave in the same manner seen during cascade simulations in graphite. To produce comparisons of higher accuracy, diamond cascades were simulated using the same initial 20 directions selected for graphite cascades for energies up to 1000 eV. High range energies, 1500 and 2000 eV, were simulated across a selection of six initial PKA directions (identical to the graphite PKA directions). The six directions were selected to give a good representation of each possible primary direction available during a cascade simulation.

Low energy cascades through diamond were simulated at 25, 50, 75, 100 and 250 eV. There were no defects produced in any cascades with an initial PKA energy of 25 eV. This is because the initial kinetic energy given to the system is below the threshold energy for damage in diamond. The threshold displacement energy for diamond calculated during simulations in this chapter was found to be 50 eV. This value is further supported by work published by Wu *et al.* [104].

Figure 5.5 represents a low energy cascade through diamond.

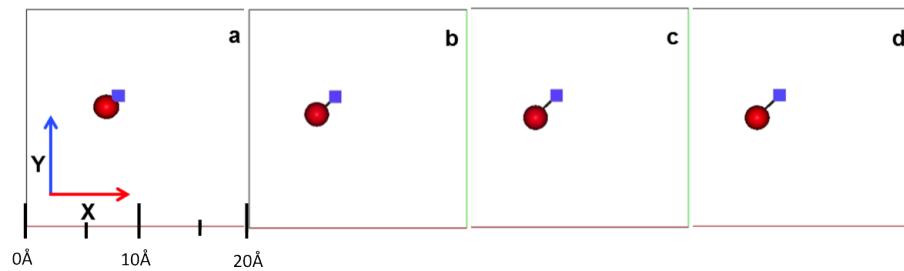


**Figure 5.5:** Diamond cascade with initial PKA energy 50 eV after: (a) 0.014 ps, (b) 0.032 ps, (c) 0.124 ps and (d) 0.621 ps. Initial PKA direction 1 from table 3.1. Initial cell temperature 300°C. The red circles denote interstitials and the blue squares denote vacancies. The path of the displaced atom is traced.

Figure 5.5 (a) shows the initial path of the PKA. The PKA continues to move around a fixed position in the cell for 0.124 ps, figures 5.5 (b) and (c). The kinetic energy of the PKA falls below its threshold energy resulting in an interstitial being formed, figure 5.5 (d).

Figure 5.6 tracks the number of displaced atoms at any given point of time during the simulation.

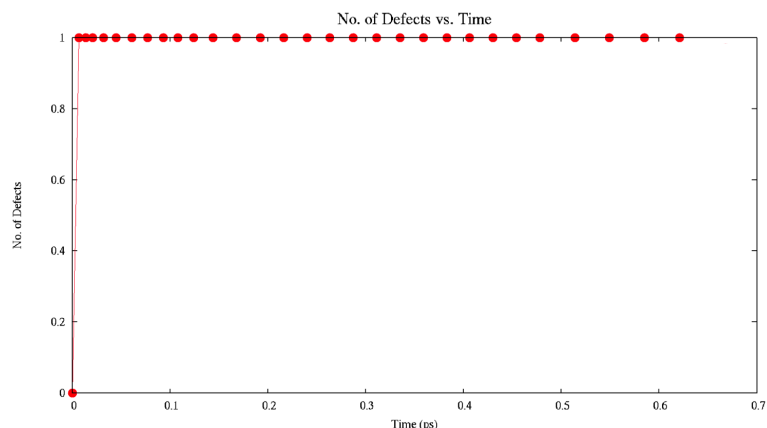


**Figure 5.6:** Graph indicating the number of defects present during a diamond cascade at 50 eV. Initial PKA direction 1 from table 3.1. The initial cell temperature was 300°C.

Figure 5.6 shows the PKA forms an interstitial almost instantaneously. The PKA does not possess further kinetic energy to cause cascades through the cell or to travel back to re-combine in its original lattice position. Therefore, one interstitial is present in the final lattice.

The distance travelled by displaced atoms is tracked in figure 5.7.

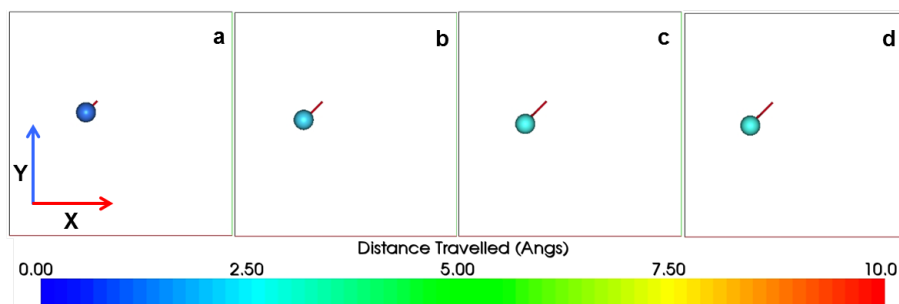


**Figure 5.7:** Diamond cascade with initial PKA energy 50 eV after: (a) 0.014 ps, (b) 0.032 ps, (c) 0.124 ps and (d) 0.621 ps. The colour of the scalar bar indicates the distance moved by atoms during the cascade. Initial PKA direction 1 from table 3.1. Initial cell temperature 300°C.

The initial displacement of the PKA can be seen in figure 5.7 (a). The PKA reaches its final displacement of 2.636 Å at 0.124 ps. Diamond cascade simulations at 50 eV produce very little, if any damage to the final lattice cell.

Cascade simulations at 50 eV had a maximum number of one defect present in the final lattice and 74% of the cascades had no defects at all. Low energy cascades through diamond with an initial kinetic energy of 75 eV resulted in a maximum number of one final defect being seen in 63% of cascade simulations.

The remaining 37% of cascades had no defects present after the simulation had stabilised. Cascades with an initial PKA energy of 100 eV had a maximum number of two defects in the final lattice cell. Over 70% of cascades had at least one defect present which was formed as a direct result of the collision cascade. The top end of the low energy cascades has been simulated employing an initial PKA energy of 250 eV. Cascades with an initial kinetic energy of 250 eV saw a maximum number of two defects present in the final lattice cell. Half of all the simulations with an initial PKA energy of 250 eV produced one defect whilst the other half produced two defects after the simulation had stabilised. There were no simulations at 250 eV where the lattice remained completely undamaged.

The average number of atoms displaced during a cascade ranges from zero to five during low energy simulations. Cascades with an initial PKA energy 25 eV have no displaced atoms during a cascade as there are no atoms present in the lattice with kinetic energy greater than the threshold displacement energy. On average there is a 48% difference between the total number of displaced atoms (where an atom has been removed from its initial position) and the final number of defects present in the lattice for cascades with initial energies less than 250 eV. Cascades with initial PKA energies of 50 and 75 eV have a maximum number of two displaced atoms whereas at 250 eV a maximum of five displaced atoms was observed. Cascade simulations at 250 eV had an average number of three displaced atoms during simulations.

During low energy cascades, the PKA does not tend to travel far from its original lattice position. The average final displacement of the PKA for cascades with initial energies between 50 and 100 eV lies in the range 0.7 to 2.3Å. PKA's from cascades with an initial kinetic energy of 25 eV have no final displacement as the initial kinetic energy given to the cell was below the threshold energy. All cascades with an initial PKA energy of 250 eV have a final PKA displacement greater than 0.25Å with an average PKA final displacement of 5.9Å. A maximum final displacement for the PKA of 9.7Å, was observed during a cascade at 250 eV. Further figures of low energy cascades in diamond are presented in Appendix II.

Mid-range energy cascades through diamond have been simulated at 500, 750 and 1000 eV.

Figure 5.8 is an example of a mid-range energy cascade through diamond.

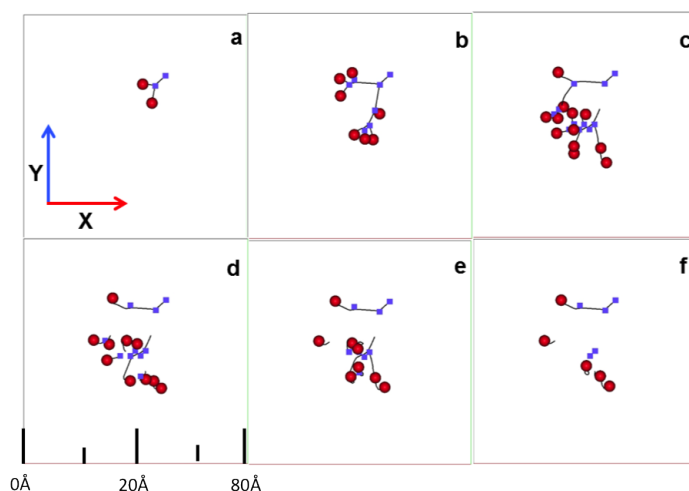


**Figure 5.8:** Diamond cascade with initial PKA energy 1000 eV after: (a) 0.005 ps, (b) 0.017 ps, (c) 0.037 ps, (d) 0.073 ps, (e) 0.155 ps and (f) 0.908 ps. Initial PKA direction 1 from table 3.1. Initial cell temperature 300°C. The red circles denote interstitials and the blue squares denote vacancies. The path of each displaced atom is traced.

A primary collision occurs 0.005 ps into the cascade resulting in two branches of the cascade being formed (figure 5.8 (a)). Displaced atoms continue to collide with atoms in the cell, figure 5.8 (b). Due to the structure of diamond, the branch cascades overlap (figures 5.8 (c) and (d)), an event not witnessed in graphite. Although a shock wave passes through the cell as a result of collisions, the kinetic energy present in the wave is insufficient to create further displaced atoms. As the simulation continues, the kinetic energy of the displaced atoms begins to fall below the threshold displacement energy resulting in displaced atoms re-combining in vacant sites or forming interstitials (figure 5.8 (e)). There are five interstitials and five vacancies present in the final cell (figure 5.8 (f)).

Figure 5.9 tracks the number of displaced atoms at any given point of time.

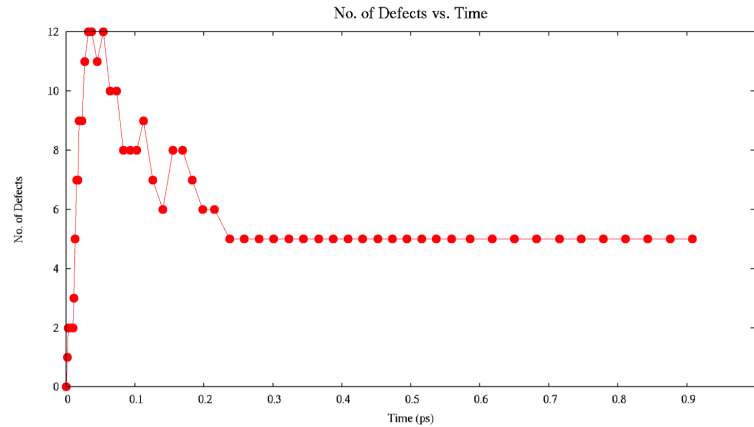


**Figure 5.9:** Graph indicating the number of defects present during a diamond cascade at 1000 eV. Initial PKA direction 1 from table 3.1. The initial cell temperature was 300°C.

The maximum number of 12 displaced atoms occurs 0.032 ps into the cascade. The split of the collision cascades results in atoms energies falling below the threshold energy at different times. This is highlighted by the varying number of defects present after the maximum number of defects and before the lattice stabilises.

The distance travelled by displaced atoms is shown in figure 5.10.

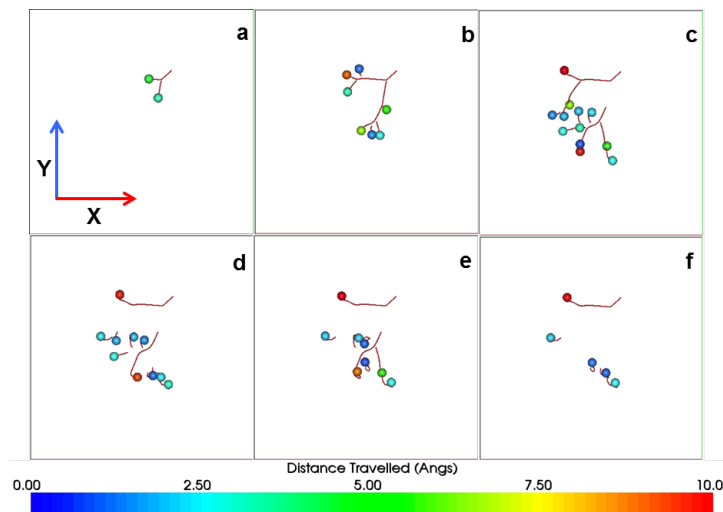


**Figure 5.10:** Diamond cascade with initial PKA energy 1000 eV after: (a) 0.005 ps, (b) 0.017 ps, (c) 0.037 ps, (d) 0.073, (e) 0.155 and (f) 0.908 ps. The colour of the scalar bar indicates the distance moved by atoms during the cascade. Initial PKA direction x1 from table 3.1. Initial cell temperature 300°C.

The path of the PKA can be traced through figures 5.10 (a), (b), (c), (d), (e) and

(f). Figure 5.10 (f) shows the final resting position of the PKA (the red atom, top of the cell) with a final displacement of  $9.66\text{\AA}$ . The atom displaced as a result of the primary collision with the PKA travels a distance of  $9.76\text{\AA}$  before coming to rest in a vacancy site (atom denoted in orange, figure 5.10 (e)). The distance travelled by displaced atoms during secondary cascades is less than  $5\text{\AA}$ .

Cascades with an initial PKA energy of 500 eV produced a minimum of two defects in the final lattice cell. The maximum number of defects formed during the cascades at 500 eV was five. Half of the simulations at 500 eV had three defects present after the cell had stabilised. Cascades with an initial PKA energy of 750 eV saw a greater spread in the final number of defects after the simulation had terminated. Two thirds of the simulations had either four or five defects present. The top end of the mid-range energy cascades were simulated using an initial PKA energy of 1000 eV. Results from cascades with an initial energy of 1000 eV saw a jump in the average maximum number of defects present to nine. All simulations had at least four defects present in the final lattice cell.

The maximum number of displaced atoms calculated during mid-range energy cascades lies in the range from three to 27. Each cascade has a different initial PKA direction and produces a unique cascade. Due to the uniqueness of the cascades, a range of values for the number of displaced atoms is calculated. The maximum number of displaced atoms occurring during a cascade with initial PKA energy of 500 eV is ten and the minimum is three. Results from cascades simulated at 1000 eV show a maximum of 27 for the number of displaced atoms. This is twice the size of the maximum number of displaced atoms found in the 750 eV cascades.

The values for the final displacement of the PKA range from a minimum of  $5\text{\AA}$  during a 500 eV cascade to  $34\text{\AA}$  during a 1000 eV cascade. The average final displacement of the PKA is  $12\text{\AA}$  during the 500 eV cascades. The final displacement of the PKA will depend on the energy transferred during collisions between the PKA and surrounding carbon atoms. At higher energies, the PKA has a higher kinetic energy, and hence tends to have a larger final displacement. The average final displacement of the PKA during 750 and 1000 eV cascades is  $15\text{\AA}$  and  $18\text{\AA}$  respectively. Further figures for mid-range energy cascades through diamond are presented in Appendix II.

High energy cascades have been simulated using initial energies of 1500 and

2000 eV.

Figure 5.11 is an example of a high energy cascade in diamond.

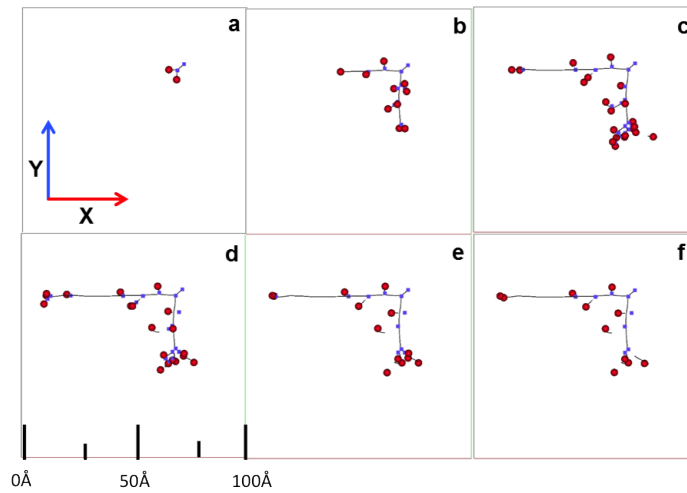


**Figure 5.11:** Diamond cascade with initial PKA energy 2000 eV after: (a) 0.003 ps, (b) 0.017 ps, (c) 0.038 ps, (d) 0.075 ps, (e) 0.146 ps and (f) 0.662 ps. Initial PKA direction 1 from table 3.1. Initial cell temperature was 300°C. The red circles denote interstitials and the blue squares denote vacancies. The path of each displaced atom is traced.

Figure 5.11 (a) shows the primary collision with the PKA and a second carbon atom in the lattice. The PKA continues in a path along the plane, colliding with surrounding atoms which in turn displace further atoms, figure 5.11 (b), (c) and (d). The PKA comes to rest forming an interstitial. The atom displaced as a direct result of the primary collision, travels normal to the plane colliding with atoms in the lattice and creating secondary cascades. Figure 5.11 (f) shows the final lattice after it has stabilised. There are now 11 interstitials and 11 vacancies present.

Figure 5.12 tracks the maximum number of atoms displaced as a function of time.

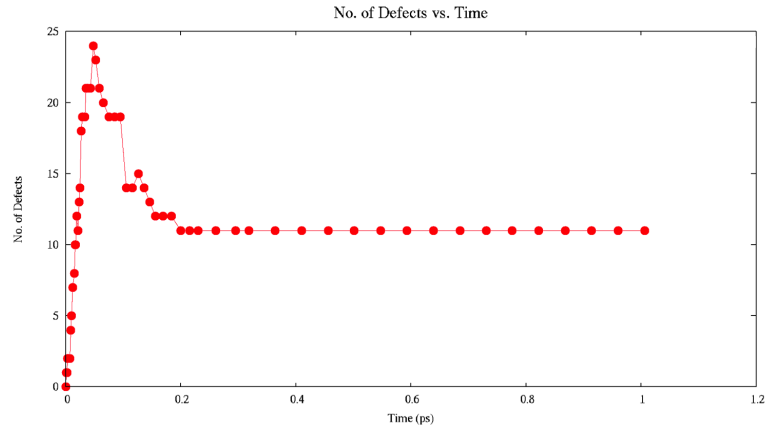


**Figure 5.12:** Graph indicating the number of defects present during a diamond cascade at 2000 eV. Initial PKA direction 1 from table 3.1. The initial cell temperature was 300°C.

The maximum number of 24 defects occurs 0.048 ps into the simulation. During the 2000 eV cascade, a greater number of defects is produced alongside the path of the PKA and the secondary displaced atom. There is only one cluster site present at the end of the secondary displacement atom's branch. This results in no further peaks of defect formation being present in figure 5.12. The simulation stabilised at 0.200 ps leaving 11 interstitials and 11 vacancies present in the cell.

Figure 5.13 displays the distance travelled by displaced atoms during a 2000 eV cascade.

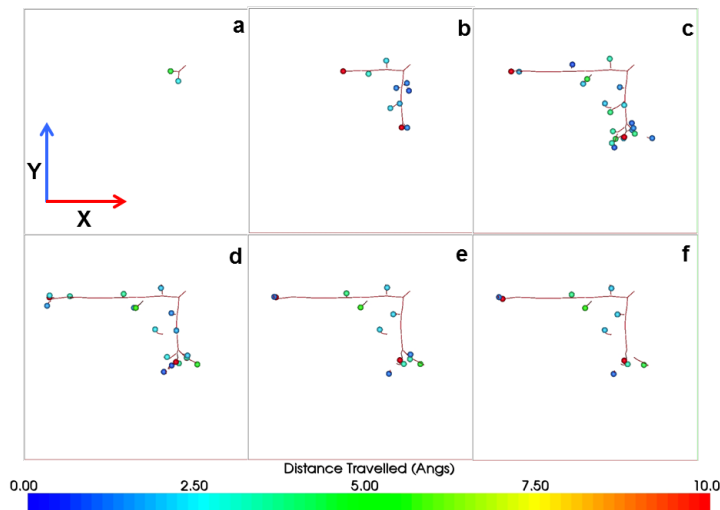


**Figure 5.13:** Diamond cascade with initial PKA energy 2000 eV after: (a) 0.003 ps, (b) 0.017 ps, (c) 0.038 ps, (d) 0.075, (e) 0.146 and (f) 0.662 ps. The colour of the scalar bar indicates the distance moved by atoms during the cascade. Initial PKA direction 1 from table 3.1. Initial cell temperature 300°C.

The PKA and the neighbouring atom displaced as a direct result of the initial collision with the PKA, are highlighted in figure 5.13 (f) as the two red atoms, both atoms have travelled a distance of over 30Å. Atoms displaced as a result of secondary collision cascades have been displaced by less than 5Å from their initial starting position. The final displacement of the PKA is 35.698Å.

High energy cascades have produced the greatest amount of damage to the overall structure of the initial cell. Simulations at 1500 eV had a minimum of six defects present and one third of the cascades have ten defects present after the lattice had stabilised. Over 80% of cascades simulated at 2000 eV had over eight defects present in the final cell. The maximum number of final defects seen in a 2000 eV cascade through diamond was 11.

The maximum number of displaced atoms during a high energy cascade is on average 44% larger than the final number of defects present in the final lattice cell. At 2000 eV, the average number of atoms displaced as a direct result of the collision cascade is 24 compared to 18 at 1500 eV. There is a greater range in the number of displaced atoms at higher energies. The maximum number of displaced atoms lies in the range 12 to 24 for 1500 eV cascades and 14 to 33 for 2000 eV cascades.

The final displacement of the PKA is greatest during high energy cascades in diamond. During 1500 eV cascades, the average final displacement of the PKA

was  $18\text{\AA}$ . The PKA can penetrate further through the cell due to the increase in initial kinetic energy given to the PKA. Cascades with an initial PKA energy of 2000 eV witness a final displacement of the PKA at  $49\text{\AA}$ . This is the maximum value seen across all the diamond simulations. The average distance travelled by the PKA during cascades with an initial energy of 2000 eV is  $37\text{\AA}$ .

Further figures for high energy cascades through diamond are presented in Appendix II.

Cascades in diamond thus produce interstitials and vacancies which have previously been seen in simulations and experimental research [105]. The split interstitial was the most common defect seen in cascade simulations presented in this chapter. Figure 5.14 is an example of a split interstitial formed in diamond.

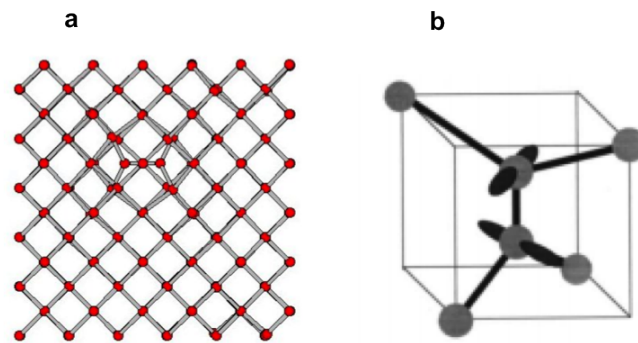


**Figure 5.14:** (a) Split interstitial as seen in EDIP cascades presented in this thesis. (b) Split interstitial as seen in electron irradiation experiments (*D. C. Hunt, et al., Physical Review B* **61**, 3863 (2000)) [105].

Figure 5.14 is a split interstitial which was formed as the result of a cascade simulation. The split interstitial has a formation energy of approximately 7eV [105]. This is the lowest interstitial formation energy seen in diamond.

## Quantitative Cascade Data

Statistical sampling of data from diamond simulations has been performed for 20 directions with energies up to and including 1000 eV and 6 directions with energies above 1000 eV up to and including 2000 eV. Table 5.1 shows the average number of defects present in the final cell after a cascade through diamond with an initial PKA energy between 25 and 1000 eV.

Initial PKA Energy (eV)	$N_{defects}$
25	0
50	0.263
75	0.632
100	0.842
250	1.526
500	2.895
750	4.600
1000	5.800

**Table 5.1:** The average number of defects present in the final lattice after a cascades through diamond with initial PKA energies up to 1000 eV. The initial cell temperature was 300°C.

Six of the directions were also simulated with high initial PKA energies. The average final number of defects present was 8.167 for 1500 eV and 10.0 for 2000 eV.

The average number of defects present in the final cell for energies up to 1000 eV along with values calculated for high energies is presented in graphical form in figure 5.15.

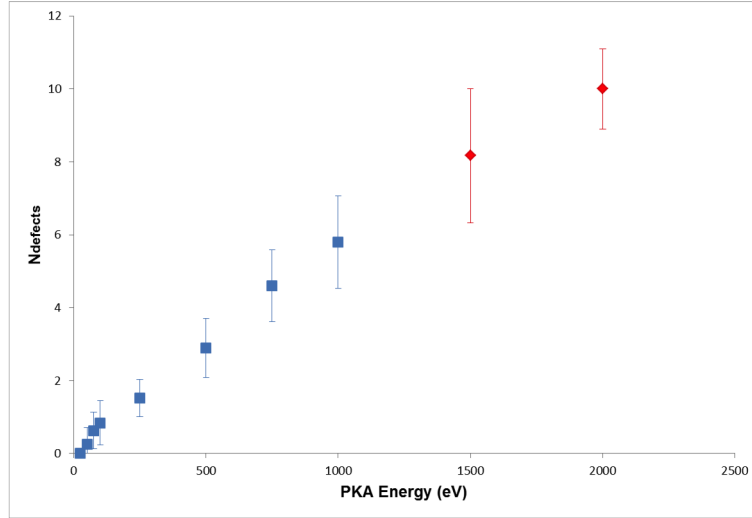


**Figure 5.15:** Average number of defects present in final lattice as a function of energy. Error bars denote one standard deviation.

Figure 5.15 shows a roughly linear trend, the number of defects in the final cell increases as the initial PKA energy increases. The equation for the linear trend line can be seen in equation 5.1.

$$N_{defects}(E) = 0.0053E \quad (5.1)$$

where  $E$  is the initial PKA energy.

Table 5.2 shows the average maximum number of displaced atoms at a given energy.

Initial PKA Energy (eV)	Max $N_{defects}$
25	0.000
50	0.579
75	1.263
100	1.789
250	3.053
500	6.895
750	9.733
1000	12.867

**Table 5.2:** The average maximum number of displaced atoms during cascaded through diamond with initial PKA energies up to 1000 eV. The initial cell temperature was 300°C.

The average maximum number of displaced atoms calculated across six of the directions was 17.833 for 1500 eV and 24.667 for 2000 eV.

Figure 5.16 shows the average maximum number of displaced atoms during low and high energy cascades.

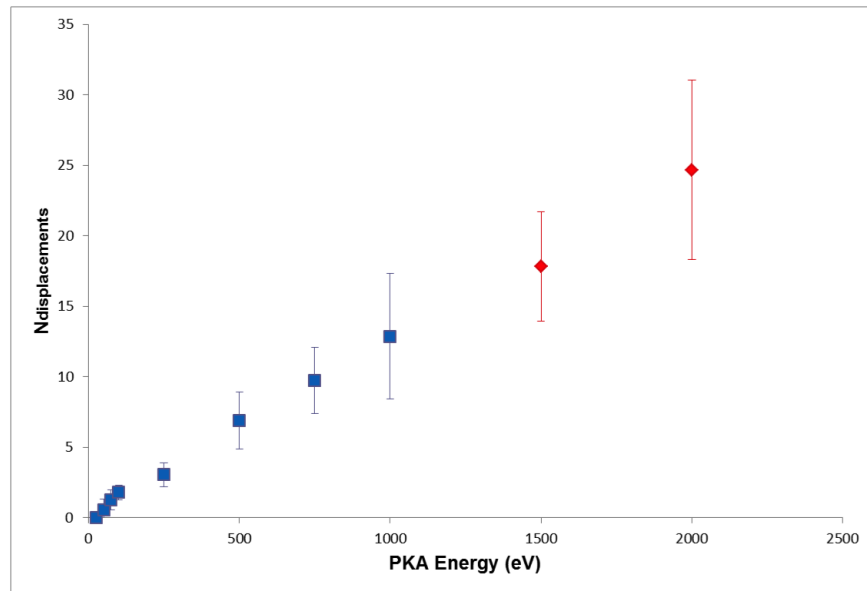


**Figure 5.16:** The maximum number of defects produced as a function of energy. Error bars denote one standard deviation.

The number of displaced atoms increases as the initial PKA energy increases. Equation 5.2 is the linear equation for the graph in figure 5.16. The intercept is set to zero as there can be no displaced atoms if there is no initial energy given to the cell.

$$N_{displacements} = 0.0124E \quad (5.2)$$

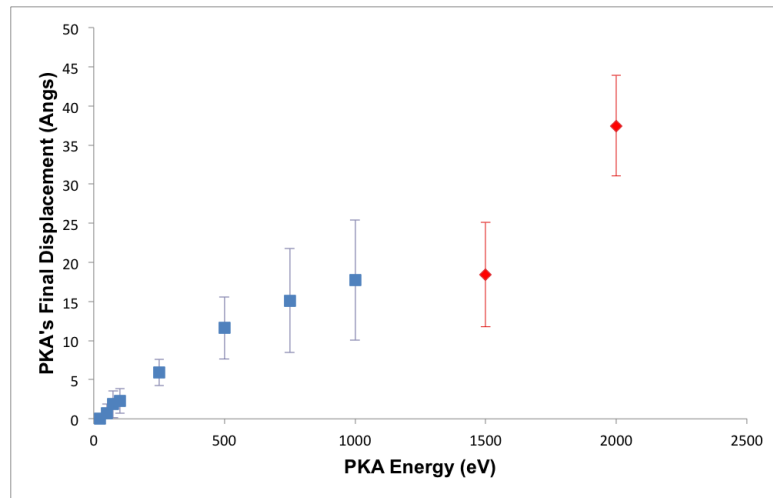
where  $E$  is the initial PKA energy.

Table 5.3 shows the average final displacement,  $x$ , of the PKA.

Initial PKA Energy (eV)	Final PKA Displacement (Å)
25	0.000
50	0.678
75	1.856
100	2.267
250	5.917
500	11.623
750	15.082
1000	17.726

**Table 5.3:** The final displacement of the PKA in diamond cascades with initial PKA energies up to 1000 eV. The initial cell temperature was 300°C.

High energy cascades produced on average a final displacement of 17.844 Å and 37.456 Å for 1500 and 2000 eV cascades respectively. The average final displacement of the PKA during cascades for high and low initial PKA energies is presented in figure 5.17.



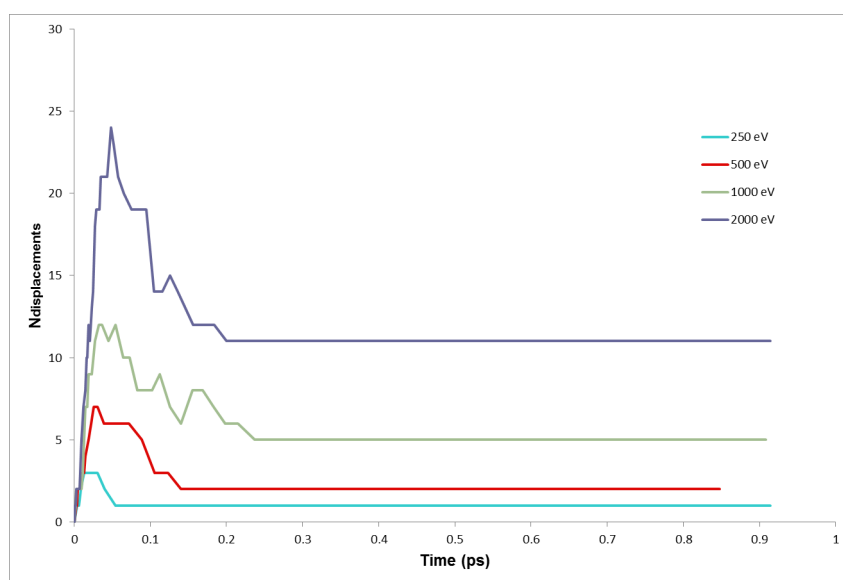
**Figure 5.17:** The final displacement of the PKA as a function of energy. Error bars denote one standard deviation.

Figure 5.17 can be analysed in three stages; there is a linear trend up to an initial PKA energy of 500 eV. The mid-range energy region, 500 and 1000 eV, sees a gradual increase in the final displacement of the PKA. At high energies, the difference between the final PKA displacement at 1500 and 2000 eV is almost doubled.

Figure 5.17 shows a linear increase in the final displacement of the PKA up

to 750 eV. PKA's in cascades with an initial energy between 750 and 1500 eV have very similar final displacements. The similarity of displacements between these energies could be a result of a high energy collision during the cascade. The PKA would have less energy after a high energy collision and would therefore not be able to travel as far through the lattice. There is a 50% increase in the average final displacement of the PKA during 1000-1500 eV cascades and 2000 eV cascades. PKA's have the ability to penetrate further through the lattice during 2000 eV cascades because of the large initial energy given to the PKA.

Figure 5.18 shows the maximum number of displaced atoms during a cascade at a given initial energy.



**Figure 5.18:** The maximum number of displaced atoms as a function of time. Cascades have an initial PKA direction  $x = 0.737604927$ ,  $y = -0.675232531$  and  $z = 0.00$ . The initial cell temperature was  $300^{\circ}\text{C}$ .

Figure 5.18 highlights how a greater initial PKA energy results in a higher number of atoms being displaced. The time a simulation takes to stabilise increases as the initial PKA energy increases. Low energy cascades (energies below 250 eV) are stable 0.05 ps after the cascade began. Mid-range cascades (e.g. 500 eV) take on average 0.15 ps to stabilise and high energy cascades (e.g. 2000 eV) take 0.25 ps to stabilise. Figure 5.18 shows the maximum number of displaced atoms occurring during a simulation increases as the initial PKA energy is increased. Each time the initial PKA energy was doubled, in simula-

tions presented in figure 5.18, the maximum number of displaced atoms was also doubled.

Unlike graphite, cascades in diamond are not directionally dependent and tend to be localised around the initial PKA position. This is due to the cubic symmetry and tight  $sp^3$  bonding present in diamond. There is also the presence of a shock wave in diamond cells which is not observed in graphite cascades. Cascades in diamond are similar to those seen in metals thus highlighting the uniqueness of graphite cascades. A full comparison between graphite and diamond can be seen in Chapter 6.

## 5.2 Amorphous Carbon Analysis

Amorphous carbon does not have any crystalline structure and is found in impure forms of carbon (e.g., coal and soot) [36]. Amorphous carbon has both  $sp^2$  and  $sp^3$  bonds. It also has localised  $\pi$  electrons. Simulations undertaken for this report include high density amorphous carbon, with a density of 3.0g/cc and low density amorphous carbon, with a density of 2.0g/cc. The initial cells were created using the method explained in Chapter 3, section 3.2.4.

### 5.2.1 High Density Amorphous Carbon

High density amorphous carbon (3.0g/cc) is simulated with an initial energy of 500 eV. The simulation ran for 0.292ps before stabilising. Figure 5.19 show a snap-shot of the final image.

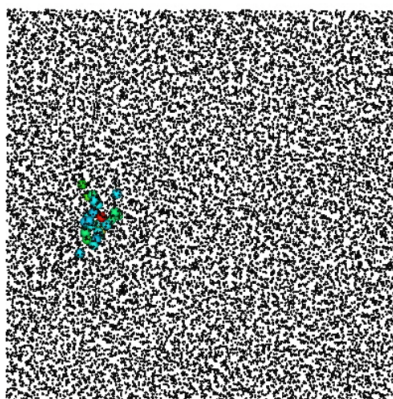


**Figure 5.19:** A snap-shot of the final image during a high density amorphous (3.0g/cc) cascade. The initial PKA energy is 500 eV and initial PKA direction  $x = 1$ ,  $y = 2$  and  $z = 1$ . The initial temperature was set to 300°C. Coloured atoms denote displaced atoms.

The displaced atoms in figure 5.19, appear to be larger than other atoms in the structure. However, this is not the case. Due to the sheer volume of atoms present in amorphous carbon, the displaced atoms have been enlarged and coloured to enable the human eye to identify them. High density carbon cascades, figure 5.19, produce localised collisions. This occurs because high density amorphous carbon has a very compact structure.

With each collision, energy transfer occurs. The more collisions that occur, the less energy is transferred within a collision. Due to the high density of

the material the PKA collided with another atom almost instantly. The initial collision caused a cascade of collisions to take place. However, the cascade did not have enough kinetic energy to penetrate the whole cell due to the large volume of atoms compacted closely together. Displaced atoms can thus only be located near the initial PKA position.

Cascades in amorphous carbon at 500 eV do not affect the whole cell. Unlike graphite, cascades are not directionally dependent and they are localised to the initial PKA position. Due to the structure of high density amorphous carbon, it is difficult to determine if a displaced atom has formed a defect or has recombined with the lattice. It is for this reason, simulations of high and low density amorphous carbon highlight the number of displaced atoms instead of the number of defects.

To accurately compare high density amorphous carbon to graphite, simulations were undertaken with three of the initial PKA directions selected for graphite. Figure 5.20 is an example of a cascade through high density amorphous carbon with an initial PKA energy 50 eV. The distance travelled by each displaced atom is tracked.

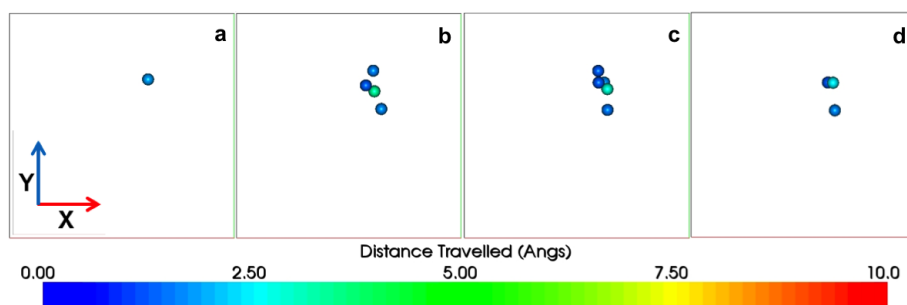


**Figure 5.20:** High density amorphous carbon cascade with initial PKA energy 50 eV after: (a) 0.007 ps, (b) 0.045 ps, (c) 0.108 ps and (d) 2.259 ps. Initial PKA direction 1 from table 3.1. The colour of the scalar bar indicates the distance moved by atoms during the cascade. Initial cell temperature 300°C.

The distance travelled by displaced atoms during a 50 eV cascade through high density amorphous carbon is less than 3Å. Figure 5.20 (d) shows the final lattice after the cascade has stabilised. The final displacements of the three atoms in figure 5.20 (c) are less than 2.50Å.

Every cascade over 25 eV has resulted in the displacement of atoms. Displaced atoms in cascades simulated within the energy range 25 - 100 eV all had a final displacement less than 3.5Å.

Figure 5.21 is an example of a cascade through high density amorphous carbon with an initial PKA energy 500 eV.

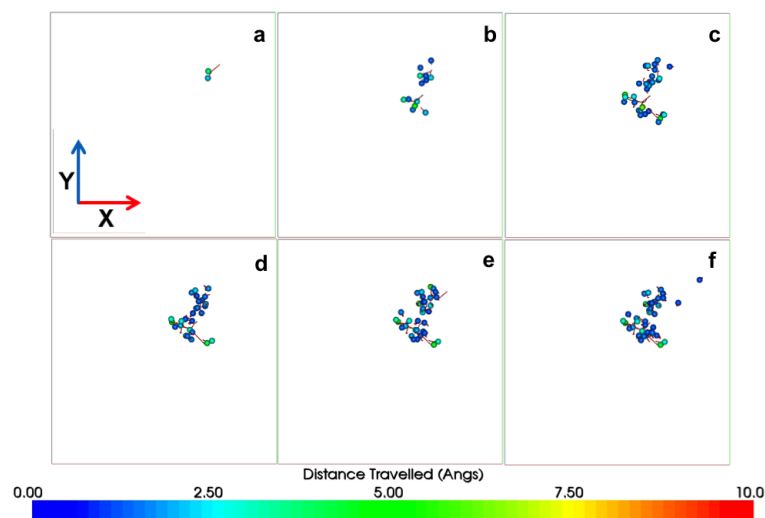


**Figure 5.21:** High density amorphous carbon cascade with initial PKA energy 500 eV after: (a) 0.006 ps, (b) 0.034 ps, (c) 0.068 ps, (d) 0.201 ps, (e) 0.337 ps and (f) 1.541 ps. Initial PKA direction 1 from table 3.1. The colour of the scalar bar indicates the distance moved by atoms during the cascade. Initial cell temperature 300°C.

The initial PKA travels  $1.0\text{\AA}$  through the cell before colliding with a neighbouring carbon atom. Displaced atoms travel an average distance of  $0.75\text{\AA}$  from their initial lattice positions. Figure 5.21 (f) shows the final stabilised lattice where there are 45 displaced atoms present. The maximum distance travelled by a displaced atom is  $5\text{\AA}$ .

Cascades within the energy range 250 - 500 eV have produced a minimum of 11 displaced atoms in the final cell. The maximum number of displaced atoms occurring during a 500 eV cascade is 53. Displaced atoms form in a single cluster close to the initial PKA site. The final displacement of atoms during cascades at 250 and 500 eV is always less than  $5\text{\AA}$ .

Figure 5.22 is an example of a cascade through high density amorphous carbon with an initial PKA energy of 2000 eV.

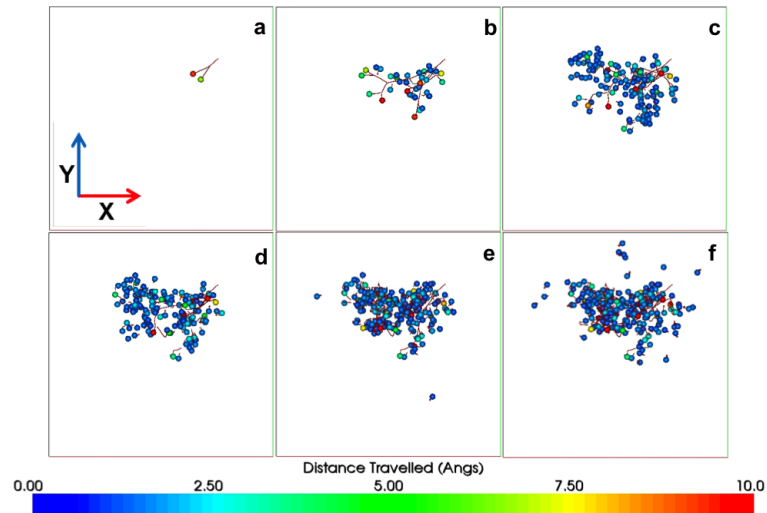


**Figure 5.22:** High density amorphous carbon cascade with initial PKA energy 2000 eV after: (a) 0.007 ps, (b) 0.030 ps, (c) 0.074 ps, (d) 0.120 ps, (e) 0.782 ps and (f) 1.943 ps. Initial PKA direction 1 from table 3.1. The colour of the scalar bar indicates the distance moved by atoms during the cascade. Initial cell temperature 300°C.

At high energies, cascades through high density amorphous carbon continue to form in a cluster. Figures 5.22 (a) and (b) show the initial displacement of the PKA is greater than 10Å. The PKA and atoms displaced as a result of initial collisions travel further through the cell than atoms displaced in a later collision. This is due to the large initial kinetic energy given to the PKA. Over 70% of displaced atoms in the final lattice, figure 5.22 (f), have a final displacement of less than 2Å. The majority of atoms do not travel far from their initial lattice position. The maximum number of displaced atoms during the cascade was 267.

Quantitative cascade data for high density amorphous carbon has been taken over three initial PKA energies ranging between 25 - 500 eV. The initial energy range was selected so further comparisons are practical between high and low density amorphous carbon.

The maximum number of displaced atoms occurring during cascades through high density amorphous carbon is presented in figure 5.23.

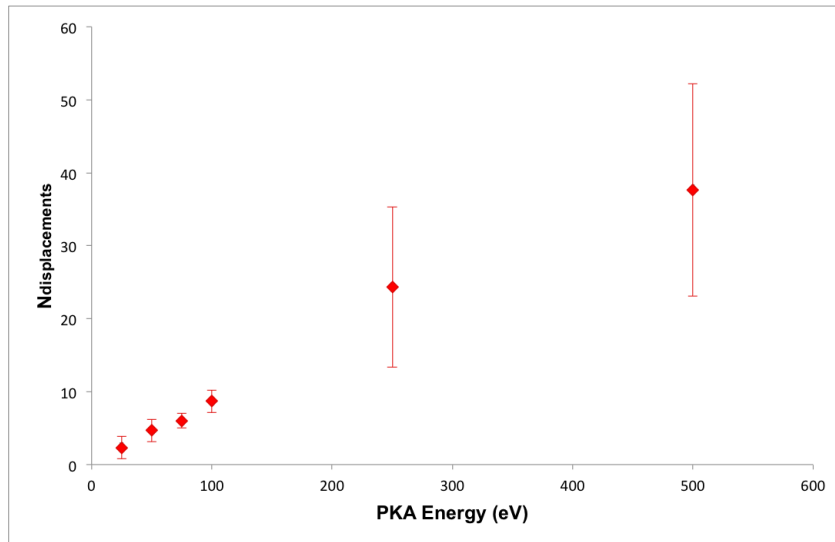


**Figure 5.23:** The maximum number of displaced atoms as a function of energy. Error bars denote one standard deviation. The initial cell temperature was 300°C.

The graph in figure 5.23 highlights the fact that the number of displaced atoms increases as the initial PKA energy increases. The average number of displaced atoms during cascades through high density amorphous carbon shows a linear trend presented in equation 5.3.

$$N_{displacements} = 0.0801E \quad (5.3)$$

where  $E$  is the initial PKA energy.

## 5.2.2 Low Density Amorphous Carbon

Damage in low density amorphous carbon (2.0g/cc) was simulated under the same conditions as the graphite cascades. Figure 5.24 is a snap-shot of the final lattice after a cascade through low density amorphous carbon with an initial PKA energy of 500 eV, initial PKA direction  $x = 1$ ,  $y = 2$  and  $z = 1$  has stabilised.

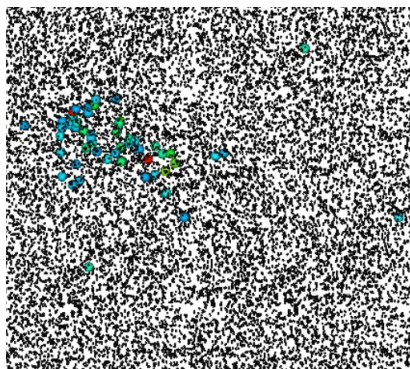


**Figure 5.24:** A snap-shot of the final image during a low density amorphous (2.0g/cc) cascade. The PKA is given an initial energy of 500 eV and initial direction  $x = 1$ ,  $y = 2$  and  $z = 1$ . The initial temperature was set to 300°C. Coloured atoms denote displaced atoms.

The low density carbon produced cascades mainly localised to the PKA collision origin. However, movement of other atoms around the cell can also be seen. This is partially due to the result of shock waves passing through the cell. The shock wave is similar to those seen in diamond. The shock waves do not have a major effect on the overall structure. Atoms are further displaced as a direct result of collision cascades during the simulation. The structure of low density amorphous carbon is such that atoms travelling on a certain path can move a distance in the cell before colliding with a subsequent atom. This phenomenon has also been seen in graphite due to the layers of graphene.

Three initial PKA directions from graphite have been selected and simulated in low density carbon so an accurate comparison can be made. Due to the high volume of displaced atoms occurring in low density amorphous carbon cascades, energies in the range of 25 - 500 eV have been simulated. Figure 5.25 is an example of a cascade through low density amorphous carbon with an initial PKA energy 50 eV.

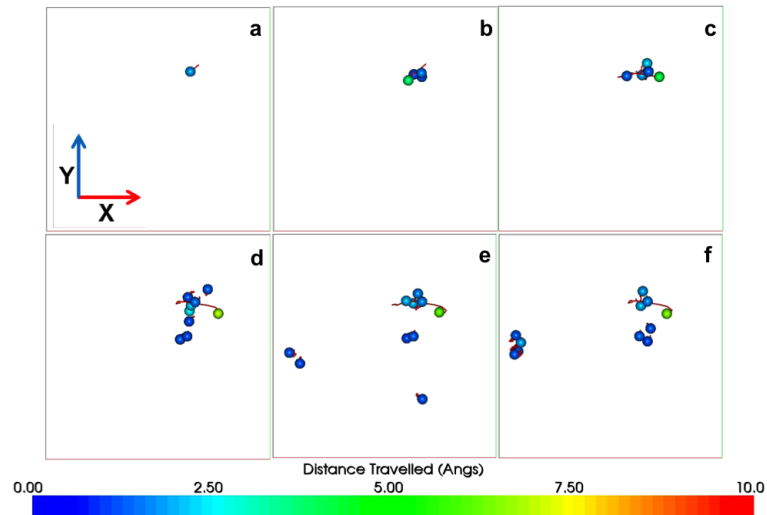


**Figure 5.25:** Low density amorphous carbon cascade with initial PKA energy 50 eV after: (a) 0.007 ps, (b) 0.026 ps, (c) 0.83 ps, (d) 0.155 ps, (e) 0.441 ps and (f) 2.621 ps. Initial PKA direction 1 from table 3.1. The colour of the scalar bar colour indicates the distance moved by atoms during the cascade. Initial cell temperature 300°C.

The collision cascade remains local to the initial PKA site until 0.441 ps, figure 5.25 (e). The displacement of atoms outside the initial cluster is due to a shock wave passing through the lattice. The shock wave was created as a direct response to the initial collision. The initial collisions sent vibrations through the cell which have resulted in the displacement of atoms outside of the cluster. Throughout the simulation, a maximum of 15 atoms were displaced. Figure 5.25 (d), (e) and (f) show the average distance travelled by atoms in the cluster is 1Å. Due to the structure of low density amorphous carbon, a few atoms can travel a short distance through the lattice before colliding with another carbon atom. This results in final displacements of 5Å being observed (figure 5.25 (f)). Cascades with energies ranging from 25 - 100 eV saw a maximum of 25 atoms displaced. The average number of displaced atoms occurring in cascades at 100 eV was double the number observed in 25 eV cascades. Displaced atoms are mainly found in a cluster near to the original PKA position. Less than 20% of atoms displace outside of the main cluster in cascades with initial PKA energy in the range of 25 - 100 eV. The average final displacement of atoms in cascades with an initial energy below 100 eV is 2Å.

Figure 5.26 is an example of a cascade through low density amorphous carbon with an initial energy of 500 eV.

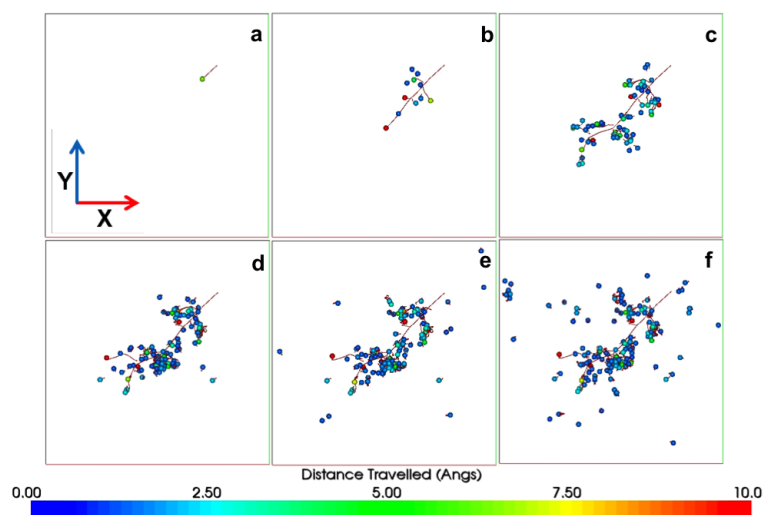


**Figure 5.26:** Low density amorphous carbon cascade with initial PKA energy 500 eV after: (a) 0.007 ps, (b) 0.040 ps, (c) 0.104 ps, (d) 0.359 ps, (e) 0.974 ps and (f) 2.491 ps. Initial PKA direction 1 from table 3.1. The colour of the scalar bar indicates the distance moved by atoms during the cascade. Initial cell temperature 300°C.

Figure 5.26 (a) shows the initial path of the PKA. After 0.040 ps, there is evidence of secondary collision cascades (figure 5.26 (b)). Figures 5.26 (c) and (d) show the formation of main cluster site. A shock wave is created as a direct result of initial collisions. The shock wave has created further displaced atoms which can be seen in figures 5.26 (e) and (f). The maximum number of displaced atoms was 218.

The PKA has travelled 3Å from its initial lattice site after 0.007 ps, figure 5.26 (a). Figure 5.26 (b) shows atoms displaced as a direct result of an initial collision travel further through the cell. The final displacement of atoms in the main cluster is on average less than 1Å. Evidence can be seen in figures 5.26 (d), (e) and (f). Figure 5.26 (f) highlights displaced atoms away from the main defect cluster, all of which have a final displacement of less than 1Å.

Cascades with energies ranging from 250 - 500 eV saw a maximum of 218 atoms displaced during the cascade. The majority of displaced atoms occurred in a cluster. On average, a quarter of displaced atoms occurred away from the main clusters. Atoms displaced outside the clusters are formed from a combination of displaced atoms travelling through the cell without colliding with another carbon atom and the effects of a shock wave. Displaced atoms do not travel far from their original lattice site. In cascades with energies of the range 250 - 500 eV, the average distance travelled by a displaced atom is 1Å.

Quantitative cascade data for low density amorphous carbon has been taken over three initial PKA energies with initial PKA energies ranging from 25 - 500 eV.

Figure 5.27 presents the maximum number of displaced atoms occurring during cascades through low density amorphous carbon.

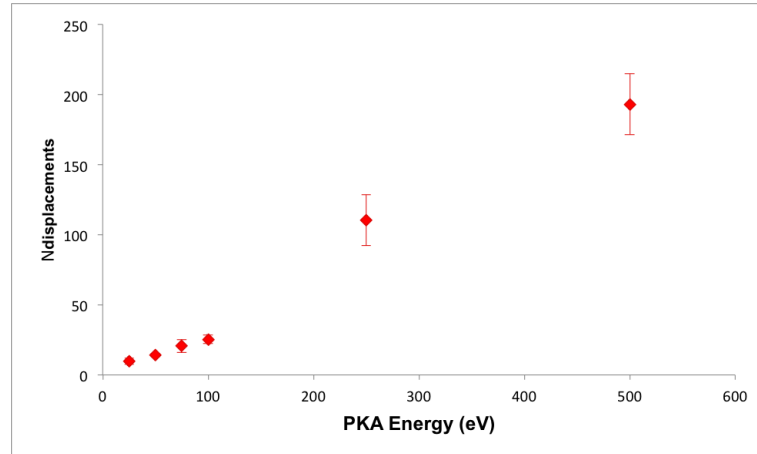


**Figure 5.27:** The maximum number of displaced atoms as a function of energy. Error bars denote one standard deviation.

Figure 5.27 highlights how the number of displaced atoms increases as the initial PKA energy increases. The average number of displaced atoms in the lattice cell at 25 eV is nine compared to 193 in cascades with an initial energy of 500 eV. There is a 95% increase in the average number of displaced atoms in the final lattice cell at 25 eV compare to 500 eV. Low density amorphous carbon cascades have not produced one final lattice cell without any atoms being displaced when simulated with an initial energy of 25 eV or greater. The average number of displaced atoms during cascades through high density amorphous carbon shows a linear trend presented in equation 5.4.

$$N_{displacements} = 0.3898E \quad (5.4)$$

where  $E$  is the initial PKA energy.

### 5.3 Glassy Carbon Analysis

The final material to be analysed is glassy carbon. Glassy carbon is 100%  $sp^2$  bonded which makes it ideal to compare to graphite [37]. Glassy carbon has a high temperature resistance and high purity; it also has a low density and low electrical resistance. It is a very hard material, has a low thermal resistance to chemical attack and is impermeable to gases and liquids. Glassy carbon should not be confused with amorphous carbon because it consists of two-dimensional structural elements and does not exhibit 'dangling bonds'.

Figure 5.28 is an example of a cascade in glassy carbon, the blue atom is the PKA (this can be seen within the blue ring).

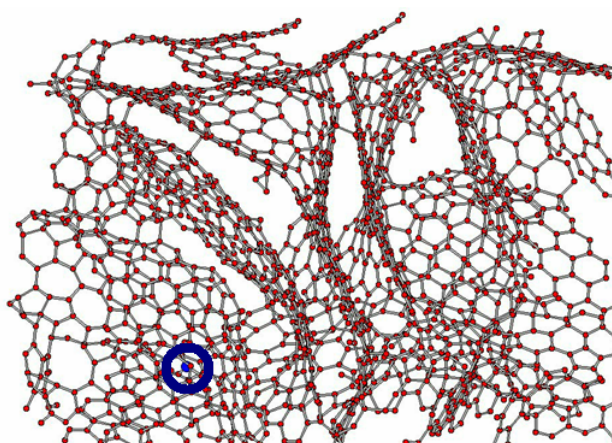


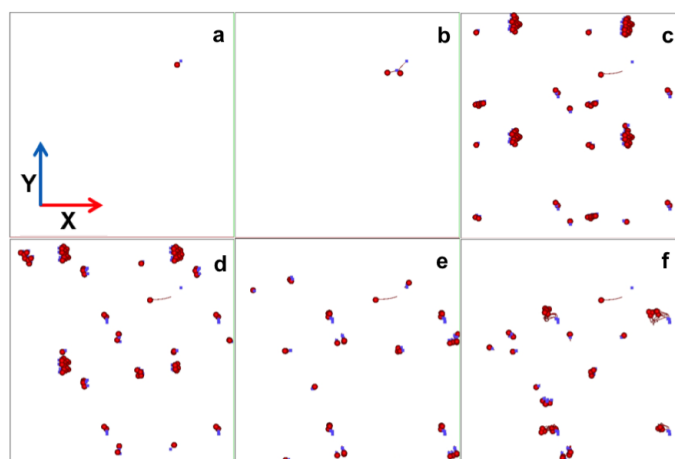
**Figure 5.28:** A snap-shot from a glassy carbon cascade, the blue ring denotes the initial position of the PKA. The initial PKA direction was:  $x = 1$ ,  $y = 2$  and  $z = 1$  and the initial PKA energy was 250 eV. The initial cell temperature was 300°C.

The structure of glassy carbon means there are a lots of empty spaces where displaced atoms can pass through without colliding with another atom. During a collision, the PKA's direction can be altered. If the PKA's direction is altered, it is then free to move through the cell creating further cascades. Atoms displaced as a result of the cascades obtain kinetic energy transferred through the collision. The displaced atoms are then free to travel through the cell creating further cascades which results in the formation of interstitials and vacancies.

Atoms can travel further during glassy carbon cascades without causing collisions because of the high amount of vacant space. It is for this reason that a cascade simulation in glassy carbon produces displaced atoms all over the

structure and not just concentrated around the initial PKA position.

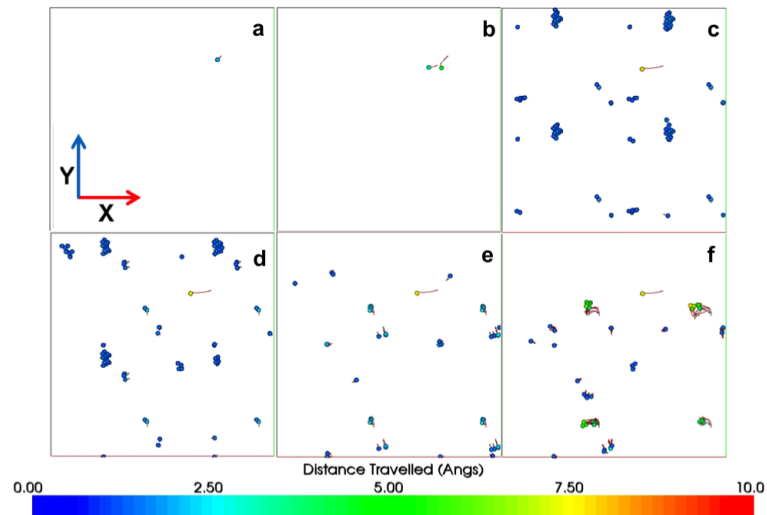
To compare glassy carbon to graphite, it has been simulated in an initial direction seen in graphite cascades. Figure 5.29 is an example of a cascade through glassy carbon with an initial PKA energy of 50 eV.



**Figure 5.29:** A typical glassy carbon cascade with initial PKA energy 50 eV after: (a) 0.007 ps, (b) 0.037 ps, (c) 0.230 ps, (d) 0.337 ps, (e) 0.587 ps and (f) 2.624 ps. Initial PKA direction 1 from table 3.1. Initial cell temperature 300°C. The red circles denote interstitials and the blue squares denote vacancies, the path of each displaced atom is traced.

Figures 5.29 (a) and (b) show the initial path of the PKA and the primary collision. Due to the structure of the material, displaced carbon atoms can pass through the lattice without colliding with any other atoms. Vibrations are carried through the cell in the form of a shock wave. The shock wave displaces atoms which are not necessarily near the initial PKA site. Evidence of this can be seen in figures 5.29 (c), (d), (e) and (f). There are 50 interstitials and vacancies present in the lattice after the simulation has stabilised.

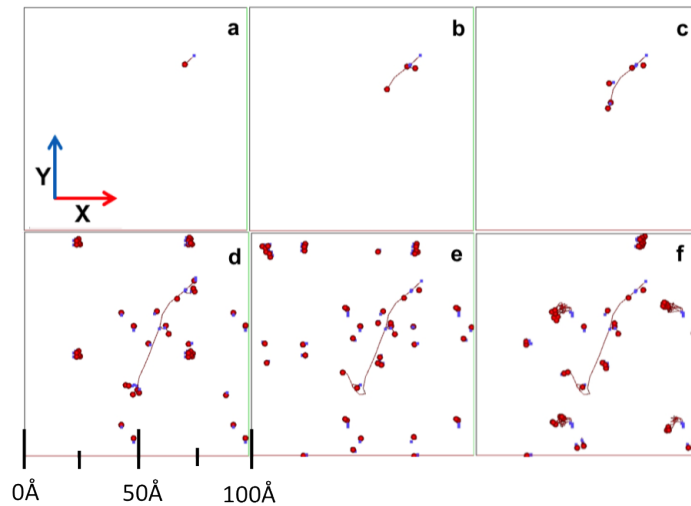
Figure 5.30 tracks the distance travelled by displaced atoms.



**Figure 5.30:** Glassy carbon cascade with initial PKA energy 50 eV after: (a) 0.007 ps, (b) 0.037 ps, (c) 0.230 ps, (d) 0.337 ps, (e) 0.587 ps and (f) 2.624 ps. Initial PKA direction 1 from table 3.1. The colour of the scalar bar indicates the distance moved by atoms during the cascade. Initial cell temperature 300°C.

Figure 5.30 (b) shows the primary collision between the PKA and a carbon atom in the lattice. The displacement of the PKA and the displaced carbon atom 0.037 ps into the cascade are 4.5Å and 5Å respectively. The displaced carbon atom has the greatest displacement along the z plane. The PKA has a final displacement of 7.5Å. The initial distance travelled by atoms displaced as a result of the shock wave was 0.4Å. Figure 5.30 (f) shows the final equilibrated lattice, the average distance travelled of atoms displaced by the shock wave is now 4Å.

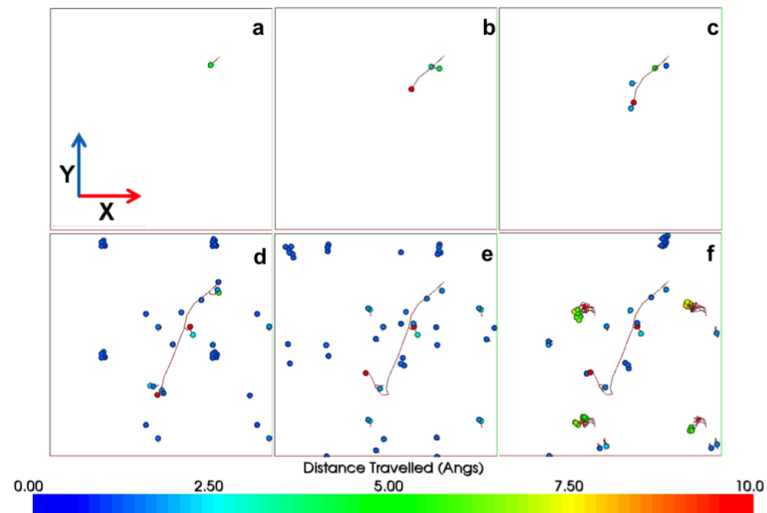
An example of a cascade through glassy carbon with an initial PKA energy of 250 eV is presented in figure 5.31.



**Figure 5.31:** Glassy carbon cascade with initial PKA energy 250 eV after: (a) 0.007 ps, (b) 0.032 ps, (c) 0.047 ps, (d) 0.147 ps, (e) 0.392 ps and (f) 3.448 ps. Initial PKA direction 1 from table 3.1. Initial cell temperature 300°C. The red circles denote interstitials and the blue squares denote vacancies. The path of each displaced atom is traced.

Figures 5.31 (a), (b) and (c) show the initial path and collisions of the PKA. The PKA collides with surrounding carbon atoms as it travels through the cell resulting in the formation of defects. A shock wave initiated by collision cascades passes through the cell creating further defects, figures 5.31 (d), (e) and (f). The final stabilised lattice, figure 5.31 (f), shows that the defects are spread across the whole cell and not clustered together as seen in the high and low density amorphous carbons. There are 59 interstitials and vacancies present in the final cell.

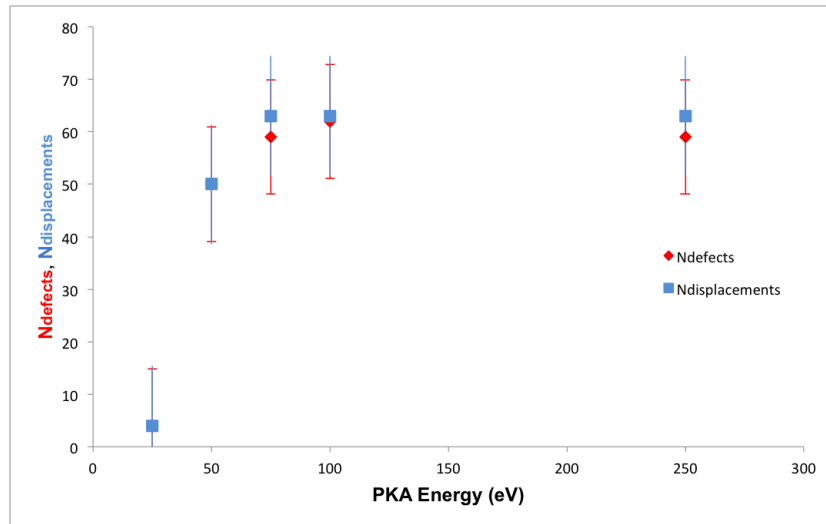
Figure 5.32 tracks the distance travelled by displaced atoms.



**Figure 5.32:** Glassy carbon cascade with initial PKA energy 250 eV after: (a) 0.007 ps, (b) 0.032 ps, (c) 0.047 ps, (d) 0.147 ps, (e) 0.392 ps and (f) 3.448 ps. Initial PKA direction 1 from table 3.1. The colour of the scalar bar indicates the distance moved by atoms during the cascade. Initial cell temperature 300°C.

The PKA travels over  $10\text{\AA}$  during the simulation, figure 5.32 (f). Atoms displaced due to the shock wave initially had a displacement less than  $1\text{\AA}$  as seen in figures 5.32 (d) and (e). As the simulation continued, the distance travelled by the displaced atoms increased. Figure 5.32 (f) shows the final stabilised lattice, displaced atoms have travelled on average  $5\text{\AA}$  from their initial lattice position.

Figure 5.33 presents the number of defects observed in the final stabilised lattice cell during cascades through glassy carbon in one direction.



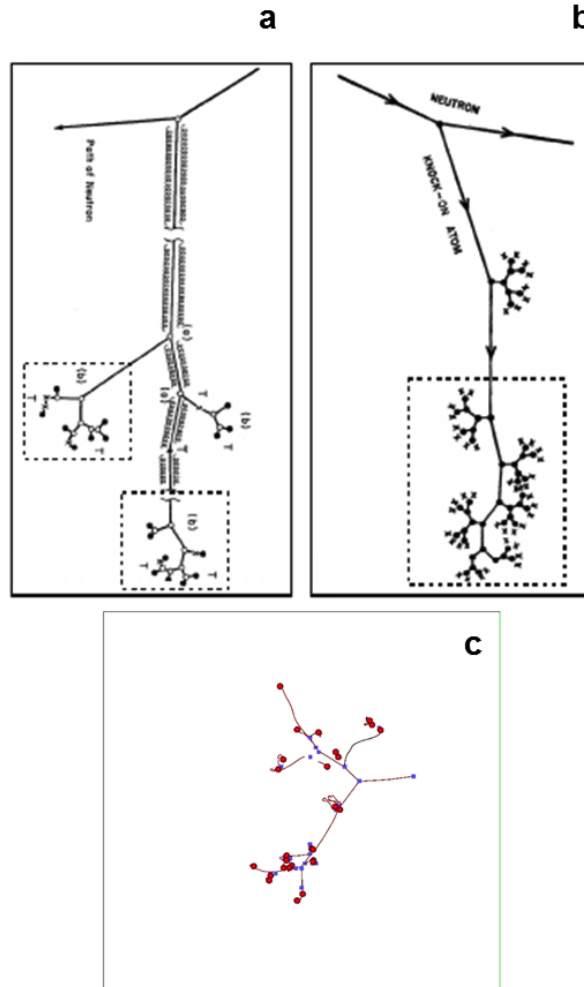
**Figure 5.33:** The average number of defects present in the final lattice cell,  $N_{defects}$ , as a function of energy (in red). The maximum number of displaced atoms,  $N_{displacements}$  as a function of energy (in blue). Error bars denote standard error.

Figure 5.33 shows that at 25 eV only four defects are formed. As the initial kinetic energy is increased to 50 eV, there is a significant difference in the number of defects formed. This is due to the shock wave passing through the cell having a larger amount of kinetic energy which results in the displacement of further atoms in the cell. The number of defects produced gradually increases between 50 and 75 eV and then remains almost constant up to 250 eV. The maximum number of displaced atoms closely follows the final number of defects formed in the stabilised lattice. Cascades with initial energies 75, 100 and 250 eV have on average a difference of 5% between the maximum number of displaced atoms and the final number of defects present. This figure suggests the majority of displaced atoms are forming interstitials instead of re-combining into the lattice at vacancy sites.

In summary, cascades through diamond resulted in minimal damage to the final structure and interstitials observed agree with previous literature [105]. Cascades through high and low density amorphous carbon and glassy carbon result in a high number of atoms being displaced during cascades.

## Discussion

One of the main insights to emerge from this study is the profound difference between cascades in graphite as compared to other widely-studied solids. The branching structure, the absence of localised melting, and the Kinchin-Pease-type defect generation [78] are all examples of behaviour which place graphite in a special category. Equally interesting is that many of these insights were correctly qualitatively understood long ago. Figures 6.1 (a) and (b) compare two literature schematics of cascades from fast neutron damage in graphite taken from Nightingale [106] and Simmons [49]. Figure 6.1 (c) is a cascade with initial PKA energy 2 keV presented in this thesis. There is general agreement in the overall schematics in particular the branching structure of the trajectories.



**Figure 6.1:** Comparison between literature models of graphite radiation damage and simulations presented in this thesis. (a) Schematic from Nightingale (p. 213 in Ref [106]) (b) Schematic from Simmons (p. 20 in Ref [49]) (c) Cascade simulation through graphite with initial PKA energy 2000 eV. (The dotted boxes in the upper schematics have been added to highlight the cascade portion within the diagram).

A definite answer cannot yet be given as to the origin of the branching behaviour (figure 6.1). Although the most probable reason is due to the low-packing function which permits 2-body collisions. All of these ideas are amenable to computer simulation through controlled comparison studies, and represent a promising direction for future work.

Graphite cascades are directionally dependent. Figure 6.2 shows a snap-shot of two graphite cascades with an initial PKA energy of 2000 eV.

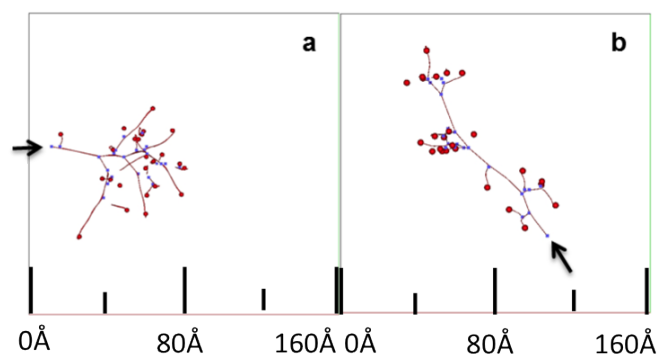


**Figure 6.2:** (a) Cascade through graphite with initial PKA energy 2000 eV. Initial PKA direction 9 from table 3.1. (b) Cascade through graphite with initial PKA energy 2000 eV. Initial PKA direction 2 from table 3.1. The red circles denote interstitials and the blue squares denote vacancies. The path of each displaced atom is traced.

The initial direction of the PKA in figure 6.2 (a) is parallel to the graphite layers (the arrow indicates the PKA's initial direction). The PKA collides with a neighbouring atom which alters the PKA's direction of travel. As a result of the PKA's new direction, channelling occurs before the PKA collides with further atoms in the lattice. The collisions result in the initiation of secondary cascades which in turn produce defects in the cell. Figure 6.2 (b) has an initial PKA direction  $45^\circ$  to the plane (the arrow indicates the PKA's initial direction). The PKA collides with neighbouring atoms resulting in the formation of defects. Channelling occurs during the simulation allowing the PKA to pass through layers of the lattice without colliding with atoms.

The position of defects present in a lattice after a cascade through graphite primarily depend on the initial PKA direction. However, as figures 6.2 (a) and (b) show, collisions with neighbouring atoms can result in focusing or channelling which can drastically alter the path of the PKA and further displace atoms.

Figure 6.3 highlights channelling seen during a cascade at 1 keV.

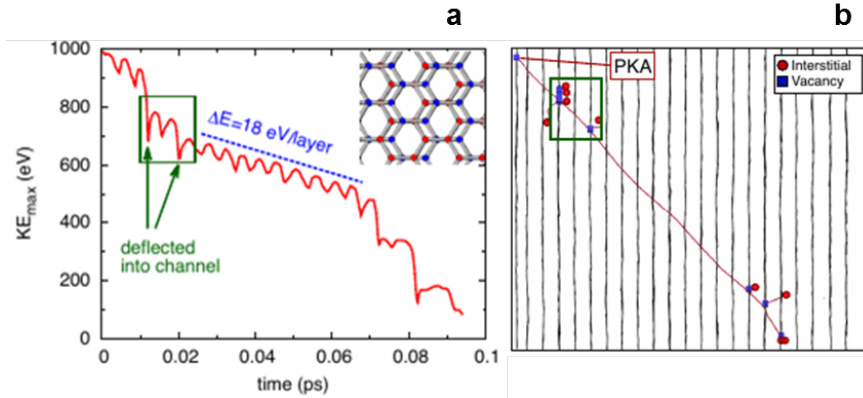


**Figure 6.3:** (a) Maximum kinetic energy as a function of time. Green arrows indicate the collisions which deflect the PKA into the channel. Inset at top-right of panel denotes the pseudo-channels of graphite; blue and red circles represent the A and B planes, respectively. (b) A cascade through graphite with an initial PKA energy 1000 eV. Channelling occurs along a  $\langle 10\bar{1}2 \rangle$  direction. The red circles denote interstitials and the blue squares denote vacancies. The path of each displaced atom is traced.

The PKA in figure 6.3 is deflected into a channelling direction having  $\langle 10\bar{1}2 \rangle$  orientation. Whilst in the channel, the PKA undergoes a series of collisions in which it passes through the middle of a hexagonal ring of atoms, losing kinetic energy on entry and regaining a portion of this upon exit. The PKA consistently loses 18 eV per energy layer. As the kinetic energy loss per layer is less than the threshold displacement energy, the disruption is transient and the lattice quickly recovers. The PKA passes through nine layers losing around 160 eV and travels over  $30\text{\AA}$  without creating a single permanent defect.

The most frequent channels found in a cubic lattice are  $\langle 110 \rangle$  channels [79]. However, it is immediately apparent that in figure 6.3 this is not the case. It is in fact a pseudo-channel in which the PKA must follow an undulatory path as it progresses through one layer to the next. To the author's knowledge, pseudo-channelling has not been previously identified for graphite. This is due to the difficulty of anticipating the pseudo-channel in the first place. Measurements of channelling through graphite pose significant experimental difficulties associated with the preparation of the sample and its alignment relative to the incident beam even for straightforward channels such as parallel or perpendicular to the c-axis. Channelling in graphite cascades has previously been observed down  $\langle 0001 \rangle$  [107] and  $\langle 11\bar{2}0 \rangle$  [108] directions. Simulations presented in this thesis have shown that while channelling is not a common

occurrence, it is certainly possible under certain conditions.

The closest connection to previous work on channelling witnessed along  $\langle 10\bar{1}2 \rangle$  plane (figure 6.3) is the calculation of Kaxiras and Pandey [109]. Their calculations showed that graphite has a potential energy loss of 19.5 eV (close to the kinetic energy loss rate observed in the simulations presented in this thesis) suggesting that the PKA has to gain  $\approx 18$  eV before passing through a graphite layer.

The main factor which limits channelling is that the atoms are invariably initially located on a lattice site and hence displacement tends to cause an immediate collision with a nearby atom.

The average number of displaced atoms during graphite cascades, Chapter 4, figure 4.47, and the final number of defects present after a graphite cascade, Chapter 4, figure 4.45 shows excellent correlation with the Kinchin and Pease and Norgett-Robinson-Torrens models respectively. This result is rather remarkable in itself as the KP [78] and NRT [80] treatments historically have not been found to have much predictive power [97] [110]. This is particularly true in metal or oxide systems where defect re-combination in the post-ballistic phase can lead to vastly fewer defects than displacements. The KP [78] and NRT [80] models work extremely well for graphite, even with regard to the empirical factor of 0.8 which relates displacements to defects in the NRT model.

Collision cascade simulations through graphite, Chapter 4, section 4.4, have allowed a value for the final PKA displacement to be calculated. Cascades with an initial PKA energy of 1000 eV have produced an average PKA displacement of 30Å. This is significantly lower than the value of 67Å reported by Simmons [49]. As expected, the average final displacement of the PKA increases as a function of the initial PKA energy. However, there are a few exceptions to this case; channelling can dramatically increase the distance the PKA travels through the lattice, collisions between the PKA and neighbouring atoms can result in the PKA re-bouncing through the cell and can also significantly alter the direction of travel, all of which can decrease the final displacement of the PKA. Simmons also reported the energy loss per collision as 196 eV [49] which is an overestimation when compared to the 112 eV per collision value observed in simulations presented within this thesis.

Cascades through graphite at high temperatures (900 °C) did not produce a significant difference in the maximum number of displaced atoms during a cascade or the number of defects present in the final lattice cell. Cascades

with an initial PKA energy of 1000 eV simulated with an initial temperature of 900°C have on average 3% more defects present in the final lattice than cascades with an initial temperature of 300°C. It is clear from results that even at high energies, an increase in temperature does not have a significant effect on the overall damage present in a final graphite cell.

Establishing a value for the threshold displacement energy,  $E_d$ , for graphite has historically been problematic. Table 2.3 in Chapter 2, section 2.9, highlights some of the different values of  $E_d$  from previous literature. These values cover a wide range spanning 10 to 60 eV [85] [111]. A value of  $E_d = 25$  eV has been determined from cascades presented in this thesis. This value has been determined from results presented in this thesis and by the KP [78] and NRT [80] relationships. It is statistically sound and unambiguously shows that a value of 60 eV, suggested by Burchell [112], is much too high. Yazyev *et al.* [84] also estimated an  $E_d$  value of 25 eV from their density functional theory calculations, while Smith and Beardmore [6] reported 34.5 eV and Herh *et al.* [7] reported around 45 eV. It should be noted that further MD cascades and analysis would provide an even more refined estimate of  $E_d$  and so the present number should not be considered the final value.

Threshold displacement energy cascades, Chapter 4, section 4.5, have produced interstitial and vacancy arrangements in keeping with current literature. The agreeable comparison between interstitials and vacancies presented in this thesis and from DFT calculations [100], validates the reason for employing EDIP molecular dynamics to simulate radiation damage in graphite.

## 6.1 Graphite and Diamond

Thermal spike simulations have produced remarkable results in graphite. It was not expected that initial energies up to 1000 eV given to a cell would result in so little damage being produced.

To highlight the uniqueness of graphite, diamond has been simulated under the same initial conditions. Figure 6.4 shows the final lattice cells after a thermal spike in graphite and diamond.

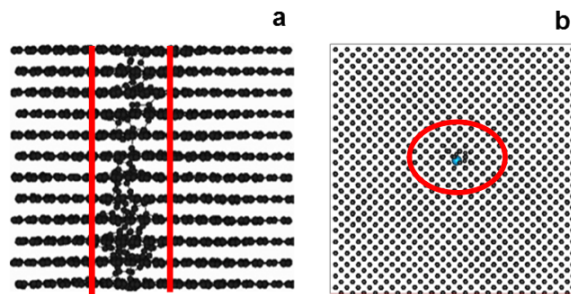


**Figure 6.4:** (a) Thermal spike through graphite with initial energy  $1 \times 10^5$  eV. The thermal spike is denoted by the red lines.  
(b) Thermal spike through diamond with initial energy 1000 eV. The thermal spike is denoted by the red ring.

There is a stark difference between the final lattice cell of graphite and diamond after a  $1 \times 10^5$  eV thermal spike. Whilst the graphite cell retains its overall structure, figure 6.4 (a) shows there is evidence of damage present in the form of interstitials and vacancies. The final diamond lattice, figure 6.4 (b) has only one defect present. The primary reason for the difference in damage created in the graphite and diamond cells is due to their structures.

The structure of diamond plays an important role during cascade simulations. Figure 6.5 compares snapshots from 2000 eV cascades through graphite and diamond.

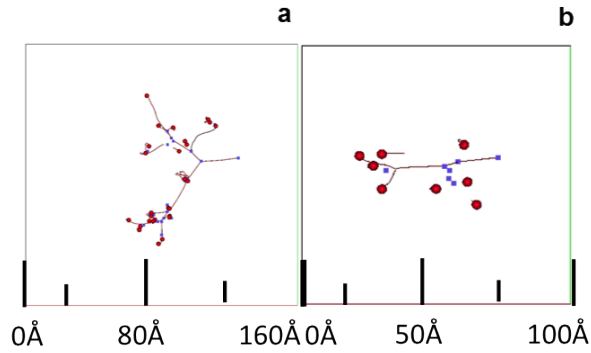


**Figure 6.5:** (a) Cascade through graphite with initial energy 2000 eV (b) Cascade through diamond with initial energy 2000 eV. The red circles denote interstitials and the blue squares denote vacancies. The path of each displaced atom is traced.

The graphite cascade, figure 6.5 (a) has branching cascades. Secondary cascades have formed on the initial branches as a result of collisions. This is in stark contrast to the final diamond cell, figure 6.5 (b). Defects in the diamond cascade formed along the initial path of the PKA. During the diamond simulation, defects were formed in a cluster around the initial PKA position. The final number of defects present in the graphite cascade was 28. This is significantly greater than the 10 defects present in the final diamond cascade (figure 6.5 (b)). The final phenomena witnessed in diamond is a shock wave. The shock wave transports kinetic energy through the lattice resulting in the displacement of atoms. This is not observed in graphite because of its layered structure.

Figure 6.6 shows the maximum number of displaced atoms as a function of time for cascades in graphite and diamond.

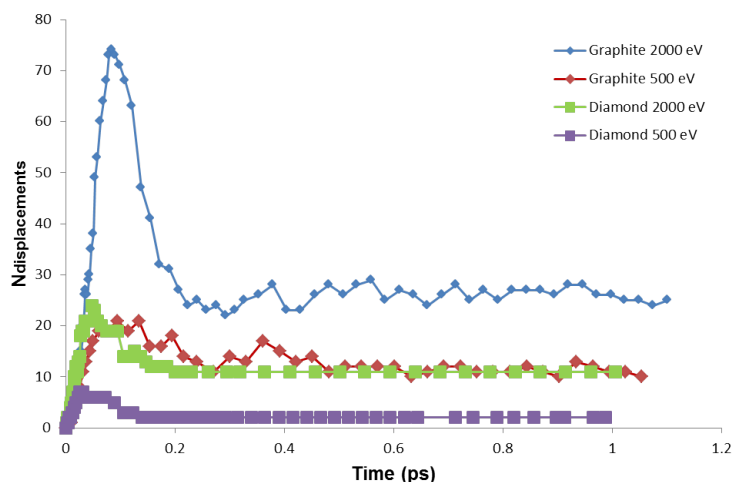


**Figure 6.6:** Graph showing the number of displaced atoms as a function of energy for: graphite cascades with initial energy 2000 eV (blue) and 500 eV (red), diamond cascades with initial energy 2000 eV (green) and 500 eV (purple). (Results are for the 20 initial PKA directions given in table 3.1)

The graphite cascade with initial PKA energy 2000 eV from the graph in figure 6.6 had a maximum of 74 displaced atoms. This was almost three times greater than the number of displaced atoms observed in the 2000 eV diamond cascade which had 11 defects present in the final lattice cell. This is almost the same as the final number of defects present in the lattice after a graphite cascade with an initial PKA energy of 500 eV. There are only two defects present after the cascade through diamond with an initial PKA energy of 500 eV which is significantly lower than the ten defects present after the graphite cascade with initial PKA energy of 500 eV. A further point to note is the time taken for each cascade to stabilise. Cascades in diamond stabilise with a greater efficiency than those in graphite. Figure 6.6 shows the time taken for a diamond cascade with an initial PKA energy of 2000 eV stabilises after 0.156 ps whereas the 2000 eV graphite cascade takes 0.224 ps to stabilise. A similar difference can be seen in the time a cascade takes to stabilise at lower energies. Figure 6.6 shows the graphite cascades with initial PKA energy of 500 eV takes 0.215 ps to stabilise which is significantly greater than the 0.14 ps it takes the 500 eV diamond cascade to stabilise.

The two main statistical quantities of MD cascade simulations are the final number of defects present,  $N_{defects}$  and the maximum number of displaced atoms  $N_{displacements}$ . Figure 6.7 shows the average number of defects present in diamond and graphite cascades.

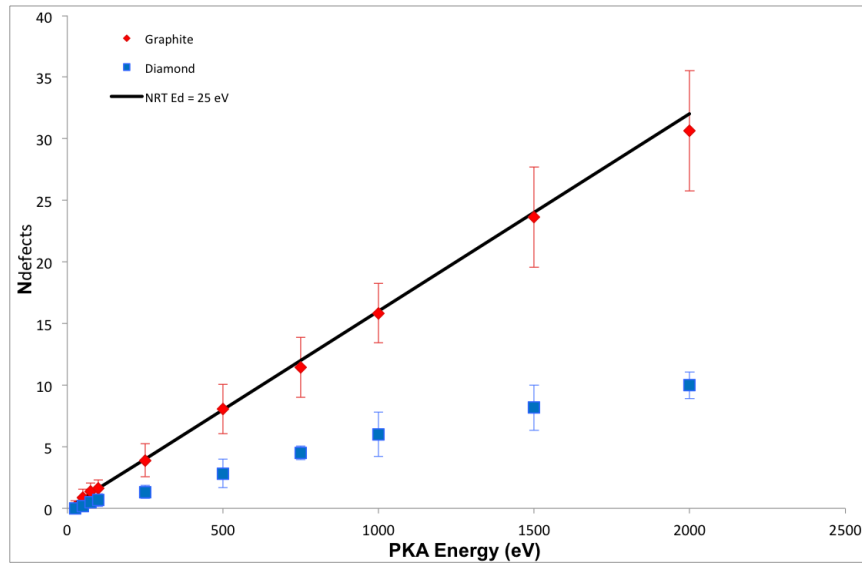


**Figure 6.7:** Graph showing the average number of defects present in the final lattice cell as a function of energy. Graphite is shown in red plotted along with the Norgett-Robinson-Torrens model with  $E_d = 25$  eV (black line). Diamond is shown in blue.

Figure 6.7 shows that both graphite and diamond follow linear trends between the number of defects present in the final lattice cell and the initial PKA energy. The NRT model fits well to the simulated graphite data. Figure 6.7 shows a small number of defects may be present in a graphite cascade with initial energy 25 eV. However, in diamond, there will be no defects formed in a cascade with initial PKA energy 25 eV as this is below the threshold displacement energy of diamond which has calculated to be 50 eV [104]. On average, there are three times as many defects present in the final lattice cell of graphite as there are in diamond. The error bars fitted to the diamond cascade data (figure 6.7) are smaller than those fitted to the graphite cascade data. This implies there is less variance between the number of defects formed during diamond cascades than there is in graphite cascades.

Figure 6.8 shows the maximum number of displaced atoms during a cascades,  $N_{displacements}$  as a function of energy for graphite and diamond.

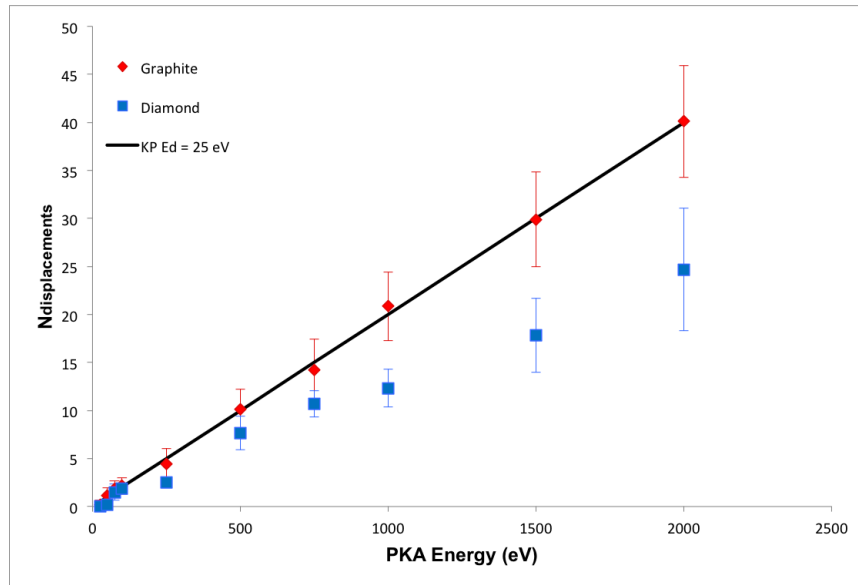


**Figure 6.8:** Graph showing the average number of displaced atoms as a function of energy. Graphite is shown in red plotted along with the Kinchin and Pease model with  $E_d = 25$  eV (black line). Diamond is shown in blue.

The maximum number of displaced atoms during a cascade in graphite or diamond follows a linear trend (figure 6.8). Graphite agrees with the Kinchin and Pease model when the threshold displacement energy is taken to be  $E_d = 25$  eV. The maximum number of displaced atoms seen in a graphite cascade is 53 compared to 33 observed in a diamond cascade. The difference between the number of displaced atoms is on average twice as great in graphite cascades than in diamond cascades.

The last comparison to be made between graphite and diamond is the final displacement of the PKA. Figure 6.9 shows the average final displacement of the PKA in graphite and diamond.

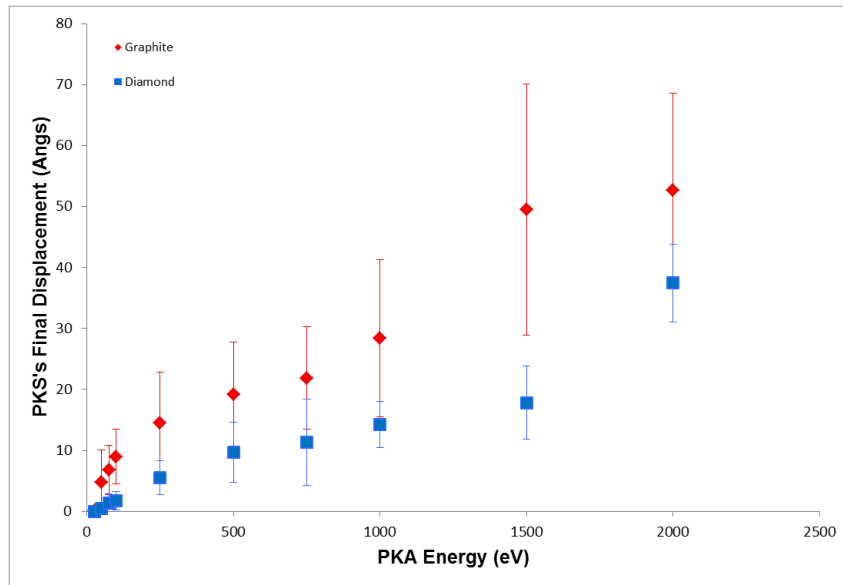


**Figure 6.9:** Graph showing the average final displacement of the PKA as a function of energy in graphite (red) and diamond (blue).

Figure 6.9 shows how the average final displacement of the PKA gradually increases in low and mid-range energy cascades (between 25 and 1000 eV). The final displacement of the PKA in mid-range energy cascades is almost half the size of the value observed in high energy cascades. The graph in figure 6.9 shows that diamond follows the same pattern as graphite in that there is a gradual increase in the final PKA displacement in low and mid-range energies. Cascades with an initial PKA energy of 2000 eV have on average a one and a half times greater final PKA displacement than in diamond.

A comparison between graphite and diamond cascades has shown how the final damage to a cell is dependent on the material's structure. The final number of defects present and the maximum number of atoms displaced in both graphite and diamond cascades follow a linear trend. High energy cascades in graphite have resulted in, on average, three times as many defects present in the final lattice cell as are seen in diamond. Due to the structure of diamond, a shock wave can pass through the cell as a direct result of initial collisions. The number of displaced atoms is one and a half times greater in graphite cascades than in diamond. A final point to note is that even at high energies, both graphite and diamond retain their overall structure after a cascade has stabilised.

## 6.2 Carbon Materials

### 6.2.1 High and Low Density Amorphous Carbons

Comparisons between high and low density amorphous carbon further emphasise what a unique material graphite is. Figure 6.10 are snap-shots of the final lattice cell from cascades in graphite, high and low density amorphous carbon.

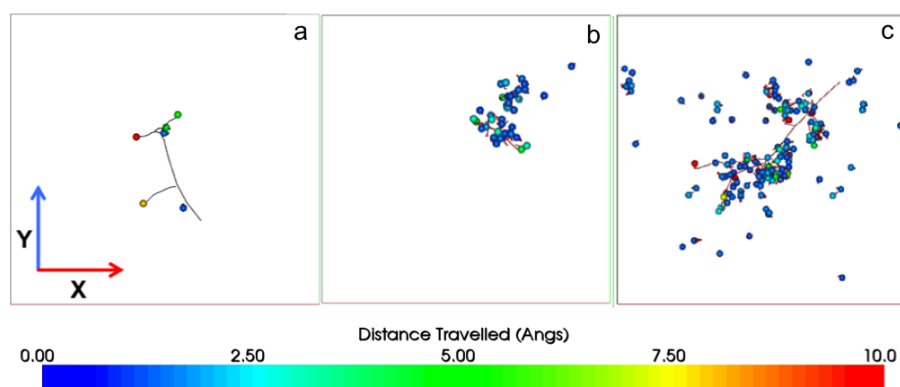
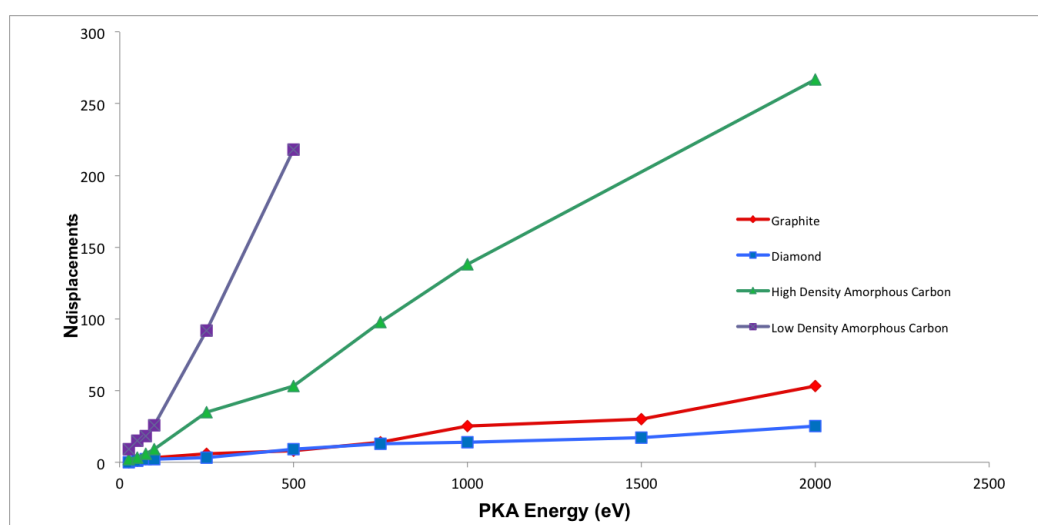


**Figure 6.10:** (a) The final lattice cell after a cascade in graphite with an initial PKA energy of 500 eV. (b) The final lattice cell after a cascade in high density amorphous carbon with an initial PKA energy of 500 eV. (c) The final lattice cell after a cascade in low density amorphous carbon with an initial PKA energy of 500 eV. Initial PKA direction 1 from table 3.1 and initial PKA temperature of 300°C. The red circles denote interstitials and the blue squares denote vacancies. The path of each displaced atom is traced.

Figure 6.10 (a) shows the defects present in the final lattice of a graphite cell after a cascade with an initial PKA energy of 500 eV. During the cascade, a maximum of eight atoms were displaced and there are six defects present in the final lattice. In stark contrast, a cascade through high density amorphous carbon, figure 6.10 (b), had 45 displaced atoms present in the final cell. Atoms displaced as a direct result of the collision cascade in high density amorphous carbon formed in a cluster centred around the initial PKA position. This is very different behaviour than that witnessed during the graphite cascade. The PKA in the graphite cascade has passed through several layers of the cell resulting in defects forming along the path of the PKA. Cascades in low density amorphous carbon with an initial PKA energy of 500 eV produce substantial damage to the final lattice (figure 6.10 (c)). Displaced atoms occurred as a direct result of the collision cascade, they formed in clusters along the initial

path of the PKA. A shock wave was also witnessed in low density amorphous carbon cascades. This was similar to the shock wave observed in diamond cascades. Unlike diamond, the shock wave in low density amorphous carbon did possess enough kinetic energy to displace atoms. Evidence of these displacements can be seen around the main defects clusters in figure 6.10 (c). The maximum number of displaced atoms observed in the low density amorphous carbon cascade was 218.

Figure 6.11 shows the maximum number of defects present after cascades in graphite, diamond and high and low density amorphous carbons as a function of PKA energy.



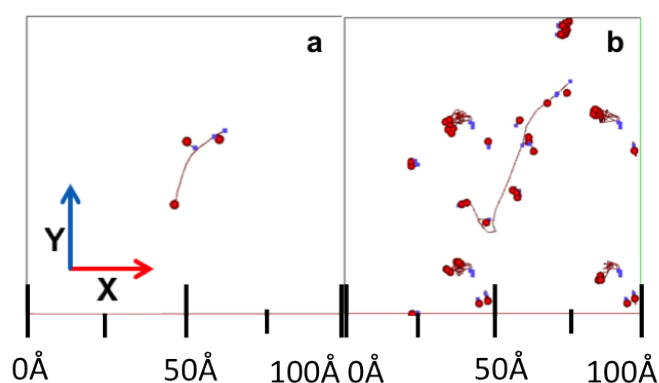
**Figure 6.11:** The maximum number of displaced atoms present during a cascades in graphite (red), diamond (blue), low (purple) and high (green) density amorphous carbon as a function of energy. With an initial PKA direction 1 from table 3.1 and initial PKA temperature of 300°C.

Figure 6.11 shows the number of displaced atoms increases as a function of energy in each material. The maximum number of displaced atoms during a 250 eV cascade through graphite is six, which is significantly lower than the 92 observed in the low density amorphous carbon cascade. High density amorphous carbon has 35 displaced atoms during a 250 eV cascade. This is nine times greater than the number of displaced atoms during a 250 eV cascade through diamond. Low density amorphous carbon has 218 atoms displaced during a 500 eV cascade. High energy cascades with an initial PKA energy of 2000 eV in diamond have a maximum number of 25 displaced atoms. This is 91% less than the number of displaced atoms observed in a high density

amorphous carbon cascade with initial PKA energy of 2000 eV. There are 81% more displaced atoms witnessed during a 2000 eV cascade in high density amorphous carbon compared to a 2000 eV cascade through graphite.

## 6.2.2 Glassy Carbon

The final material to be analysed is glassy carbon which is 100%  $sp^2$  bonded. Due to the cavities in glassy carbons' structure, high energy cascades are difficult to simulate. This is because channelling and focusing during glassy carbon cascades are a common occurrence. Figure 6.12 shows snap-shots of the final lattice cells in graphite and glassy carbon after a collision cascade with an initial PKA energy of 250 eV.



**Figure 6.12:** (a) Cascade through graphite with an initial PKA energy of 500 eV and initial PKA direction 1 from table 3.1. (b) Cascade through glassy carbon with an initial PKA energy of 500 eV and initial PKA direction 1 from table 3.1. The initial PKA temperature was 300°C. The red circles denote interstitials and the blue squares denote vacancies. The path of each displaced atom is traced.

Figure 6.12 (a) shows defects in the final lattice after a 250 eV cascade through graphite. The PKA has collided with neighbouring atoms in the lattice resulting in the displacement of atoms. There are three defects present in the final cell. Figure 6.12 (b) shows a snap-shot of the final glassy carbon lattice after a cascade with an initial PKA energy of 250 eV. Due to the structure of glassy carbon, the PKA can penetrate large distances through the cell without colliding with neighbouring atoms. This results in the defects forming across the whole cell. There are 59 defects present in the glassy carbon cell which is 95% greater than in the graphite cell. A shock wave was created during the glassy carbon cascade which resulted in the displacement of further atoms.

Figure 6.13 shows the number of final defects and the maximum number of displaced atoms present in a lattice cell after a cascade in graphite and glassy carbon.

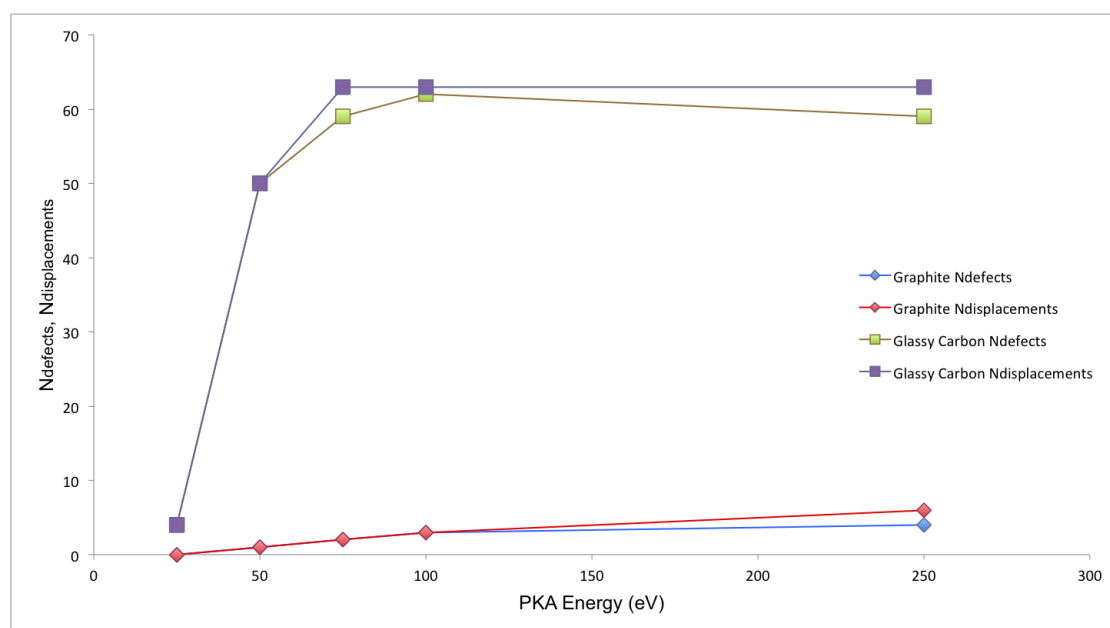


**Figure 6.13:** Graph showing: the final number of defects present in graphite cascades (red) and glassy carbon (green) as a function of energy and the maximum number of displaced atoms in graphite (blue) and glassy carbon (purple) as a function of energy. The initial cell temperature was 300°C.

The number of defects and displaced atoms during graphite cascades gradually increases as a function of energy. However, glassy carbon has peaked in the number of final defects and the maximum number of displaced atoms during the cascade with an initial PKA energy of 75 eV. This occurs as a direct result of glassy carbon's structure. On average, there is a difference of 3% between the maximum number of displaced atoms and the final number of defects present in the final lattice cell during glassy carbon cascades. This is less than the average difference of 8% occurring in graphite cascades. Cascades through glassy carbon highlight evidence of channelling and focusing. Analysis of glassy carbon simulations where channelling and focusing occurred aided in the search for these events in graphite which have historically been notoriously difficult to simulate.

The vast difference in the number of atoms displaced and final number of defects present in a lattice cell is largely dependent on a material's structure and bonding. This is reflected in the results shown in figures ?? and 6.11. Dia-

mond is a strong and robust material, even during cascades at high energies, few atoms are displaced and there is very little damage to the final lattice cell. Graphite cascades see a greater number of atoms displaced as a direct result of collision cascades and the occasional channelling. However, due to the layered structure of graphite, displaced atoms can re-combine in vacant lattice positions resulting in little damage being present in the final cell even after high energy cascades. Due to the sheer number of atoms present in cascades through high density amorphous carbon, cascades tend to form localised clusters of displaced atoms around the initial PKA site. The formation of such localised clusters results in a high number of atoms being displaced within the cell. Cascades through low density amorphous carbon displace atoms across the whole cell. At low energies, significant damage can be seen in the final cell. This is partially due to the PKA being able to travel through the cell which results in the formation of secondary collision cascades. Atoms can be displaced during a cascade through low density amorphous carbon as a result of a shock wave. This can displace atoms even if they are a significant distance away from the initial PKA site. Glassy carbon produces cascades which are highly dependent on the initial direction of the PKA. Low energy cascades through glassy carbon have produced significant numbers of defects in the final lattice cell. Channelling has been observed through glassy carbon, a phenomena which also occurs on a select number of graphite planes.

The comparisons between graphite, diamond, high and low density amorphous carbon and glassy carbon cascades, has highlighted how unique a material graphite is.

## 6.3 Future Work

Looking to future simulations of cascades in graphite, there are several directions of research which could be undertaken.

Further studies could include research into how temperature affects the evolution of the cascade and the associated relaxation dynamics. As discussed by Kelly, a large experimental literature exists for graphite on dimensional change, mechanical behaviour and thermal properties [113]. However, simulations have not been applied to the atomistic perspective.

Combining defect analysis carried out in this work with density functional theory calculations of defect energetics and activation barriers for migration and recombination would be particularly beneficial for understanding graphite structural evolution.

Collision cascades with energies exceeding 2000 eV are currently difficult to simulate because at higher energies, the numerics of a cascade become difficult to manage. For example, to contain a 5000 eV cascade through graphite with a  $2\sigma$  confidence level, a cell of 2 million atoms is required. Cascades have been simulated in a variety of oxides with initial PKA energies of 40 keV [114]. However, to undertake a cascade of this magnitude in graphite, a cell containing 1 billion atoms is required and this is far beyond what is presently practicable for carbon. Further development of MD potentials for carbon may result in very high energy cascade simulations being a reality.

Results in Chapter 4 emphasised how cascades through graphite are directionally dependent. Further cascade simulations with different initial PKA directions to those used in this thesis would allow statistical predictions, in particular for the threshold displacement energy, to be generated with a greater accuracy.

Simulations of successive PKAs would be interesting and would provide further information regarding defect production and defect type.

Further comparisons between cascades in graphite, carbon materials, metals and oxides would highlight features unique to graphite.

## Conclusion

Thermal spike simulations in graphite have produced remarkable results. It was not expected that such a large amount of kinetic energy given to the system would produce so little damage. Thermal spike simulations through diamond, Chapter 5, produced even fewer defects in the final cell than for graphite. This is due to the structural difference between graphite and diamond.

Collision cascade simulations through graphite produced results in agreement with previous literature [49] [106] and have shown graphite cascades are directionally dependent. As expected, the average final displacement of the PKA increases as a function of the initial PKA energy. However, there are a few exceptions to this case channelling can dramatically increase the distance the PKA travels through the lattice, collisions between the PKA and neighbouring atoms can also significantly alter the direction of travel. Channelling has been observed during simulations and the  $\langle 10\bar{1}2 \rangle$  channel has been identified. Channelling predominantly occurs during high energy cascades. However, it has been witnessed during a handful of low and mid-range energy cascades.

Graphite cascades have produced data which is consistent with the Kinchin and Pease [78] and Norgett-Robinson-Torrens models [80]. This result is somewhat remarkable in itself as historically these two theories have not had much predictive power, particularly in metal or oxide systems where defect recombination in post-ballistic phase can lead to vastly fewer defects than displacements. Cascade simulations at 1000 eV have produced an average PKA displacement of 25 eV.

Cascades through graphite at high temperatures did not produce a significant difference in the maximum number of displaced atoms formed during a cas-

cade or the number of defects present in the final lattice cell to those performed at 300°C. This result is of significant interest for the development of generation IV reactors which operate at temperature of around 1000°C.

Threshold displacement energy cascades have produced interstitials and vacancies in keeping with current literature justifying the accuracy of EDIP as an MD potential to model graphite [5] [100] [101] [86].

The comparison between collision cascade simulations through; graphite, diamond, glassy carbon, high and low density amorphous carbon have highlighted how unique a material graphite is. Simulation results showed how the structure of a material affects the collision cascade.

Diamond produced very few defects in the final cell compared to graphite and the defects which did form remained close to the initial PKA site. Cascades through diamond gave evidence of a shock wave being produced as a direct result of collisions between neighbouring atoms. This phenomena did not occur during graphite cascades. High density amorphous carbon cascades formed in clusters and remained localised to the initial PKA site. Low density amorphous carbon produced vast amounts of displaced atoms in the final cell compared to graphite even during low energy cascades. During mid-range energy cascades through low density amorphous carbon, the majority of defects formed in clusters along the path of the initial PKA. Glassy carbon cascades resulted in the formation of defects across the whole lattice. This is due to the large vacant spaces in glassy carbon which allows channelling to occur. Each of the carbon materials analysed produced unique results which were immensely different from graphite.

In summary, molecular dynamics simulations of radiation damage cascades have been performed in: graphite, diamond, glassy carbon, high and low density amorphous carbons. To the best of the author's knowledge, this is the first comprehensive study of its kind. A striking difference in behaviour has been observed between graphite cascades and carbon materials. Graphite cascades have exhibited a fractal-like branching structure and binary-collision-type behaviour. Statistical analysis across 20 initial directions and a large number of energies shows the production of displacements and defects is well-described by the Kinchin and Pease, and the Norgett-Robinson-Torrens models respectively. The simulations quantify the important quantities such as the range of the primary knock-on atom and the average energy loss per collision as well as producing a starting point for future studies of defect generation under

irradiation.

Information produced within this thesis is invaluable for understanding the role of graphite under irradiation, a topic of great importance for lifetime extension of existing nuclear reactors and next-generation designs operating at high temperature.

# References

- [1] W. J. Weber, R. C. Ewing, C. R. A. Catlow, T. Diaz de la Rubia, and C. Knoshita. Radiation effects in crystalline ceramics for the immobilization high-level nuclear waste and plutonium. *Journal of Materials Research*, 13(1434), 1998.
- [2] D. J. Bacon, F. Gao, and Y. N. Osetsky. The primary damage state in fcc, bcc and hcp metals as seen in molecular dynamics simulations. *Journal of Nuclear Materials*, 276(1), 2000.
- [3] N. A. Marks. *Computer-based Modeling of Novel Carbon Systems and Their Properties: Beyond Nanotubes*. Springer, 2010.
- [4] C. P. Ewels, R. H. Telling, A. A. El-Barbary, M. I. Heggie, and P. R. Briddon. *Physical Review Letters*, 91(025505), 2003.
- [5] R. H. Telling and M. I. Heggie. *Philosophical Magazine*, 87(4797), 2007.
- [6] R. Smith and K. Beardmore. Molecular dynamics studies of particle impacts with carbon-based materials. 272(Md):255–270, 1996.
- [7] B. D. Hehr, A. I. Hawari, and V. H. Gillette. *Nuclear Technology*, 160(251), 2007.
- [8] G. B. Neighbour. *Management of Aging Graphite Reactor Cores*. The Royal Society of Chemistry, 2007.
- [9] J. Haller. URL <http://www.euronuclear.org/events/enc/enc2012/transactions/ENC2012-transactions-plant-operations.pdf>.
- [10] Technology roadmap update for generation iv nuclear energy systems. URL <https://www.gen-4.org/gif/upload/docs/application/pdf/2014-03/gif-tru2014.pdf>.
- [11] J. B. Gibson, A. N. Goland, M. Milgram, and G. H. Vineyard. *Physical Review*, 120(1229), 1960.
- [12] M. S. Daw and M. I. Baskes. *Physical Review Letters*, 50(1285), 1983.
- [13] M. S. Daw and M. I. Baskes. *Physical Review B*, 29(6443), 1984.

- [14] G. V. Lewis, C. R. A. Catlow, and P. D. Battle. *Physics C Solid State*, 18 (1149), 1985.
- [15] T. S. Bush, J. D. Gale, C. R. A. Catlow, and P. D. Battle. *Journal of Materials Chemistry*, 4(831), 1994.
- [16] R. Smith. *Proceedings of the Royal Society A*, 431(143), 1990.
- [17] D. W. Brenner. *Physical Review B*, 42(9458), 1990.
- [18] M. I. Heggie. *Journal of Physics: Condensed Matter*, 3(3065), 1991.
- [19] K. Nordlund, J. Keinonen, and T. Mattila. Formation of Ion Irradiation-Induced Small-Scale Defects on Graphite Surfaces. *Physical review letters*, 77(4):699–702, July 1996. ISSN 1079-7114. URL <http://www.ncbi.nlm.nih.gov/pubmed/10062880>.
- [20] N. Marks. *Journal of Physics: Condensed Matter*, 63(035401), 2001.
- [21] N. Marks. Modelling diamond-like carbon with the environment-dependent interaction potential. *Condensed Matter*, 14 (2901), 2002.
- [22] J. F. Ziegler, J. P. Biersack, and U. Littmark. *The Stopping and Range of Ions in Solids*, volume 1. Pergamon, New York, 1985.
- [23] A. Epstein. *Fossil Fuels Improve the Planet*. Center for Industrial Progress, 2013.
- [24] URL <http://data.worldbank.org/indicator/EG.USE.COMM.FO.ZS>.
- [25] T. Gray. *The Elements: A Visual Exploration of Every Atom in the Universe*. Black Day and Leventhal Publishers Inc., 2012.
- [26] URL [http : //www.chem.duke.edu/jds/cruisechem/nuclear/discovery.html](http://www.chem.duke.edu/jds/cruisechem/nuclear/discovery.html).
- [27] A. Allisy. From the curie to the becquerel. *Metrologia*, 31(467), 1995.
- [28] B. Bernstein. The uneasy alliance: Roosevelt, churchill, and the atomic bomb, 1940-1945. *The Western Political Quarterly*, 29:202–230, 1976.
- [29] URL [http : //www.chem.duke.edu/jds/cruisechem/nuclear/discovery.html](http://www.chem.duke.edu/jds/cruisechem/nuclear/discovery.html).
- [30] J. Craig, D. Vaughan, and B. Skinner. *Resources of the Earth, Second Edition*. Prentice Hall, New Jersey, 1996.
- [31] URL <http://www.iaea.org/newscenter/news/2004/obninsk.html>.
- [32] URL <http://www.world-nuclear.org/info/Country-Profiles/Countries-0-S/Russia-Nuclear-Power/>.

- [33] URL  
<http://www.world-nuclear.org/info/nuclear-fuel-cycle/power-reactors/nuclear-power-reactors/>.
- [34] M. H. Klaproth. Encyclopædia britannica online. Retrieved 07 August, 2014. URL  
<http://www.britannica.com/EBchecked/topic/319885/Martin-Heinrich-Klaproth>.
- [35] P. Atkins, T. Overton, J. Rourke, M. Weller, and F. Armstrong. *Inorganic Chemistry*. OUP Oxford 5th Edition, 2009.
- [36] P. Atkins and J. de Paula. *Physical Chemistry*. OUP Oxford 10th Edition, 2014.
- [37] H. J. Krappe and K. Pomorski. *Theory of Nuclear Fission*, volume 838. Lecture Notes in Physics, Springer, 2012.
- [38] C. Wagemans. *The Nuclear Fission Process*. CRC Press, 1991.
- [39] K. D. Kok. *Nuclear Engineering Handbook*. CRC Press, 2009.
- [40] N. A. Stanton. *Human Factors in Nuclear Safety*. CRC Press, 1996.
- [41] T. Kiguchi and Y. Oka. *Nuclear Reactor Design (An Advanced Course in Nuclear Engineering)*. Springer, 2014.
- [42] *Fundamentals of Nuclear Science and Engineering, Second Edition*. CRC Press, 2007.
- [43] T. Jackson. *The Elements: An Illustrated History of the Period Table*. Worth Press Ltd., 2012.
- [44] URL  
[https://www.gov.uk/government/uploads/system/uploads/attachment\\_data/file/210410/TableofUKnuclearreactors.pdf](https://www.gov.uk/government/uploads/system/uploads/attachment_data/file/210410/TableofUKnuclearreactors.pdf).
- [45] URL <http://namrc.co.uk/intelligence/uk-new-build-plans/>.
- [46] URL <http://www.world-nuclear.org/info/Nuclear-Fuel-Cycle/Nuclear-Wastes/Decommissioning-Nuclear-Facilities/>.
- [47] J. Browne. *Seven Elements that have Changed the World: Iron, Carbon, Gold, Silver, Uranium, Titanium, Silicon*. W and N, 2013.
- [48] W. Reynolds. *Physical Properties of Graphite*. Elsevier Publishing Co. Ltd, 1968.
- [49] J. H. W. Simmons. *Radiation Damage in Graphite*. Pergamon Press, 1965.
- [50] D. Frenkel and B. Smit. *Understanding Molecular Simulation (From Algorithms to Applications) 2nd Edition*. Academic Press, 2001.

- [51] B. J. Alder and T. E. Wainwright. *Journal of Chemical Physics*, 27(1208), 1957.
- [52] B. J. Alder and T. E. Wainwright. *Journal of Chemical Physics*, 31(459), 1959.
- [53] D. C. Rapaport. *The Art of Molecular Dynamics Simulation*. Cambridge University Press, 1995.
- [54] J. Tersoff. Empirical interatomic potential for carbon, with applications to amorphous carbon. *Physical Review Letters*, 61(2879), 1988.
- [55] J. Tersoff. New empirical approach for the structure and energy of covalent systems. *Physical Review B*, 37(12), 1987.
- [56] J. Ferrante, J. R. Smith, and J. H. Rose. *Physical Review B*, 50(1385), 1983.
- [57] J. H. Rose, J. R. Smith, and J. Ferrante. *Physical Review B*, 28(1835), 1983.
- [58] P. M. Morse. Diatomic molecules according to the wave mechanics. ii. vibrational levels. *Physical Review*, 34:57–64, 1929.
- [59] L. Lindsay and D. A. Broido. Optimized tersoff and brenner empirical potential parameters for lattice dynamics and phonon thermal transport in carbon nanotubes and graphene. *Physical Review B*, 81(205441), 2010.
- [60] N. Marks. *Amorphous Carbon and Related Materials*. Number Chapter 3. Springer Science, 2010.
- [61] J. H. Los and A. Fasolino. *Physical Review B*, 68(2), 2003.
- [62] J. H. Los, L. M. Ghiringhelli, E. J. Meijer, and A. Fasolino. *Physical Review B*, 68(14), 2005.
- [63] S. J. Stuart, A. B. Tutein, and J. A. Harrison. A reactive potential for hydrocarbons with intermolecular interactions. *Chemical Physics*, 112(6472), 2000.
- [64] A. S. Barnard and S. P. Russo. *Molecular Physics*, 100(1517), 2002.
- [65] M. Z. Bazant and E. Kaxiras. Environment-dependent interatomic potential for bulk silicon. *Physical Review B*, 56(14), 1997.
- [66] J. F. Justo, M. Z. Bazant, E. Kaxiras, V. V. Bulatov, and S. Yip. Interatomic potential for silicon defects and disordered phases. *Physical Review B*, 58(5), 1997.
- [67] D. W. M. Lau, D. G. McCulloch, and N. A. Marks. *Applied Physics Letters*, 75(233408), 2007.

- [68] R. C. Powles, N. A. Marks, and D. W. M. Lau. Self-assembly of sp<sup>2</sup>-bonded carbon nanostructures from amorphous precursors. *Physical Review B*, 79(075430), 2009.
- [69] I. Suarez-Martinez and N. A. Marks. *Applied Physics Letters*, 99(033101), 2011.
- [70] I. Suarez-Martinez and N. A. Marks. *Carbon*, 48(3592), 2010.
- [71] I. Suarez-Martinez and N. A. Marks. *Carbon*, 50(5441), 2012.
- [72] N. A. Marks, M. Lattemann, and D. R. McKenzie. *Physical Review Letters*, 108(075503), 2012.
- [73] N. A. Marks. Generalizing the environment-dependent interaction potential for carbon. 63(3)(035401), 2000.
- [74] H. Y. Chan, K. Nordlund, J. Peltola, H. J. L. Gossmann, N. L. Ma, M. P. Srinivasan, F. Benistant, and L. Chan. The effect of interatomic potential in molecular dynamic simulations of low energy ion implantation. *Nuclear Instruments and Methods in Physics Research Section B*, 288: 240–244, 2005.
- [75] J. P. Biersack and J. F. Ziegler. Refined universal potentials in atomic collisions. *Instruments and Methods*, 194:93–100, 1982.
- [76] N. A. Marks, J. M. Bell, G. K. Pearce, D. R. McKenzie, and M. M. M. Bilek. *Diamond and Related Materials*, 12(2003), 2003.
- [77] G. K. Pearce, N. A. Marks, D. R. McKenzie, and M. M. M. Bilek. *Diamond and Related Materials*, 14(921), 2005.
- [78] G. H. Kinchin and R. S. Pease. *Journal of Nuclear Energy*, 1(200), 1954.
- [79] M. W. Thompson. *Defects and Radiation Damage in Metals*. Cambridge University Press, 1969.
- [80] M. J. Norgett, M. T. Robinson, and I. M. Torrens. *Journal of Nuclear Energy*, 33(50), 1975.
- [81] I. M. Torrens and M. T. Robinson. *Radiation-Induced Voids in Metals*, volume 739. USAEC Report, 1972.
- [82] C. Erginsoy, G. H. Vineyard, and A. Englert. *Physical Review*, 133(A595), 1964.
- [83] C. Erginsoy, G. H. Vineyard, and A. Shimizu. *Physical Review*, 139 (A118), 1965.

- [84] Oleg Yazyev, Ivano Tavernelli, Ursula Rothlisberger, and Lothar Helm. Early stages of radiation damage in graphite and carbon nanostructures: A first-principles molecular dynamics study. *Physical Review B*, 75(11):1–5, March 2007. ISSN 1098-0121. doi: 10.1103/PhysRevB.75.115418. URL <http://link.aps.org/doi/10.1103/PhysRevB.75.115418>.
- [85] S. J. Zinkle and C. Kinoshita. *Journal of Nuclear Materials*, 251(200), 1997.
- [86] M. I. Heggie, I. Suarez-Martinez, C. Davidson, and G. Haffenden. *Journal of Nuclear Materials*, 413(150), 2011.
- [87] J. J. Thomson. On the structure of the atom: an investigation of the stability and periods of oscillation of a number of corpuscles arranged at equal intervals around the circumference of a circle; with application of the results to the theory of atomic structure. *Philosophical Magazine*, 7 (237), 1904.
- [88] M. Robinson, N. A. Marks, K. R. Whittle, and G. R. Lumpkin. Sensitivity of the threshold displacement energy to temperature and time. *Physical Review B*, 85(104105), 2012.
- [89] E. Fermi. *Neutron Physics for Nuclear Reactors: Unpublished Writings by Enrico Fermi*. World Scientific Publishing Company, 2010.
- [90] M. Heggie and C. Latham. *Computation Nanoscience, Chapter 12, The Atomic-, Nano-, and Mesoscale Origins of Graphite's Response to Energetic Particles*. Number 388-413. Royal Society of Chemistry, 2011.
- [91] Y. Nakamura, editor. *New Developments in Nuclear Fusion Research*. NOVA Publishers, 2006.
- [92] *DOE Fundamentals Handbook, Nuclear Physics and Reactor Theory*, volume 1 of 2. U.S. Department of Energy Washington, D.C. 20585, 1993.
- [93] M. I. Heggie and R. H. Telling. Radiation defects in graphite. *Philosophical Magazine*, 87(31):4797–4846, 2007.
- [94] D. Kanjijal. Swift heavy ion-induced modification and track formation in materials. *Current Science*, 80(1560), 2001.
- [95] M. Toulemonde, W. Assmann, C. Dufour, A. Meftah, F. Studer, and C. Trautmann. Experimental phenomena and thermal spike model description of ion tracks in amorphisable inorganic insulators. *Materials Physics*, 52(263), 2006.
- [96] URL <https://www-nds.iaea.org/stopping/>.
- [97] D. J. Bacon, F. Gao, and Y. N. Osetsky. *Nuclear Instruments and Methods in Physics Research Section B*, 153(87), 1999.

- [98] K. Nordlund, M. Ghaly, R. S. Averback, M. Caturla, T. Diaz de la Rubia, and J. Tarus. Defect production in collision cascades in elemental semiconductors and fcc metals. *Physical Review B*, 57(7556), 1998.
- [99] N. A. Marks. *Physical Review B*, 56(2441), 1997.
- [100] C. Latham, M. I. Heggie, J. A. Gamez, I. Suarez-Martinez, C. P. Ewels, and P. R. Briddon. *Journal of Physics: Condensed Matter*, 20(39), 2008.
- [101] A. A. El-Barbary. *Physical Review B*, 68(144107), 2003.
- [102] R. H. Telling, C. P. Ewels, A. A. El-Barbary, and M. I. Heggie. *Nature Materials*, 2(333), 2003.
- [103] N. A. Marks, N. C. Cooper, D. R. McKenzie, D. G. McCulloch, P. Bath, and S. P. Russo. *Physical Review B*, 65(075411), 2002.
- [104] W. Wu and S. Fahy. Molecular-dynamics study of single-atom radiation damage in diamond. *Physical Review B*, 49(5), 1993.
- [105] D. C. Hunt, D. J. Twitchen, M. E. Newton, J. M. Baker, T. R. Anthony, W. F. Banholzer, and S. S. Vagarali. Identification of the neutral carbon <100> split interstitial in diamond. *Physical Review B*, 61(3863), 2000.
- [106] R. E. Nightingale. *Nuclear Graphite*. Academic Press, New York and London, 1962.
- [107] E. Yagi, T. Iwata, T. Urai, and K. Ogiwara. *Nuclear Matter*, 334(9), 2004.
- [108] M. Balarin. *Physica Status Solidi*, 2(60), 1962.
- [109] E. Kaxiras and K. C. Pandey. *Physical review letters*, 61(2693), 1988.
- [110] R. E. Voskoboinikov, Yu. N. Osetsky, and D. J. Bacon. Computer simulation of primary damage creation in displacement cascades in copper. i. defect creation and cluster statistics. *Nuclear Materials*, 377: 385–395, 2008.
- [111] F. Banhart. *Reports of Progress in Physics*, 62(1181), 1999.
- [112] T. D. Burchell. *Carbon Materials for Advanced Technologies*. American Carbon Society, 1994.
- [113] B. T. Kelly. *Physics of Graphite*. Applied Science Publishers, 1981.
- [114] K. Trachenko, M. T. Dove, E. Artacho, I. T. Todorov, and W. Smith. *Physical Review B*, 73(174207), 2006.

APPENDIX I

# Cascades Through Graphite

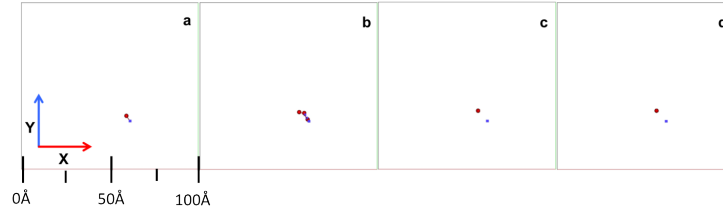
# List of Figures

1	Graphite cascade with initial PKA energy 50 eV, initial temperature 300°C and initial PKA direction 2 from table 3.1 . . . . .	187
2	The number of defects formed during a cascade through graphite with initial PKA energy 50 eV, initial temperature 300°C and initial PKA direction 2 from table 3.1 . . . . .	187
3	Distance travelled by atoms during a graphite cascade with initial PKA energy 50 eV, initial temperature 300°C and initial PKA direction 2 from table 3.1 . . . . .	188
4	Graphite cascade with initial PKA energy 250 eV, initial temperature 300°C and initial PKA direction 15 from table 3.1 . . . . .	188
5	The number of defects formed during a cascade through graphite with initial PKA energy 250 eV, initial temperature 300°C and initial PKA direction 15 from table 3.1 . . . . .	189
6	Distance travelled by atoms during a graphite cascade with initial PKA energy 250 eV, initial temperature 300°C and initial PKA direction 15 from table 3.1 . . . . .	189
7	Graphite cascade with initial PKA energy 500 eV, initial temperature 300°C and initial PKA direction 15 from table 3.1 . . . . .	190
8	The number of defects formed during a cascade through graphite with initial PKA energy 500 eV, initial temperature 300°C and initial PKA direction 15 from table 3.1 . . . . .	191
9	Distance travelled by atoms during a graphite cascade with initial PKA energy 500 eV, initial temperature 300°C and initial PKA direction 15 from table 3.1 . . . . .	191
10	Graphite cascade with initial PKA energy 1000 eV, initial temperature 300°C and initial PKA direction 2 from table 3.1 . . . . .	192
11	The number of defects formed during a cascade through graphite with initial PKA energy 1000 eV, initial temperature 300°C and initial PKA direction 2 from table 3.1 . . . . .	192
12	Distance travelled by atoms during a graphite cascade with initial PKA energy 1000 eV, initial temperature 300°C and initial PKA direction 2 from table 3.1 . . . . .	193

13	Graphite cascade with initial PKA energy 1500 eV, initial temperature 300°C and initial PKA direction 2 from table 3.1 . . . . .	194
14	The number of defects formed during a cascade through graphite with initial PKA energy 1500 eV, initial temperature 300°C and initial PKA direction 2 from table 3.1 . . . . .	194
15	Distance travelled by atoms during a graphite cascade with initial PKA energy 1500 eV, initial temperature 300°C and initial PKA direction 2 from table 3.1 . . . . .	195
16	Graphite cascade with initial PKA energy 2000 eV, initial temperature 300°C and initial PKA direction 15 from table 3.1 . . . . .	196
17	The number of defects formed during a cascade through graphite with initial PKA energy 2000 eV, initial temperature 300°C and initial PKA direction 15 from table 3.1 . . . . .	196
18	Distance travelled by atoms during a graphite cascade with initial PKA energy 2000 eV, initial temperature 300°C and initial PKA direction 15 from table 3.1 . . . . .	197

# I Low Energy Cascades Through Graphite

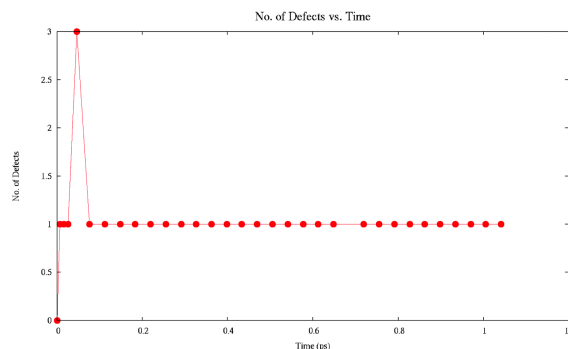
Figure 1 represents an example of a 50 eV cascade in graphite with initial PKA direction 2 from table 3.1.



**Figure 1:** Graphite cascade with initial PKA energy 50 eV after: (a) 0.007 ps, (b) 0.040 ps, (c) 0.140 ps and (d) 1.290 ps. Initial PKA direction 2 from table 3.1. The initial temperature is 300°C. The red circles denote interstitials and the blue squares denote vacancies. The path of each displaced atom is traced.

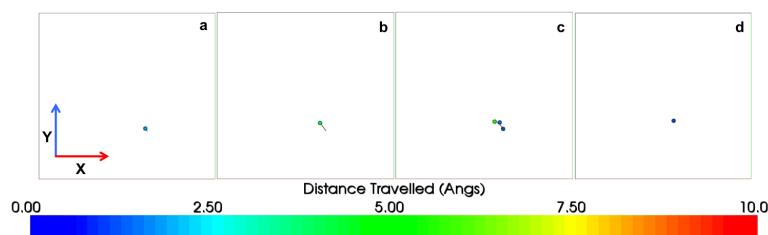
Figure 1 (a) shows the PKA leaving its initial position. After 0.04 ps, three defects and vacancies are present within the cell, figure 4.6 (b). The energy of the original PKA has been transferred during the collisions resulting in the atoms having an energy less than the threshold displacement energy. The PKA and a second carbon atom recombine into separate vacancies leaving the final displaced atom to form an interstitial. The final number of defects and vacancies present is one.

Figure 2 denotes the number of defects as a function of time. The PKA passes through several layers of the lattice before colliding. This is further evidence of channelling at low energies. The channelling can be seen on the graph between 0.007 and 0.046 ps. The peak on the graph represents the PKA colliding with atoms. Thus the PKA is no longer travelling in a channelled direction. Figure 2 plateaus to one defect after the initial peak as the PKA and one other second atom have re-combined within the lattice. The maximum number of defects during the cascade, three, occurs at 0.046 ps.



**Figure 2:** Graph indicating the number of defects present during a graphite cascade at 50 eV. Initial PKA direction 2 from table 3.1. The initial temperature is 300°C.

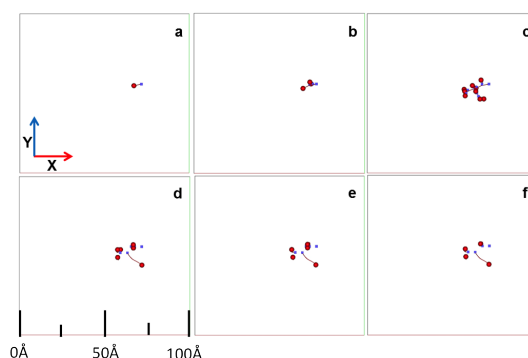
The distance the PKA travelled from the initial starting point can be seen in figure 3.



**Figure 3:** Graphite cascade with initial PKA energy 50 eV after: (a) 0.007 ps, (b) 0.021 ps, (c) 0.046 ps and (d) 2.006 ps. The initial temperature is 300°C. The colour of the scalar bar indicates the distance moved by atoms during the cascade. Initial PKA direction 2 from table 3.1.

The images in figure 3 show how far displaced atoms have travelled during the cascade. The final defect produced has travelled 1.20Å from its original lattice position, as expected at low energies, the displacement of the atoms is small. The PKA travelled the furthest through the cascade (figure 3 (c)), the PKA's final displacement was 5.54Å.

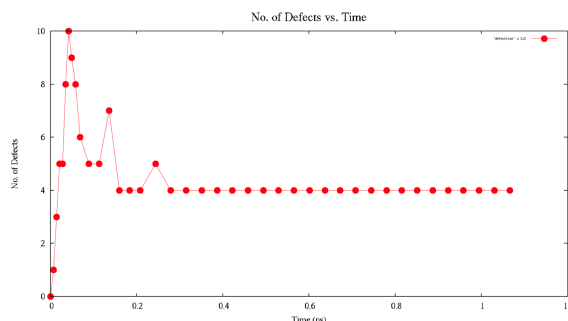
Figure 4 is an example of a cascade through graphite with an initial energy of 250 eV.



**Figure 4:** Graphite cascade with initial PKA energy 250 eV after: (a) 0.007 ps, (b) 0.021 ps, (c) 0.042 ps, (d) 0.058 ps, (e) 0.160 ps and (f) 2.138 ps. Initial PKA direction 15 from table 3.1. The initial temperature is 300°C. The red circles denote interstitials and the blue squares denote vacancies, the path of each displaced atom is traced.

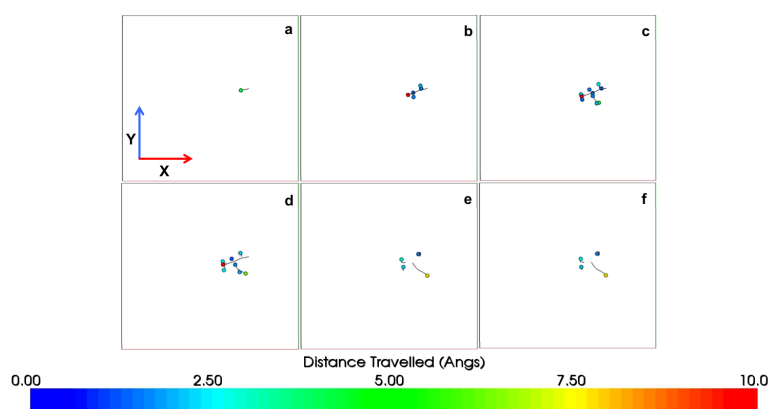
Figure 4 (a) represents the initial stage of the cascades at 0.007 ps. The PKA has left its initial position and travelled between the planes before colliding with a carbon atom at 0.010 ps (figure 4 (b)). The initial collision causes a cascade to be created. This can be seen clearly after 0.04 ps (figure 4 (c)). Each time a collision occurs, energy is transferred between atoms until the PKA's energy is less than the threshold energy and no further collisions can take place (figures 4 (d), (e) and (f)).

Figure 5 represents the total number of defects formed at any given point in time for this case. The maximum number of defects formed is 10 and this occurs 0.042 ps into the cascade. After 0.240 ps the graphite cell has stabilised leaving four defects and four vacancies.



**Figure 5:** Graph indicating the number of defects present during a graphite cascade at 250 eV. Initial PKA direction 15 from table 3.1. The initial temperature is 300°C.

The images in figure 6 symbolise the distance travelled by each atom in the cascade. The PKA has travelled the furthest through the cascade before coming to rest in a vacancy left by displaced carbon atom. The distance travelled by all other displaced atoms is less than 8Å. The total displacement of the PKA is 22.06Å.



**Figure 6:** Graphite cascade with initial PKA energy 250 eV after: (a) 0.007 ps, (b) 0.021 ps, (c) 0.042 ps, (d) 0.058 ps, (e) 0.160 ps and (f) 2.138 ps. The colour of the scalar bar indicates the distance moved by atoms during the cascade. Initial PKA direction 15 from table 3.1. The initial temperature is 300°C.

## II Mid-Range Energy Cascades Through Graphite

Figure 7 is an example of a cascade through graphite with an initial PKA energy of 500 eV.

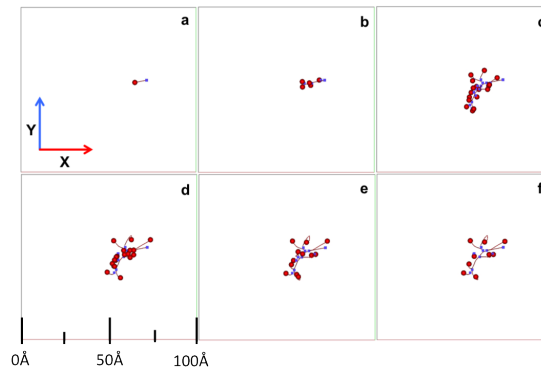


**Figure 7:** Graphite cascade with initial PKA energy 500 eV after: (a) 0.007 ps, (b) 0.010 ps, (c) 0.040 ps, (d) 0.110 ps, (e) 0.540 ps and (f) 4.400 ps. Initial PKA direction 15 from table 3.1. The initial temperature is 300°C. The red circles denote interstitials and the blue squares denote vacancies. The path of each displaced atom is traced.

Figure 7 (a) show the initial stage of the cascades at 0.007 ps. The PKA has left its initial position and has travelled between the planes before colliding with a carbon atom 0.010 ps (figure 7 (b)). As a direct result of the initial collision, a series of secondary cascades begin to form. The secondary cascades can be seen after 0.040 ps (figure 7 (c)). Figure 7 (d), is an example of channelling. Between 0.200 and 0.400 ps, displaced atoms have travelled through the graphite lattice without colliding with another atom. The carbon atoms which appear to have broken away from the main cascade clusters have continued to move through the lattice until colliding with further atoms and forming interstitials within the cell. One atom of particular interest collides with a carbon atom and rebounds back on its original path. This can be seen by observing the red trace line in figures 7 (e) and (f) (the atom of interest can be seen in the middle of the top row of atoms). The final number of interstitials and vacancies present after the cell has stabilised is nine.

During channelling, other atoms in the cell continue to cause collisions, form defects or come to rest in vacancies. Figure 8, shows the total number of defects throughout the cascade. Figure 8 shows a decrease in defect formation between 0.195 and 0.270 ps. This is the time period in which channelling occurs. The number of defects formed increases from 11 to 17 during the time period 0.270 and 0.360 ps. It is during this time the channelled atoms have collided and further secondary cascades are formed.

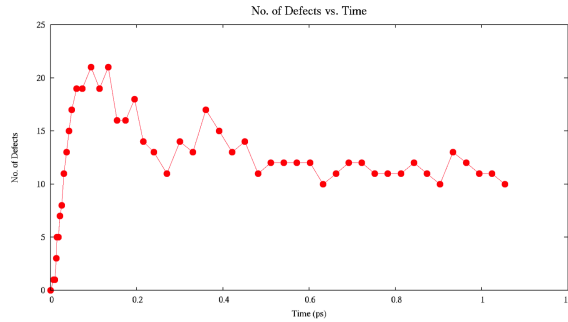


**Figure 8:** Graph indicating the number of defects present during a graphite cascade at 500 eV. Initial PKA direction 15 from table 3.1. The initial temperature is 300°C.

The images in figure 9 symbolise the distance travelled by each atom in the cascade. Figure 9 (e) and (f) clearly show one of the focused atoms which collided with a neighbouring carbon atom and as a result recoiled back into the lattice. The total distance travelled by all displaced atoms is less than 8.5Å and the final displacement of the PKA atom is 28.21Å.

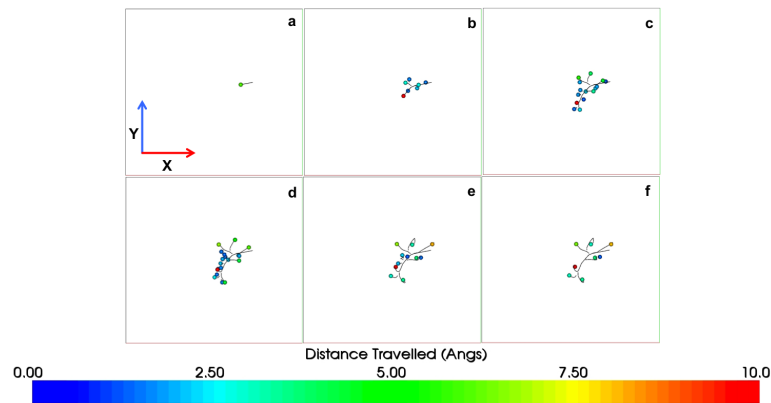


**Figure 9:** Graphite cascade with initial PKA energy 500 eV after: (a) 0.007 ps, (b) 0.022 ps, (c) 0.043 ps, (d) 0.060 ps, (e) 0.270 ps and (f) 3.195 ps. The colour of the scalar bar indicates the distance moved by atoms during the cascade. Initial PKA direction 15 from table 3.1. The initial temperature is 300°C.

Figure 10 is an example of a graphite cascade with an initial PKA energy of 1000 eV.

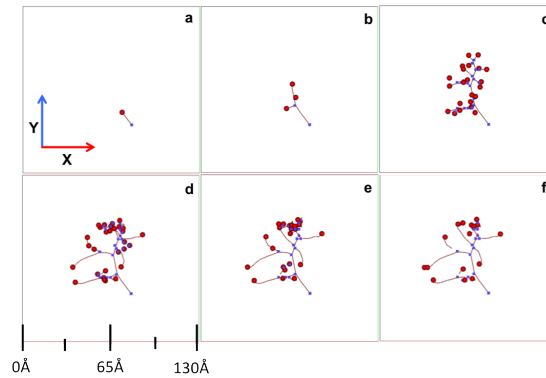


**Figure 10:** Graphite cascade with initial PKA energy 1000 eV after: (a) 0.00 ps, (b) 0.01 ps, (c) 0.04 ps, (d) 0.12 ps, (e) 0.23 ps and (f) 4.72 ps. Initial PKA direction 2 from table 3.1. The initial temperature is 300°C. The red circles denote interstitials and the blue squares denote vacancies, the path of each displaced atom is traced.

The initial behaviour of the PKA in figures 10 (a) and (b) follows closely to that of the 500 eV cascade (Chapter 4, figure 4.12) . However, at 0.04 ps (figure 10 (c)) the number of collisions occurring is so great, the energy transferred between each atom decreases rapidly. Whilst there are a great number of cascades occurring, the cascades stay clustered together. The interstitials begin to recombine at vacant lattice sites and by 0.23 ps the cell has stabilised. The final number of interstitials and vacancies present is 18.

Figure 10 demonstrated the cascades cluster behaviour, figure 11 supports this theory.

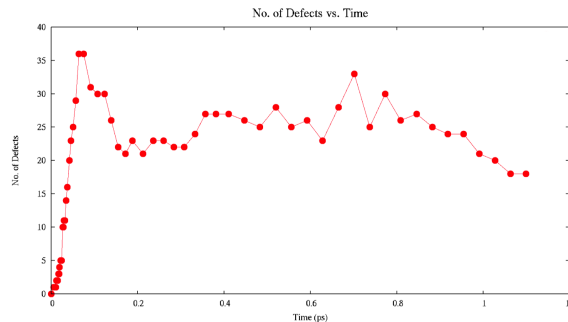


**Figure 11:** Graph indicating the number of defects present during a graphite cascade at 1000 eV. Initial PKA direction 2 from table 3.1. The initial temperature is 300°C.

Figure 11 shows an initial peak in the number of defects present. The maximum number of defects, 36, occurs at 0.064 ps. The graph does not plateau as has been seen with previous cascades. It continues to peak and trough. This behaviour is due to the formation of multiple low energy secondary cascades. The secondary cascades produced have small amounts of energy and therefore do not travel far from their initial lattice position.

Displaced atoms may have enough energy to recombine and then leave the lattice site causing defects to be created and resolved.

A clear way to view the cluster principle is by observing the distance travelled by displaced atoms. Figures 12 (c), (d), (e) and (f) highlight how in cluster regions atoms have minimal displacement. The majority of atoms in figure 12 (f) have a displacement greater than 3Å. This emphasises the point that the further from the original lattice site or cluster region the more likely an interstitial is to be formed. The PKA reaches its threshold energy at 0.030 ps and comes to rest forming an interstitial. The final displacement of the PKA is 7.25Å.

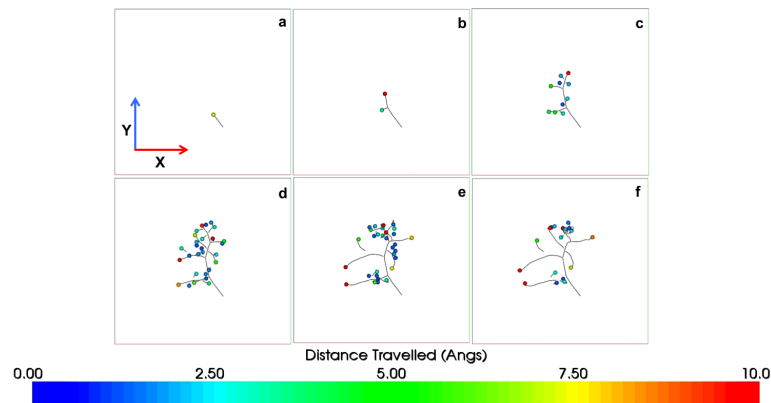


**Figure 12:** Graphite cascade with initial PKA energy 1000 eV after: (a) 0.006 ps, (b) 0.015 ps, (c) 0.028 ps, (d) 0.057 ps, (e) 0.107 and (f) 3.309 ps. The colour of the scalar bar indicates the distance moved by atoms during the cascade. Initial PKA direction 2 from table 3.1. The initial temperature is 300°C.

### III High Energy Cascades Through Graphite

Figure 13 is an example of a cascade through graphite with an initial PKA energy of 1500 eV.

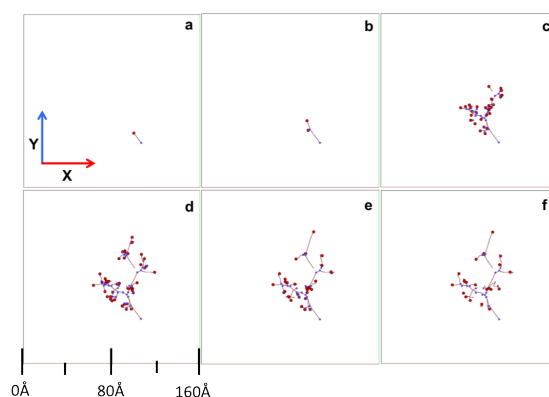


**Figure 13:** Graphite cascade with initial PKA energy 1500 eV after: (a) 0.007 ps, (b) 0.010 ps, (c) 0.040 ps, (d) 0.100 ps, (e) 0.180 ps and (f) 3.810 ps. Initial PKA direction 2 from table 3.1. The initial temperature is 300°C. The red circles denote interstitials and the blue squares denote vacancies. The path of each displaced atom is traced.

Figure 13 (a) shows the initial direction of the PKA. By 0.010 ps (figure 13 (b)) secondary cascades can be seen. As the cascade progresses, a collision causes the formation of two branches of cascades. This can be seen in figure 13 (c). By 0.100 ps (figure 13 (d)) there is a clearly defined path separating two regions of cascades. Figure 13 (e) and (f) show the cascade as it begins to stabilise. There is now one main region of defects and seven other defects which have formed away from the main cluster. The total number of interstitials and vacancies after completion of the cascade is 25.

Figure 14 represents the total number of displaced atoms at a given point in time during a graphite cascade with initial PKA energy 1500 eV.

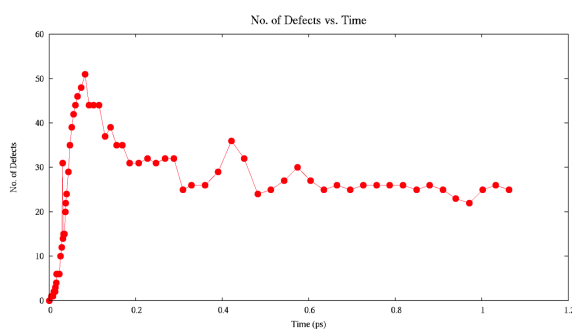


**Figure 14:** Graph indicating the number of defects present during a graphite cascade at 1500 eV. Initial PKA direction 2 from table 3.1. The initial temperature is 300°C.

Figure 14 shows an initial peak of defects, the maximum number of defects formed is 51 at 0.083 ps. After the initial peak of defects, the cascade follows a similar pattern to the cascade behaviour in the 1000 eV cascade, figure 11. As the cascade proceeds, the formation and recombination of carbon atoms

can be seen as a series of peaks and troughs until the cell begins to stabilise at 0.6 ps.

The distance travelled by displaced atoms is represented in figure 15.

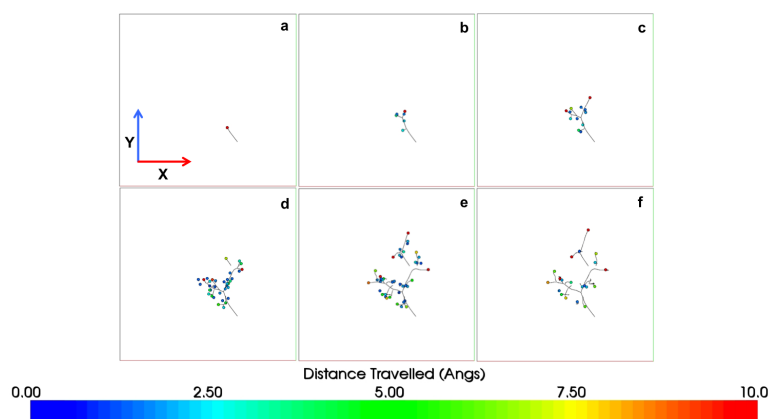


**Figure 15:** Graphite cascade with initial PKA energy 1500 eV after: (a) 0.008 ps, (b) 0.017 ps, (c) 0.029 ps, (d) 0.048 ps, (e) 0.115 and (f) 3.814 ps. The colour of the scalar bar indicates the distance moved by atoms during the cascade. Initial PKA direction 2 from table 3.1. The initial temperature is 300°C.

Figure 15 (a) shows the initial movement of the PKA. The PKA travels through two layers of the lattice before colliding with carbon atoms in the cell and creating a collision cascade. A collision between the PKA and a neighbouring carbon atom forces the PKA to differ from its original direction. The PKA continues to travel through the cell before forming an interstitial and coming to rest by 3.814 ps. The total displacement of the PKA is 8.17Å. Figures 15 (c) and (d) show little movement from displaced atoms. If we compare these two figures to figure 15 (e) there is significantly more movement and the distance travelled by a displaced atom has increased on average 25%. The majority of the final defects have moved over 3Å from their initial starting point, figure 15 (f).

Figure 16 shows a cascade through graphite with an initial PKA energy of 2000 eV.

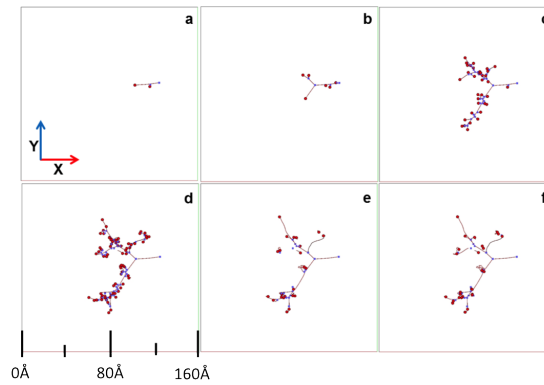


**Figure 16:** Graphite cascade with initial PKA energy 2000 eV after: (a) 0.007 ps, (b) 0.010 ps, (c) 0.040 ps, (d) 0.090 ps, (e) 0.220 ps and (f) 4.960 ps. Initial PKA direction 15 from table 3.1. The initial temperature is 300°C. The red circles denote interstitials and the blue squares denote vacancies. The path of each displaced atom is traced.

The PKA in figure 16 (a) collided with neighbouring atoms which initiated the formation of secondary collision cascades. Figure 16 (b) highlights a significant collision between the PKA and a neighbouring atom. The PKA transferred half of its remaining energy to the second carbon atom which resulted in the cascade being split into two main directions, figure 16 (c). The PKA and second carbon atom continued to travel through the cell colliding with other carbon atoms and creating further secondary collision cascades, figure 16 (d). The energy of the carbon atoms in the cell fell below the threshold energy resulting in atoms recombining within the lattice and the formation of defects. The final image of the 2000 eV cascade (figure 16 (f)) differs significantly to the final image of the cascade at 1500 eV (Chapter 4, figure 4.18). This difference occurs because of the collision at 0.010 ps in the 2000 eV cascade, a fact that is highlighted by the final number of defects present upon the cascades completion. The final number of interstitials and vacancies present after the cell has stabilised is 28.

Figure 17 shows the number of defects present throughout this cascade.

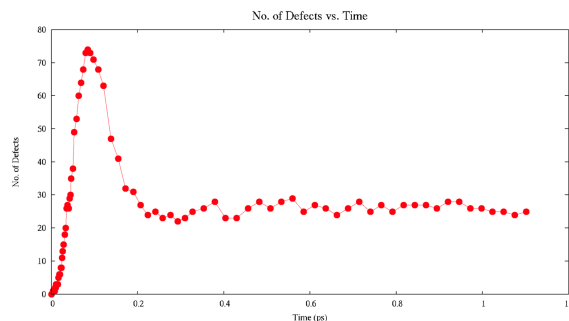


**Figure 17:** Graph indicating the number of defects present during a graphite cascade at 2000 eV. Initial PKA direction 15 from table 3.1. The initial temperature is 300°C.

Figure 17 reaches the maximum number of defects, 74, at 0.084 ps. No channelling occurred during this simulation, a fact which is supported by the absence of any further peaks.

Figure 18 represents the distance travelled by displaced atoms during a 2000 eV cascade.

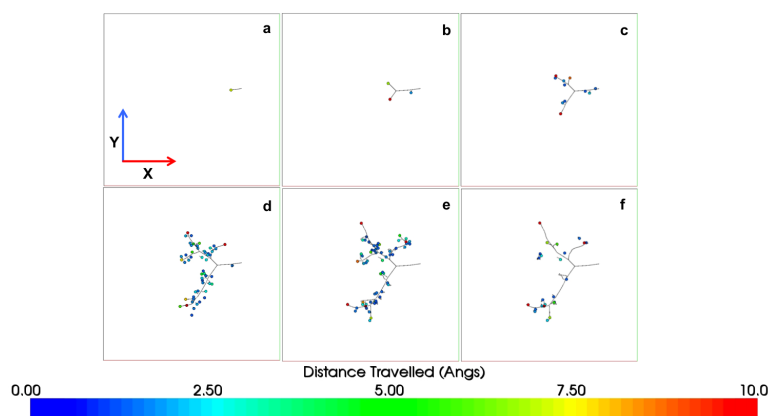


**Figure 18:** Graphite cascade with initial PKA energy 2000 eV after: (a) 0.004 ps, (b) 0.015 ps, (c) 0.025 ps, (d) 0.058 ps, (e) 0.121 ps and (f) 2.719 ps. The colour of the scalar bar indicates the distance moved by atoms during the cascade. Initial PKA direction 15 from table 3.1. The initial temperature is 300°C.

Figure 18 (b) allows the path of the PKA (denoted in red) to be followed after the initial head-on collision. The PKA continued to travel through the lattice at a 90° angle to the second carbon atom. In figure 18 (d) half of the displaced atoms had moved over 2.50Å and by the time the cell has stabilised (figure 18 (f)) four atoms had travelled over 10Å from their initial lattice site. The final displacement of the PKA was 41.78Å.

APPENDIX II

# **Cascades Through Carbon Materials**

# List of Figures

1	Diamond cascade with initial PKA energy 250 eV, initial cell temperature 300°C and initial PKA direction 1 from table 3.1 . . . . .	200
2	The number of defects formed during a cascade through diamond with initial PKA energy 250 eV, initial cell temperature 300°C and initial PKA direction 1 from table 3.1 . . . . .	200
3	The distance travelled by atoms during a diamond cascade with initial PKA energy 250 eV, initial cell temperature 300°C and initial PKA direction 1 from table 3.1 . . . . .	201
4	Diamond cascade with initial PKA energy 500 eV, initial cell temperature 300°C and initial PKA direction 1 from table 3.1 . . . . .	202
5	The number of defects formed during a cascade through diamond with initial PKA energy 500 eV, initial cell temperature 300°C and initial PKA direction 1 from table 3.1 . . . . .	202
6	The distance travelled by atoms during a diamond cascade with initial PKA energy 500 eV, initial cell temperature 300°C and initial PKA direction 1 from table 3.1 . . . . .	203
7	Diamond cascade with initial PKA energy 1500 eV, initial cell temperature 300°C and initial PKA direction1 from table 3.1 . . . . .	203
8	The number of defects formed during a cascade through diamond with initial PKA energy 1500 eV, initial cell temperature 300°C and initial PKA direction 1 from table 3.1 . . . . .	204
9	The distance travelled by atoms during a diamond cascade with initial PKA energy 1500 eV, initial cell temperature 300°C and initial PKA direction 1 from table 3.1 . . . . .	205

Further examples of cascades through diamond are presented within this appendix.

Figure 1 is an example of a cascade through diamond with an initial PKA energy of 250 eV.

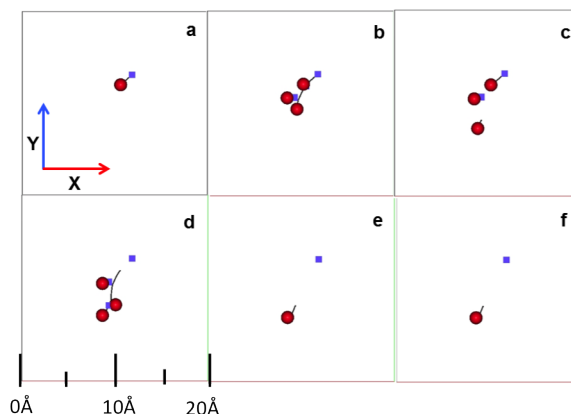


**Figure 1:** Diamond cascade with initial PKA energy 250 eV after: (a) 0.004 ps, (b) 0.013 ps, (c) 0.025 ps, (d) 0.031 ps, (e) 0.168 ps and (f) 0.621 ps. Initial PKA direction 1 from table 3.1. The initial temperature is 300°C. The red circles denote interstitials and the blue squares denote vacancies. The path of each displaced atom is traced.

The initial path of the cascade is denoted in figure 1 (a). The PKA collided with two atoms which resulted in the formation of three interstitials and three vacancies, figure 1 (b). Energy transferred during the collisions allowed the displaced atoms to cause further secondary collisions, figure 1 (d). The PKA and a further two displaced atoms recombined with the lattice in vacancy sites leaving one interstitial and one vacancy present in the final cell.

Figure 2 shows the total number of displaced atoms in the lattice at any given point in time during this simulation.

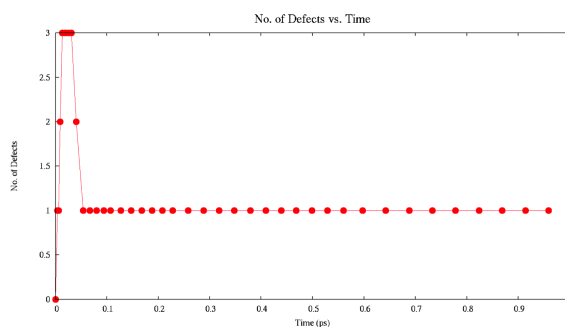
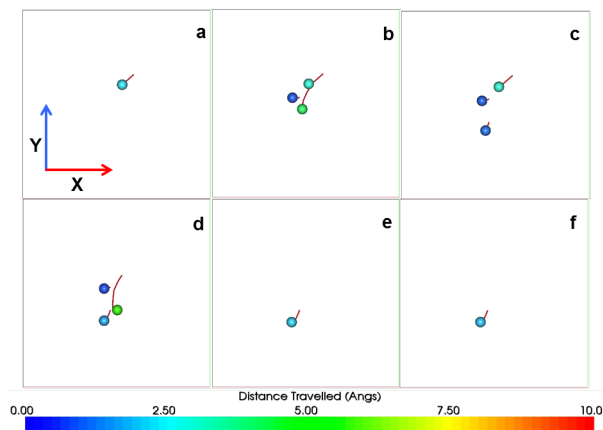


**Figure 2:** Graph indicating the number of defects present during a graphite cascade at 250 eV. Initial PKA direction 1 from table 3.1. The initial temperature is 300°C.

The maximum number of displaced atoms three, occurs 0.013 ps into the

cascade. Displaced atoms recombined in vacancies created in the lattice site before stabilising 0.054 ps into the cascade (figure 2).

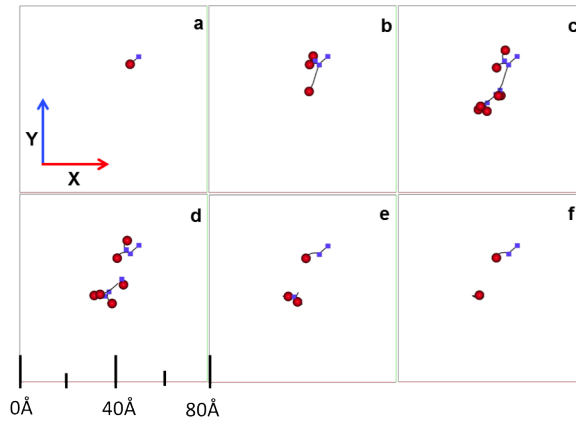
Figure 3 tracks the distance travelled by displaced atoms during a cascade with initial PKA energy 250 eV.



**Figure 3:** Diamond cascade with initial PKA energy 250 eV after: (a) 0.004 ps, (b) 0.013 ps, (c) 0.025 ps, (d) 0.031, (e) 0.168 and (f) 0.959 ps. The colour of the scalar bar indicates the distance moved by atoms during the cascade. Initial PKA direction 1 from table 3.1. The initial temperature is 300°C.

Figures 3 (a), (b) and (c) track the path of the PKA before it re-combined in a vacancy site 0.031 ps into the cascade (figure 3 (d)). The total distance travelled by any atom is less than 5 Å and the final displacement of the PKA was 2.329 Å.

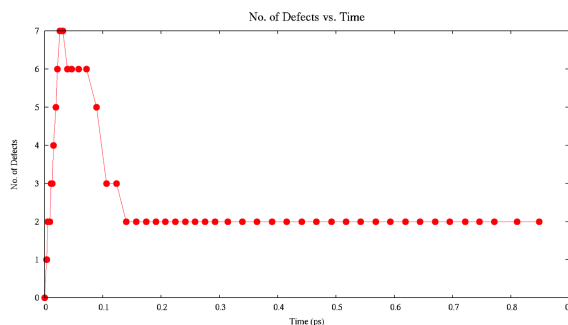
Figure 4 is an example of a diamond cascade with an initial PKA energy of 500 eV.



**Figure 4:** Diamond cascade with initial PKA energy 500 eV after: (a) 0.003 ps, (b) 0.011 ps, (c) 0.026 ps, (d) 0.046 ps, (e) 0.123 ps and (f) 0.848 ps. Initial PKA direction 1 from table 3.1. The initial temperature is 300°C. The red circles denote interstitials and the blue squares denote vacancies, the path of each displaced atom is traced.

Figure 4 (b) demonstrates initial defect production during a diamond cascade. Displaced atoms collided with carbon atoms in the cell resulting in further displaced atoms being seen. After 0.026 ps passed, there were seven defects present in the cell. The energy of the displaced atoms fell below the threshold displacement energy. A shock wave passed through the cell but did not cause any damage to the overall lattice. As the energy of displaced atoms fell, the atoms recombined in the lattice at vacancy sites or formed interstitials. There were two defects present in the final cell.

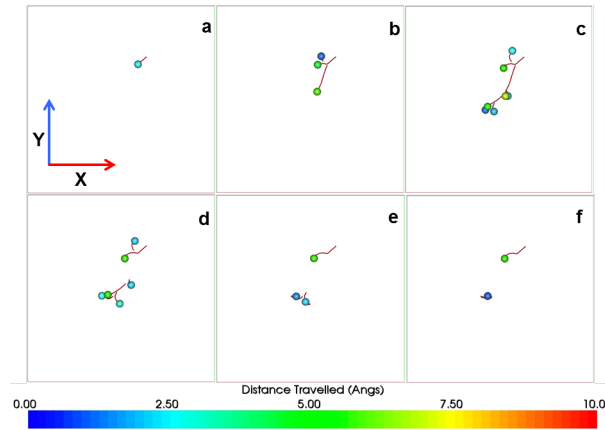
Figure 5 tracks the total number of displaced atoms as a function of time.



**Figure 5:** Graph indicating the number of defects present during a graphite cascade at 500 eV. Initial PKA direction 1 from table 3.1. The initial temperature is 300°C.

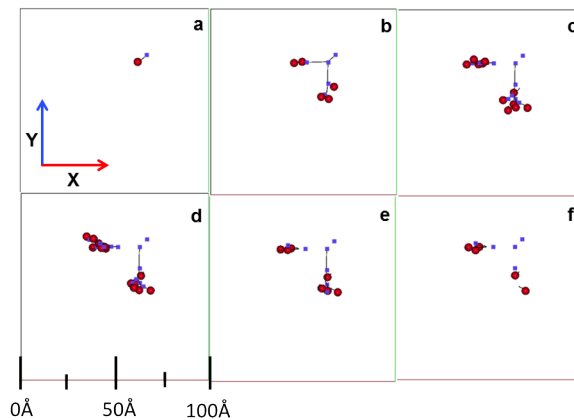
Figure 5 has a maximum number of displaced atoms, seven occurring at 0.026 ps. Unlike graphite cascades, there is no evidence of channelling and the cell stabilised after 0.140 ps leaving two remaining defects present.

Figure 6 follows the paths of displaced atoms during the cascade.



**Figure 6:** Diamond cascade with initial PKA energy 500 eV after: (a) 0.003 ps, (b) 0.011 ps, (c) 0.026 ps, (d) 0.046, (e) 0.123 and (f) 0.848 ps. The colour of the scalar bar indicates the distance moved by atoms during the cascade. Initial PKA direction 1 from table 3.1. The initial temperature is 300°C.

Figure 6 (b) shows the aftermath of the primary collision between the PKA and a further two neighbouring carbon atoms in the lattice. The PKA remained in a fixed interstitial position after 0.026 ps into the cascade (figure 6 (c)). The second displaced atom travelled through the cell creating secondary collision cascades. Figure 6 (d) shows no displaced atoms travelled a distance greater than 5Å. The path of the PKA can be tracked through figures 6 (a), (b), (c), (d), (e) and (f) and had a final displacement of 5.416Å. Figure 7 is an example of a diamond cascade with an initial PKA energy of 1500 eV.



**Figure 7:** Diamond cascade with initial PKA energy 1500 eV after: (a) 0.003 ps, (b) 0.017 ps, (c) 0.038 ps, (d) 0.074 ps, (e) 0.141 ps and (f) 0.858 ps. Initial PKA direction 1 from table 3.1. The initial temperature is 300°C. The red circles denote interstitials and the blue squares denote vacancies, the path of each displaced atom is traced.

The cascade in figure 7 followed a similar path to the 1000 eV cascade (Chapter 5, figure 5.8). Two branches of cascades were created as a result of a primary collision with the PKA, figure 7 (b). Due to the higher value of initial energy which was given to the PKA, the cascades penetrated further through the cell before a cluster of defects was formed (7 (c)). The energy of the displaced atoms decreased with each collision. This resulted in the displaced atoms coming to rest in vacancies or forming interstitials (figure 7 (e)). Figure 7 (f) shows the final lattice which had six interstitials and six vacancies present.

Figure 8 shows the maximum number of defects present as a function of time.

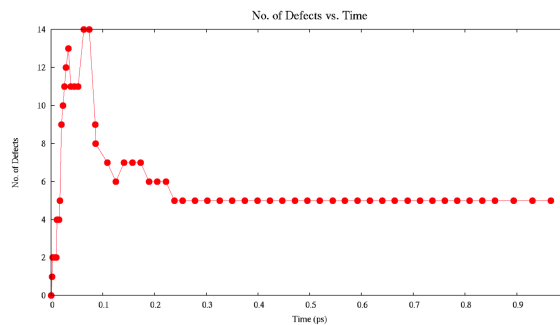


**Figure 8:** Graph indicating the number of defects present during a graphite cascade at 1500 eV. Initial PKA direction 1 from table 3.1. The initial temperature is 300°C.

As a result of the primary collision of the PKA, the formation of the two branches of cluster defects saw a greater period of time pass before the maximum number of defects was observed. The maximum number of 14 defects occurred 0.063 ps into the cascade. The cascade then stabilised at 0.238 ps leaving five defects present in the final lattice.

Figure 9 tracks the distance travelled by displaced atoms.

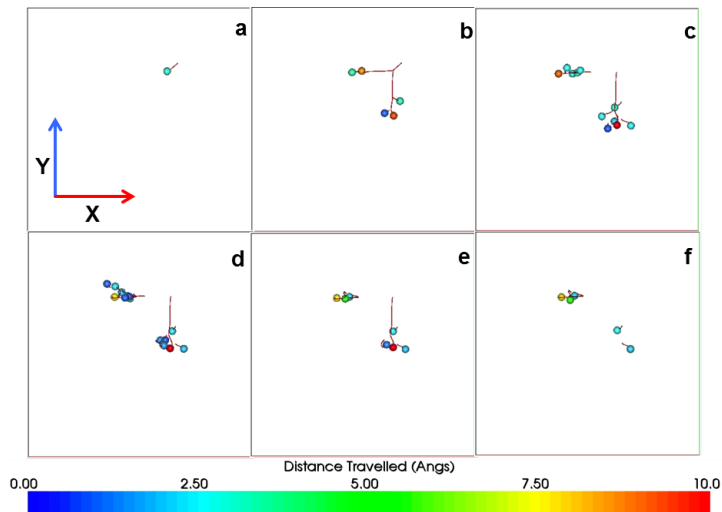


**Figure 9:** Diamond cascade with initial PKA energy 1500 eV after: (a) 0.003 ps, (b) 0.017 ps, (c) 0.038 ps, (d) 0.074, (e) 0.141 and (f) 0.858 ps. The colour of the scalar bar indicates the distance moved by atoms during the cascade. Initial PKA direction 1 from table 3.1. The initial temperature is 300°C.

Figure 9 (b) shows the aftermath of the primary collision with the PKA. At 1500 eV displaced atoms penetrated further through the lattice with some atoms travelling distances over  $5\text{\AA}$ , figure 9 (c). Figure 9 (f) shows the final lattice, the defects present have travelled distances less than  $7.5\text{\AA}$  from their initial lattice site. The final displacement of the PKA was  $8.381\text{\AA}$ .

## APPENDIX III

# Publications

1. **H. J. Christie**, M. Robinson, D. L. Roach, D. K. Ross, I. Suarez-Martinez and N. A. Marks, *Simulating Radiation Damage Cascades in Graphite*, (In press, Carbon (2014))
2. **H. J. Christie**, M. Robinson, D. L. Roach, D. K. Ross, I. Suarez-Martinez and N. A. Marks, *A Comparative Study Between Graphite and Non-Graphitic Carbon Allotropes* (To be submitted to Carbon (2014))
3. D. L. Roach, A. C. Hannon, D. K. Ross, **H. J. Christie**, A. N. Jones, L. McDermott and B. J. Marsden *Investigation of the Structure of Irradiated Graphites from Neutron Diffraction* (In preparation for Carbon (2014))
4. **H. J. Christie**, D. L. Roach, D. K. Ross, M. Robinson and N. A. Marks *A Molecular Dynamics Study of Channelling and Focusing Effects for Radiation Damage Cascades in Graphite* (In preparation (2015))

## Conference Contributions

5. **H. J. Christie**, D. L. Roach and D. K. Ross, *Molecular Dynamics Simulations of Cascades in Nuclear Graphite*, The Annual College of Science and Technology Research Showcase 2014, Salford, UK, 18th June 2014 (Poster Presentation)
6. **H. J. Christie**, D. L. Roach, N. Marks and D. K. Ross, *Molecular Dynamics Simulations of Cascades in Nuclear Graphite*, 4th CSE PG Conference, Salford, UK, 13th November 2013 (Oral Presentation)
7. **H. J. Christie**, D. L. Roach, D. K. Ross, M. Robinson, I. Suarez-Martinez, A. McKenna, M. Heggie, *Molecular Dynamic Simulations of Cascades in Nuclear Graphite*, INGSM-14, Seattle, USA, 15th - 18th September 2013 (Oral Presentation)

8. **H. J. Christie**, *Radiation Damage in Graphite*, The Annual College of Science and Technology Research Showcase 2013, Salford, UK, 19th June 2013 (Poster Presentation)
9. **H. J. Christie**, M. Robinson, D. L. Roach, D. K. Ross, I. Suarez-Martinez and N. A. Marks, *Molecular Dynamic Simulations of Cascades in Graphite*, Salford Postgraduate Annual Research Conference, Salford, UK, 6th - 7th June 2013 (Oral Presentation)
10. **H. J. Christie**, M. Robinson, D. L. Roach, D. K. Ross, I. Suarez-Martinez and N. A. Marks, *Cascade Simulations in Carbon Based Materials*, Salford Postgraduate Annual Research Conference, Salford, UK, 6th - 7th June 2013 (Poster Presentation)
11. **H. J. Christie**, M. Robinson, D. L. Roach, D. K. Ross, I. Suarez-Martinez and N. A. Marks, *Molecular Dynamic Simulations of Cascades in Graphite*, ISIS User Group Meeting, Warwick University, UK, 8th - 9th April 2013 (Poster Presentation)
12. N. Marks, M. Robinson, I. Suarez-Martinez, **H. J. Christie**, D. Roach, D. K. Ross, A. McKenna, M. Heggie, *Radiation Damage in Nuclear Graphite*, 2012 MRS Fall Meeting and Exhibit, Boston, USA, 25th - 30th November 2012
13. **H. J. Christie**, D. L. Roach, N. Marks and D. K. Ross, *Molecular Dynamics Simulations of Cascades in Nuclear Graphite*, 3rd CSE PG Conference, Salford, UK, 14th November 2012 (Oral Presentation)
14. **H. J. Christie**, *Radiation Damage in Graphite*, The Annual College of Science and Technology Research Showcase 2012, Salford, UK, 20th June 2012 (Poster Presentation)

# Simulating Radiation Damage Cascades in Graphite

H. J. Christie,<sup>1</sup> M. Robinson,<sup>2</sup> D. L. Roach,<sup>1</sup> D. K. Ross,<sup>1</sup> I. Suarez-Martinez,<sup>2</sup> and N. A. Marks<sup>3</sup>

<sup>1</sup>*Physics and Materials Research Centre, School of Computing,  
Science and Engineering, University of Salford, Salford, Greater Manchester, UK*

<sup>2</sup>*Nanochemistry Research Institute, Department of Chemistry, Curtin University, Perth, Australia*

<sup>3</sup>*Discipline of Physics and Astronomy, Curtin University, Perth, Australia\**

(Dated: June 1, 2014)

Molecular dynamics simulation is used to study radiation damage cascades in graphite. High statistical precision is obtained by sampling a wide energy range (100–2500 eV) and a large number of initial directions of the primary knock-on atom. Chemical bonding is described using the Environment Dependent Interaction Potential for carbon. Graphite is found to exhibit a radiation response distinct from metals and oxides primarily due to the absence of a thermal spike which results in point defects and disconnected regions of damage. Other unique attributes include exceedingly short cascade lifetimes and fractal-like atomic trajectories. Unusually for a solid, the binary collision approximation is useful across a wide energy range, and as a consequence residual damage is consistent with the Kinchin-Pease model. The simulations are in agreement with known experimental data and help to clarify substantial uncertainty in the literature regarding the extent of the cascade and the associated damage.

PACS numbers: 81.05.uf,61.43.Bn,61.80.-x

## I. INTRODUCTION

Despite being one of the original nuclear materials, remarkably few molecular dynamics simulations have been performed to understand radiation response in graphite. Whereas a vast computational literature exists for radiation processes in metals and oxides (see Refs. 1–4 for reviews) only a handful of simulations exist for graphite due to historical difficulties associated with describing bonding in carbon.<sup>5</sup> Aside from point defect energetics,<sup>6,7</sup> and threshold displacement energies,<sup>8–10</sup> little is known atomistically about cascade behaviour, recovery following ballistic displacement or temperature-driven dynamical effects. In a modern context, understanding of radiation processes in graphite is motivated by lifetime extensions of existing graphite-moderated reactors,<sup>11,12</sup> and future Generation-IV technologies such as the high-temperature graphite-moderated design.<sup>13</sup>

The simulation of radiation damage using molecular dynamics (MD) has a long history, extending back to the first ever MD publication in 1960 on focussed collision sequences in copper.<sup>14</sup> A great number of radiation cascade simulations were performed over the following decades, facilitated by the development of the embedded atom method<sup>15,16</sup> for metals and Buckingham-type potentials<sup>17,18</sup> for ionic solids and oxides. At first glance many cascades look the same, commencing with a ballistic phase in which the kinetic energy of the primary knock-on atom (PKA) is rapidly deposited into a small region, followed by transient localised melting in the form of a thermal spike, and concluding with rapid cooling and partial recrystallization. Depending on the material type and chemistry, the entire process results in disordered structures such as stacking fault tetrahedra, isolated point defects, amorphous pockets or extended defect clusters. For highly radiation tolerant materials

(e.g. rutile TiO<sub>2</sub> [Ref. 19]) it is even possible to have no residual defects at all, such is the extent of the driving force towards the crystalline state. Regardless of the outcome, the behavior is typically dictated by an interplay between the native crystal structure and dynamic recombination/annealing of defects.

To the best of our knowledge, the first reported simulation of radiation cascade effects in graphite was performed in 1990 by Smith,<sup>20</sup> who used the Tersoff potential<sup>21</sup> to study self-sputtering and related phenomena. Further work by Smith and Beardmore<sup>8</sup> expanded the computational techniques to include potentials proposed by Brenner<sup>22</sup> and Heggie<sup>23</sup> and examined bombardment with Ar and C<sub>60</sub> species. Key results included quantification of ion-surface interactions and an estimate of the threshold displacement energy  $E_d$  of 34.5 eV. Similar studies were performed by Nordlund *et al.*<sup>24</sup> using a long-range extension of the Tersoff potential to quantify defect creation responsible for hillocks observed at the surface of graphite. Their potential has been used to study ion irradiation in a variety of sp<sup>2</sup> carbon systems [for a comprehensive review see Ref. 25] but it has not been applied to damage cascades in graphite. In work motivated by next-generation reactor design, Hehr *et al.*<sup>10</sup> modified the Brenner potential to study temperature-dependance of  $E_d$ , finding values of 44.5 eV at 300 K and 42.0 eV at 1800 K. They did not, however, report any calculations of radiation damage cascades.

Here we report graphite cascade simulations using the Environment Dependent Interaction Potential (EDIP) for carbon<sup>26,27</sup> coupled with the standard Ziegler-Biersack-Littmack (ZBL) potential<sup>28</sup> to describe close-range pair interactions. Originally developed to study thin film deposition of amorphous carbon, EDIP has since been applied to study numerous other carbon forms including carbon onions,<sup>29,30</sup> glassy carbon,<sup>30,31</sup>

peapods,<sup>32</sup> nanotubes<sup>30,33</sup> and nanodiamond.<sup>34</sup> Our article is structured as follows: in Section II we detail our methodology for linking the EDIP and ZBL potentials and outline our procedure for performing simulations and defect analysis. In Section III we consider first the qualitative behaviour of cascades in graphite, considering specific examples which illustrate binary-collision-type behavior and channeling. This is followed by quantitative analysis averaged over a large number of PKA directions, examining cascade properties such as timescale, length scale and defect production. We conclude in Section IV with a discussion of how radiation damage in graphite is fundamentally different to metals and oxides and link our results with historical models in the literature.

## II. METHODOLOGY

The radiation damage cascades are simulated using molecular dynamics (MD) with equilibrium interactions governed by the Environmental Dependent Interatomic Potential (EDIP) for carbon.<sup>26,27</sup> The potential is based on an earlier EDIP potential for silicon,<sup>35</sup> where the key elements are two-body and three-body interactions modulated by an atomic bond-order term derived from the coordination. The carbon variant of EDIP includes a more sophisticated aspherical coordination counting term which provides an excellent description of bond-making and breaking, in particular the energy barrier for conversion between  $sp^2$  and  $sp^3$  hybridization such as occurs in the graphite/diamond transformation. Its ability to also accurately describe disordered states makes EDIP ideal for studying radiation damage.

To accurately model the close-range interactions between atoms the pair potential within the EDIP formalism, is smoothly switched to the Ziegler-Biersack-Littmark (ZBL) pair potential [Ref. 28]. Due to the environmental dependence, this transition is less straightforward than with pair potentials where interpolation functions such as cubic splines can be used to connect the potentials. Our approach uses two Fermi-type scaling functions ( $SF_{EDIP}$ ,  $SF_{ZBL}$ ) which are defined using three parameters; the positions of the midpoint of each function ( $r_{EDIP}$  and  $r_{ZBL}$ ) and the width  $w$  of the switching region. After a trial-and-error process, values of  $r_{EDIP}=1.05$  Å,  $r_{ZBL}=0.45$  Å, and  $w=0.07$  Å were selected to ensure a smooth transition between the two regimes and to avoid inflexion points associated with changes in curvature. A plot of the switching functions along with the effective pair potential for a coordination number of three are shown in Fig. 1. Note that this is the same approach as employed in previous EDIP simulations of ion impact<sup>36,37</sup> where the scaling function approach was first introduced and briefly defined.

Simulations were carried out in lattices equilibrated at 300 K and after the PKA was initiated the motion was followed for 5 ps. At the conclusion of the simulation steepest descent minimization was performed prior

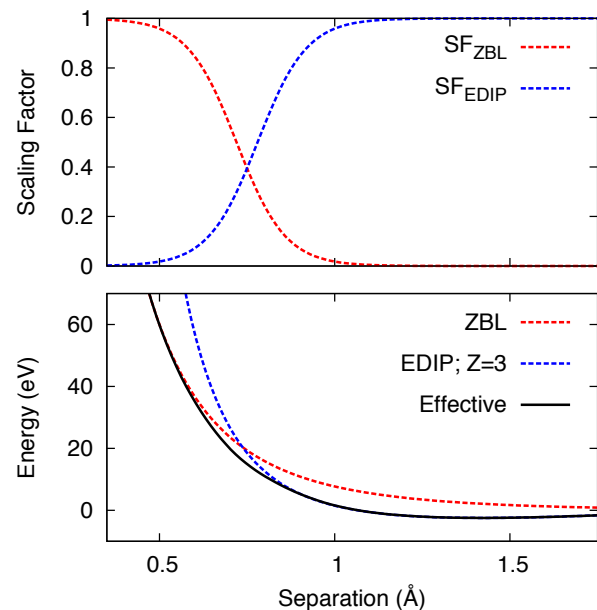


FIG. 1. Top panel: Fermi-type scaling function applied to connect the EDIP and ZBL pair potentials. Bottom panel: Example curves for a coordination number  $Z=3$  illustrating the application of the scaling functions. Note that the intersection between the two pair potentials varies as a function of  $Z$ , and that  $Z$  can be non-integral.

to defect analysis. Periodic boundary conditions were employed in each of the cartesian directions along with a 3.5 Å thermal layer to remove excess kinetic energy during the cascade simulations. In addition, a layer of atoms perpendicular to the basal plane were held fixed to prevent any net transverse motion of the planes. To produce a representative set of collision cascades, a range of PKA energies and directions of initial velocity were sampled. Cascades were initiated with PKA energies of 100, 250, 500, 750, 1000, 1500, 2000 and 2500 eV within orthorhombic supercells as large as  $157.7 \times 152.6 \times 153.6$  Å<sup>3</sup> and containing up to 440,448 atoms. As in the work of Robinson *et al.*,<sup>38</sup> the initial directions of the PKA were determined by uniformly distributing points on a unit sphere (the so-called Thomson problem<sup>39</sup>) to select the direction of the initial velocity. This methodology allows for an arbitrary number of directions to be chosen. The data presented here is a composite of two uncorrelated data sets, one with 10 uniformly distributed data points and a second containing 20 points. To assist in retaining the cascade within the simulation cell, the location of the PKA atom was chosen such that the direction of initial motion was towards the centre of the supercell.

Cascades were analysed using various quantitative measures. The number of defects were computed using a vacancy radius  $v_r$  of 0.9 Å. This value was also used to determine atomic displacements. Coordination numbers are determined using a nearest-neighbour cutoff of 1.85 Å. At higher PKA energies the graphite planes are

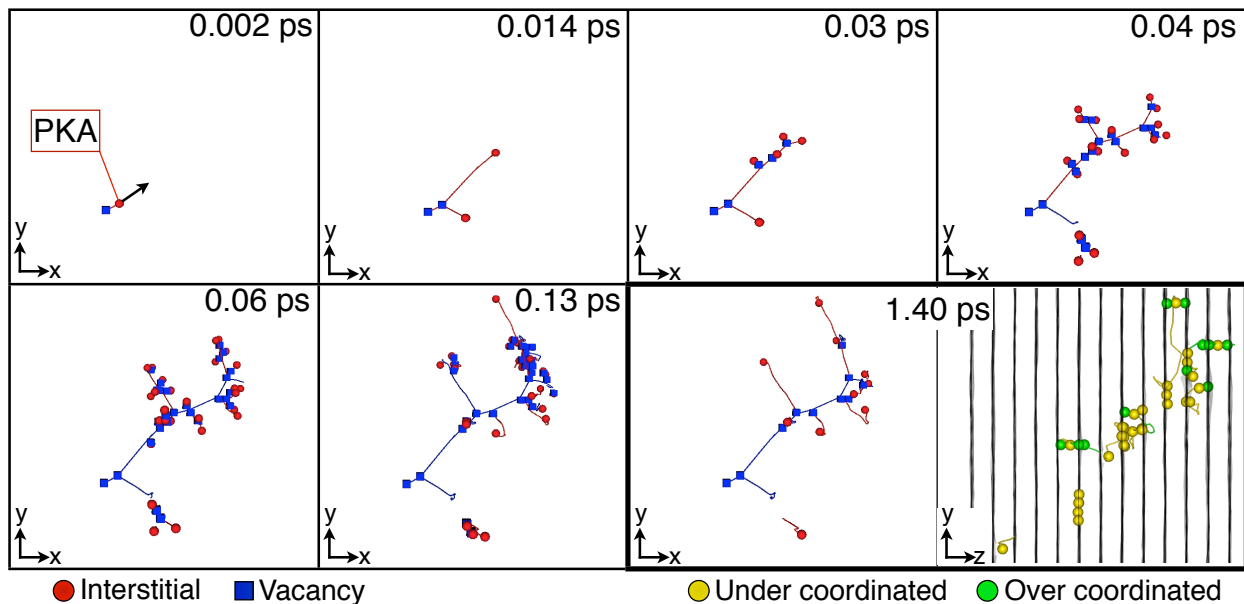


FIG. 2. Typical cascade in graphite with a 1 keV primary knock-on atom (PKA). Interstitials and vacancies are shown as red circles and blue squares respectively. For the time-series snapshots the atoms which remain on crystalline lattice sites are not shown. Panel (a) shows the system shortly after the PKA is initiated, while panel (g) is the final state. In the final image [panel (h)] atoms which are over- and under-coordinated are shown as green and yellow spheres respectively. This is the same structure as the final state, differing only in the rotation of the view to highlight the graphitic planes shown in gray.

prone to a degree of buckling which can hinder the calculation of both displacements and defects. This problem is circumvented by determining the components of displacement perpendicular to the basal plane for all 3-fold coordinated atoms. If the magnitude of this displacement lies within a pre-defined range of  $0.7 \text{ \AA}$  and  $2v_r$ , then these atoms are removed from further defect analysis.

### III. RESULTS

#### A. Individual Cascades

Figure 2 shows a representative example of a 1 keV cascade in graphite. Blue squares denote vacancies while red circles denote interstitials. In the first frame ( $t=0.002 \text{ ps}$ ) the PKA has moved on the order of the vacancy radius and has left behind a vacancy; the initial direction of the PKA is indicated by the arrow. After 0.014 ps the PKA has already experienced a close-approach collision with another carbon atom, effectively splitting into two sub-cascades. In the third and fourth frame ( $t=0.03$  and  $0.04 \text{ ps}$ ) it is clear that the upper sub-cascade is the more energetic of the two and continues to exhibit a branching structure with each successive collision. In contrast, the less energetic sub-cascade is already close to its end-of-range point. By 0.06 ps the entire cascade is close to maximum extent, with most of the remaining excess kinetic energy concentrated in a handful of atoms. At

0.13 ps the atoms no longer have sufficient energy to create new defects and self-induced annealing becomes the dominant process. The relaxation process is extremely rapid, and the structure at 1.40 ps is essentially identical to that when the simulation concludes. By this stage the number of defects has decreased considerably, from a peak of 37 interstitials at 0.11 ps, to 10 at 1.40 ps.

The final frame at the bottom-right of Fig. 2 shows an alternative view of the final structure, involving a rotation to highlight the cascade relative to the graphitic planes and a colour-coding to indicate variations from the standard coordination number of three. At the bottom left a single undercoordinated atom results from the vacancy created by the PKA, while the green overcoordinated atoms mostly arise in the graphitic planes adjacent to an interstitial atom position between two-layers, thereby increasing the coordination number of the in-layer atoms to four. This is particularly apparent for the defect complex at the top of the panel where the yellow trajectory trace follows the path of the mobile atom which has moved between adjacent layers for a short distance, eventually creating an interlayer defect. Density functional theory calculations<sup>40</sup> have identified a closely related configuration, known as the spiro interstitial due to its resemblance to the spiro-pentane molecule. Some of the structural details of the spiro interstitial (specifically, the two sets of triangular C-C bonds) differ to the MD simulation, but the origin of the discrepancy is well-known and arises from neglect of three-centre terms,

a common approximation in pair potentials and tight-binding methodologies.<sup>41</sup> The key observation is that the interlayer defect is indeed prevalent in the simulations and is strongly correlated with over-coordinated atoms created by interstitials.

One of the striking features in Fig. 2 is the fractal-like branching structure of the defect trajectories. This arises from the highly energetic collisions involving the PKA and subsequently displaced lattice atoms. To convey a sense of the strength of these interactions we computed the maximum kinetic energy of any atom,  $KE_{\max}$ , and plotted this quantity as a function of time (see Fig. 3). The arrows in the figure highlight the moments of close approach in which the PKA (or another more energetic atom) interacts strongly with an atom on a lattice site. At the instant of closest approach the velocities are transiently very small and the forces are enormous; the repulsion between the two atoms then splits the cascade and converts potential energy into kinetic energy spread between the two atoms. Correspondingly, each branching point seen in the time-series snapshots of Fig. 2 can be correlated to one of the close-approaches denoted by the arrows in Fig. 3.

Consideration of the details in Fig. 3 reveals an aspect which is initially surprising, namely, an extremely short time period when atoms have substantial kinetic energy. Cascade simulations in metals and oxides with PKA energies in the keV range typically evolve on the timescale of a picosecond or so, and yet here the maximum kinetic energy has fallen below 10 eV after just 90 fs. To quantify this behavior we counted the number of atoms with a kinetic energy exceeding thresholds of 1 and 10 eV. The latter is a measure of the number of “fast atoms” which might be reasonably expected to be associated with motion of atoms to a different lattice site or defect configura-

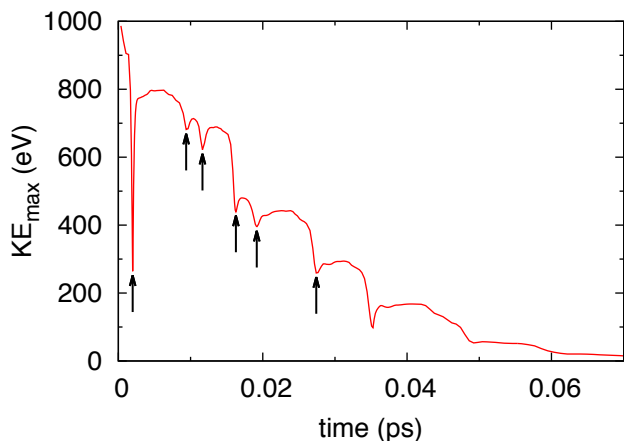


FIG. 3. Kinetic energy of the most energetic atom as a function of time in the 1 keV cascade in Fig. 2. Vertical arrows indicate collisions with small impact parameters that transfer large amounts of kinetic energy to a lattice atom and effectively split the cascade into separate trajectories.

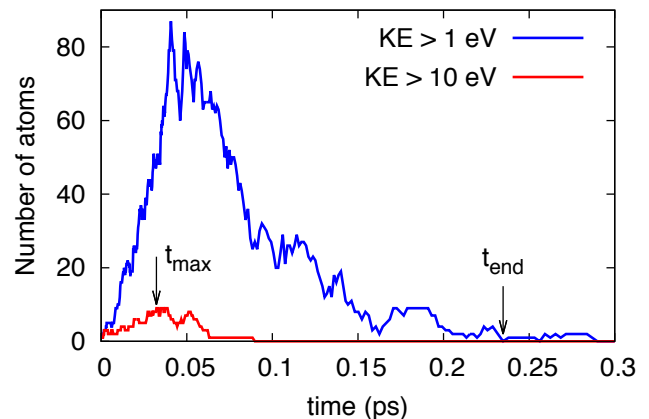


FIG. 4. Number of atoms with kinetic energy greater than 10 eV (red line) and 1 eV (blue line) in a 1 keV cascade as a function of time. Data applies for the cascade shown in Fig. 2. The arrows indicate two key cascade quantities  $t_{\max}$  and  $t_{\text{end}}$  as defined in the text.

tion, while the lower threshold conveys a sense of the rate at which the high thermal conductivity of the surrounding matrix removes heat from the cascade. Figure 4 plots the time-dependence of both quantities and confirms the earlier impression from Fig. 3. The maximum number of fast atoms (red trace) is achieved after just 32 fs, while the number of “warm atoms” (blue trace) first reduces to zero at 235 fs. These two quantities are indicated by arrows in Fig. 4, and in preparation for later use we denote them  $t_{\max}$  and  $t_{\text{end}}$ , respectively. This exceptionally rapid time evolution is common to all cascades considered in this study and is quantified statistically in the following section. Given the striking difference compared to other materials we calculated the speed of sound in a diamond rod, and reproduced the known experimental value of around 12 km/s. This confirms that the rapid dynamics of the cascade is a bonafide effect and highlights the value of studying graphite as a contrasting materials system as compared to the well-known radiation effects in metals and oxides.

On a technical level, the short-lived but highly energetic events in Figs. 3 & 4 highlight the importance of the variable timestep algorithm. When the PKA is initiated the equations of motion are well-integrated using a timestep of 0.018 fs, but during the first collision this falls to just 0.0022 fs for a brief period, before increasing to a maximum of 0.025 fs midway between the first and second collisions. With each collision the timestep is temporarily reduced and the cycle repeats, and the timestep gradually trends upwards towards a constant value of 0.23 fs by the end of the simulation. Across each collision the conservation of energy is excellent, leading to shifts no greater than 0.1 eV and typically far less. Due to the efficiency of the variable timestep algorithm, the total simulation of 5 ps was completed in fewer than 30,000 timesteps, with around 10,000 steps required to

cover the first picosecond.

A second example of a 1 keV cascade in graphite is shown in Fig. 5(a), this time employing a different initial PKA direction. In this instance the cascade proceeds in a manner very different to that in Fig. 2. A branching structure is not observed, and instead the PKA is deflected into a channeling direction with a  $10\bar{1}2$  orientation. Once in the channel the PKA travels a substantial distance without creating permanent defects, losing energy at a constant rate of 18 eV per layer traversed. The kinetics of this process is summarized by Fig. 5(b) which shows the time evolution of the most energetic atom in the cascade. Up until an end-of-range collision at 0.083 ps, the atom in question is always the PKA. Whilst in the channel the PKA undergoes a series of collisions in which it passes through the middle of a hexagonal ring of atoms, losing kinetic energy on entry and regaining a portion of this upon exit. Since the energy loss of

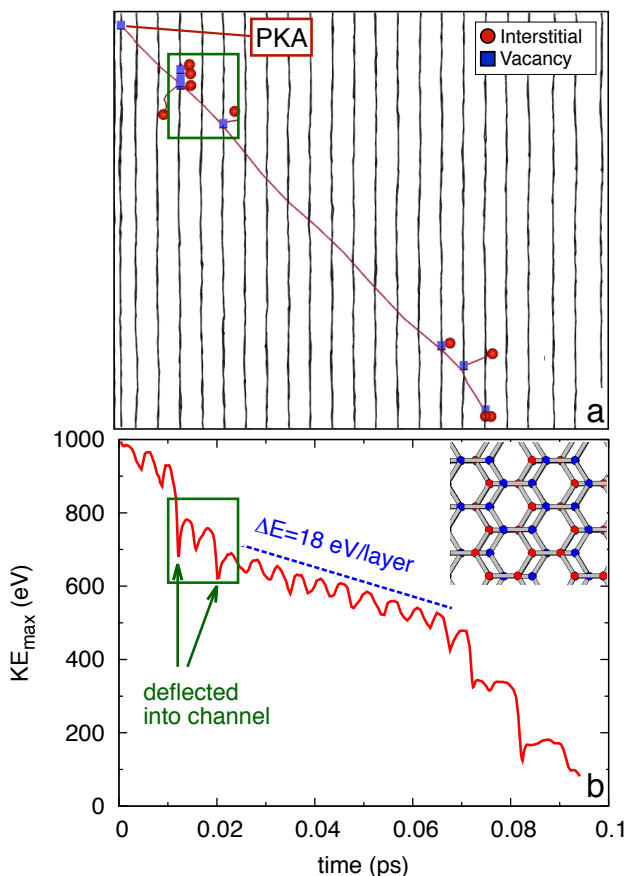


FIG. 5. (a) Snapshot for a 1 keV graphite cascade in which channeling occurs along a  $\langle 10\bar{1}2 \rangle$  direction. The PKA was initiated at the top-left of frame, travelling towards the bottom-right. (b) Maximum kinetic energy as a function of time. Green arrows indicate the collisions which deflect the PKA into the channel. Inset at top-right of panel denotes the pseudo-channels of graphite; blue and red circles represent the A and B planes, respectively.

18 eV/layer is below the threshold displacement energy (which we show below to be around 25 eV), the disruption is transient and the lattice quickly recovers. The process is repeated nine times, during which the PKA travels more than 30 Å and loses around 160 eV without creating a single permanent defect.

The channeling direction along which the PKA travels is shown in ball-and-stick form in the inset within Fig. 5(b). It is immediately apparent that this is not a prototypical channel such as found in a lattice with cubic symmetry, but instead a pseudo-channel in which the PKA must follow an undulatory path as it progresses through one layer to the next. We are not aware of this channeling direction having previously been identified for graphite, a situation that perhaps reflects the difficulty of anticipating the pseudo-channel in the first place. Even for conceptually straightforward channels such as those parallel or perpendicular to the c-axis, there are significant experimental difficulties associated with preparation of the sample and its alignment relative to the incident beam.<sup>42</sup> We return to this question of channeling in Section IV where we discuss the simulations in the context of the historical literature.

## B. Statistical analysis

Having outlined some of the qualitative features of radiation cascades in graphite, we now proceed to a quantitative treatment of various key properties. Statistical sampling is a crucial element of any cascade simulation analysis, and particularly so for graphite where the low packing fraction and anisotropic crystalline structure facilitates strong variations in radiation response as a function and direction. Up to thirty directions are sampled for each PKA energy, providing a high degree of precision which enables extraction of clear trends in the data.

Figure 6 shows the energy dependence of the quantities  $t_{\max}$  and  $t_{\text{end}}$  defined in Fig. 4. The solid points show the average value while the error bars denote one standard deviation. The magnitude of the latter indicates the high degree of variability between individual cascade events and highlights the importance of sampling many uncorrelated directions. Due to the large number of simulations, the standard error in the mean is around a factor of 5 smaller than the ranges shown in the figure, and hence the solid points provide a good estimate of the true mean of both quantities. One of the surprising facts to emerge from Fig. 6 is the weak energy dependence of the time of peak defects (upper panel), and spike cooling time (lower panel). For example, increasing the PKA energy by a factor of four from 500 eV to 2 keV changes  $t_{\max}$  by only 70% and  $t_{\text{end}}$  by 55%. This behavior reflects the fractal-like branching structure seen earlier in Fig. 2 where the cascade behavior is almost entirely ballistic, involving repeated splitting into a series of sub-cascades. Accordingly, increasing the PKA by a large factor makes only a relatively small difference to the cascade lifetime.

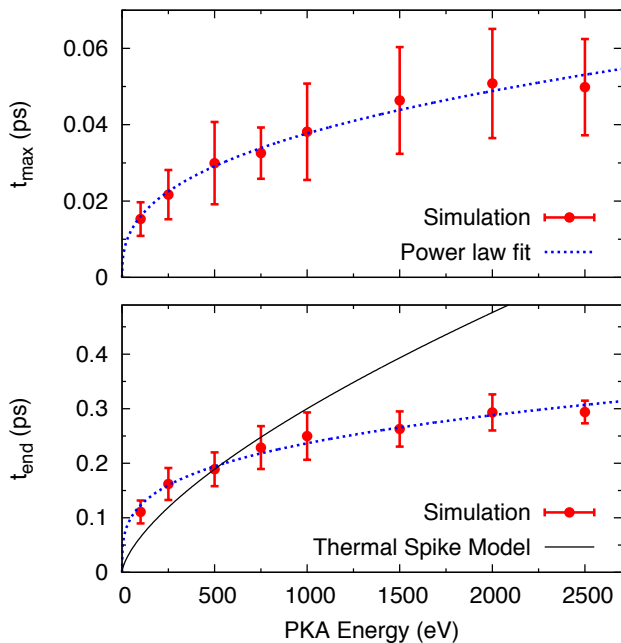


FIG. 6. (a) Dependence of  $t_{\max}$  as a function of PKA energy where  $t_{\max}$  is defined as the first time corresponding to the highest number of fast atoms, i.e.  $KE > 10$  eV. (b) Dependence of  $t_{\text{end}}$  as a function of PKA energy, where  $t_{\text{end}}$  is defined as the first instant at which there are no “warm atoms” (i.e. atoms with  $KE > 1$  eV).

To quantify the difference between graphite cascades and those in most other materials we show in the lower panel of Fig. 6 the energy dependence for a thermal spike produced when the energy of the PKA is delivered into a relatively compact region and induces local melting. Presuming a spherical spike for simplicity, an analytic solution<sup>43</sup> of the heat diffusion equation shows that the cooling time varies as  $E^{2/3}$ , where  $E$  is the PKA energy. This energy variation is shown as a solid black line in Fig. 6, using the data point at 500 eV as an arbitrary anchor point. Clearly the graphite cascades have an energy dependence entirely unlike the thermal spike model, confirming the previous visual impressions seen in Figs. 2 & 5 that localised melting and extended disordering do not occur in graphite.

Fitting to the simulation data reveals that both data sets are well-described by a power-law expression of the form  $aE^x$ , shown as a blue-dotted line in each panel. The fit holds over more than an order of magnitude, extending even to relatively low energies approaching the threshold displacement energy. For  $t_{\max}$ , which is the noisier of the two data sets due to smaller numerical values, the exponent  $x$  is 0.37, while for the cascade lifetime  $t_{\text{end}}$  the value  $x$  is 0.28 and the fitting quality is excellent. Since the exponent is so small, increasing the PKA energy to much larger values, for example, to 20 keV, only increases the spike lifetime by 80% relative to a 2.5 keV cascade. While we do not presently have a physical inter-

pretation for this power-law behaviour, the quality of the fit is striking and it would be instructive to test the trend for much higher energies and to examine whether it can be exploited in simplified, non-MD, models of cascade evolution.

Figure 7 shows the energy dependence of the size of the cascade and the range of the PKA. The latter is determined by simply taking the difference between the initial and final positions of the PKA atom, while the cascade length is defined as the largest distance between any two defects in the cascade. For the purposes of this analysis, a defect was defined as any atom with a local potential energy greater than  $-7$  eV/atom. Since the cohesive energy of graphite in the EDIP formalism is  $-7.361$  eV/atom, this corresponds to a strain energy of around 0.35 eV/atom. Visual inspection of the atoms identified in this way showed this measure provided a simple and accurate measure of the region affected by the cascade. As in Fig. 6, each data point is an average across as many as 30 different directions and the error bars denote one standard deviation. Also shown in Fig. 7 are straight line fits to the two data sets. To a good approximation both the PKA range and cascade extent scale linearly with energy. The gradient of both quantities are quite similar,  $0.27 \text{ \AA/eV}$  for the PKA range and  $0.31 \text{ \AA/eV}$  for the cascade extent. For the highest energy cascade of 2.5 keV the PKA range is around 85% of the cascade extent, and slightly smaller at lower energies. An immediate consequence of this linear variation is that increasing the PKA energy comes at high computational cost; numerical specifics and possible alternative strategies are outlined in the Discussion.

To quantify the process by which the PKA energy is converted into displacements we tracked the maximum kinetic energy  $KE_{\max}$  in every simulation and analyzed its time dependence. Motivated by data such as that

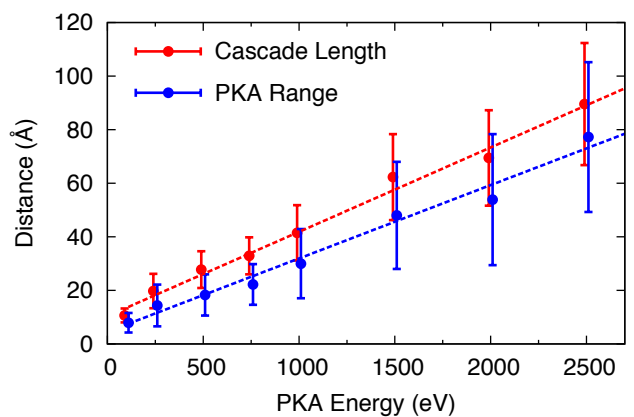


FIG. 7. Cascade length (red) and PKA range (blue) as a function of PKA energy. Error bars denote one standard deviation, and the lines are linear fits to the data. For visual clarity, the data sets are offset slightly to the left and right of the relevant energy value.

shown in Fig. 3, a collision was recorded if  $KE_{\max}$  increased by more than 5 eV following a minimal value. This metric robustly identifies all of the heavy collisions indicated by arrows in Fig. 3, as well as the much larger number of collisions for the channeling process in Fig. 5. Once  $KE_{\max}$  becomes sufficiently small, circa 50–100 eV, collisions are no longer identified since a subsequent rise in kinetic energy does not occur following a close approach.

The results of the analysis are summarized in Fig. 8, with the circles indicating the average number of collisions and the error bars indicating one standard deviation. The straight line is a linear fit to the data and intersects the average values with high accuracy; a companion plot employing the standard error of the mean is not shown as the resultant uncertainties are comparable in size to the circles used in the figure. Considering a PKA energy of 1 keV as an example, we see that on average less than 10 collisions are required to thermalize the PKA, and that accordingly the branching cascade seen in Fig. 2, with 9 collisions, is more typical than the channeling cascade (Fig. 5) which thermalizes after 19 collisions. From the inverse slope of the linear fit to the data we see that a typical collision loses 112 eV, a result which is consistent with visual inspection of the branching cascade. The linear behaviour holds over the entire energy range considered, and makes a useful starting point for estimating the behavior of more energetic cascades.

Two of the most crucial quantities to quantify in a radiation cascade simulation are the number of displaced atoms and the number of defects created. As noted in Section II, we define defects and displacements using a vacancy radius of 0.9 Å. The energy dependence of both data sets is shown in Fig. 9, along with the theoretical behavior predicted by the Kinchin-Pease (KP) [Ref. 44] and Norgett-Robinson-Torrens (NRT) [Ref. 45] models.

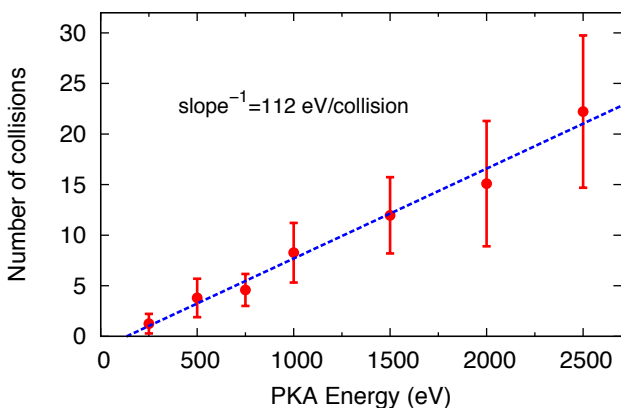


FIG. 8. Number of heavy collisions en-route to thermalization as a function of PKA energy. The analysis employs  $KE_{\max}$  (see Fig. 3) as discussed in the text. The blue line is a linear fit to the data, and the inverse value of the slope corresponds to an average energy loss of 112 eV/collision.

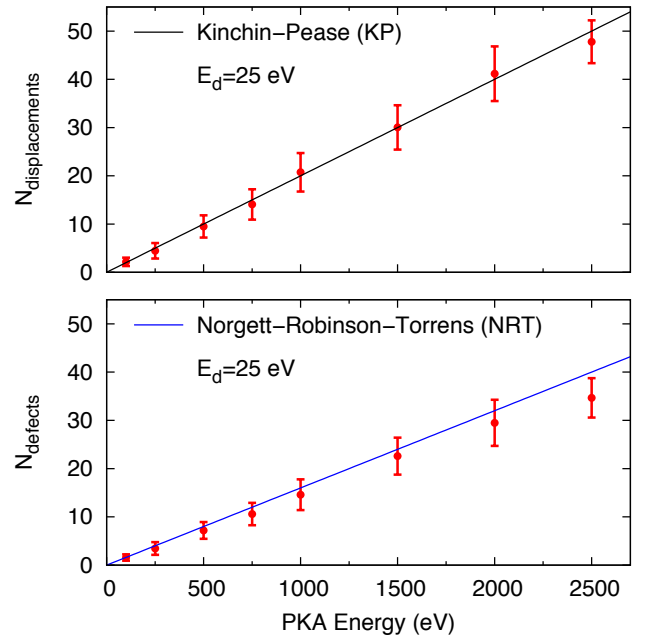


FIG. 9. Number of displacements (upper panel) and defects (lower panel) as a function of PKA energy. Error bars indicate the standard deviation. Defects are identified using a vacancy radius of 0.9 Å. The solid lines show the Kinchin-Pease and Norgett-Robinson-Torrens relationships assuming a threshold displacement energy,  $E_d$ , of 25 eV.

Both models employ the threshold displacement energy,  $E_d$ , as a single parameter; in the KP model the number of displacements is computed as  $E/(2E_d)$ , where  $E$  is the PKA energy, while in the modification of NRT an additional multiplicative factor of 0.8 is included to empirically describe recombination. Consistent with the experimental and computational literature, a value of  $E_d=25$  eV was assumed for the two models. The simulations show excellent correlation with the two theories, a result which is somewhat remarkable in itself since the KP and NRT treatments historically haven't had much predictive power, particularly in metal or oxide systems where defect recombination in the post-ballistic phase can lead to vastly fewer defects than displacements. For graphite, however, the simple models work extremely well, even down to the empirical factor of 0.8 which relates displacements to defects.

#### IV. DISCUSSION & CONCLUSION

One of the main insights to emerge from this study is the profound difference between cascades in graphite as compared to other widely-studied solids. The branching structure, absence of localized melting, and Kinchin-Pease-type defect generation are all examples of behavior which place graphite in a special category. Equally interesting is that many of these insights were correctly

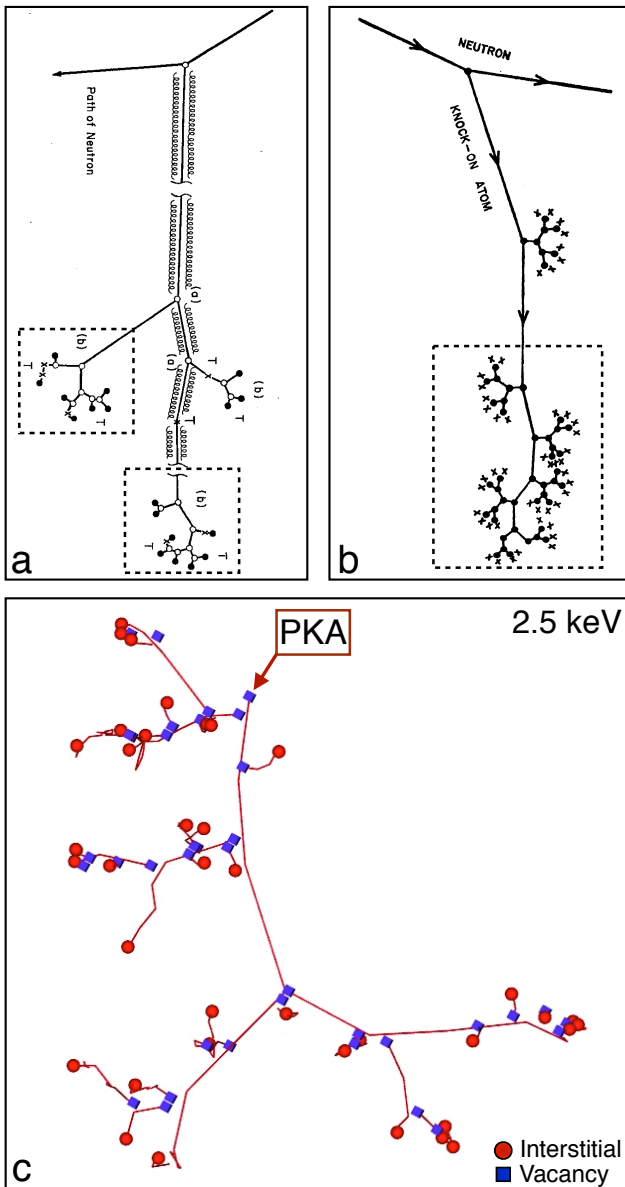


FIG. 10. Comparison between literature models of graphite radiation damage and simulations performed in this work. The dotted boxes in the upper schematics have been added to highlight the cascade portion within the diagram. (a) Schematic from Nightingale (p. 213 in Ref. 46). (b) Schematic from Simmons (p. 20 in Ref. 47), (c) Cascade simulation for a PKA energy of 2.5 keV. Schematics reprinted with permission from Elsevier.

qualitatively understood long ago, as demonstrated by Fig. 10, which compares two literature schematics of cascades from fast neutron damage in graphite [panels (a,b)] with a 2.5 keV simulation from this work. Both schematics date from the 1960's, with panel (a) from Nightingale<sup>46</sup> and panel (b) from Simmons.<sup>47</sup> Although one could argue the minor details of the schematics, the broad picture is clearly correct, particularly regarding the

branching structure of the trajectories. As for the origin of this behavior, a definitive answer cannot yet be given, but possible reasons include the low mass of carbon relative to many solids, the high thermal conductivity of graphite, and the low-packing fraction. All of these ideas are amenable to computer simulation through controlled comparison studies, and represent a promising direction for future work.

Where the simulations offer a clear advance over previous empirical understanding is in quantitation. Key quantities such as the threshold displacement energy, PKA range, mean free path, etc, have been subject to considerable uncertainty. In the case of the range of the PKA, Simmons<sup>47</sup> quotes a value of 67 Å for a 1 keV PKA, as compared to the 30 Å computed here. The same source similarly overestimates energy loss per collision, listing a value of 196 eV per collision as compared to our value of 112 eV per collision. Earlier hard-sphere results reported in Nightingale<sup>46</sup> disagree to an even larger extent, predicting a mean-free-path between collisions of 84 Å for a 1 keV PKA. Establishing  $E_d$  for graphite has also been highly problematic, with literature estimates covering a wide range, spanning 10 to 60 eV [Refs. 48 and 49]. In contrast, our value of 25 eV determined by the Kinchin-Pease and NRT relationships is statistically sound and unambiguously shows that a value of 60 eV is much too high, a point similarly noted by Burchell.<sup>50</sup> We note that Yazyev *et al.*<sup>9</sup> also estimated an  $E_d$  value of 25 eV from their density functional theory calculations, while Smith and Beardmore<sup>8</sup> reported 34.5 eV, and Hehr *et al.*<sup>10</sup> reported around 45 eV. As a caveat, we note that direct analysis of MD trajectories can provide an even more refined estimate of  $E_d$ , and so the present number should not be considered the final value.

Regarding channeling, there have been a few experimental studies,<sup>42,51</sup> but the measurements are difficult and sample preparation and alignment are paramount. Channeling down a  $\langle 0001 \rangle$  channel (i.e. parallel to the  $c$ -axis) has been observed (see Fig. 1 in Ref. 51 for a schematic), and long ago it was proposed<sup>52</sup> that channeling might occur in the  $\langle 1120 \rangle$  direction. The simulations show that while channeling is not a common occurrence, it is certainly possible under certain conditions. To the best of our knowledge the channeling process shown in Fig. 5 has not been previously described or envisaged and is an excellent example how computer simulation can provide new insights into radiation phenomena. The closest connection with previous work is the calculation of Kaxiras and Pandey<sup>53</sup> which found that a hexagon centre defect in graphite has an energy of 19.5 eV, close to the energy loss rate observed in the simulations, suggesting that the PKA has to climb up the potential hill of  $\sim 18$  eV before being squeezed out again. Finally, we note that one of the factors which limits channeling is that the atoms are invariably initially located on a lattice site and hence displacement tends to cause an immediate collision with a nearby atom. A different situation exists for interstitial carbons, but such atoms are

present in low numbers and cannot be considered typical.

Looking to future simulations of cascades in graphite, several conclusions immediately present themselves. Firstly, there are promising prospects to study how temperature affects the evolution of the cascade and the associated relaxation dynamics. As discussed by Kelly,<sup>54</sup> a large experimental literature exists for graphite on dimensional change, mechanical behavior and thermal properties. However, simulations have not been applied to the atomistic perspective. It would be particularly fruitful to combine defect analysis as carried out in this work with density functional theory calculations of defect energetics and activation barriers for migration and recombination. This knowledge would be particularly beneficial for understanding graphite structural evolution under irradiation such as the recently proposed ruck-and-tuck model.<sup>55</sup> On a technical level, one unexpected detail is that wall thermostats are not essential as the simulation cells are sufficiently large that the excess kinetic energy of the PKA is easily accommodated within the cell. For the simulations performed here, the excess energy was typically 0.005 eV/atom and hence the temperature rise is of the order tens of Kelvin. More significant is the very large number of atoms required to contain the cascade as the PKA energy rises. Extrapolating the data in Fig. 7 to higher energies shows that very large simulation cells are required to reliably avoid the cascade interacting with the boundaries. To contain a 5 keV cascade at a  $2\sigma$  confidence level (97.5%) requires a cell of 2 million atoms; the required supercell side-length is 263 Å, comprising 253 Å from the extrapolation of the mean cascade length plus two standard deviations, and a boundary layer of 10 Å. Higher energies make the numerics even more extreme, as the number of atoms required scales as  $E^3$  due to the linear variation shown in Fig. 7. For example, 40 keV cascades have been simulated in a variety of oxides,<sup>56</sup> but the same calculations in graphite would require 1 billion atoms, far beyond what is presently practicable for carbon. For large systems it may be preferable

instead to develop a stochastic approach based upon the atomistically-derived information extracted from molecular dynamics. Such a scheme should in-principle be possible given the high statistical reproducibility evident in the computational data presented here.

In summary, we have performed molecular dynamics simulations of radiation damage cascades in graphite. To the best of our knowledge, this is the first comprehensive study of its kind. We find strikingly different behavior to metals and oxides, with the graphite cascades exhibiting a fractal-like branching structure and binary-collision-type behavior. Statistical analysis across a large number of initial directions and energies shows that no thermal spike is produced, and that the production of displacements and defects is well-described by the Kinchin-Pease and Norgett-Robinson-Torrens models, respectively. The simulations quantify important quantities such as the range of the primary knock-on atom and the average energy loss per collision, as well as providing a starting point for future studies of defect generation under irradiation. This information is invaluable for understanding the role of graphite under irradiation, a topic of great importance for lifetime extension of existing nuclear reactors and next-generation designs operating at high temperature.

#### ACKNOWLEDGMENTS

The project used advanced computational resources provided by the iVEC facility at Murdoch University. Discussions with Malcolm Heggie and Alice McKenna are acknowledged. HJC, DLR and DKR thank the Engineering and Physical Sciences Research Council and the Technology Strategy Board for their support through grants EP/I003312/1 and 101437, respectively. ISM and NAM thank the Australian Research Council for fellowships, and MR thanks the Australian Nuclear Science and Technology Organisation for support.

---

\* Mail: N.Marks@curtin.edu.au

<sup>1</sup> W. J. Weber, R. C. Ewing, C. R. A. Catlow, T. Diaz de la Rubia, L. Hobbs, and C. Knoshita, *J. Mater. Res.* **13**, 1434 (1998).

<sup>2</sup> K. Nordlund, M. Ghaly, R. S. Averback, M. Caturla, T. Diaz de la Rubia, and J. Tarus, *Phys. Rev. B* **57**, 7556 (1998).

<sup>3</sup> D. J. Bacon, F. Gao, and Y. N. Osetsky, *Nucl. Instrum. Meth. B* **153**, 87 (1999).

<sup>4</sup> D. J. Bacon, F. Gao, and Y. N. Osetsky, *J. Nucl. Mater.* **276**, 1 (2000).

<sup>5</sup> N. A. Marks, *Computer-based Modeling of Novel Carbon Systems and Their Properties: Beyond Nanotubes*, edited by L. Colombo and A. Fasolino (Springer, 2010).

<sup>6</sup> C. P. Ewels, R. H. Telling, A. A. El-Barbary, M. I. Heggie, and P. R. Bridson, *Phys. Rev. Lett.* **91**, 025505 (2003).

<sup>7</sup> R. H. Telling and M. I. Heggie, *Philos. Mag.* **87**, 4797 (2007).

<sup>8</sup> R. Smith and K. Beardmore, *Thin Solid Films* **272**, 255 (1996).

<sup>9</sup> O. V. Yazyev, I. Tavernelli, U. Rothlisberger, and L. Helm, *Phys. Rev. B* **75**, 115418 (2007).

<sup>10</sup> B. D. Hehr, A. I. Hawari, and V. H. Gillette, *Nucl. Technol.* **160**, 251 (2007).

<sup>11</sup> G. B. Neighbour, ed., *Management of Ageing in Graphite Reactor Cores* (The Royal Society of Chemistry, 2007).

<sup>12</sup> J. Haller, <http://www.euronuclear.org/events/enc/enc2012/transactions/ENC2012-transactions-plant-operations.pdf>, accessed: 2014-05-20.

<sup>13</sup> "Technology Roadmap Update for Generation IV Nuclear Energy Systems," <https://www.gen-4.org/gif/upload/docs/application/pdf/2014-03/gif-tru2014.pdf>,

- accessed: 2014-05-20.
- <sup>14</sup> J. B. Gibson, A. N. Goland, M. Milgram, and G. H. Vineyard, *Phys. Rev.* **120**, 1229 (1960).
  - <sup>15</sup> M. S. Daw and M. I. Baskes, *Phys. Rev. Lett.* **50**, 1285 (1983).
  - <sup>16</sup> M. S. Daw and M. I. Baskes, *Phys. Rev. B* **29**, 6443 (1984).
  - <sup>17</sup> G. V. Lewis and C. R. A. Catlow, *J. Phys. C Solid State* **18**, 1149 (1985).
  - <sup>18</sup> T. S. Bush, J. D. Gale, C. R. A. Catlow, and P. D. Battle, *J. Mat. Chem.* **4**, 831 (1994).
  - <sup>19</sup> G. R. Lumpkin, K. L. Smith, M. G. Blackford, B. S. Thomas, K. R. Whittle, N. A. Marks, and N. J. Zaluzec, *Phys. Rev. B* **77**, 214201 (2008).
  - <sup>20</sup> R. Smith, *Proc. Roy. Soc. Lond. A* **431**, 143 (1990).
  - <sup>21</sup> J. Tersoff, *Phys. Rev. Lett.* **61**, 2879 (1988).
  - <sup>22</sup> D. W. Brenner, *Phys. Rev. B* **42**, 9458 (1990).
  - <sup>23</sup> M. I. Heggie, *J. Phys.: Condens. Mat.* **3**, 3065 (1991).
  - <sup>24</sup> K. Nordlund, J. Keinonen, and T. Mattila, *Phys. Rev. Lett.* **77**, 699 (1996).
  - <sup>25</sup> A. V. Krashennikov and K. Nordlund, *J. Appl. Phys.* **107**, 071301 (2010).
  - <sup>26</sup> N. A. Marks, *Phys. Rev. B* **63**, 035401 (2001).
  - <sup>27</sup> N. Marks, *J. Phys.: Condens. Mat.* **14**, 2901 (2002).
  - <sup>28</sup> J. F. Ziegler, J. P. Biersack, and U. Littmark, *The Stopping and Range of Ions in Solids*, Vol. 1 (Pergamon, New York, 1985).
  - <sup>29</sup> D. W. M. Lau, D. G. McCulloch, N. A. Marks, N. R. Madson, and A. V. Rode, *Phys. Rev. B* **75**, 233408 (2007).
  - <sup>30</sup> R. C. Powles, N. A. Marks, and D. W. M. Lau, *Phys. Rev. B* **79**, 075430 (2009).
  - <sup>31</sup> I. Suarez-Martinez and N. A. Marks, *Appl. Phys. Lett.* **99**, 033101 (2011).
  - <sup>32</sup> I. Suarez-Martinez, P. J. Higginbottom, and N. A. Marks, *Carbon* **48**, 3592 (2010).
  - <sup>33</sup> I. Suarez-Martinez and N. A. Marks, *Carbon* **50**, 5441 (2012).
  - <sup>34</sup> N. A. Marks, M. Lattemann, and D. R. McKenzie, *Phys. Rev. Lett.* **108**, 075503 (2012).
  - <sup>35</sup> J. F. Justo, M. Z. Bazant, E. Kaxiras, V. V. Bulatov, and S. Yip, *Phys. Rev. B* **58**, 2539 (1998).
  - <sup>36</sup> N. A. Marks, J. M. Bell, G. K. Pearce, D. R. McKenzie, and M. M. M. Bilek, *Diam. Relat. Mater.* **12**, 2003 (2003).
  - <sup>37</sup> G. K. Pearce, N. A. Marks, D. R. McKenzie, and M. M. M. Bilek, *Diam. Relat. Mater.* **14**, 921 (2005).
  - <sup>38</sup> M. Robinson, N. A. Marks, K. R. Whittle, and G. R. Lumpkin, *Phys. Rev. B* **85**, 104105 (2012).
  - <sup>39</sup> J. J. Thomson, *Philos. Mag.* **7**, 237 (1904).
  - <sup>40</sup> R. H. Telling, C. P. Ewels, A. A. El-Barbary, and M. I. Heggie, *Nature Materials* **2**, 333 (2003).
  - <sup>41</sup> N. A. Marks, N. C. Cooper, D. R. McKenzie, D. G. McCulloch, P. Bath, and S. P. Russo, *Phys. Rev. B* **65**, 075411 (2002).
  - <sup>42</sup> B. S. Elman, G. Braunstein, M. S. Dresselhaus, G. Dresselhaus, T. Venkatesan, and B. Wilkens, *J. Appl. Phys.* **56**, 2114 (1984).
  - <sup>43</sup> N. A. Marks, *Phys. Rev. B* **56**, 2441 (1997).
  - <sup>44</sup> G. H. Kinchin and R. S. Pease, *J. Nucl. Energy* **1**, 200 (1954).
  - <sup>45</sup> M. J. Norgett, M. T. Robinson, and I. M. Torrens, *Nucl. Eng. Des.* **33**, 50 (1975).
  - <sup>46</sup> R. E. Nightingale, ed., *Nuclear Graphite* (Academic Press, New York and London, 1962).
  - <sup>47</sup> J. H. W. Simmons, ed., *Radiation Damage in Graphite* (Pergamon Press, 1965).
  - <sup>48</sup> S. J. Zinkle and C. Kinoshita, *J. Nucl. Mat.* **251**, 200 (1997).
  - <sup>49</sup> F. Banhart, *Rep. Prog. Phys.* **62**, 1181 (1999).
  - <sup>50</sup> T. D. Burchell, ed., *Carbon Materials for Advanced Technologies* (American Carbon Society, 1994).
  - <sup>51</sup> E. Yagi, T. Iwata, T. Urai, and K. Ogiwara, *J. Nucl. Mater.* **334**, 9 (2004).
  - <sup>52</sup> M. Balarin, *Phys. Status Solidi* **2**, 60 (1962).
  - <sup>53</sup> E. Kaxiras and K. C. Pandey, *Phys. Rev. Lett.* **61**, 2693 (1988).
  - <sup>54</sup> B. T. Kelly, ed., *Physics of Graphite* (Applied Science Publishers, 1981).
  - <sup>55</sup> M. I. Heggie, I. Suarez-Martinez, C. Davidson, and G. Haf-fenden, *J. Nucl. Mater.* **413**, 150 (2011).
  - <sup>56</sup> K. Trachenko, M. T. Dove, E. Artacho, I. T. Todorov, and W. Smith, *Phys. Rev. B* **73**, 174207 (2006).